Vortex-model-based Multi-objective Optimization of Winglets for Wind Turbines using Machine Learning

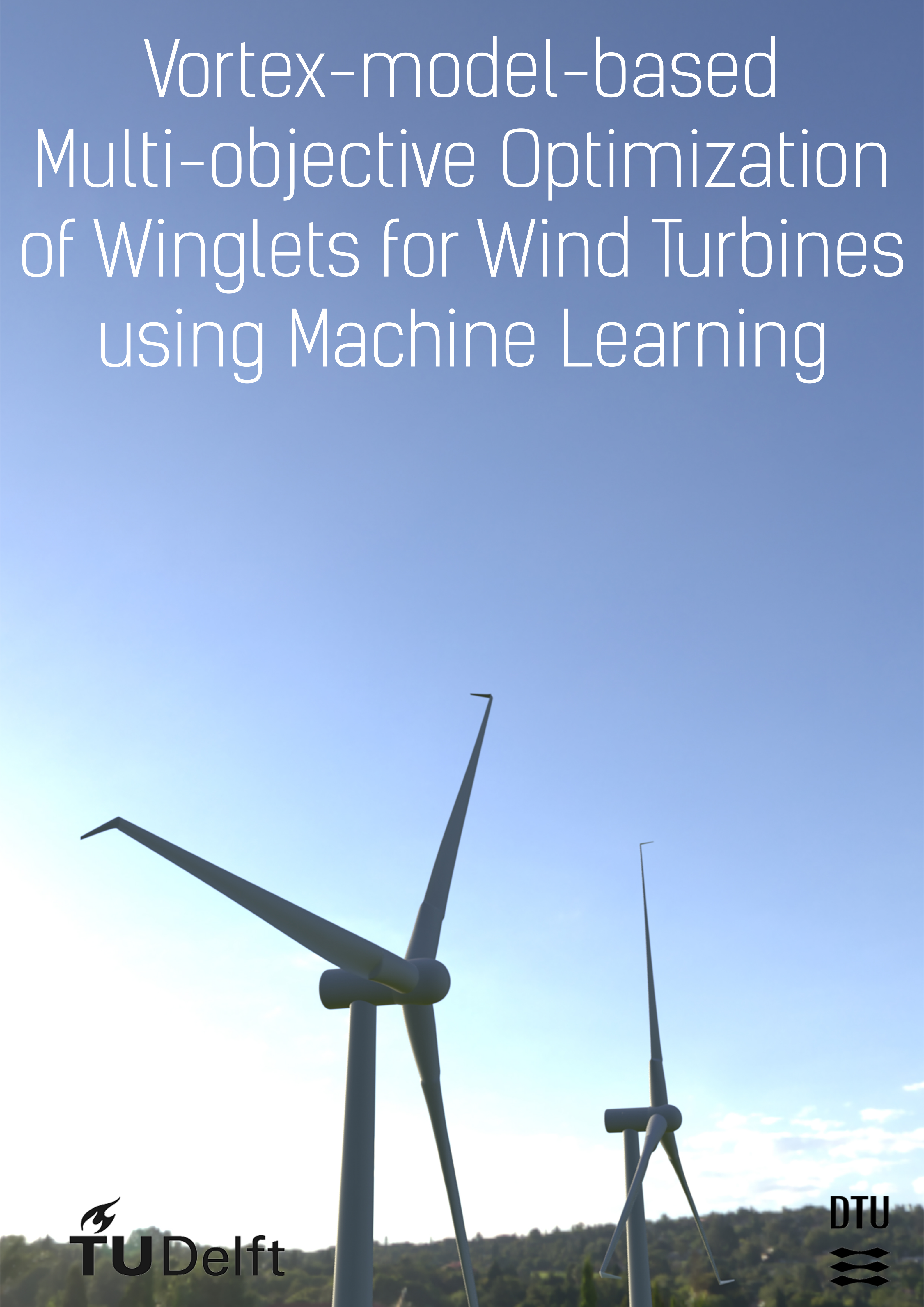

This page is intentionally left blank.

Vortex-model-based Multi-objective Optimization of Winglets for Wind Turbines using Machine Learning

Master of Science Thesis

by

Nick Leenders

to obtain the degree of: Master of Science in Aerospace Engineering at the Delft University of Technology and Master of Science in Engineering (European Wind Energy) at the Technical University of Denmark

Student number:	4392949 (TUD), s193520 (DTU)		
Project Duration:	November 2020 - July 2021		
Supervisors:	Wei Yu	Assistant Professor	Delft University of Technology
	Mac Gaunaa	Senior Scientist	Technical University of Denmark
	Clym Stock-Williams	Researcher	TNO Delft
	Marco Caboni	Researcher	TNO Delft

July 31, 2021

Amsterdam, The Netherlands

Abstract

In order to reduce the levelised cost of energy, the rotors of wind turbines are increasing in size. To increase the energy yield, wind turbine rotors need to have an innovative tip design; such as winglets. Winglets are used widely in aircraft design; however, they remain mostly absent in state-of-the-art wind turbine design. The low-fidelity wind turbine design models used by industry, such as BEM, are insufficient to capture the full 3D flow physics in such an innovative design. Therefore, high-fidelity methods, such as vortex methods, are becoming more and more important in such a design phase in wind energy research. Single-objective optimisation has been applied in earlier works to maximise power production. Winglets have shown the potential of increasing power production while simultaneously increasing the design-driving loads (DDLs), for example, the thrust or flapwise bending moment. This work focuses on optimisation using machine learning of a winglet that increases power production without increasing DDLs.

A parameterised design for a winglet on a wind turbine is created. Different design constraints, such as DDLs or a diameter constraint, are explored to determine under which constraints and conditions a winglet can have an added value to the wind turbine blade design. Multi-objective Bayesian optimisation is used to maximise the rotor's power production and minimise DDLs. Surrogate models, created using machine learning techniques such as Gaussian Processes and Bayesian Neural Networks, are used in combination with an acquisition function, to determine what designs should be evaluated by the lifting line model AWSM. This has the goal to obtain designs that lie on the Pareto front of two or more objectives. The recent Bayesian Neural Networks were able to find the Pareto front most effectively in this work. Furthermore, the results show that different DDL constraints led to different winglet designs, with noticeable differences between upwind and downwind winglet designs obtained by the optimiser. Both a downwind and upwind winglet were found to be able to increase power without increasing the thrust, root flapwise bending moment and flapwise bending moment at 80% of the rotor radius.

Acknowledgements

This thesis has been created almost entirely from home office. First from my room in Copenhagen, after that my room at my parent’s place in Weert for a brief period, and now finally, from my room in Amsterdam. Working on my thesis solely from home office can be a challenge, which would have not been possible without the people that have helped me during this period.

First of all, I would like to thank my supervisors Wei Yu, Mac Gaunaa and Marco Caboni for being there almost every online weekly meeting to listen to my updates and help me out with any questions I had. I would also like to thank Carlos Simão Ferreira and Clym Stock-Williams for helping me out there during the start-up phase of my project. A thank you also goes out to Vivek Ahuja, who helped me with the FlightStream setup in the early stages of the project.

I would like to thank my friends and housemates, with whom I could always go for a coffee or beer, which has helped me to stay motivated in this time.

Besides that, I would like to thank my fellow students from EWEM, who made the last two years a great time. Especially the activities outside classes, such as our trip to Sweden has been an unforgettable experience.

Finally and most importantly, I would like to thank my family and parents especially for supporting my studies and all other opportunities I took during my studies. As well as my brother, with whom I could always have a laugh during the few months I lived at my parents’ place during this period.

Contents

List of Figures

List of Tables

Nomenclature

Abbreviations

AEP	Annual Energy Production
ARD	Automatic Relevance Determination
BEM	Blade Element Momentum
BNN	Bayesian Neural Network
BO	Bayesian Optimisation
CFD	Computational Fluid Dynamics
CoE	Cost of energy
DDL	Design driving load
EHVI	Expected Hypervolume Improvement
EI	Expected Improvement
GA	Genetic Algorithm
GP	Gaussian Process
GPU	Graphics processing unit
LHC	Latin Hypercube
MLP	Multilayer perceptron
NN	Neural Network
PoI	Probability of Improvement
RANS	Reynolds-averaged Navier Stokes
RBF	Radial Basis Function
RF	Random Forest
RMSE	Root mean squared error
SGD	Stochastic Gradient Descent

List of Symbols

α	Angle of attack	degrees
α_{eff}	Effective angle of attack	degrees
α_{ind}	Induced angle of attack	degrees
$\gamma_{w,r}$	Winglet root twist	degrees
$\gamma_{w,t}$	Winglet tip twist	degrees
λ	Winglet sweep angle	degrees

Ω	Rotational velocity of a wind turbine	rad/s
ϕ	Winglet cant angle	degrees
ψ	Hidden units	-
σ	Activation function	-
τ_w	Winglet taper ratio	-
$\hat{f}$	Surrogate function	-
a	Axial induction factor	-
b	Wing length or blade length	m
C_D	Drag coefficient	-
C_L	Lift coefficient	-
C_M	Moment coefficient around span-wise axis	-
C_P	Power coefficient	-
C_{pres}	Pressure distribution	-
$c_{w,r}$	Winglet root chord	m
$c_{w,t}$	Winglet tip chord	m
D_{ind}	Induced drag	N
ext_R	external radial induced velocity	m/s
f	Objective function	-
F_{rw}	Force exerted by the rotor on the wake	N
F_{wr}	Force exerted by the wake on the rotor	N
h	Winglet height	m
$m_{f,0.8}$	Flapwise bending moment at 80% of the blade's radius	Nm
$m_{f,0.9}$	Flapwise bending moment at 90% of the blade's radius	Nm
$m_{f,r}$	Root flapwise bending moment	Nm
N_{chord}	Panels in the chordwise direction	-
N_{span}	Panels in the spanwise direction	-
p	Pressure	N^2/m
P_{AD}	Power extracted from an actuator disk	W
r_w	Winglet radius	m
u_i	induced wake convection speed	m/s
U_R	Velocity at actuator disk	m/s
U_∞	Free stream velocity in x	m/s
U_{ind}	Induced velocities in axial direction	m/s
V_{ind}	Induced velocities in tangential direction	m/s

w	Downwash	m/s
W_{ind}	Induced velocities in radial direction	m/s
$x_{w,r}$	Winglet root x-location	m
$y_{w,r}$	Winglet root y-location	m

1

Introduction

Rotors of wind turbines are increasing in size to reduce the Cost of Energy (CoE), by increasing the wind turbine's Annual Energy Production (AEP). By improving wind turbine blades using winglets, the energy yield can be increased. Although winglets are already commonly used in modern aeroplanes, they are mostly absent in state-of-the-art wind turbine blade designs. A winglet displaces the trailing vortex at the blade's tip and changes the induced velocities at the blade, which could increase the overall power production of the rotor. Ultimately, this changes the blade's load distribution, which could also increase unwanted loads in the flapwise direction of the blade. Whether a winglet can be beneficial to the blade's design is highly dependent on the set constraints, as different constraints can result in very different rotor designs as argued by Loenbaek et al. [1]. This work will therefore investigate under which constraints the design of a wind turbine can actually benefit from a winglet, by minimising the flapwise loads from the winglet while maximising the power. For aeroplanes, winglets are usually pointing upwards due to ground clearance, however, for wind turbines, upwind and downwind are both viable options. Downwind winglets on wind turbines have the issue of decreasing the tower clearance. For simplification, it is therefore assumed that whenever a downwind winglet is considered, a downwind rotor is used.

To analyse the effects of a winglet on wind turbine design, aerodynamic analysis tools are used in this thesis. Examples of such tools are lifting line codes, 3D panel codes, or Navier-Stokes solvers. The latter will be termed CFD in this thesis. One of these aerodynamic analysis methods will be chosen to perform optimisations of the blade's geometry. However, these aerodynamic analysis methods, which can provide an insight into aerodynamic loads, have long-running times. Moreover, the use of different constraints and objectives can require many iterations of the aerodynamic analysis method. Surrogate-assisted modelling can hence reduce the number of iterations needed to reach an optimum design. Machine learning methods such as Bayesian Neural Networks by Briffoteaux et al. [2] or Gaussian Processes in Bayesian Optimisation by Stock-Williams et al. [3] have recently shown promising results in surrogate-assisted optimisation.

1.1. Objective and research questions

The objective of the research is to find a feasible method to design a winglet for a wind turbine blade and to use this method to investigate under what constraints a winglet can contribute to the design of a wind turbine blade. The objective is therefore stated with the main research question with corresponding sub-objectives:

"To find a feasible method for parameterised design optimisation for the multi-objective design of a winglet for a wind turbine blade, under different kinds of constraints."

- What is an effective parameterisation method for a wind turbine winglet?
- How do different design constraints influence the design of the winglet and is it possible to increase power under those constraints, without an increase in flapwise loads?

- How to implement an automatic workflow for which the optimiser can optimise the parameterised design, without the need for human interaction?
- What are the benefits of using advanced machine learning techniques, such as Gaussian Processes (GP) or Neural Networks (NN), for surrogate modelling to reduce computational time when optimising wind turbine winglet design?
- How do upwind or downwind winglets compare to each other on the optimisation for different objectives?

1.2. Approach

This section explains the approach that will be taken to answer this thesis' research questions.

Firstly, a suitable aerodynamic analysis tool has to be chosen. The aerodynamic analysis model needs to have a short enough runtime to investigate different objectives and constraints. Moreover, the model needs to be able to work with a parameterised design. CFD has therefore been ruled out due to its long run times and the need for a volume mesh, which could create difficulties with a parameterised winglet. Vortex models are therefore chosen in this thesis as the aerodynamic analysis tool.

Secondly, two vortex models will be compared after which one of the models is chosen to perform winglet optimisations. One of the optimisation methods is a 3D panel code, which requires a mesh. Therefore, a parameterised geometry has to be created which can be meshed. For the lifting line code, no mesh is required, so this will be a simpler task for lifting line. A parameterisation method will be chosen that can cover the design space to the highest possible degree, keep the number of design parameters to a minimum and is able to provide a clear overview of the influence of the design parameters.

Thirdly, the optimisations will be divided into different cases to investigate what optimum designs will be found by the optimiser for different objectives and constraints. This will be done to investigate the effect of different objectives and constraints for both upwind and downwind winglets. This work will concern multi-objective optimisation, where power will be maximised for and DDLs will be minimised for. Different DDLs will be minimised in different optimisation cases so it can be investigated whether power can be increased without the increase of a DDL. As it is unknown beforehand if this is achievable, multi-objective optimisation is used instead of constrained optimisation, so if an increase in power without an increase in DDL is not possible, a Pareto front of solutions can still be presented.

The optimisation technique that will be used to this end is Bayesian Optimisation (BO). BO builds a probabilistic model of the objective function, where the objective function is the aerodynamic performance evaluated by the aerodynamic analysis tool in this case. The probabilistic model is called the surrogate model, for which usually a Gaussian Process (GP) is used. However, other surrogate models will be explored in this thesis as well, which are Bayesian Neural Networks (BNN) and Random Forest (RF). BO uses an acquisition function to search the surrogate model effectively to decide what design should be evaluated by the aerodynamic analysis tool. This way, BO can explore and exploit the design space effectively to find the Pareto front for two or more objectives.

1.3. Report outline

The aforementioned research questions in section 1.1 will be answered with the approach introduced in section 1.2 in this thesis. The structure of the thesis is as follows:

- Chapter 2 describes the current state of the art in winglet design for wind turbines. This chapter defines the research gap in the field by looking at previous research done on wind turbine winglets and parameterised design optimisation.
- Chapter 3 will discuss the setup that is used to design the geometry of the wind turbine and winglet and describes the 3D panel code and lifting line code that is used as the aerodynamic analysis method. The aerodynamic analysis methods will be validated against reference results from CFD in this chapter and ultimately one aerodynamic analysis method will be chosen to continue with.
- Chapter 4 will present the objectives, that are maximised or minimised, of the design and what constraints are chosen to assess whether a wind turbine blade can benefit from a winglet under those constraints. Different optimisation cases will be set up to investigate the effect of different

objectives and constraints. The optimisation cases will be described in this chapter. Furthermore, BO will be explained more thoroughly in this chapter.

- Chapter 5 will present the results for different optimisation cases and show the performance of some of the designs found by the optimiser.
- Chapter 6 will describe the used surrogate-assisted optimisation models' working principles in more detail. A comparison between different models will be done to investigate what surrogate model is best suited for this optimisation task.
- Chapter 7 will discuss the results found from the optimisation cases and discuss the difference between them. Any other findings from the optimisations will also be discussed here.
- Chapter 8 will summarise the findings obtained throughout this thesis and includes recommendations for further research on the topic.

2

State of the art

This chapter will present the theoretical basis as well as the relevant prior literature to identify the research gap. Section 2.1 will explain the aerodynamic principles of winglets. In section 2.2, firstly, different parameterisation methods will be presented and shortly discussed. Secondly, the importance of constraints and the effect on the design of a winglet is shown. In section 2.3 the different aerodynamic analysis methods for design optimisation found in the literature will be shown and their appliance will be discussed. Section 2.4 will discuss the different surrogate-assisted optimisation methods.

2.1. Aerodynamic phenomena around a winglet

This section concerns the aerodynamic phenomena that apply to a winglet. Firstly, section 2.1.1 will explain the principles of a winglet for an aeroplane accompanied by relevant research. Aeroplane winglets are discussed at first as more research has been conducted on winglets in this area. Secondly, section 2.1.2 explains the differences in aerodynamic principles between a winglet for a wind turbine and an aeroplane. Relevant research about the analysis of winglets as well as the results of winglet optimisation studies is presented.

2.1.1. A non-rotating winglet

As this thesis focuses on the design of a winglet, this subsection will explain the principles of a winglet. As there is more research done on winglets for the non-rotating case, as is the case for aircraft, research will be presented for aircraft only first, where the next subsection will present research for winglets on wind turbines. A simple representation of winglet parameters is shown in fig. 2.1, which is used as the convention throughout this thesis.

A winglet functions to displace and spread out the trailing vortices generated at the tip of a wing.

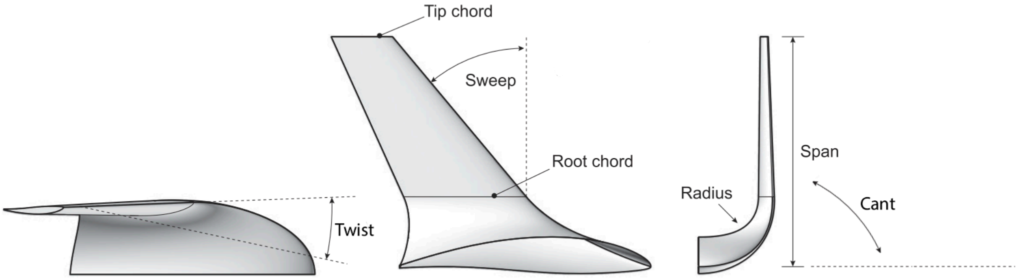

Figure 2.1: Winglet parameters taken from Hansen and Mühle [4]

For non-rotating cases, this ultimately reduces the induced drag. Induced drag can be explained by considering a finite wing as a vortex filament, which consists of a bound vortex, that is fixed on a certain location on the lifting line. Due to the Helmholtz theorem, a vortex filament cannot end in a fluid, so from this finite lifting line two trailing vortexes are created and a shed vortex as shown in fig. 2.2 for a lifting line with length b. The shed vortex is extended into infinity when there is no change in circulation and its influence is therefore neglected in steady situations.

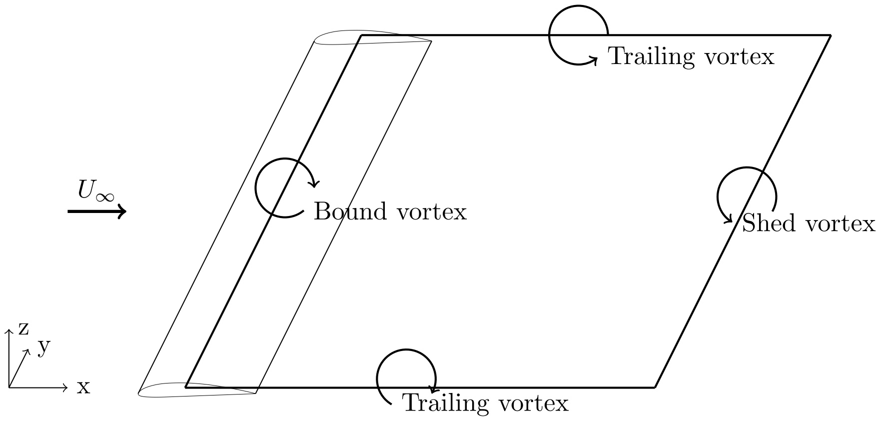

Figure 2.2: Vortices for a finite wing. Based on Katz and Plotkin [5]

Now consider the trailing vortex in the yz-plane, as in fig. 2.3, where $y = -b/2$ at the root and $y = b/2$ at the tip of the lifting line. The influence of the root vortex is ignored in this figure. The presence of the trailing vortex makes flow 'leak' from under the lifting line (the pressure side) towards above the lifting line (the suction side), so the fluid moves from the high-pressure region to the low-pressure region. This effect induces a velocity perpendicular to the free stream, which then results in a higher downwash at the tip. The downstream profile can be calculated using the Biot-Savart law, as shown in eq. (2.1) [6], assuming no change in circulation in time.

$$\mathbf{dV} = \frac{\Gamma}{4\pi}\frac{\mathbf{dl}\times\mathbf{r}}{|\mathbf{r}|^3} \tag{2.1}$$

The Biot-Savart law can then be used to calculate the induced velocity at a point P by a semi-infinite vortex as in eq. (2.2).

$$V = \frac{\Gamma}{4\pi h} \tag{2.2}$$

Where h is the distance between the semi-infinite vortex and point P. Considering only the trailing vortex at the tip, the resulting downwash can be calculated using the Biot-Savart law as in eq. (2.3).

$$w(y) = -\frac{\Gamma}{4\pi(b/2 - y)} \tag{2.3}$$

It can be seen from the equation that as y approaches $b/2$, the downwash approaches infinity, which is nonphysical. Prandtl [7] solved this problem by instead of taking one horseshoe element as done in fig. 2.2, taking a superposition of an infinite amount of horseshoe vortices, giving the modified downwash distribution in eq. (2.4).

$$w\left(y_0\right) = -\frac{1}{4\pi}\int_{-b/2}^{b/2}\frac{(d\Gamma/dy)dy}{y_0 - y} \tag{2.4}$$

It is immediately apparent from the equation that one way to minimise the downwash is to minimise $(d\Gamma/dy)$, which is done by decreasing the gradient in the spanwise load distribution leading to higher spreading of the vorticity. The effect of a higher downwash close to the tip can be seen in the xz-plane, close to the tip of the lifting line, in fig. 2.4. The increased downwash creates an induced angle of attack on the aerofoil, which lowers the effective angle of attack on the aerofoil. This induced angle of attack changes the direction of the lift as shown in the figure. Due to the change in direction of the lift vector, it now has a horizontal component in the direction of the freestream, which is called induced drag. The lift is therefore reduced while the drag is increased. Prandtl found that when the lift distribution along this lifting line has an elliptical shape, the downwash is constant. The elliptical loading distribution results

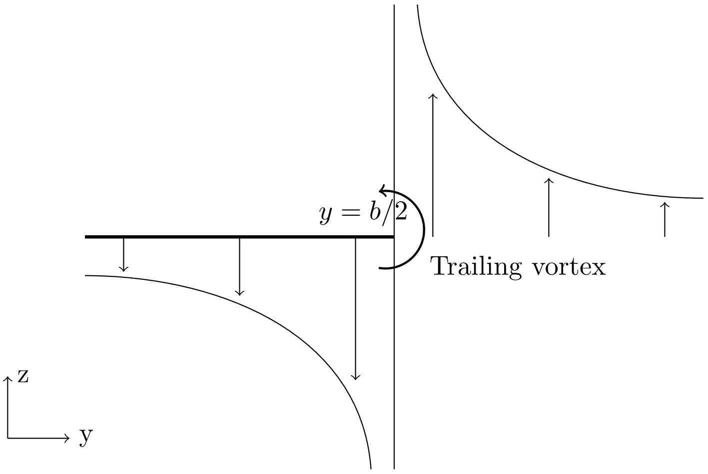

Figure 2.3: Theoretical downwash distribution close to the tip due to only the trailing vortex at the tip

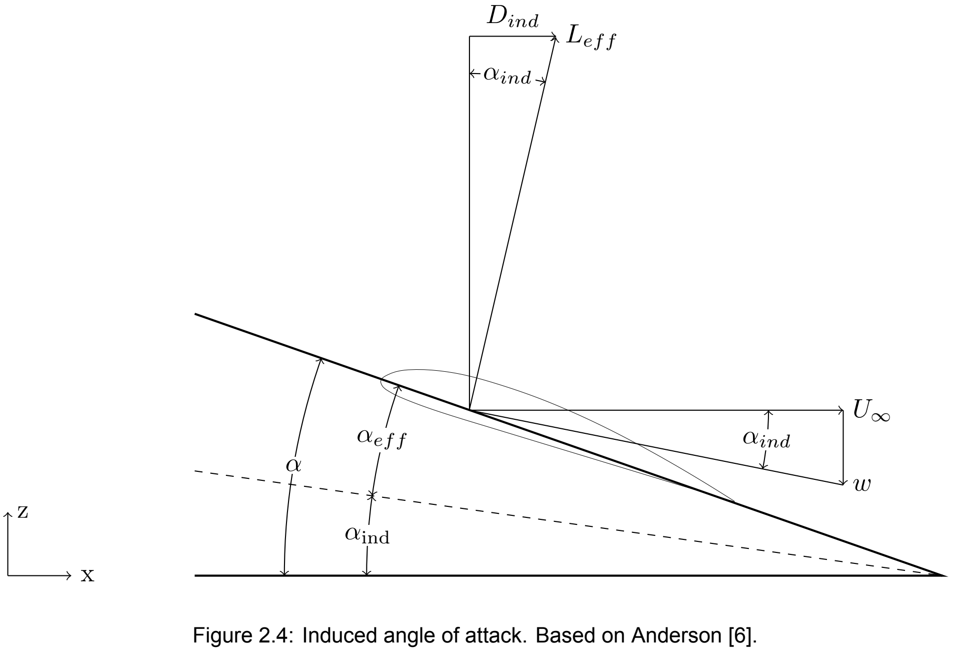

Figure 2.4: Induced angle of attack. Based on Anderson [6].

in minimum induced drag. It was found that in the induced drag can be calculated using eq. (2.5).

$$D_{\text{ind}} = L^2/q\pi b^2 e \tag{2.5}$$

Where e is the span efficiency, which was found to have a value of $e = 1$ for the elliptical lift case. Throughout the history of aircraft wing development, many different concepts have been used to minimise induced drag. The most simple way is to increase the span (b) of a wing, as can be seen from eq. (2.5), while keeping the surface area the same. One can then see that the induced drag of a wing is reduced by 10% for an increase in the span of 5% [8]. This is the reason why glider aircraft have long slender wings. Issues with this concept are restrictions at airports of a maximum span or the increase in root bending moment, which increases with b^3.

Another concept that is often used is planform design. The chord distribution could be varied and is seen in the elliptical wing of the Spitfire. Also, a twist distribution can be used to obtain an elliptical lift distribution with any planform. Phillips and Hunsaker [9] have shown that twist distribution can be found analytically using the aforementioned Prandtl's lifting line. Sweep in the wingtips is also used to reduce the induced drag. Burkett [10] found that by sweeping the wingtip aft, induced drag reductions of 4% are possible. However, the Munk [11] stagger theorem contradicts this finding. Munk's stagger theorem states that the induced drag of all wings with the same projected shape and same projected circulation on a plane perpendicular to the freestream is equal. The same can be shown with a Trefftz-plane analysis, which is a method to calculate the integral value of the induced drag by analysing the flow far downstream of the wing in the so-called Trefftz-plane, which is perpendicular to the freestream. The streamwise coordinates of the wing do not influence the results on the Trefftz-plane and therefore all wings with the same projected shape and projected circulation will result in the same induced drag. Therefore, it is disputed if the findings from Burkett [10] are correct.

Lastly, non-planar surfaces have been used widely to reduce the induced drag. These shapes could be box planes, bi-planes, spanwise camber, tip sails or winglets. Using a Trefftz plane wake analysis, Kroo [8] found the span efficiencies, termed e in eq. (2.5), of different non-planar concepts, shown in fig. 2.5. As can be seen from the analysis, the shape resulting in the lowest induced drag would be the shape i, the box plane. However, as this analysis did not include profile drag, the total drag of the box plane might be higher than a planar wing. Gage [12] used a genetic algorithm as an optimisation method and a vortex-lattice method for aerodynamic analysis, to find the optimum wing topology including profile drag and induced drag, under a lift, span and height constraint. It was found that the optimum shape for minimum total drag was obtained by the C-shaped wing, which has a very similar shape to shape h in fig. 2.5. With the C-shape being a similar shape to a wing with a winglet, this analysis shows the potential for reducing induced drag using a winglet design.

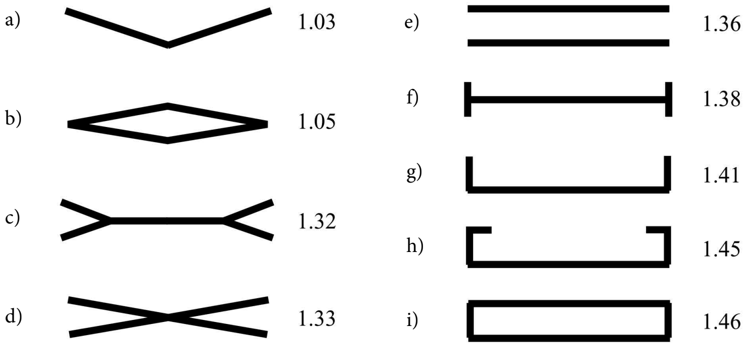

Figure 2.5: Non-viscous span efficiencies for different optimally loaded nonplanar systems for a span constraint. Taken from Kroo [8]

Numerous wingtip devices have been used throughout history in the development of wings, for example, endplates or vertical fins. Still considering the non-rotating case, a very simple winglet in the form of a vertical fin can be used to move the wing's trailing vortex away from the wing. As illustrated in fig. 2.6. As seen from the figure, the trailing vortex is now further away from the wing, moving the velocities induced by the trailing vortex away from the wing. As on the wing itself, there are now fewer induced

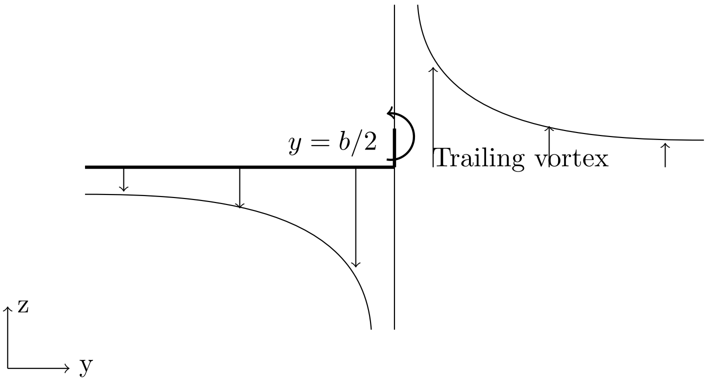

Figure 2.6: Modified theoretical downwash distribution with the presence of a winglet

velocities by the trailing vortex, which therefore results in a lower induced angle of attack and thus a lower induced drag.

Adding a winglet will increase the profile drag of a wing, due to the added wetted area. The art is therefore to design a winglet that reduces the induced drag, while not increasing the profile drag by too much, decreasing the total drag as much as possible. The term winglet was first used in Whitcomb [13]. Instead of using a simple physical barrier, Whitcomb used an aerodynamically designed lifting surface to oppose the flow around the wingtip. It was concluded by Whitcomb that the vertical aspect of a winglet must carry a side load to be effective. This is due to the winglet generating a forward lift component, in the thrust direction, as illustrated in fig. 2.7. Whitcomb tested a tip extension, an upwards pointing winglet and also an upward-pointing winglet with an added downwards pointing winglet. Aircraft usually have upwards pointing winglets instead of downward-pointing winglets, as a downwards pointing winglet has ground clearance issues. It was found that the added downwards pointing winglet, has only a marginal benefit over an upper winglet.

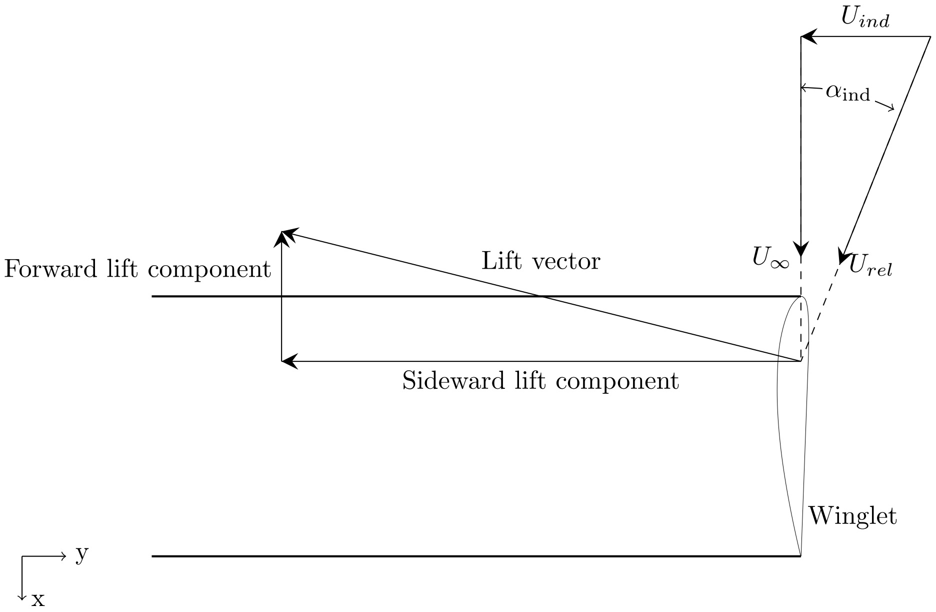

Figure 2.7: Thrust component for a winglet. Based on Guerrero, Sanguineti, and Wittkowski [14].

After Whitcomb developed the winglet, many other configurations have been investigated, where a few are shown in fig. 2.8.

Tip sails include multiple small, high aspect ratio wingtip devices at different angles. The vortex diffuser

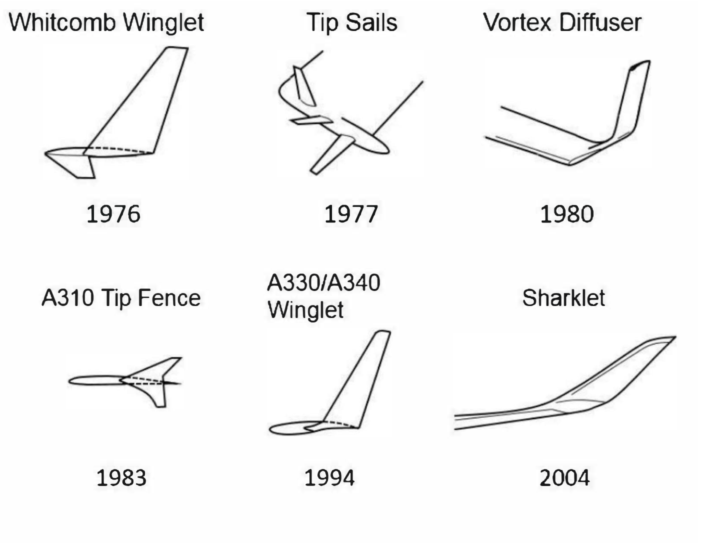

Figure 2.8: Non-planar wingtip device geometry and year of publication. Taken from Skinner and Zare-Betash [15].

[16] is used to intercept the trailing vortex just aft of the wing's trailing edge by mounting an aerofoil-shaped device that is swept back downstream. This device was used on supersonic aircraft, however. A tip fence [17] is made to reduce the induced drag with a minimum influence on added loads such as the bending root moment, which is usually the case for a regular winglet. After the tip fence, the newer A330 and A340 from aircraft company Airbus were equipped with a Whitcomb-like winglet again, however, after that, the newer A380 went back to a slightly bigger tip fence again. Apparently, for the given constraints the tip fence was the best alternative again [18]. Airbus' recent A350 is equipped with 'Sharklets', with a smoother progression from the wing to the very tip. Which is made to avoid potential transonic wave drag increment associated with mutual interference effects as explained by Whitehouse [18].

As can be seen, commercial aeroplanes, even from the same manufacturer, have very different kinds of winglet-like designs. This can be the cause of different constraints when retrofitting or updating an aircraft, or because their designs are changed to improve the company's image by showing they have the latest, most efficient, high technology aircraft in their fleet [18]. No studies were found comparing these different kinds of tip designs.

Design variable or optimisation studies have been done for winglets pointing to the wing's suction side. However, it should be noted for these studies that winglets in commercial aircraft also help in reducing the wave drag, which is drag due to compressibility effects, which is not the case for studies done on wind turbines. Guerrero, Sanguineti, and Wittkowski [14] investigated the effect of changing the cant and sweep angle on C_L and C_D of such a winglet at a flight speed of 0.84 Mach, where its performance in different flight conditions such as climb and cruise are investigated using CFD. It was found that a sweep angle of 60° of the winglet gave the overall best result, with 8.8% and 22.1% reduction of total drag in cruise and climb conditions respectively for a 0° cant angle (tip extension). A cant angle of 15° for cruise level climb conditions and an angle of 45° for cruise conditions, resulted in the best results. Which results in a total drag reduction of 0.8% and 2.2% respectively compared to a 0° cant angle (tip extension). Suggesting that there is a small benefit of a winglet over a wingtip extension for this design case. Higher cant angles resulted in worse performance, however. The effect of adding sweep mostly affected the wave drag, which is not relevant for wind turbines. The effect of increasing the cant angle is quite low, especially in cruise conditions. The higher reduction in drag for climb conditions, however, may hint that the effect of changing the cant angle is mostly on the induced drag, as aircraft climb with a high C_L.

Panagiotou, Kaparos, and Yakinthos [19] present an optimisation for a winglet on a medium-altitude unmanned vehicle. The objective in designing such aircraft is to maximise the flight time, which is done

by maximising $\frac{C_L^{\frac{3}{2}}}{C_D}$. By using a winglet, the flight time was increased by 10%. However, it was found that this improvement was for a large part due to the added reference area. It was also found that the lower the cant angle, the higher the $\frac{C_L}{C_D}$, meaning a tip extension was a better option in this study.
In Elham and Van Tooren [20] a multi-objective design optimisation has been done for a winglet, where the drag and wing weight is minimised. Using seven design variables for the winglet it was shown that with no constraint on span and wing weight, a tip extension ($0°$ cant angle) is a better choice than a winglet. However, for a maximum increase in weight of 5.5%, a winglet proved to be the better option. When applying span constraints winglets are a better option as well, with a vertical winglet being the best option for a wing weight increase less than 6% and a $75°$ cant for no wing weight constraint. The study showed that the optimum winglet or wing extension highly depends on the set constraints. Where most other optimisation studies used the bending root moment as a constraint as it is an indicator for the wing weight, this study calculated the wing weight using finite element analysis and semi-empirical methods. A winglet changes the loading distribution resulting in a higher shear force in the outboard-section (after 50% of the semi-span). This shear results in a spanwise bending distribution which is higher in the outboard-section but about the same at the root, showing that the bending root moment is not a good indicator for wing weight, which was already suggested in 1977 by Heyson, Riebe, and Fulton [21].

More consistent wingtip design is seen in sailplanes compared to commercial aircraft. Sailplane design is a quite challenging multi-point design as a sailplane does not have one cruise speed, but the optimum flight speed depends on weather conditions. Most sailplane competitions have a maximum allowable span, therefore a winglet can increase the aircraft's total lift-over-drag ratio. However, argued in Maughmer [22], even with an unlimited allowed span, sailplanes can benefit more from a winglet than a wing extension of the same length. This is due to that minimum-induced drag depends on maximising both span and span efficiency. As it with increasing aspect ratio it becomes increasingly difficult to obtain an elliptical spanwise load distribution, using a tip extension results in a decreased span efficiency as the aspect ratio is increased. For lower aspect ratio wings this is usually not the case as the benefit of increasing the aspect ratio outweighs the decrease in span efficiency. Moreover, the abrupt change in span loading caused by the tip extension will cause excessive shedding of vorticity into the wake, increasing induced drag. Adding a winglet does not cause such a gradient in the spanwise load distribution. However, Loek Boermans[1], another sailplane designer, disagreed with this theory and concluded that a winglet is only beneficial to a glider's design with a span constraint present.

2.1.2. From non-rotating to rotating

This subsection will explain the principles of a winglet for a rotating case and show the differences with the non-rotating case. Furthermore, the results of parameter and optimisation studies are presented.

In wind energy, a wind turbine can be regarded as a porous disk which extracts energy from the freestream flow, called actuator disk theory, which is a one-dimensional problem as U_∞ and p are constant in the radial direction. The general idea is shown in fig. 2.9. The disk exerts a force on the flow, which is multiplied by the velocity at the disk to obtain the power of the wind turbine. The velocity at the rotor called U_R, calculated as in eq. (2.6).

$$U_R = (1-a)\,U_\infty \tag{2.6}$$

Which is used to calculate the power as in eq. (2.7).

$$P_{AD} = F_{rw}\,U_R \tag{2.7}$$

The maximum power of an actuator disk is called the Betz limit, which gives the maximum power that can be extracted from the wind. The aerodynamic method most often used in industry, BEM, is based on this theory. In BEM, the Prandtl Tip Loss Correction is used to correct the momentum part of BEM for an infinite number of blades. The Prandtl tip loss correction reduces the induction factor close to

---

[1] Personal contact with Loek Boermans, a retired TU Delft professor and sailplane designer

the tips of the blade which effect becomes more pronounced at lower tip speed ratios [23].

BEM is a 2D method. For the analysis of a winglet, a 3D method is required, however. For an analysis of the increase in the theoretical power increase by using a winglet, the actuator disk theory can be slightly extended.

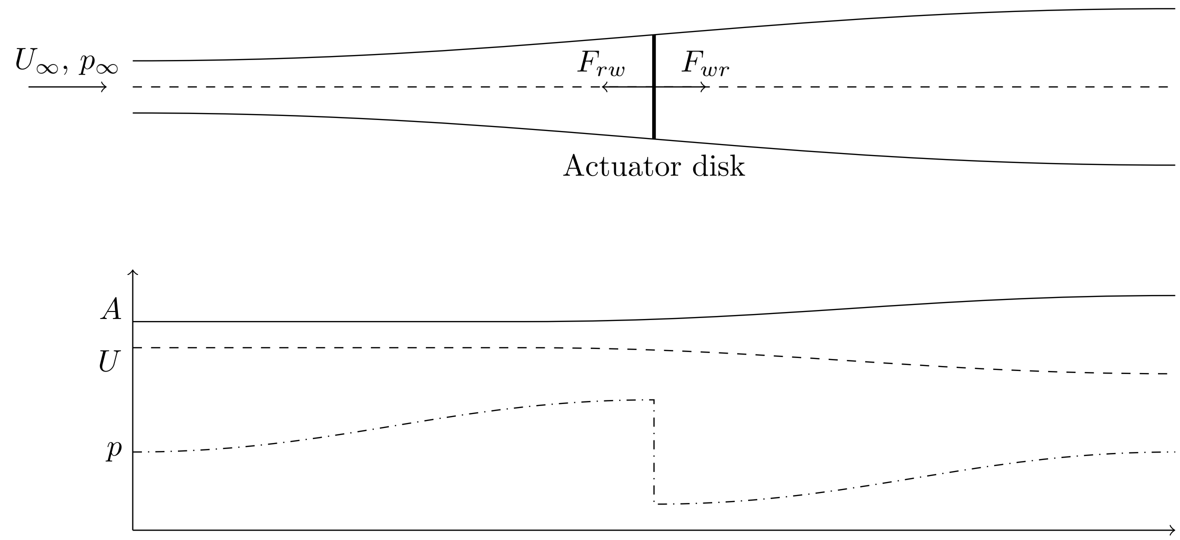

Figure 2.9: Actuator disk model and its effect on the freestream velocity and pressure. Based on Ferreira [23].

Gaunaa and Johansen [24] present an analytical lifting line analysis on a wind turbine winglet to calculate the aerodynamic power, called 'actuator cap theory', where the assumptions were, firstly, that total bound vorticity of the cap considered is constant and secondly, an infinite number of blades is considered. Actuator cap theory is used for the following explanation.

Consider the blade along the x-axis represented by a lifting line for the blade and winglet in fig. 2.10. The lift of a lifting line can be calculated with the Kutta–Joukowski theorem as in eq. (2.8).

$$\vec{\mathrm{L}}_{\mathrm{wing}} = \rho \mathrm{V}_{\mathrm{rel}} \times \vec{\Gamma} \tag{2.8}$$

Now considering a blade of length R on the x-axis in fig. 2.10, the forces on the line representing the blade and the line representing the winglet can be calculated using eq. (2.9) and eq. (2.10), where u_{ind} are the axial induced velocities in the positive z-direction, v_{ind} are the tangential induced velocities in the positive y-direction and w_{ind} the radial induced velocities is the positive x-direction.

$$\vec{F}_{\text{main}} = \rho\Gamma \begin{bmatrix} 0 \\ U_\infty + u_{ind} \\ \Omega z - v_{ind} \end{bmatrix} \begin{matrix} \leftarrow \text{radial forces} \\ \leftarrow \text{tangential forces (power)} \\ \leftarrow \text{axial forces (thrust)} \end{matrix} \tag{2.9}$$

$$\vec{F}_{\text{winglet}} = \rho\Gamma \begin{bmatrix} \Omega \cdot z + v_{ind} \\ -w_{ind} \\ 0 \end{bmatrix} \begin{matrix} \leftarrow \text{radial forces} \\ \leftarrow \text{tangential forces (power)} \\ \leftarrow \text{axial forces (thrust)} \end{matrix} \tag{2.10}$$

These are the forces for a downwind winglet, with an upwind winglet the forces change sign. It can be shown by integrating the tangential loads of both the blade and winglet and multiplying by the rotational velocity, that the contribution of U_{ind} in eq. (2.10) is cancelled out by the increase or decrease (depending on a downwind or upwind winglet) in the power production of the main wing. Therefore, the downwind winglet itself have a negative contribution to the power production, it does, however, help to reduce the effect of the trailing vortex on the blade. This increases the effective axial induced velocities on the blade, increasing the power production from the blade. In actuator cap theory, the negative power production from the downwind winglet and positive power production of the blade cancel each other out. For an upwind winglet it is the opposite, where the negative power production from the blade cancels the positive power production from the winglet out. The way a winglet is able to increase the

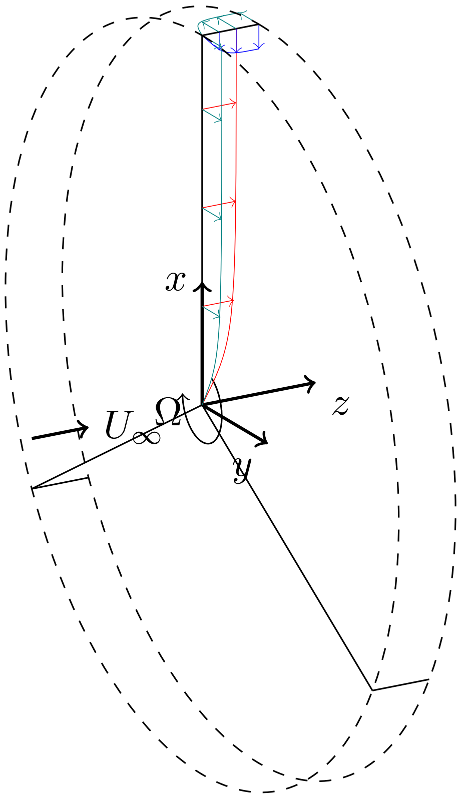

Figure 2.10: The coordinate system of a winglet on a wind turbine with tangential forces (power) is shown in green, axial forces (thrust) in red and radial forces in blue. Directions of forces are shown in the direction they act on the blade and winglet for a downwind winglet. Based on Gaunaa and Johansen [24].

total power production of the rotor is by reducing the tip losses. The Betz limit, therefore, remains the maximum for the achievable C_P.
As can be seen from eq. (2.10), the winglet itself has no thrust generation. Although, due to the increased loading near the tip due to the winglet, adding a winglet will increase the thrust of a wind turbine. It is therefore not possible to add a winglet without increasing the thrust of a wind turbine, without redesigning the blade.
The downwind winglet increases the power on the blade, which is done by displacing the trailed vorticity downstream and out of the main rotor plane. The increased circulation on the blade generally results in lower effective axial velocity in the wake, which leads to a positive radial flow due to mass conservation. The positive radial flow gives a negative power production of the downwind winglet itself.
An upwind winglet, which has a positive power production, will trail its vorticity at an upstream position, which will then reduce the axial velocity on the rotor, leading to a decrease in power on the blade.
This is more clearly seen for helicopters as shown in Muller [25]. With multi-bladed rotors, one blade encounters the tip vortex of another blade just after its formation, due to a helicopter rotor's high rotational velocity. The idea in this research was to add a downwards pointing winglet to push down the vortex path generated by the tips. An upward and downward winglet was both tested and it was seen from experimental results that the downward winglet indeed succeeded in pushing down the blade's vortex path. This resulted in improvement of rotor performance, structural blade loading and noise emission.

Numerical analyses of winglets on wind turbine blades have been done as well. Johansen and Sørensen [26] used CFD to investigate up- and downwind winglets and the effect of twist on winglets. All winglet designs were vertical winglets ($90°$ cant angle). It was found that downwind winglets indeed performed better overall, increasing power productions for low and high wind speeds. The highest increase of power for both up and downwind winglets was found for higher wind speeds with the maximum increase at $U_\infty = 10 m/s$, after which the power increase went down again. It should be noted that the rotational speed was kept constant, so with higher wind speed, the TSR decreased. From Prandtl's Tip Loss Correction is known that the tip losses are higher with lower TSR. The influence of the twist angle of the winglet could be seen in the results, where a change of a few degrees can change the power production by a few percent, even resulting in a power decrease due to the winglet at low wind speeds. Adding a winglet resulted in a thrust increase in every case, with even higher increases in thrust than in power for most cases. Especially the downwind winglet produced more thrust, even at wind speeds where upwind winglets produced more power.

Johansen and Sørensen [27] also investigated the effect of winglet height, curvature radius and sweep on vertical winglets. As expected, power and thrust increased for increasing winglet height. However, sweeping the winglet did not increase power, contrary to previous results found for aircraft, hinting that the effect of sweep could have been mostly due to drag components present at higher Mach numbers. Lower curvature radius resulted in a higher power but also in higher thrust.

Ferrer and Munduate [28] investigated different kinds of winglet shapes for wind turbines using CFD. It was found that highly tapered wingtips have the best power to thrust ratio. Khaled et al. [29] investigated the use of winglets on a model scale turbine using CFD. For a set winglet height, it was found that the optimum cant angle was around $45°$, for which the power was higher than a winglet with a cant angle of $0°$ (tip extension) or $90°$ (vertical winglet). This conflicts with the findings thus far concluding that more power is obtained by a tip extension. However, the winglet heights considered were quite small (1% - 7%). Gaunaa and Johansen [24] found that for small winglets ($\sim 2\%$), the power increase for a winglet and tip extension of the same length is approximately the same. Moreover, this particular research was done on a custom-designed model wind turbine, with a relatively low C_P. It is possible that the load distribution was quite far from optimal and that a $45°$ so happened to make the load distribution more optimal, while $0°$ and $90°$ cant angles resulted in less elliptical shapes. The same power increase might have been achieved with a modified twist and chord distribution.

Moreover, the researches from [26][27][28][29] were all not optimisation studies, meaning a winglet was added to a blade to was not designed to have a winglet. A winglet changes the loading distribution on the blade, which could be far from optimal when the winglet is added. It is therefore hard to draw conclusions about the benefit of a winglet by just attaching a winglet to a blade without changing the blade's design.

Optimisation studies on wind turbine winglets have been conducted as well, although the literature on wind turbine winglet optimisation is thin, especially for multi-objective design. Zahle et al. [30] conducted an optimisation study using CFD for a wind turbine blade tip extension on the IEA 10MW turbine, to maximise AEP, without increasing the out-of-plane bending moment at 90% of the blade length. The chord and twist of the blade were allowed to vary from 90% of the blade length, which is how the load constraint could be achieved. The tip extension was only allowed to bend upwind in this study, so downwind winglets were not considered. It was found that the shape leading to the most increase in power (2.6%) without an increase in bending moment was a tip extension with a winglet-like shape. The root out-of-plane bending moment and thrust were both decreased for this design. The increase in power was most apparent for lower wind speeds. Under the same constraints, a straight blade extension only achieved an increase in power of 0.76%, showing that a winglet can be beneficial over a straight tip extension under certain load constraints. It was also found in this study that it was beneficial to sweep the winglet downstream for power production, hinting that downstream sweep might be beneficial to the design of a winglet for a wind turbine. No reason for this increase in power production was given.

A multi-objective winglet design was done in Reddy et al. [31]. The C_P was maximised while the C_T and moment coefficient around span-wise axis (C_M) , were minimised. One of the designs found on the Pareto front had an increase of 4.5% in C_P, no increase in C_M and 4.0% increase in C_T. This study is the only multi-objective wind turbine winglet optimisation study published to the author's knowledge.

Hansen and Mühle [4] developed an optimisation method for a model-scale wind turbine. The power coefficient of the wind turbine operating at its best TSR is used as the objective function. No loading constraint was set and the cant angle was set to $90°$. The model-scale wind turbine was first designed with BEM. The optimum winglet for this turbine was found using CFD simulations, after which the winglet was built and tested in the wind tunnel. An increase of power of 8.9% with an increase in thrust of 7.4% was found. It was noted that, because the design concerns a model-scale wind turbine, the Reynolds number was much smaller, leading to laminar separation bubbles. The winglet also only increased the performance in a small range of operational conditions.

Elfarra, Sezer-Uzol, and Akmandor [32] conducted another single-objective optimisation study on a winglet for the NREL VI rotor. Although it was shown that the power of the turbine could be increased by 9% using a winglet, the NREL VI rotor is a rotor with a relatively low C_P, as it is designed as a rotor to conduct measurements on. The same increase in C_P might have been obtained by a redesign of the rotor without a winglet.

2.2. Parameterisation and Constraints

An optimum design is highly dependent on the chosen parameters as well as the set constraints as seen from previously mentioned optimisation studies. Section 2.2.1 will show the different parameterisation methods that are found in the literature and explain them. Section 2.2.2 will elaborate on different constraints that are used and explain why these constraints are used.

2.2.1. Parameterisation

According to Giannakoglou [33], a parameterisation method has the following requirements:

- Be flexible allowing to cover the design space to the highest degree, so solutions with 'non-traditional' shapes can be found
- Be able to keep the number of design parameters as low as possible
- Be free of slope or curvature discontinuities at surfaces
- Be free of variables that have little effect on the aerodynamic performance
- Preferably be directly linked to the constraints

The parameterisation from fig. 2.1, used thus far in this thesis, is one way that is often used to parameterise a winglet, where the parameters can be changed to directly change the shape. In Refs. [4] [29] [31] the winglet was parameterised in such a manner. However, there are other ways to parameterise the geometry which can lead to more possible shapes. B-splines, which are based on a set of control points that act as 'attraction points' which determine the spline's shape is used in Vučina, Marinić-Kragić, and Milas [34].

Bézier curves are another method based on control points, which are used in, for example, Refs. [30][35] [36] to define the geometry. Sessarego et al. [37] uses Bézier curves to design the blade's chord and twist distribution, from which an example is shown in fig. 4.2. Stock-Williams et al. [3] also proposed a way to set a priori constraints on an aerofoil shape, largely avoiding nonphysical design.

A difference between B-splines and Bézier curves is that changing one control point influences the whole curve for Bézier curves whereas B-splines only several segments are influenced depending on the degree of the B-spline [38]. Although these methods have the advantage of more possible shapes over directly optimising the winglet parameters, more parameters might be needed, where for B-splines the amount of properties is even higher than for Bézier curves. This makes the optimisation problem more difficult and could increase the time to obtain an optimum design.

Gaunaa and Johansen [24] only optimised the loading of the blade, by optimising the blade's chord, for a given $\frac{c_l}{c_d}$, which reduces the problem's degree of freedoms with a factor of two, as the twist is obtained as post-processing step from the relative flow direction, lifting line geometry and 2D angle of attack which was determined for the loading optimisation.

2.2.2. Constraints

As seen from previous research, set constraints influence the optimum design. Examples of constraints seen are geometric constraints or load constraints. Production costs constraints could also be present, however as winglets are not common in today's wind turbine design, it is hard to estimate these costs. A preliminary cost analysis could be made if the stresses on the winglet are known, which could determine the increase in mass, which is an indicator for the cost as shown by Sieros et al. [39].

The consensus is that winglets are only beneficial when a span length constraint is present. For wind turbines, this could be the case onshore when the blade is constrained due to noise requirements. Offshore a span constraint could also be present due to the required height from the tip of the rotor to the waterline. Higher span would need larger floating structures which increases the costs as mentioned by Hansen and Mühle [4].

A winglet will change the load distribution and will therefore also increase out-of-plane loads over the entire blade unless the twist and chord distribution near the tip is modified as done by Zahle et al. [30]. The loads that are constrained or minimised for wind turbines are usually static aerodynamic DLLs. A few examples of these loads are given in Loenbaek et al. [1]. For example, the thrust is minimised or constrained when there is a loading limit on the tower or foundation of a wind turbine but this constraint does not directly limit the design of the rotor itself. The root flapwise bending moment could be constrained as well as a wind turbine blade has less stiffness in the flapwise direction and the internal structure is mostly designed to provide stiffness in that direction. The flapwise bending moment location is chosen to be the root since the flap-wise aerodynamic loads need to be transferred via the blade structure to the root of the blade. However, an aeroplane winglet study from Elham and Van Tooren [20] has shown that when comparing a wing without winglet and a wing with winglet, the ratio between of bending moments along the span of the wing, the increase in bending moment ratio is much higher near to the tip, this shown in fig. 2.11.

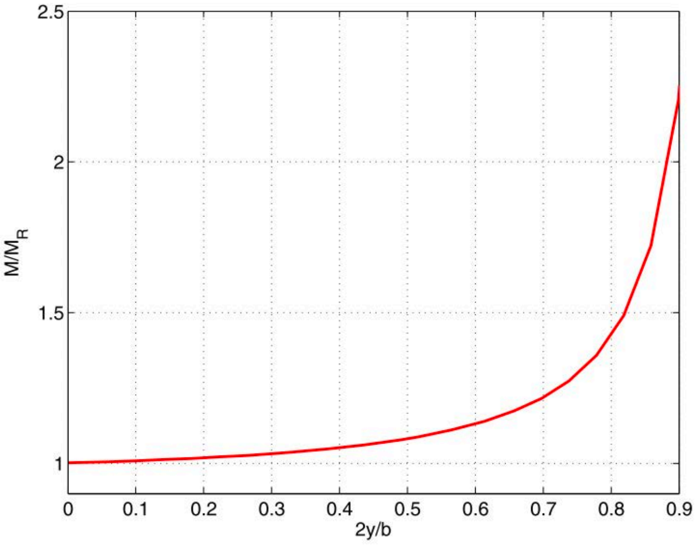

Figure 2.11: Bending moment of reference wing with winglet (M_R) compared to bending moment of a wing with winglet (M) as function of half-span ($2y/b$). Taken from Elham and Van Tooren [20].

The tip deflection could be constrained as tip clearance between the blade and tower becomes critical with long and slender blades. This would require an aeroelastic analysis, however.

Loenbaek et al. [1] also show, using 1D momentum theory, that the optimum design of a wind turbine is very dependent on which of these static aerodynamic DDLs are chosen. Where constraining the thrust led to an infeasible design with an infinite rotor radius and thus, an infinite increase in root flapwise bending moment and tip deflection. Constraining the root flapwise bending moment could increase the AEP by 19.9% by increasing the radius, which would increase the tip deflection by 109%. Constraining the tip deflection could increase the AEP by 5.7%, without any increase in the thrust and root flapwise bending moment. Although this study concerns a 1D momentum theory rotor and not optimisation with a higher fidelity method, it does show the big influence of a constraint on an optimum design. This is likely why Zahle et al. [30] have constrained the flapwise bending moment at 90% of the blade span, which could result in less tip deflection than when constraining the bending moment at the root.

Although not including a winglet, Madsen et al. [35] constrained the flapwise bending moment over the whole span.

Also concerning a blade optimisation without a winglet, Sessarego, Ramos-Garcia, and Shen [40] chose to constrain C_T .

In Reddy et al. [31] the C_T and C_M were minimised while maximising for C_P.

2.3. Aerodynamic analysis methods

Before a geometry can be optimised, aerodynamic analysis modelling needs to be performed to determine the aerodynamic forces on said geometry. This section will explain the pros and cons of a few aerodynamic analysis methods and present prior research where these methods have been used.

2.3.1. BEM

In BEM, the aforementioned 2D momentum theory is coupled with local events taking place at the actual blades [41]. The actuator disk is then divided into radially independent annular elements, with no flow across the elements. The flow at each radially independent annular element can be determined now using the axial and tangential induction factor, after which strip theory is used, where wind tunnel measurements of the C_l and C_d polars of aerofoils are used to get the aerodynamic forces on the rotor. Prandtl's correction is applied to the axial and tangential induction, to correct for a finite number of blades and the tip effects. Prandtl's correction is a function of the number of blades, TSR, radial position and axial and tangential induction.

The radial independence in BEM is a key assumption, which holds for plane rotors with straights blades as shown by Branlard and Gaunaa [42], where the radial dependency is analysed using vortex cylinders. However, when rotors are analysed that are non-planar, the radial independence no longer holds. For non-planar rotors, such as rotors with a winglet, the radial induced velocities would need to be evaluated to determine relative wind speed and angle of attack on the sections along the blade. As BEM has no framework for radial induced velocity, BEM is not suited to analyse a rotor with a winglet.
In BEM, the 3D tip effects are calculated by a correction factor, which is derived for planar rotors, which is not adequate to calculate the effect of an added winglet.

2.3.2. CFD

Although CFD has a quite broad definition, the method referred to is usually a method where a mesh is made of the geometric domain, using, for example, the finite-volume method. This is then used to solve the Euler or Navier-Stokes equations, which are based on the conservation of mass, momentum and energy. The Navier-Stokes solvers have the advantage to be able to solve for a viscous flow, using turbulence modelling. The most used turbulence model in optimisation studies is RANS turbulence models, based on time-averaging the Navier-Stokes equations, used in aforementioned Refs. [4] [30] [31] [32] [34] [35] [36]. For the design of a winglet, this is a quite important property, as the design of a winglet is a trade-off between decreasing the induced drag more than the increase in profile drag. Barrett and Ning [43], who compared CFD, a panel method and wind tunnel test for the optimisation of wind turbine blades, concluded that the choice of aerodynamic analysis method has a large influence on the optimum design and stresses the need for high fidelity methods.
CFD has some disadvantages as well, however. The aforementioned mesh needs to be constructed manually in the case of a structured mesh, which can be time-consuming. When the geometry is changed, the mesh needs to change as well based on the change in geometry parameters, which can be a challenging task in the highly multi-dimensional design space of a winglet and can lead to mesh failure. Fixed or automatically generated unstructured mesh could be used as well, however, to obtain accurate results for turbulence modelling, quite strict requirements for the mesh size are in place to resolve (or not resolve) the boundary layer in turbulence models [44].
Moreover, CFD simulations can take a long time. Madsen et al. [35] optimised a wind turbine blade for three different mesh sizes. An optimisation case using a fine mesh took $12734.7h$ in CPU time. There was a requirement for a fine mesh in this study, as a coarser mesh showed large errors in the mesh dependence study. Skinner and Zare-Betash [15] argue that CFD ultimately restricts the allowable design space due to computational needs or through how the baseline design is allowed to deform due to the mesh and therefore chose a panel method for aerodynamic analysis.

2.3.3. Vortex methods

Vortex methods are based on the potential flow assumption governed by Laplace's equations [5]. Some vortex methods are lifting line, lifting surface and panel codes. All these methods aim to find a singularity distribution, consisting of, for example, vortices, sources or doublets. A simple explanation of lifting line was already given in section 2.1.1, where a wing or blade is modelled by a vortex filament on the quarter-chord, with two trailing vortices parallel to the freestream, and a shed vortex, which is shed at the aerofoil's trailing edge, into the wake. A single vortex ring cannot describe the lift distribution, therefore many vortex rings should be superimposed to describe the lift distribution.

Put simply, for the lifting surface method there is not a single vortex filament at the quarter-chord of the wing or blade, but multiple vortex filaments along the camber line of an aerofoil. This way there is also a lift distribution along in the chord direction of the wing or blade, giving a variation of lift in x and y. A method making use of lifting surfaces is for example the vortex lattice method. There is also the panel method, where vortex filaments are placed along the pressure and suction side of an aerofoil, thus representing the actual shape of an aerofoil, for a visual explanation see fig. 2.12. Lifting line and lifting surface assume a thin-aerofoil, where with panel methods thicker aerofoils can be used as is done in XFOIL [45]. An advantage of vortex methods is that induced velocities are directly computed with the Biot-Savart law from eq. (2.1). As a winglet modifies the induced velocities around a wing or blade, a vortex method can give a good insight into these induced velocities.

Vortex methods can be modelled with a free wake model or a frozen wake model. In frozen wake models, the wake is only affected by the unperturbed flow and geometric constraints. The wake, therefore, follows the freestream or a prescribed path. Free wake methods take the circulation of the blade and the wake itself, called 'self-induction', into account, resulting in wake deformation [23]. Free wake models are therefore more computationally expensive.

As mentioned before, vortex methods are based on potential flow theory, assuming inviscid and irrotational flow. Therefore, vortex methods have the disadvantage of not accounting for viscosity, which is important for the trade-off between induced drag and profile drag in designing a winglet. For low-speed flows, as is generally the case in wind energy, flows are mostly inviscid, except for thin regions near a solid surface, where this thin region is called the boundary layer. The effect of viscosity mostly comes from the boundary layer in these flows. The laminar boundary can be solved and coupled with a potential flow solver to account for viscosity [5]. This has been done for a couple of commercial and academic panel codes such as Flightstream [46] and MIRAS [47]. Another simpler option is to include the profile drag from known $\frac{C_L}{C_D}$ polars, as in done in Refs. [24] [15]. This has the disadvantage of having to use existing aerofoils for which $\frac{C_L}{C_D}$ polars are available. Therefore the shape of the winglet is limited.

Vortex models have been used for optimisation studies as well. Gaunaa and Johansen [24] used a free-wake lifting line model to optimise a winglet, where a winglet was able to increase C_P by about 2.5%, where the results were validated by CFD, although CFD predicted a slightly lower increase in C_P of 1.7%. Elham and Van Tooren [20] used a Q3D, which is a vortex lattice method combined with a 2D panel method to obtain the profile drag, to optimise a winglet as well. Sessarego et al. [37] used the aeroelastic panel method MIRAS to optimise the chord- and twist distribution for a wind turbine, it was concluded that the panel method did not provide performed better than BEM for this optimisation case. Sessarego et al. [48] again used MIRAS to now optimise the sweep and pre-bend of a wind turbine, which makes more sense to optimise for, as BEM does not model the aerodynamics of curved blades as accurately as higher-fidelity methods. The study found an increase in power of 1% for an increase in thrust of 0.02% for the redesign of the blade.

2.4. Surrogate modelling and optimisation

This section will give a brief overview of surrogate modelling in engineering optimisation and discuss its necessity. Section 2.4.1 will explain the concept of how surrogate modelling can aid in optimisation. Surrogate modelling will be discussed in section 2.4.2 and some examples from optimisation studies will be given. Section 2.4.3 will give some examples of the optimiser that are used, with a short explanation of their principles.

2.4.1. Surrogate-assisted optimisation

One of the major obstacles in engineering optimisation is the long-running time of simulations and the lack of analytic gradients. Optimisation studies with CFD simulations can take days as shown by

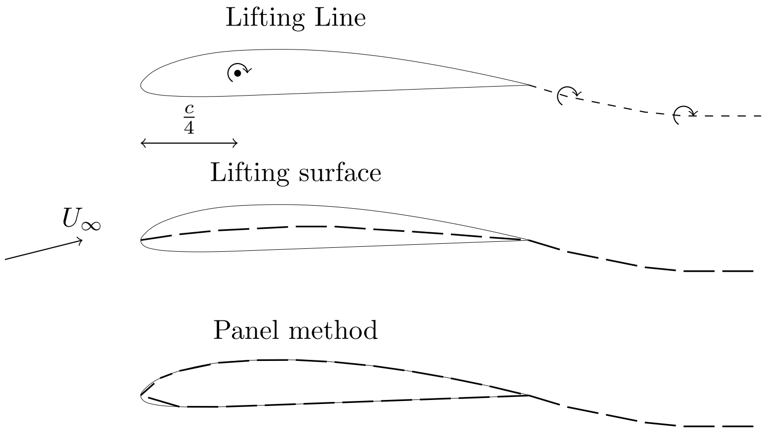

Figure 2.12: Simplified 2D representation of lifting line, lifting surface and panel method. Based on Ferreira [23].

Madsen et al. [35], but even panel method simulations can take quite some time, where every single simulation by Sessarego et al. [48] took 17h using one-hundred and sixty 2.8 GHz processors. Single optimisations are rarely performed because one might need to try out different constraints, or modified objectives. The idea of the surrogate modelling approach is therefore to develop fast mathematical approximations to the long-running simulations models [49]. Surrogate models are probabilistic models that need to be able to provide estimation with uncertainty for given input functions. Using these surrogate models can be called surrogate-assisted optimisation, where the idea is shown in fig. 2.13. Whenever a new design needs to be evaluated, the objective function(s) $f(x)$ needs to be called, where

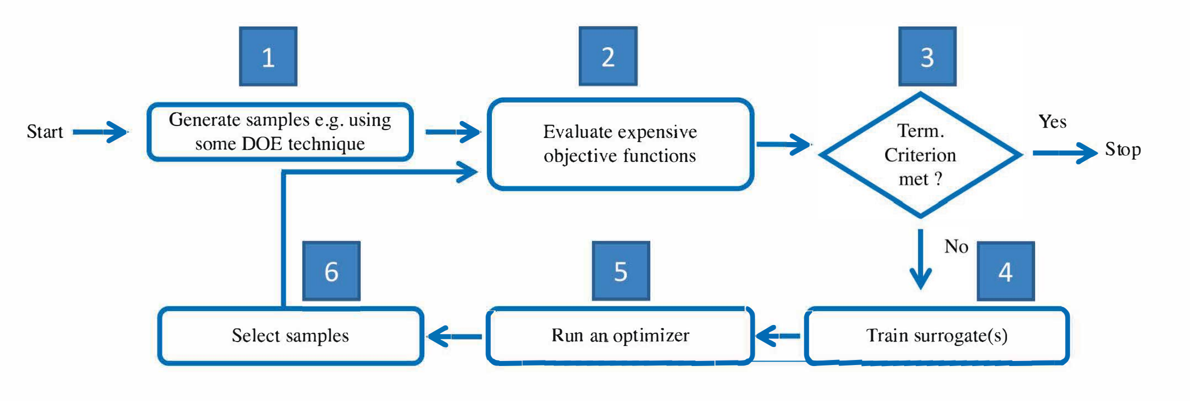

Figure 2.13: A generic framework for a surrogate-assisted optimisation method. Taken from Chugh [50].

the input variables x are, for example, the winglet parameters. The output of f could then be, for example, the C_P and flapwise bending moment at some location. One would like a cheap-to-evaluate model $\hat{f}$. The surrogate $\hat{f}$ needs to be 'trained' with data from f, with the goal for $\hat{f}$ is to generalise well, meaning it will also be able to predict unseen data accurately, or with at least robust uncertainty estimates. This can be done by proper design or selection of a surrogate model and by having a good sampling plan. When making a sampling plan, it can be a good idea to investigate what effect the different design parameters have on the result of f. It can be investigated if a change of different input parameters has a high or small effect on f, but also if the effect of a parameter is, for example, nonlinear or interactive. The simplest way to create a sample from the design space is to create samples by linearly spacing all design parameters, called the full factorial sampling technique. A problem with this is, however, that when these samples are projected on an axis, there will be a lot of overlap between the samples. Requiring a large number of samples for the input space, scaling to the power of the number of dimensions. It can be argued however that the sampling of individual parameters can be improved by making sure that in these projections the samples are spaced as uniform as possible, this can be done by Latin Hypercube (LHC) [49]. LHC is often found in optimisation studies, as in the aforementioned Refs. [4][20][30][37][48].

After a sampling plan has been created, f is evaluated for each sample and $\widehat{f}$ is trained, it is desired to improve $\widehat{f}$ by generating more samples from the design space, based on the results obtained from f, these samples are called 'infill points'. This allows to quickly converge to an optimum design. However, the goal is to reach the global optimum and not getting stuck at a local optimum. It is therefore needed to use infill criteria (also called acquisition functions) to balance exploration and exploitation, where exploration points are chosen where the surrogate variance is high, for exploiting points are chosen where the surrogate mean is high. This can be done with methods that balance exploitation and exploration, such as Probability of Improvement (PoI), as explained by Keane, Forrester, and Sobester [49], or Expected Improvement (EI) as explained by Brochu, Cora, and Freitas [51]. The exploration and exploitation can then be stopped when, for example, the probability or expectation of improvement meets a certain threshold.

2.4.2. Surrogate models

In state-of-the-art wind turbine optimisation studies, surrogate-assisted optimisation is often used. The three most used surrogate models that are identified are Neural Networks, Gaussian Processes and Radial Basis Functions.

Neural Networks

An NN is a machine learning algorithm that is known for being able to map input-to-output well for a wide range of problems [29]. An NN consists of an input layer, at least one hidden layer and an output layer. Each layer consists of neurons, which are a collection of inputs, weights and an activation function. When taking the simplest architecture, a feed-forward network or MLP, each neuron of a layer is connected to each neuron of the next layer. All connections have a weight value, that is iteratively updated which is called 'training', and an activation function. The activation function is required to make the NN non-linear. This is usually written as $\widehat{f}(\mathbf{x}) = \sigma(\mathbf{w}^{\mathrm{T}}\psi)$, where $\widehat{f}$ is the output of the NN, x is the input, w are the weights and ψ the hidden units and σ the activation function. It is possible to build the hidden layer out of multiple layers, this is called deep-learning, which has shown good results on more complicated input such as images [52]. However, also Fadare [53] found increasing accuracy with multiple hidden layers for prediction of the mean wind speed with as input latitude, longitude, altitude and month of the year.

Although neural networks are used quite extensively in wind forecasting research, they have only been used in a few cases in surrogate-assisted design optimisation.

Khaled et al. [29] used an MLP, with one neuron and one hidden layer, with as input the winglet height, cant angle and wind speed and as output the C_P and C_T.

Elfarra, Sezer-Uzol, and Akmandor [32] has used an NN with as input the cant and twist angle of a winglet and as output the power. No information was found on the architecture of the NN.

Ribeiro, Awruch, and Gomes [36] optimised an aerofoil for a wind turbine. The inputs for the MLP surrogate model were the control points for a Bézier curve with n points, where the hidden layer consisted of one layer with $2n + 1$ neurons. The outputs were the C_L and C_D of the aerofoil. Ten samples were used to train the MLP. It was found that the total computational time to find the optimum aerofoil was half the time when not using a surrogate model, which corresponded to a reduction of 10h. Where the surrogate-assisted approach found approximately the same optimum as optimisation without a surrogate model.

Sessarego et al. [48] used NNs on the sweep and pre-bend of a wind turbine blade. Six parameters describing the pre-bend and sweep were used as input, the hidden layer consisted of one layer and two neurons and the output was the C_P and C_T. A sample size of 20 was used to train the NN. Both an MLP and a radial basis network were used and it was found that the radial basis neural network outperformed the MLP.

All of these studies have not used deep learning by using multiple hidden layers, it is, therefore, unknown if deep learning could benefit the surrogate model for the design of a wind turbine winglet. These studies have also not used any infill points after training on the initial sample. An NN does not provide the user with uncertainty which is what, for example, EI relies upon. Recently developed Bayesian Neural Networks, discussed in Valentin Jospin et al. [54], could potentially overcome this issue, however.

Gaussian Processes

GPs construct a joint probability distribution over the input variables assuming a multivariate Gaussian distribution [55]. Where a Gaussian distribution over a random variable is specified by a mean and covariance, a GP is specified by a mean and a covariance function. Active research is focused on the choice of the covariance function [3], where a zero prior mean is usually chosen. The choice of the covariance function determines the smoothness properties of samples taken from it. The smoothness can be controlled with hyperparameters. Often a Matérn kernel is chosen. GPs are often used as a surrogate model in Bayesian Optimisation as done by Stock-Williams et al. [3].

Radial basis functions

To approximate any smooth, continuous function as a combination of simple basic functions, radial basic functions can be used. Assuming error-free results from f, a radial based function approximation to $\widehat{f}$ can be written as eq. (2.11) [49].

$$\widehat{f}(\mathbf{x}) = \mathbf{w}^{\mathrm{T}}\psi = \sum_{i=1}^{n_c} w_i \psi\left(\left\|\mathbf{x} - \mathbf{c}^{(i)}\right\|\right) \tag{2.11}$$

Which is a similar notation as for the NN. $\mathbf{c}^{(i)}$ denotes the ith of the n_c basis function centres. ψ now denotes the n_c-vector containing the values of the basis functions ψ themselves, evaluated at the Euclidean distances between the prediction site x and the centres $\mathbf{c}^{(i)}$ of the basis functions [49]. $\psi(r)$ can be fixed or parametric. Examples of fixed basis function is linear $\psi(r) = r$ or cubic $\psi(r) = r^3$, a parametric basis function can be Gaussian $\psi(r) = \left(r^2 + \delta^2\right)^{1/2}$. In the case of RBF, w can be estimated with linear interpolation, as eq. (2.11) is linear in w. The earlier mentioned radial basis function network is an NN that uses an RBF as an activation function. Sessarego et al. [37] used an RBF as the surrogate model for the influence of the chord and twist distribution, defined using Bézier splines, on the C_P and C_T. Linear, cubic, thin plate spline, Gaussian, multi-quadratic and inverse multi-quadratic were all tried with a cubic basis function performing the best. Prediction-based exploitation with a custom infill strategy was used to enhance the accuracy of the surrogate model. The optimisation stopped when the minimum of the surrogate was equal to the objective function, or when eight iterations were reached.

Reddy et al. [31] used a multi-quadric basis function on a multi-objective problem with input winglet span, twist angle, dihedral angle, sweep angle, and taper ratio. The output was the C_P, C_T and C_M. However, no active infill strategy was used.

Hansen and Mühle [4] used GPs with six winglet parameters as input and the power as output. EI was used as infill criterion. The uncertainty of GPs allowed for infill points to be at regions of high uncertainty. The exploration and exploitation were stopped when the GPs had no more expected improvement.

Elham and Van Tooren [20] fitted GPs for the design of an aeroplane winglet. Also in this study, no infill criteria were used as only the Pareto fronts were presented.

2.4.3. Optimisation methods

Smith [56] identifies four main categories for optimisation, which are not necessarily mutually exclusive:

- Constrained optimisation
- Multi-objective optimisation
- Multi-modal optimisation
- Combinatorial optimisation

The design optimisation studies presented thus far have, in most cases, been constrained, aimed at finding the global optimum, given certain constraints to the output of the objective function. This could for example be load constraints for a winglet. One could also put a limit to the inputs of the objective function, which could for example be a diameter constraint that puts a limit on certain winglet parameters.

Some studies were multi-objective optimisations, where, for example, two objectives could be maximised. This will not lead to one global optimum, but several so-called Pareto optimal solutions. The hypervolume is a commonly-used metric for determining how well a multi-objective optimisation has performed. It may be the case that some definition of a global optimum is needed to determine the next infill point by infill criteria/an acquisition function. A scalarising function can be used for that, transforming multi-objective problems into single-objective (constrained) problems [50]. Stock-Williams et al. [3] discuss what would be an effective scalarising function for the acquisition function of BO. Multimodal optimisation focuses on finding the multiple local optima instead of one global optimum, which is usually used for single-objective optimisation. Combinatorial optimisation concerns finding the optimum for an objective function whose domain is discrete instead of continuous. The optimisation studies found in this literature study all used continuous parameters, however.

A distinction can also be made between single- and multi-point optimisation. When optimising for C_P and no load constraints are set, one wind speed is usually chosen to optimise, as the C_P of a blade does not change with changing wind speed and constant TSR. However, when maximising for AEP, multiple wind speeds will need to be considered. Load constraints can also require multiple optimisation points, as the load constraints are more easily violated at wind speeds closer to the rated wind speed. Zahle et al. [30] for example chose to evaluate at 6, 8 and $10\,m/s$. The wind speed $10\,m/s$ was chosen since the IEA 10MW rotor, which is a similar rotor to the DTU 10MW RWT rotor, operates close to its maximum flapwise bending at this wind speed.

Finally, optimisation algorithms can be gradient-based or gradient-free. Gradient-free algorithms have the advantage of being simpler to implement and claim to find the global optimum instead of a local optimum Gradient-based can perform better when the objective function can give efficient gradient evaluation, is computationally cheaper and has a single minimum.

Lyu, Xu, and Martins [57] found gradient-free algorithms required two to four as many iterations for a RANS-based, aerodynamic twist optimisation problem of an aeroplane wing. This concerned optimisation without a surrogate model, however.

Design optimisation studies found in this literature study used gradient-free algorithms in almost every case. A few exceptions were found, where, for example, Sessarego et al. [48] used a simple gradient-based algorithm to optimise an already trained surrogate model.

Hansen and Mühle [4] used a hybrid genetic-gradient algorithm, on a trained surrogate model, where the gradient-based algorithm is executed to ensure that the best local solution is found in the current global, best basin of attraction.

Madsen et al. [35] used a gradient-based algorithm named SNOPT with a CFD solver that can provide gradients, called an adjoint solver.

The most used optimisation algorithms that were found are genetic algorithms (GAs), which will be discussed here. Another algorithm that is used less frequently, but will be discussed as well due to its efficiency when the objective function is expensive to evaluate, is Bayesian Optimisation.

Genetic Algorithms

GAs are simple, random-based Evolutionary Algorithms that are based on Darwin's Evolutionary theory. The principle of the GA presented here is as explained by Smith [56]. First, an initial population size is created. In the initial population, there are individuals, which represent the samples. Each individual has a chromosome with genes, where the genes represent the parameters of a sample. The chromosome can be seen as an array. Each individual has a fitness value which is calculated by the objective function. A number of individuals with the highest fitness are now chosen for the mating pool. The remaining individuals in the mating pool are called parents. Parents are selected to pair at random to create offspring. Offspring contains a random number of genes from each parent. Mutation can also occur where the value of a gene is changed randomly. The new offspring population is called a generation. The whole process can start over again now. Hyperparameters that can be controlled are, for example, the population size, the mating size, which is the number of individuals chosen for each tournament selection, and the crossover and mutation probability. A principle that is often implemented is that of elitism, where the individuals that score the best on the objective function are carried to the next generation.

Ribeiro, Awruch, and Gomes [36] used a GA for the single-objective optimisation of an aerofoil for maximum $\frac{C_L}{C_D}$. Elfarra, Sezer-Uzol, and Akmandor [32] used a GA to optimise a winglet on a trained NN with the single-objective function of maximising C_P.

GAs have the advantage of being able to work for multi-objective optimisation problems as well. Two more concepts, called dominance and crowding distance, were used in the NSGA-II algorithm for this.

Firstly, the concept of dominance can be explained with the example of two solutions having different scores for different objectives functions. One solution dominates another if its score is at least as high for each objective, and is higher for at least one objective [56]. A solution is non-dominated if it is not dominated by any other solution. The non-dominated solution then lies on the Pareto front. Secondly, the concept of crowding distance is introduced, which is meant to preserve diversity in the population. Most multi-objective studies found in this literature study used NSGA-II [20][31][58], where Vučina, Marinić-Kragić, and Milas [34] used MOGA-II, a slightly different multi-objective GA.

Bayesian Optimisation

Bayesian Optimisation is based on Bayes' theorem, which states that the posterior probability of a model, the objective function f in this case, given the design space D, is proportional to the likelihood of D given f, multiplied by the prior probability of f . Which is shown in eq. (2.12).

$$P(f \mid D) \propto P(D \mid f)P(f) \tag{2.12}$$

In this case, the posterior $P(f \mid D)$ is the acquisition function, with the posterior mean function of a GPs [51]. For efficient sampling, BO uses an acquisition function to determine the next infill point, which is usually chosen to be EI. The acquisition function is responsible for scoring or estimating the likelihood that a given candidate sample is worth evaluating with the real objective function. This means that the acquisition function is high where the GP predicts a high value from f and where the uncertainty is high. Balancing these two contributions to the acquisition function is the balance between exploration and exploitation respectively. BO will converge to the optimum if the acquisition function is continuous and minimises the expected deviation from the global optimum. Bayesian optimisation has the advantage of creating the surrogate model and optimising at the same time. BO follows the idea of surrogate-assisted optimisation as shown in fig. 2.13.

For multi-objective optimisation using BO, the surrogate modelling can be done in two ways. One way is to build a surrogate for each objective function, another way is to build a surrogate for a scalarising function, which converts the multi-objective problem into a single-objective problem [50]. As an example, Stock-Williams et al. [3] considered an aerofoil optimisation with two objectives: maximum $\frac{C_L}{C_D}$ and maximum structural stiffness of the spar cap in the flapwise direction. A very simple approach would be to just maximise for the (weighted) sum or product of the two objectives, however, this would have the disadvantage of directing the optimisation down a single vector in the objective space. Manually choosing the weights could be a quite subjective or biased process. A more sophisticated way is to use the Hypervolume Improvement (HypI) scalarising function, which is based on the earlier explained Pareto dominance. For the aerofoil optimisation, two scalarising functions were analysed, namely HypI and Extended Hypervolume Improvement (xHVI), which was compared with the technique of building multiple surrogates for the different objectives using EHVI. HypI outperformed xHVI as a surrogate function and obtained the best aerodynamic performance. EHVI was able to obtain stiffer aerofoils than either mono-surrogate, however, this came at the expense of longer runtimes.

2.5. Synthesis

Almost every modern aeroplane is equipped with a winglet and much research has been done to reduce the induced drag from the tip effects, however, winglets remain mostly absent from state-of-the-art wind turbine design. As was seen from this literature study, some winglet optimisation studies for wind turbines have been performed, but are scarce. Winglets in these studies were mostly parameterised in a simple manner, not allowing much design freedom. More unconventional winglets that are seen in aircraft, such as the tip-fence, have not been investigated. Most studies are single-objective in maximising power, with a few exceptions where the optimisation has been performed with some load constraints. What remains unanswered is: under what constraints can a winglet be beneficial to the design of a wind turbine?

Optimisation studies in winglet and blade design often take the surrogate-assisted optimisation approach. Usually, one method is chosen and not compared to other methods. Some surrogate-assisted optimisation methods have been discussed in this literature study, but it is largely unknown how they compare against each other for design optimisation.

3

Aerodynamic analysis methods setup and validation

This chapter will present the reference wind turbine that is chosen to modify the blade's design with a winglet. The reference turbine will be presented in section 3.1. Furthermore, two aerodynamic analysis methods were used in this thesis. The panel code FlightStream and the lifting line method AWSM. The setup used for both models will be presented and their output will be validated against CFD data. FlightStream will be discussed in section 3.2 and AWSM in section 3.3. FlightStream and AWSM will be compared in section 3.4.

3.1. The DTU 10MW Reference Turbine

The DTU 10MW Reference Turbine is chosen as the turbine to design the winglet for. The baseline turbine design will first have to be validated using the aerodynamic analysis method. This section will shortly describe the properties of the DTU 10MW RF. The turbine's basic specification will be presented in section 3.1.1 and the operational data for different wind speeds are shown in section 3.1.2.

3.1.1. Basic specifications

The DTU10MW Reference Turbine is designed as part of the 10MW Light Rotor project and is designed, so that future design can be compared to the rotor.
The DTU 10MW RF basic specification are shown in table 3.1. This turbine has been chosen due to the freely available reference results by Bak et al. [59].

Specification	Value	Unit
V_{cut-in}	4	m/s
V_{rated}	11.4	m/s
$V_{cut-out}$	25	m/s
Rated power	10	MW
Radius	89.366	m
Hub radius	2.8	m
Tower height	119	m
Number of blades	3	-
Rotor location	Upwind	-
Power regulation	Pitch	-
Airfoil family	FFA-W3 (60% - 24.1%)	-

Table 3.1: DTU 10MW Reference Turbine basic specification, taken from Bak et al. [59]

The airfoils used in the DTU 10MW RF are the FFA-W3 airfoils with a relative thickness of 60%, 48%, 36%, 30.1% and 24.1%. All these airfoils have a blunt trailing edge. Which offer higher lift coefficients and increased structural performance, as the high trailing-edge thickness offers higher resistance to flapwise bending. However, blunt trailing-edge airfoils offer a challenge from a computation point of view, due to the unsteady vorticity shredded at the trailing edge as argued by [60].

3.1.2. Operational data

The operational data for the DTU10MW RF is shown in table 3.2. It can be seen that the tip speed ratio is at its design value from 8 m/s to 11 m/s. At lower wind speeds, the rotor has a higher tip speed ratio.

U_∞ [m/s]	P [W]	T [N]	C_P [-]	C_T [-]	pitch [deg]	ω [rad/s]	TSR [-]
5.0	809075	356231	0.423	0.931	-1.966	0.628	11.230
6.0	1557954	506214	0.471	0.919	-0.896	0.628	9.358
8.0	3848198	817034	0.491	0.834	-0.000	0.673	7.517
9.0	5496561	1036611	0.493	0.837	-0.000	0.757	7.517
10.0	7560959	1282580	0.494	0.838	-0.000	0.841	7.517
11.0	10088461	1554971	0.495	0.840	-0.000	0.925	7.517
12.0	11170165	1325141	0.423	0.602	-4.502	1.005	7.487
16.0	10875769	853625	0.174	0.218	-12.499	1.005	5.615
20.0	10677976	687705	0.087	0.112	-17.618	1.005	4.492
25.0	10192845	577394	0.043	0.060	-22.975	1.005	3.594

Table 3.2: Operational data for the DTU 10MW RF, taken from Bak et al. [59]

The DTU10MW is designed for offshore operation and IEC wind class IA, meaning a high average wind speed and high turbulence.

3.2. FlightStream

This section will cover the use of FlightStream in this thesis. FlightStream has a few key features that make it stand out from other panel codes, which will be presented in section 3.2.1. Panels codes require a distribution of panels, which is achieved by a mesh, which needs to be able to change with changing geometry. ParaPy is used for this setup, which is explained in section 3.2.2. To determine the number of panels which should be used for the validation process, a mesh convergence study will be performed in section 3.2.3. First in 2D for the lift and drag coefficients and then in 3D for the tangential and normal loads. The validation of the 2D lift and drag coefficients will be done in section 3.2.4. The validation of the tangential and normal loads will be done in section 3.2.5.

3.2.1. Working principles

FlightStream is a commercial panel code that is used as an aerodynamic modelling software for aviation mainly. The main principles of a panel code were explained in section 2.3.3. To the author's knowledge, there are no published studies where FlightStream is used for wind energy. FlightStream was considered as aerodynamic analsysis method for the following key features.

Vorticity solver

Many panel codes, such as VSAERO, use a pressure integration or, more recently, Trefftz plane analysis [61]. FlightStream, however, uses the method of integrated circulation, which works by evaluating the vorticity, using the Biot-Savart law (eq. (2.1)), at a two-dimensional cross-section directed orthogonally to the free stream along the wing or blade [62]. The net integrated vorticity of each cross-section is then calculated with Stokes' Theorem, given in eq. (3.1).

$$\Gamma_k = \int_0^L V_{\text{induced},l} \cdot \mathrm{d}l \tag{3.1}$$

The novelty of this approach is that an unstructured distribution of bound vorticity can be converted into direction net calculation of the vorticity. This reduces the representation of forces along the wing or blade to the manner the forces are represented in Prandtl's lifting line theory. The user is able to choose between the vorticity model for the calculation of the lift, drag and moments, or a model based on the pressure integration. It is, however, discussed with Ahuja [63] that the vorticity solver should be used, as results obtained by the pressure solver had a larger mismatch with the CFD reference results.

Boundary layer model for skin friction drag

FlightStream includes two models to resolve the boundary layer. Which are the Reynolds Averaged model and the Momentum Integral model, which the user is able to choose between. The user is also able to choose between a laminar, transitional or turbulent boundary layer. The boundary layer is resolved to ultimately obtain the skin friction drag, which is an important drag component when designing a winglet. This means FlightStream does not need to rely on lift drag polars to obtain the drag.

FlightStream also contains a model for flow separation, which can be turned on or off. The flow separation model is however a post-processing technique. This means that whether flow separation is turned off or on, has no effect on the calculation of the integrated vorticity and no effect on the location where the vorticity sheds from the blade.

Rotary solver

FlightStream has the option to set a rotational free stream in order to analyse propellers and wind turbines, using a prescribed wake model. With the rotary solver, it is possible to set periodic symmetric boundary conditions which allow for fast computation of the flow field. The solver is a steady-state finding solver, which will keep adjusting a convection factor until it has converged. The induction factor is calculated from the forces in the free stream direction using momentum theory. The convection factor calculated by FlightStream is used to model the wake convection speed of the whole wake. Where the wake convection speed is shown as an equation in eq. (3.2).

$$u_i = U_\infty * CONVECFACTOR \tag{3.2}$$

The wake model is a numerical wake model until a user-specified length downstream of the wind turbine. After this location, the model becomes an analytical wake model as understood by the author of this research after discussions with Ahuja [63]. Validation studies have been done on aircraft, with promising results for propeller wing interaction by [64]. However, no validation studies have been conducted on wind turbines yet with FlightStream.

3.2.2. Setup

Since FlightStream is a panel code, the panels, or mesh, has to be created. The tool that is used for this purpose is ParaPy [65]. ParaPy is a similar tool to other geometry tools such as CATIA [66], which is able to generate quad meshes that can be used as panels for FlightStream. The added advantage of ParaPy is that it is made for parameterised geometries. ParaPy does this by making efficient use of object-oriented programming and lazy evaluation, which means something is only evaluated when demanded. So, for example, whenever the winglet length is changed, only the winglet mesh is modified, instead of re-meshing the whole blade.

In this work, the blade's geometry is created by placing cross-sections of the airfoils in a space and connecting those with BSpline surfaces. Their x, y and z location, as well as their chord length, thickness and pitch axis location is retrieved from Bak et al. [59]. This reference also contains an IGES file of the geometry, which is used for validation to make sure the geometry is correct. An IGES file of the hub geometry is also given, which is used to model the hub geometry in ParaPy, as not much information is given about the shape of the DTU 10MW RF hub.

The mesh is created using built-in functions in ParaPy, which is then exported as a VTK file, which yields better results than an STL file, due to an issue of misalignment of the panels in FlightStream when using STL files. Python is then used to create a text file that is read by FlightStream to set all parameters, import the VTK files and run the simulation. This way an optimiser is free to change design parameters and run the simulation without human interaction needed. A fluxogram of the process is shown in fig. 3.1.

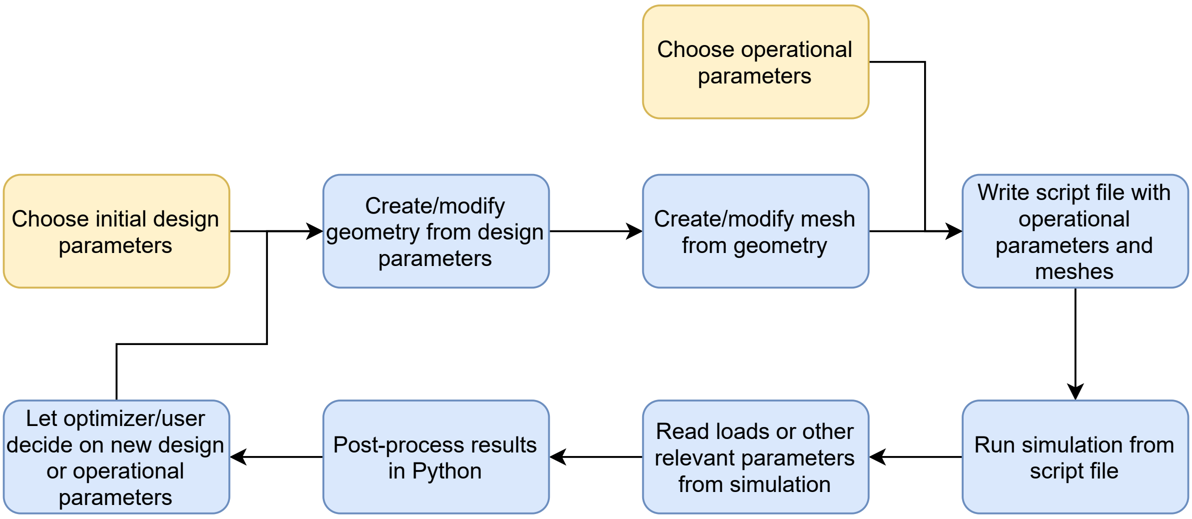

Figure 3.1: Fluxogram of the setup of ParaPy and FlightStream

Design parameters can be the chord and twist distribution, controlled with Bézier curves or winglet parameters, which will be discussed in section 4.1.1 and section 4.2 respectively.

FlightStream requires the user to manually specify the trailing edges. It is also possible to let FlightStream automatically detect the trailing edges or specify the location of the nodes that lie on the trailing edges using a text file. At the time of writing, FlightStream was not able to automatically detect the trailing edges for the used mesh, which is expected to be due to orientation, with respect to the freestream, of a wind turbine blade is different to that of an aeroplane wing. FlightStream is mainly created for aeroplane analysis and the automatic trailing edge algorithm might not be fit yet for wind turbine blades.

It was possible to use the option to specify the trailing edge nodes in a text file as the trailing edge nodes in the mesh created in ParaPy were usually at predictable indices. A function was created to find the indices of these nodes and export these nodes to FlightStream.

3.2.3. Mesh convergence

In order to decide on the number of panels required to get converged results from FlightStream, a mesh convergence study has to be performed. Firstly, this is done for the 2D case, so it can be investigated if the airfoils used in the DTU 10MW RF are analysed correctly in FlightStream.

This analysis is done by creating a wing in FlightStream with a span of $10,000m$ and a chord length of $1m$. The C_L and C_D of the whole wing are then analysed, which are FlightStream outputs. This should minimise the 3D effects on the slender wing. When an C_l of 1.3 is assumed, which is the C_l of the most outboard airfoil, the FFA-W3-241 of the DTU 10MW RF, at an angle of attack of $10°$. An angle of attack of $10°$ is chosen as this is around the maximum lift over drag angle of attack which the blade should operate at. Then assuming an Oswald efficiency factor of 0.7 for a rectangular wing NASA [67], would give the induced drag for the whole wing in eq. (3.3).

$$C_{D_i} = \frac{C_L^2}{\pi\, AR\, e} = \frac{1.5^2}{\pi \cdot 10,000 \cdot 0.7} = 7.68e-05 \tag{3.3}$$

The total 2D drag at an angle of attack of $10°$ would be 0.0124, so that would give an error of $7.68e-05/0.0124 = 0.6\%$ when comparing FlightStream to a 2D aerodynamic analysis tool. The number of spanwise panels had no significant influence on the coefficient as shown in appendix C.

The 2D aerodynamic tools that FlightStream is compared to is the panel code XFOIL and the CFD solver EllipSys2D. The results from XFOIL are obtained by running XFOIL with the same airfoil coordinates as provided to FlightStream and the EllipSys2D results are taken from Bak et al. [59].

For the distribution of the panels in chordwise direction, a cosine distribution has been used for both the suction side and pressure side panels, giving a high mesh density at the trailing and leading edge. The pressure distribution for the FFA-W3-241 at an angle of attack of $0°$ is shown in fig. 3.2. It can be seen that the pressure distribution from FlightStream overall agrees well with XFOIL, except at the trailing edge, where singularities occur. These singularities give an error in the overall results for C_l

and C_d. It is believed by the author that these singularities occur due to the blunt trailing edge of the FFA-W3 airfoils, as panel codes, such as RFOIL, become less accurate with increasing trailing edge thickness as argued by Grasso [60].

Another approach that is tried is by having a cosine distribution from leading edge to leading edge, giving a high density of panels at the leading edge and a low density of panels at the trailing edge. The pressure distribution using this panel distribution is shown in fig. 3.3. The trailing edge of the flatback airfoils has also been sharpened manually to get rid of the singularities. It can be seen in the figure that the singularities on the trailing edge have disappeared and there is still an overall good match with XFOIL. Compared to CFD, the pressure difference is slightly overestimated by FlightStream, which is usually the case with panel codes compared to CFD as argued by Martinopoulos and Missirlis [68].

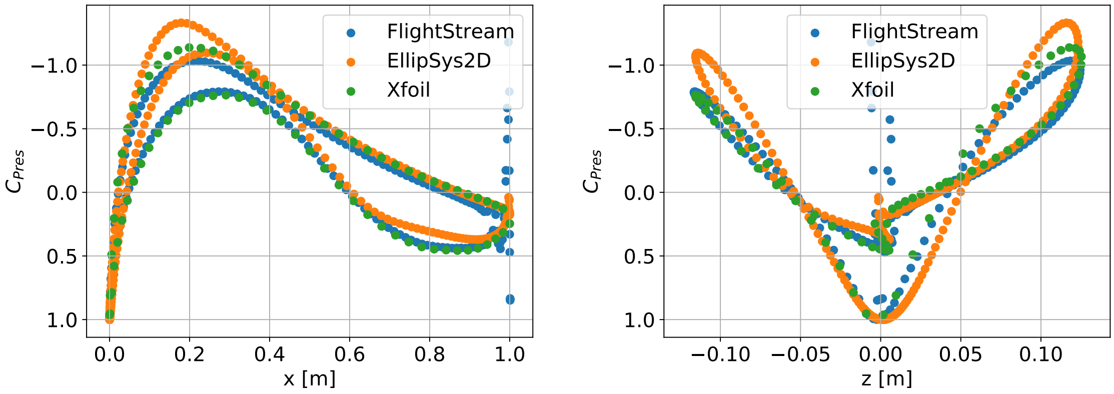

(a) Pressure coefficient in the chordwise (x) direction

(b) Pressure coefficient in thickness (z) direction

Figure 3.2: Pressure coefficient (C_{pres}) for $\alpha = 0°$ against chord (x) and thickness (z) of the FFA-W3-241 airfoil for a double cosine distribution of panels, with 80 datapoints in XFOIL and 200 panels in FlightStream

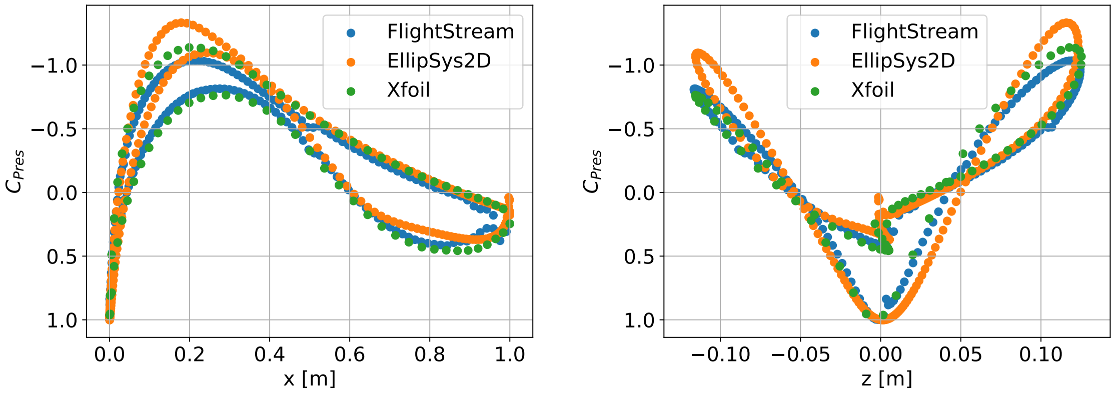

(a) Pressure coefficient in the chordwise (x) direction

(b) Pressure coefficient in thickness (z) direction

Figure 3.3: Pressure coefficient for $\alpha = 0°$ against chord (x) and thickness (z) of the FFA-W3-241 airfoil for a single cosine distribution of panels, with 80 data points in XFOIL and 200 panels in FlightStream

The cosine distribution from fig. 3.3 has been chosen to conduct the 2D mesh dependency study. An angle of attack of $10°$ has been chosen again for the aforementioned reason. The number of panels in the chordwise direction is increased with steps of 40. The resulting C_l and C_d as a function of the chordwise panels is shown in fig. 3.4. Although the values do not converge to a completely steady value, the change from 120 chordwise panels to 160 is 0.14% for C_l. C_d seems to fluctuate more with a 7.6% change between 120 and 160 panels.

The same analysis is done for the full rotor in 3D where the integrated C_P and C_T is obtained for each panel. The C_T is given by FlightStream as C_X and the C_P can be calculated from the moment around the rotational axis, which is given as C_{M_X} in FlightStream. The C_P can be obtained by eq. (3.4), provided that the reference length parameter in FlightStream is set to one, otherwise eq. (3.4) has to be multiplied by the reference length.

$$C_{P_{FlightStream}} = \frac{C_{M_X} \cdot \Omega}{U_\infty} \tag{3.4}$$

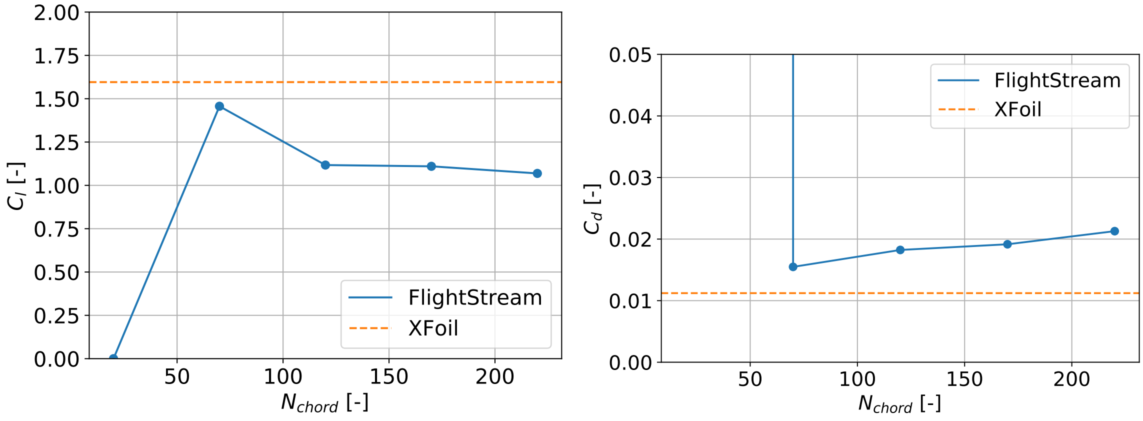

(a) Lift coefficient

(b) Drag coefficient

Figure 3.4: Mesh convergence for aerodynamic coefficients in 2D for the FFA-W3-241 at an angle of attack of $10°$

The results, using the vorticity solver, for the chordwise 3D mesh convergence are shown in fig. 3.5. The number of spanwise panels was set to 60, which will be justified later. It can be seen that the C_P and C_T for the vorticity solver have mostly converged from 120 chordwise panels, with a change of 0.26% and 0.56% from 120 to 160 panels for C_P and C_T respectively. It was not possible to run more than 160 panels due to a shortage of random access memory. It was finally chosen to work with 120 chordwise panels, cosine distributed from leading edge to leading edge, at every radial location of the blade.

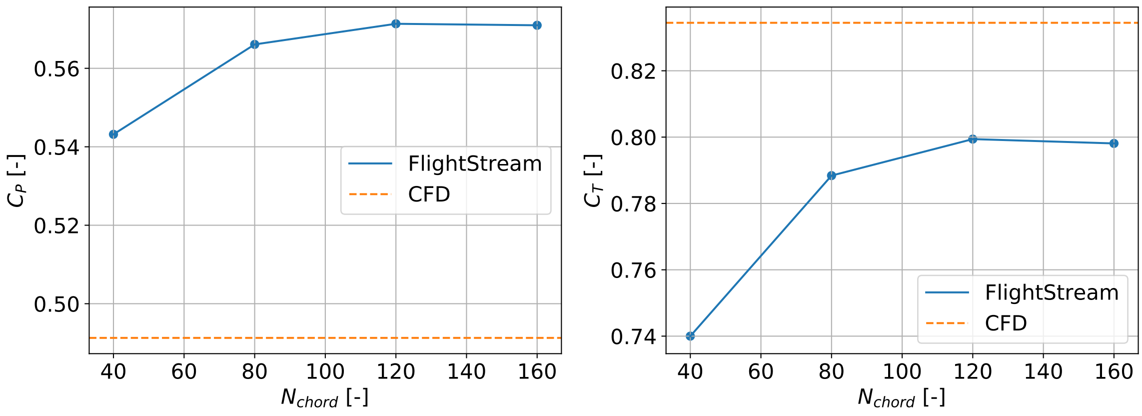

(a) Power coefficient

(b) Thrust coefficient

Figure 3.5: Mesh convergence for C_P and C_T coefficients versus the number of chordwise panels for FlightStream results from the vorticity solver compared to the reference results from CFD for the DTU10MW Reference Turbine

With this chordwise panel distribution, the number of panels in the spanwise direction needs to be determined. The panels in the spanwise direction are also cosine distributed from the root to the tip. The mesh convergence in the spanwise direction is shown in fig. 3.6.

It can be seen that both the C_P and C_T do not seem to converge with increasing spanwise panels. Where especially the C_T keeps decreasing with increasing spanwise panels. This issue is further investigated by looking at the distributed normal and tangential forces, shown in fig. 3.7. It can be seen that the loads

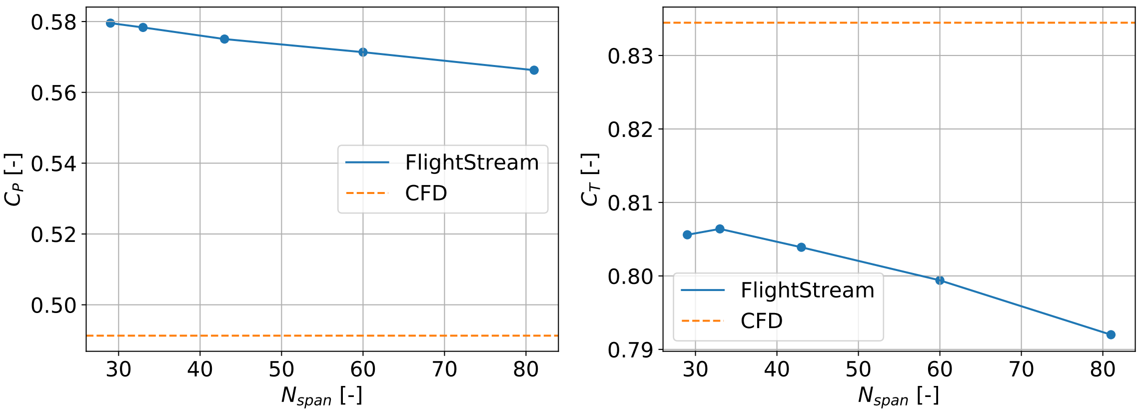

(a) Power coefficient

(b) Thrust coefficient

Figure 3.6: Mesh convergence for C_P and C_T coefficients versus the number of spanwise panels for FlightStream results calculated from the pressure distribution and vorticity compared to the reference results from CFD for the DTU10MW Reference Turbine

keep do not converge at the root of the blade for both the normal and tangential forces. Explaining why the effect on the C_T is the largest, as a change in forces at the root do not have much influence on the torque around the rotational axis. The fluctuating loads at the root are suspected to be due to singularity issues happening with panels of a very small size. From 29 to 43 panels the root seems to capture the loads less accurately at $0.05 < \frac{r}{R} < 0.1$. The shapes of the curves for $N_{span} = 60$ and $N_{span} = 80$ seems to be similar. It is therefore chosen to go with 60 panels, although C_P and C_T are still decreasing.

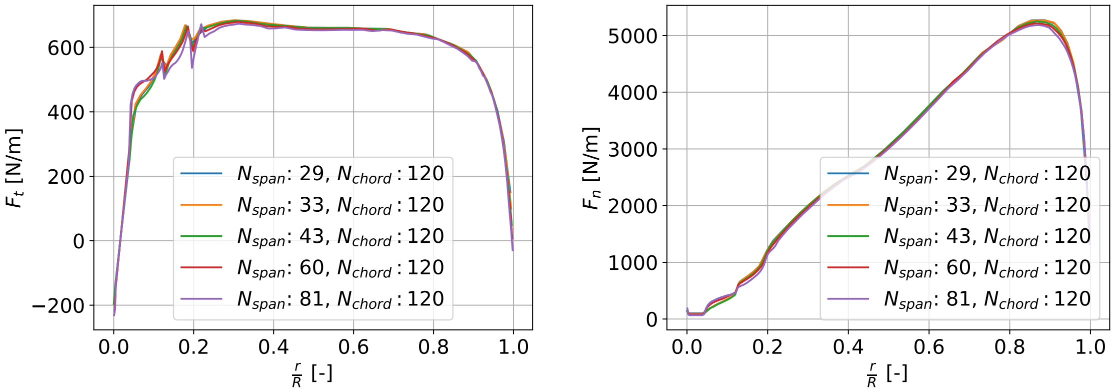

(a) Tangential loads

(b) Normal loads

Figure 3.7: Tangential and normal forces mesh convergence for increasing spanwise panels

3.2.4. 2D Validation

With the number of chordwise panels decided on for the 2D case, the C_l and C_d polars can be created. The polars for the FFA-W3-241 airfoil at a range from $\alpha = 0°$ to $\alpha = 20°$ is shown in fig. 3.8. It can be seen that, for low angles of attack, FlightStream actually has a very close match to the CFD solver, EllipSys2D, where FlightStream even matches more with the CFD reference results than XFOIL. However, as FlightStream's vorticity solver does not work with flow separation yet, the coefficients cannot be used for higher angles of attack, when flow separation starts to occur. The DTU 10MW RF should not be operating at those angles of attack in the outboard sections of the blade, as will be shown in the succeeding section for AWSM.

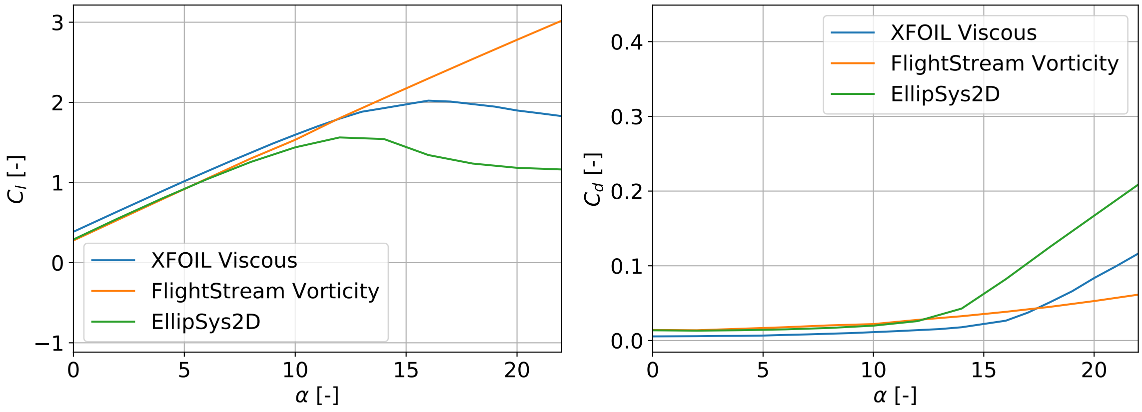

(a) Lift coefficient

(b) Drag coefficient

Figure 3.8: 2D aerodynamic coefficients for XFOIL, CFD and FlightStream for the FFA-W3-241 airfoil

3.2.5. 3D Validation

A validation study for the forces on the full blade in 3D will be done in this subsection. The number of chordwise panels is set to be 120 along the whole span of the blade and the number of spanwise panels is set to 60, both cosine distributed. As it is ruled out in the previous mesh convergence sections that the pressure solver should not be used, the results of the vorticity solver are shown here. The integrated power and thrust is shown for wind speeds $5m/s$ to $25m/s$ in fig. 3.9.

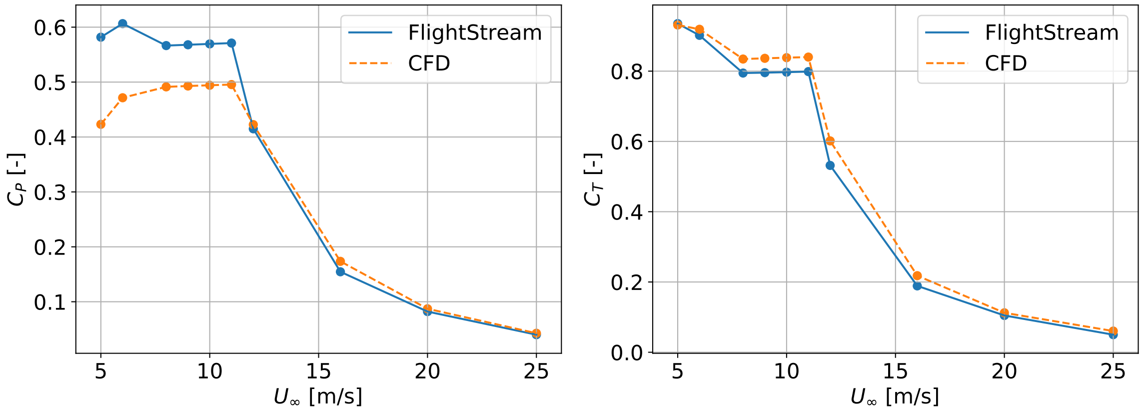

(a) Power coefficient

(b) Thrust coefficient

Figure 3.9: Power and thrust coefficients for different wind speeds

It can be seen that the C_P is over-predicted for most wind speeds below rated, however, there is no clear offset. The C_T is underpredicted by a fairly constant offset. The underprediction in C_T is an unexpected result, as panel codes usually overpredict the C_l, as panel codes have difficulty handling the complex vortex shedding which occurs on a blade with separated flow as argued by Vaithiyanathasamy et al. [69]. With an overpredicted C_l, an overpredicted C_T is expected as well.

FlightStream gives direct access to the tangential and normal forces on the blade, which are shown in fig. 3.10 for $U_\infty = 8m/s$. It should be noted that these are the inviscid forces without flow separation. As of right now, FlightStream is only able to plot the sectional forces without viscous effect and flow separation. The total integrated forces do include viscous effects and flow separation, however.

The forces that are shown here are with an $U_\infty = 8m/s$, as this wind speed is the first entry in table 3.2 where the DTU10MW is running at the optimum tip speed ratio. The first entry that satisfies this condition is chosen as compressibility effects are the lowest here, although, for higher rotational velocities and wind speeds, the tip of the DTU10MW is still operating below 0.3 Mach, for which compressibility are usually neglected.

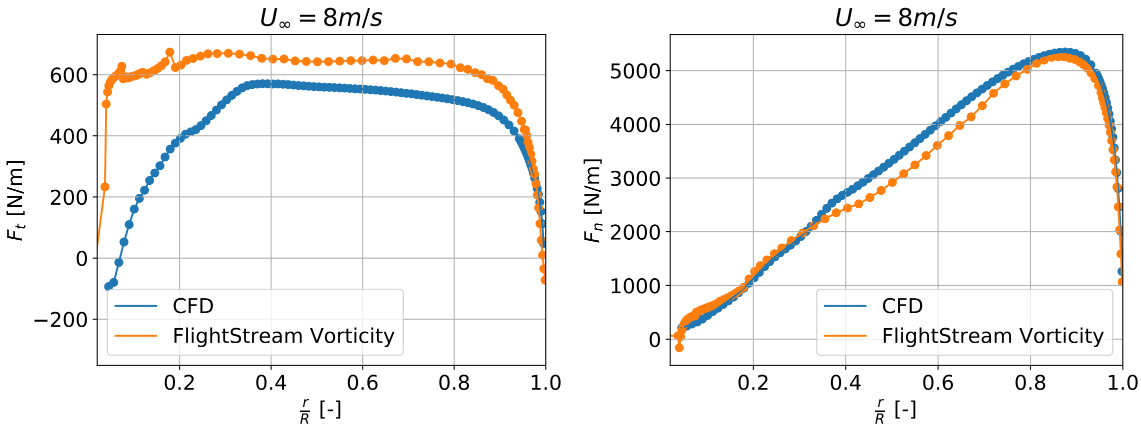

(a) The tangential forces against radius

(b) The normal forces against radius

Figure 3.10: Aerodynamic forces comparison between FlightStream and CFD reference results for the DTU10MW Reference Turbine at 8 m/s

As seen in fig. 3.10, the normal loads are underpredicted and tangential loads are overpredicted, as expected from the integral C_P and C_T. The normal loads have a relatively smaller offset than the tangential loads, which is not surprising as a small error in the angle of attack or drag forces has a bigger influence on the tangential loads.

The local C_T along the radius of the blade can be calculated with the normal loads, which is done using equation eq. (3.5).

$$C_{T,local} = \frac{N_{blades}\, F_n}{\frac{1}{2}\rho U_\infty^2\, 2\pi R} \tag{3.5}$$

Where the local C_T for both FlightStream and the CFD reference results is shown in fig. 3.11b. The same can be done for the tangential loads and local C_P with eq. (3.6).

$$C_{P,local} = \frac{N_{blades}\, F_t\, \Omega}{\frac{1}{2}\rho U_\infty 3\; 2\pi R} \tag{3.6}$$

From the local C_T the maximum obtainable local C_P can be obtained using 1D momentum theory as shown by Loenbaek [70], before the viscous losses, tip losses or wake rotation losses are applied. This can be done with eq. (3.7).

$$C_{P,local,max} = \frac{1}{2}\left(1 + \sqrt{1 - C_{T,local}}\right) C_{T,local} \tag{3.7}$$

The local C_P from the CFD reference and FlightStream results, together with the maximum obtainable local C_P calculated from the local C_T from FlightStream is shown in fig. 3.11a. It is seen that the local C_P is well above the maximum obtainable C_P for FlightStream, which is unphysical. The reason for this behaviour is expected to be due to the prescribed wake model as well as underpredicted drag forces, as will be further elaborated on in section 3.4.1, where FlightStream will be compared with the lifting line code AWSM.

3.3. AWSM

This section will discuss the validation of the lifting line code, AWSM. The working principles of AWSM will be explained in section 3.3.1, where the basics of the lifting line model will be explained and the possible vortex wake options. The setup for AWSM is simpler than for FlightStream, which setup will be presented in section 3.3.2. The convergence of the spanwise points will first be done without a winglet in section 3.3.3, after which the validation of the baseline blade, without winglet, can be done in section 3.3.4. The convergence of spanwise points of the blade with winglet is performed in section 3.3.5, after which the verification of winglet loads is done in section 3.3.6.

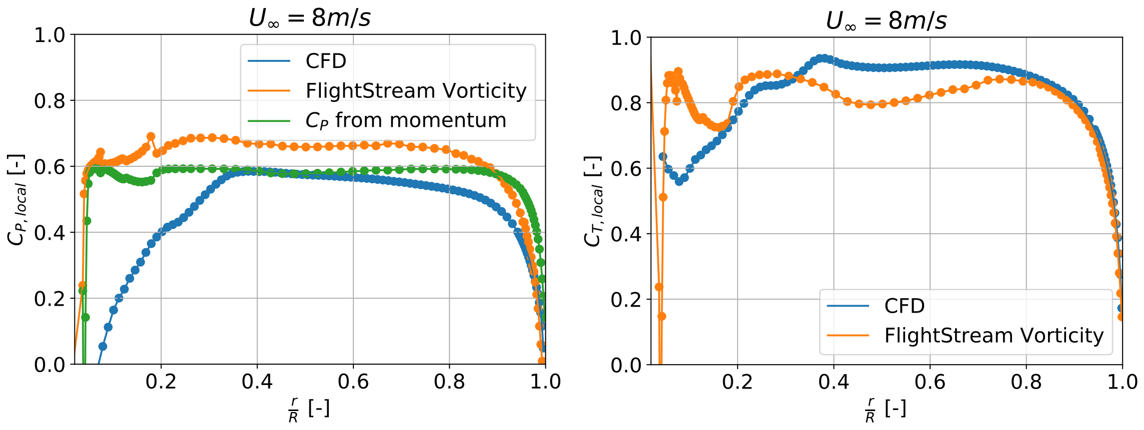

(a) Local C_P forces against radius with maximum C_P obtainable from 1D momentum theory given local C_T

(b) Local C_T

Figure 3.11: Comparison between local C_P and C_T coefficients for FlightStream and CFD reference results for the DTU10MW Reference Turbine

3.3.1. Working principles

The lifting line code used in this thesis is called Aerodynamic Wind Turbine Simulation Module (AWSM), which is developed by ECN, now part of TNO. The main principles of a lifting line code are explained in section 2.3.3. This subsection will discuss the specifics of AWSM in more detail.

Lifting line model

The main assumption with lifting line models, such as AWSM is that, as the blade is modelled as a line, the generated lift acts at the quarter chord of each cross-section of a lifting surface, which is aligned with the plane of the cross-section. This restricts the model to slender and only slightly curved geometries as argued by Van Garrel [71].

The viscosity effects are taken into account with user-defined lift, drag and moment polars, where the non-linear relationship between the angle of attack and the local lift, drag and moment coefficients are supplied, which is different from FlightStream, where all these quantities were calculated.

The effect of thickness or displacement effects is not taken into account in this model. This means that when considering potential flow theory, the flow field around an airfoil can be described using sinks and sources as in fig. 3.12a. When ignoring the effect of thickness and displacement, it leads to $\sigma = (\vec{\nabla} \cdot \vec{u}) = 0$, so the blade can be modelled with vorticity effects only as shown in fig. 3.12b. The bound vortex from the blade is placed at $\frac{1}{4}$ of the chord of an airfoil. The angle of attack, however, is evaluated at $\frac{3c}{4}$. The reason for this is shown by Lindenburg [72] who argues that when considering an airfoil with a uniform camber line and fully laminar flow, the strength of the circulation is such that the direction of the flow at $\frac{3c}{4}$ is in the direction of the camber line. The vorticity is modelled as a line integral with constant vorticity along each line in the lifting line model, where each line is part of a closed vortex ring's according to Helmholtz theorem as explained in section 2.1.1.

The induced velocity by each vortex is calculated by the Biot-Savart law in eq. (2.1). To avoid singularities, a cut-off radius parameter (δ) is introduced in the calculation of the induced velocity as shown in eq. (3.8).

$$\vec{u}_\Gamma\left(\vec{x}_p\right) = \frac{\Gamma}{4\pi} \frac{\left(r_1 + r_2\right)\left(\vec{r}_1 \times \vec{r}_2\right)}{r_1 r_2 \left(r_1 r_2 + \vec{r}_1 \cdot \vec{r}_2\right) + \left(\delta l_0\right)^2} \tag{3.8}$$

The value of δ can be chosen by the user.

AWSM uses the 3D correction model as developed by Snel, discussed further by Montgomerie et al. [73], which corrects the 2D coefficients to account for the effect of rotation, which is most noticeable in the inboard regions.

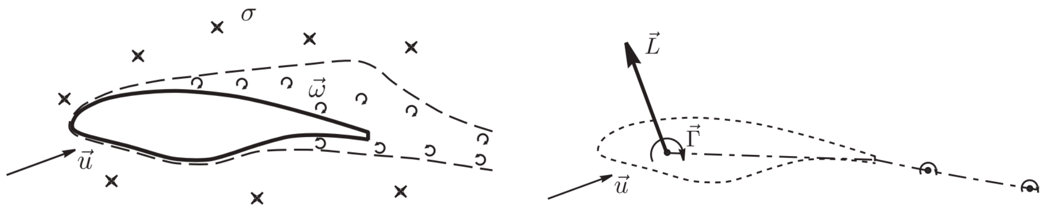

(a) Flow field around airfoil consisting of sources and vortices (b) Lifting line flow field model

Figure 3.12: Flowfield model taken from Van Garrel [71]

Vortex wake models

AWSM is a time-stepping lifting line code, whereas time advances, vorticity is shed from the trailing edge. Each timestep new vortex rings are joined with the older vortex rings, which form a vortex lattice together. The position of the downstream part of the wake is determined by the convection of the wake vortex lattice nodes, which is applied in two separate steps. The convection by the free-steam velocity and the induced velocity of the bound and trailing vortices, which is calculated for each timestep. The timestep can be chosen by the user and is advised by Boorsma and Caboni [74] to be a value corresponding to a rotation of $10°$ or less of the rotor for each timestep. So the timestep is always set to $10°$ per timestep for each rotational velocity.

AWSM gives the user the option to choose between two prescribed wake models or a free wake model. A short overview of the models is shown in fig. 3.13.

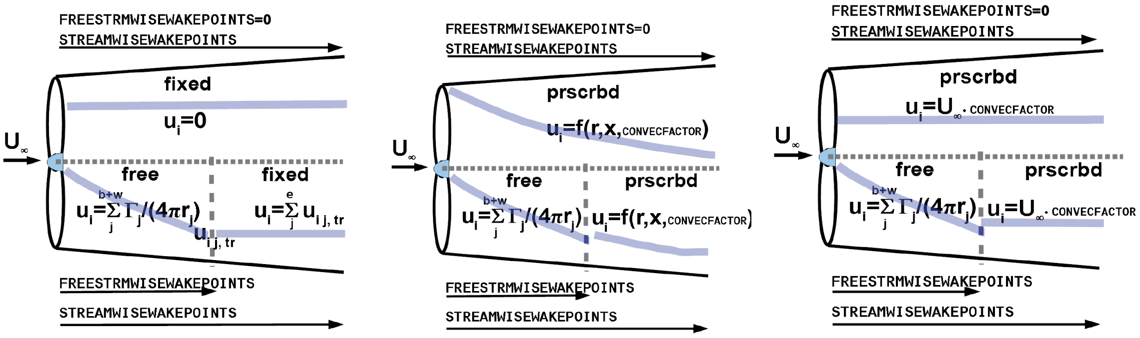

(a) Free wake (b) Prescribed wake model 1 (c) Prescribed wake model 2

Figure 3.13: Possible wake models, taken from Boorsma and Caboni [74]

For the free wake, the wake is free to roll up due to self-induction. The user is able to choose the length of the free wake, which is advised by Boorsma and Caboni [74] to be a length equal to two diameters of the rotor. The length of the free wake can be set by setting the number of free streamwise wake points, which can be calculated with eq. (3.9).

$$N_{wake,points} = \frac{L_{wake} * D}{U_\infty(1-a)dt} \tag{3.9}$$

Where L_{wake} is to be supplied in diameters and the induction factor a needs to be assumed. For the simulations in this work, a is assumed to be $\frac{1}{3}$. This assumption will be validated later. The length of the total wake can also be chosen by the user, which is set as the streamwise wake points. The value of the streamwise wake points is set to a length corresponding to three rotor diameters, as advised by Boorsma and Caboni [74]. The rest of the wake, downstream of the free wake, is fixed and convects with the undisturbed wind velocity minus the spanwise averaged induction at the free to fixed wake transition, as visually illustrated in fig. 3.13a.

Whenever a prescribed wake is used, the number of free stream wake points is set to zero and prescribed wake model one or two can be chosen. Prescribed wake model 1 is described by Currin, Coton, and Wood [75] and is illustrated in fig. 3.13b. In prescribed wake model 2, the induced wake convection speed is simply set to a fraction of the free stream, or in an equation: $u_i = U_\infty \cdot CONVECFACTOR$, which is illustrated in fig. 3.13c. This is the same wake convection model as in FlightStream, except that $CONVECFACTOR$ is calculated from the C_T using momentum theory in FlightStream, whereas in AWSM the parameter is chosen by the user.

3.3.2. Setup

AWSM, just as FlightStream, works with text files as input. The main difference is that AWSM does not use a mesh, but allows the user to input points that define the lifting line. Still, the spanwise points convergence will be termed mesh convergence in this section, for consistency. Each spanwise point has an x y z location, as well as a local chord length, thickness over chord ratio, twist and distance to pitch angle in y. The setup between ParaPy and AWSM, therefore, looks very similar to the setup from FlightStream described in fig. 3.1, with the difference that the mesh is now a set of points.

The wake length is set to three diameters as discussed in the previous subsection. The simulation time is set to the time needed for three diameters of wake to convect, multiplied by two, to ensure convergence. An example of the C_P and C_T over time is shown in fig. 3.14a, where three diameters are convected in 100 seconds for $U_\infty = 8m/s$. The change in C_P between 190 and 200 seconds is 0.04%, which is deemed small enough by the author of this thesis to be converged.

Figure 3.14b shows the wake length after 100 simulation seconds. The wake length is indeed approximately $3 \cdot 178.7m = 535m$, showing that the aforementioned assumption of $a = 1/3$ approximately gives the right wake length, however, it should be noted that this can slightly change when the loading on the rotor is changed.

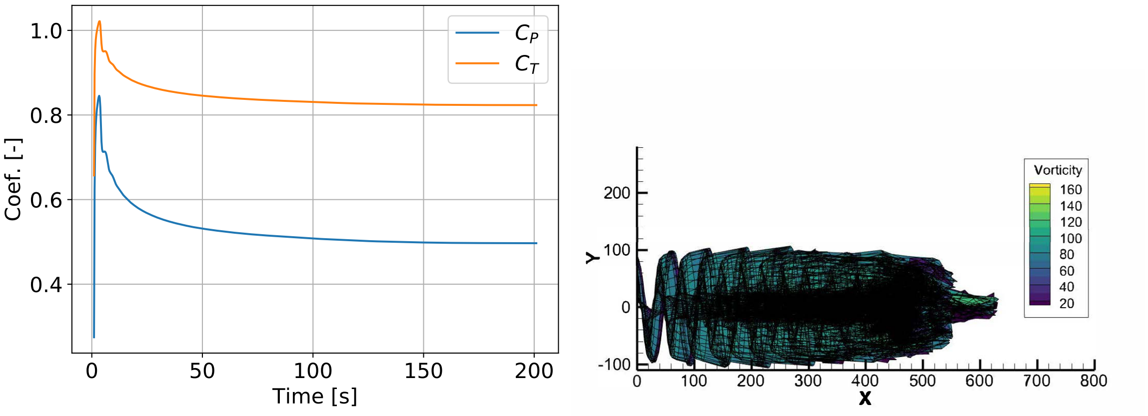

(a) C_P and C_T coefficients over time

(b) Wake length after 100 simulation seconds with a timestep of 0.27 seconds for a wind speed of $8m/s$. Plotted with Tecplot.

Figure 3.14: Power and thrust coefficients over time with wake plotted after $100s$

AWSM has many more parameters that can be modified from its standard value. Both the ground and tower effects have been turned off for the validation study. The wake cut-off radius has been changed to 20% of the element vortex line length, instead of the default of 10% to make singularities less likely. Other non-discussed parameters have been set to their default value given by Boorsma and Caboni [74].

The coordinate system for AWSM is shown in fig. B.1. The local twist of the blade can be determined with γ_e. A winglet can be made in the geometry by modifying xB. AWSM calculates β_e, which cannot be set by the user. For sweep in the blade or winglet, the distance from the pitch axis ($c14$) is used instead of the yB parameter in this research. This is done so $alpha_e$ stays unmodified, as no rotation of geometry around the azimuth is desired.

3.3.3. Mesh convergence without winglet

To decide how many points should be used during the optimisation process, a spanwise mesh convergence study also has to be done for AWSM. The points are cosine distributed as advised by Van Garrel

[71]. The points are distributed along the curvilinear radius, which is a parameter calculated by AWSM when given a collection of points in x, y and z. The blade geometry is thus first passed to AWSM with a large number of points after which AWSM outputs the curvilinear radius for each point. The points are then cosine distributed with the desired number of points and the input points are ready for an AWSM simulation. The reason for doing it in this manner is that the exact calculation of the curvilinear radius is not straightforward and unknown to the author.
Due to singularity issues occurring at the root, all points below an arbitrary length of $4m$ are removed from the input to AWSM, after the points are cosine distributed. The integrated C_P and C_T are shown in fig. 3.15a. The relative change is calculated by $\frac{a[i+1]-a[i]}{a[i]}$ and given in fig. 3.15b. In the plots shown for sectional properties, the radius r on the x-axis is defined as the z coordinate of the blade given to AWSM.

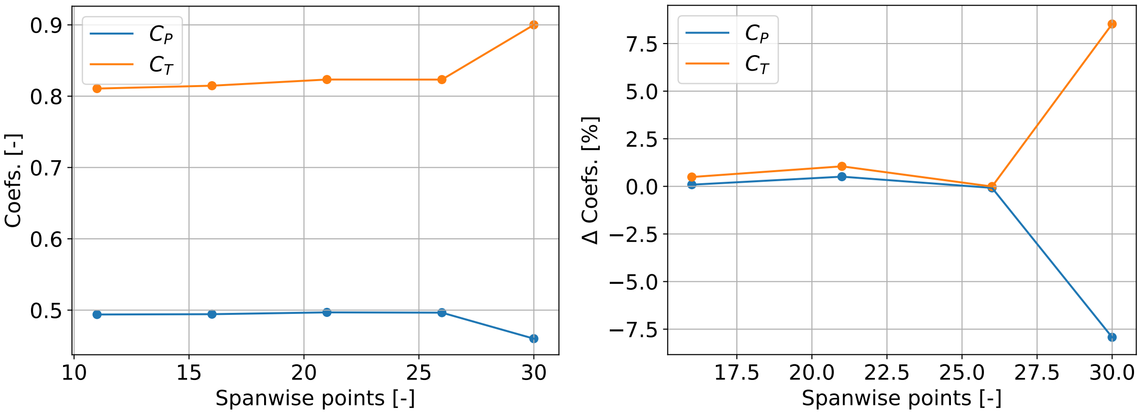

(a) Values of the integrated C_P and C_T for different numbers of spanwise points

(b) For each number of spanwise points, the relative difference in percent with the previous number of points is shown

Figure 3.15: Mesh convergence for AWSM from 11 to 26 spanwise points with steps of 6 points

Furthermore, the normal and tangential loads, the angle of attack and the circulation for different number of spanwise points is shown in fig. 3.16 and fig. 3.17.

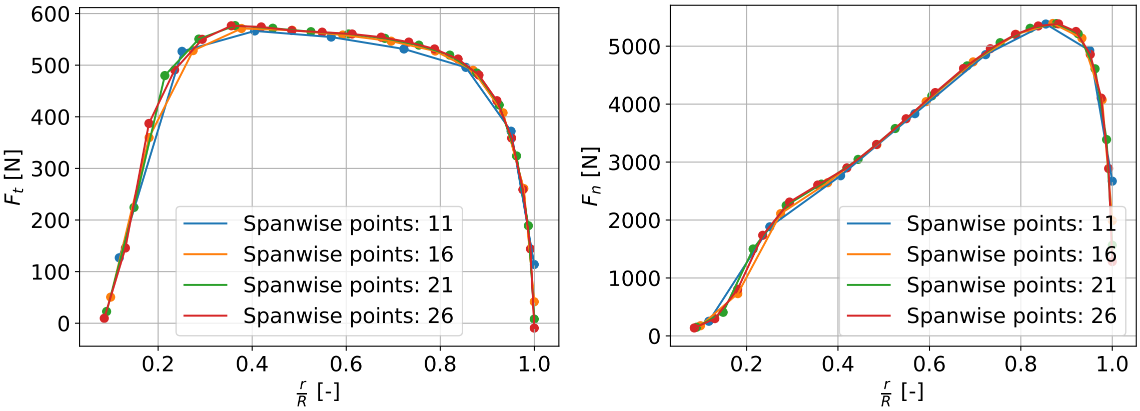

(a) Tangential loads

(b) Normal loads

Figure 3.16: Tangential and normal loads for mesh convergence without winglet

The angle of attack seems to fluctuate slightly more with an increasing number of points, however, this is only apparent closer to the root of the blade. The relative change in C_P and C_T is below 0.1 % from 21 to 26 points as shown in fig. 3.15b, which is deemed as converged. Therefore 21 spanwise points are used for the clean blade validation and optimisation. Using a higher number of points than 26 led to singularity issues, leading to divergence of the integrated C_P and C_T again, as is seen in fig. 3.15. The sectional properties for this number of points are not displayed here.

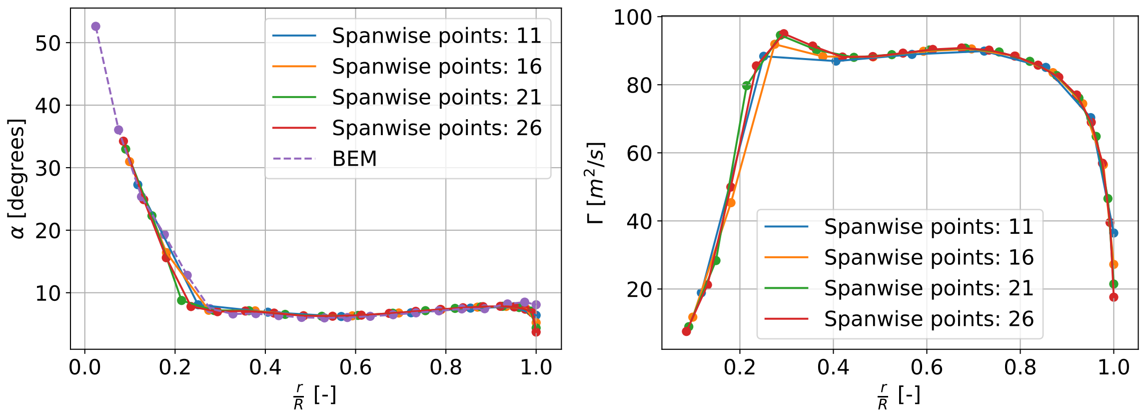

(a) Angle of attack

(b) Circulation

Figure 3.17: Angle of attack and circulation for mesh convergence without winglet

3.3.4. Validation of the baseline blade

Using the parameters and settings discussed before, the operational curve for the C_P and C_T can be made, which is shown in fig. 3.18.

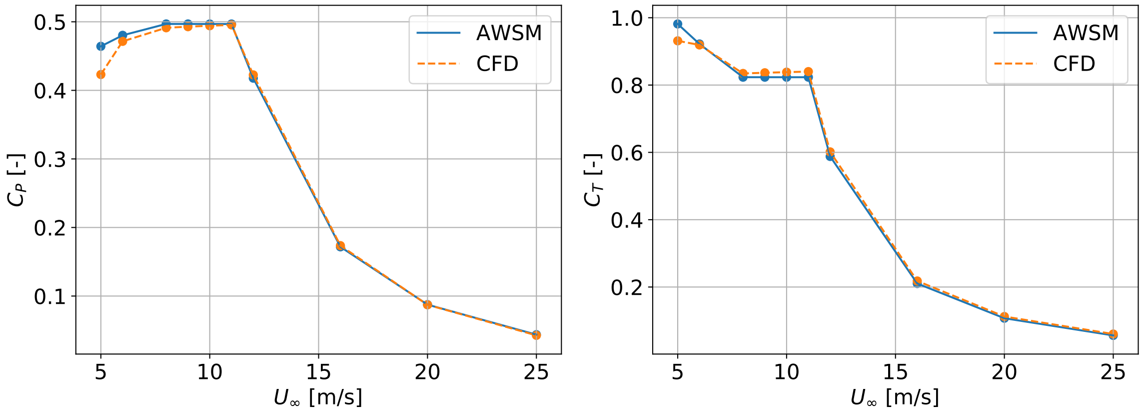

(a) Power coefficient versus wind speed

(b) Thrust coefficient versus wind speed

Figure 3.18: C_P and C_T curve for different wind speeds

A fairly close match with CFD is obtained, with an exception at $U_\infty = 5m/s$. In general, there is generally a slight overprediction for the C_P and a slight underprediction for the C_T. However, the offset is quite consistent for all wind speeds. For $U_\infty = 8m/s$, the normal and tangential forces are shown in fig. 3.19. Figure 3.19 shows that the cause of the underprediction in integral C_T is due to the lower loads close to the root of the blade. Figure 3.19a shows a slightly higher tangential load over the whole blade, however, again a lower load close to the root. The same behaviour is observed for other wind speeds, which are shown in appendix B.3.

There were no other quantities that could be compared to CFD, except for the loads. However, one can see from fig. 3.14a that the power and thrust converge to a steady value, hinting no singularities are occurring on the blade.

Figure 3.20a shows the angle attack over the radius of the blade. It can be seen that the blade operates close to each airfoil at its optimum angle of attack, resulting in a maximum $\frac{C_L}{C_D}$ for each airfoil. Linear interpolation is used to determine to $\frac{C_L}{C_D}$ between locations where one airfoil is changing into another. The same is done for $\frac{C_L}{C_D}$ values shown in fig. 3.20b, which shows that the $\frac{C_L}{C_D}$ in AWSM is around the optimum. It should be noted that AWSM uses spline interpolation to determine the C_L, C_D and C_m as a function of angle of attack, instead of linear interpolation.

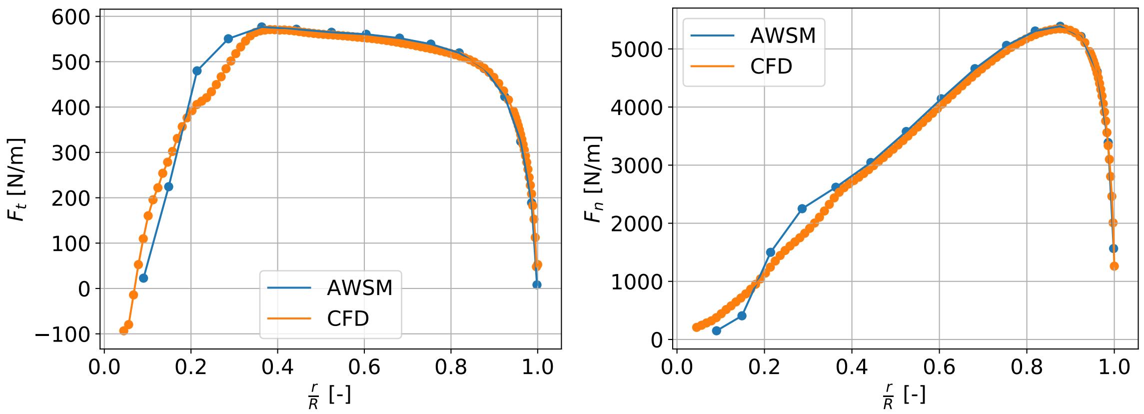

(a) Tangential

(b) Normal

Figure 3.19: Comparison between tangential and normal loads for the DTU10MW Reference Turbine for AWSM and CFD reference results at $8m/s$

(a) Angle of attack

(b) Lift over drag ratio

Figure 3.20: Comparison of angle attack and lift over drag ratio found from AWSM and the 2D optimum

3.3.5. Mesh convergence with winglet

As will be shown in section 4.2, the winglet has a kink between where the blade changes into the winglet. Especially for a straight winglet, this could introduce singularities or changes in results around this region for different distributions of points. The mesh convergence study is therefore redone for a blade with a straight winglet. The winglet of the results presented have has no sweep, a length of $4m$ (or 5.6% of the rotor radius), no twist, no taper and a radius of $0.5m$. The points are distributed along the curvilinear radius again. The integrated C_P and C_T against increasing spanwise points is shown in fig. 3.21a, with the relative change between increasing points in fig. 3.21b.

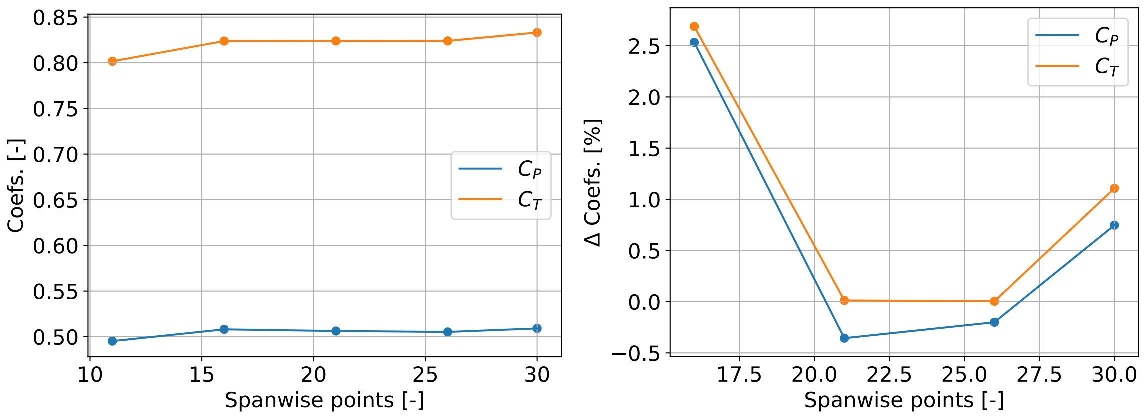

(a) Absolute change

(b) Relative change

Figure 3.21: Change of integrated C_P and C_T with increasing spanwise points

Figure 3.22 shows the sectional loads on the blade for an increasing number of spanwise points and fig. 3.23 the angle of attack and circulation distribution.

Similar trends, convergence wise, are seen at the inner section of the blade as for the clean configuration case. At the kink between the winglet, at a radius of about $80m$, there is a noticeable difference in normal and tangential loads with increasing spanwise points. Using a discretisation of 21 spanwise points does not seem to capture the shape of the curve the loads create completely, which would lead to a different result than, for example, 26 spanwise points, when integrating the load curves. This can be seen back in fig. 3.21, where a bigger change is seen for going from 21 to 26 points. Using more

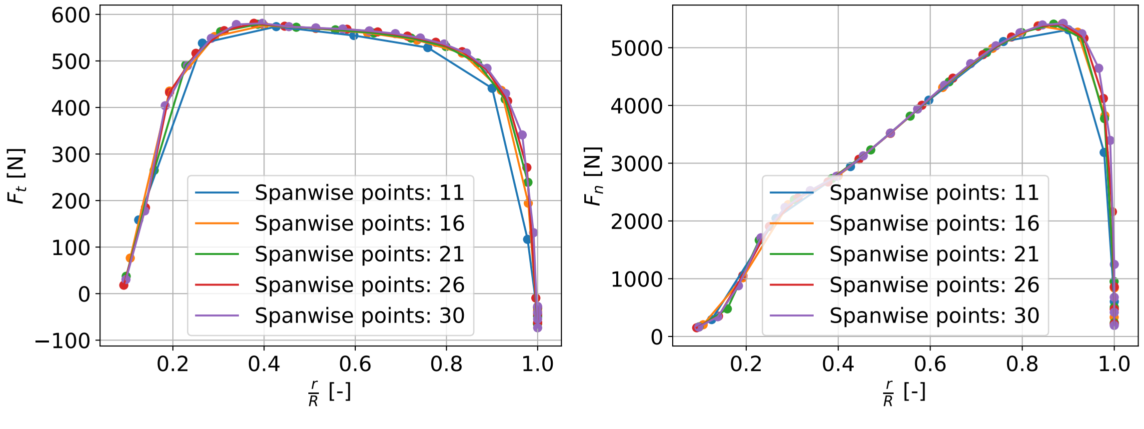

(a)

(b)

Figure 3.22: Normal and tangential forces for an increasing number of spanwise points

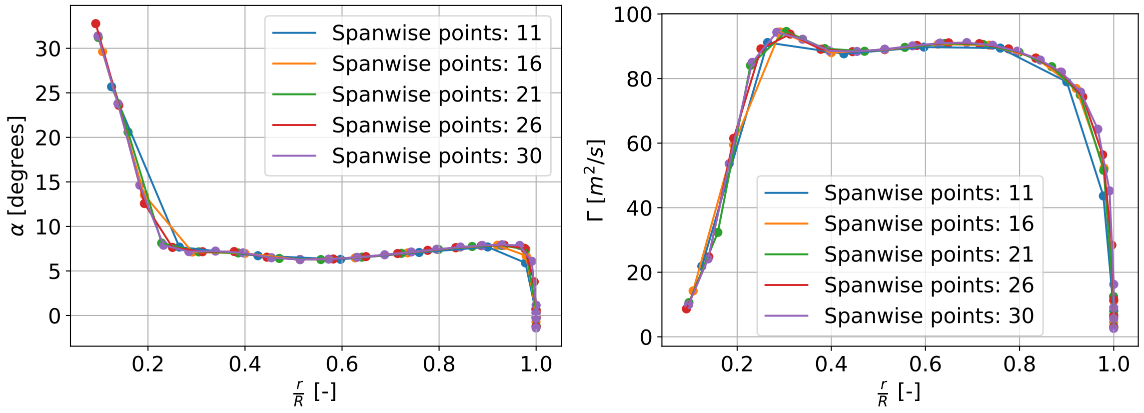

(a) Angle of attack

(b) Circulation

Figure 3.23: Angle of attack and circulation for winglet mesh convergence study

than 26 points leads to divergence of the coefficients again, however. By looking at the loads and circulation, it is decided that 26 points will be used for the winglet.

3.3.6. Winglet loads verification

To verify if the loads on the winglet are as expected from eq. (2.10), a straight winglet, ($90°$ cant) with no twist, no taper (winglet root chord is equal to the winglet tip chord), a tip and root chord of $0.6m$, no sweep and a height of $4m$ is analysed both upwind and downwind. The chord of the blade is kept the same over the whole radius.

The normal and tangential forces are shown in fig. 3.24a and fig. 3.24b.

As expected from eq. (2.10), the normal forces on the winglet are zero, as seen in fig. 3.24b at the tip. Furthermore, the tangential forces on the winglet are positive for the upwind winglet, while negative for the downwind winglet, as expected.

The upwind winglet results in a decrease in tangential forces on the blade, while the downwind winglet results in an increase in tangential forces on the blade, which is as expected from eq. (2.9). It should be noted that since these straight winglets are fitted to the blade with unchanged chord and twist, the winglet could introduce sub-optimal loads to the blade and therefore these results do not say anything meaningful about the quantified power or thrust changes and therefore do not say anything about the benefit of an up or downwind winglet. This subsection only serves to verify if the change of loads for an up or downwind winglet are in the expected direction.

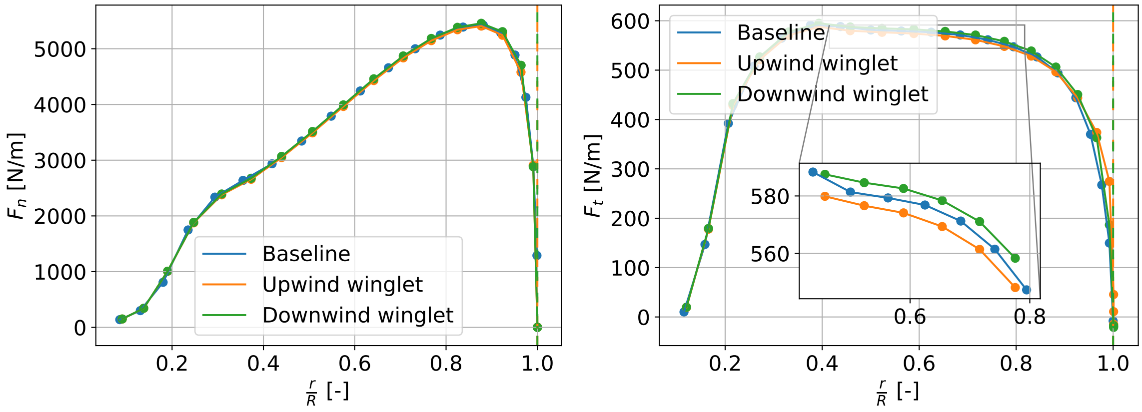

(a) Normal loads

(b) Tangential loads

Figure 3.24: Upwind and downwind winglet loads verification

3.4. Comparison of used methods

This section will show a comparison between AWSM and FlightStream and a more theoretical comparison between lifting line and panel codes in general. AWSM and FlightStream are compared in section 3.4.1. Section 3.4.2 will elaborate on some differences between lifting line and panel codes.

3.4.1. AWSM and FlightStream

As seen from previous sections, more accurate results for the loads on the rotor are obtained for AWSM than for FlightStream when comparing to the CFD reference results.

A possible explanation for the inaccuracy of the FlightStream results could be the prescribed wake model. As mentioned before, the induced wake convection speed (u_i) is constant downstream of the rotor in FlightStream, where u_i is determined using the normal forces on the blade. FlightStream outputs the wake convection speed, which is obtained after the convergence. For a simulation of $U_\infty = 8m/s$, a value of $u_i = 3.511m/s$ was obtained. An AWSM simulation, using prescribed wake model 2, as shown in fig. 3.13c, is now run where the u_i is manually set to the same value as in the FlightStream simulation, so FlightStream and AWSM should be operating with the same wake. Both wakes are shown in fig. 3.26.

The integrated C_P and C_T for FlightStream and AWSM using a prescribed wake is shown in table 3.3 and the normal and tangential loads in fig. 3.25. For reference, the CFD, AWSM free wake and FlightStream free wake results are also shown. The normal loads from both AWSM and FlightStream with prescribed wake are quite similar, except for the inner part of the blade, leading to a somewhat more accentuated difference in the integrated C_T. Although there is quite a similarity between the normal forces, the is a large difference between the tangential forces for AWSM and FlightStream prescribed. Upon request, a free wake, or unsteady wake motion as termed in FlightStream, model has been added. As seen from fig. 3.25 and table 3.3, results are relatively far off compared to the CFD reference results at the time of writing.

It was furthermore difficult to compare other quantities than the loads. FlightStream does not give direct access to the circulation distribution obtained from their vorticity solver. One could obtain the circulation from the pressure distribution, which the user does have access to in FlightStream. However, this would likely not result in the same circulation that is used to calculate the integrated coefficients given by FlightStream.

The error in the loads obtained by FlightStream is partly explained by the wake model, which explains the underprediction of the normal loads. The overprediction of the tangential loads is not fully understood. A possible explanation is the induction from the wake for $x > 35$ in fig. 3.26a not having an influence on the blade. This would likely increase the tangential loads, however, this would have led to higher normal loads than which are obtained now. Another possible explanation given by Ahuja [63] is that the wake is convected with a constant induction along the radial axis of the blade.

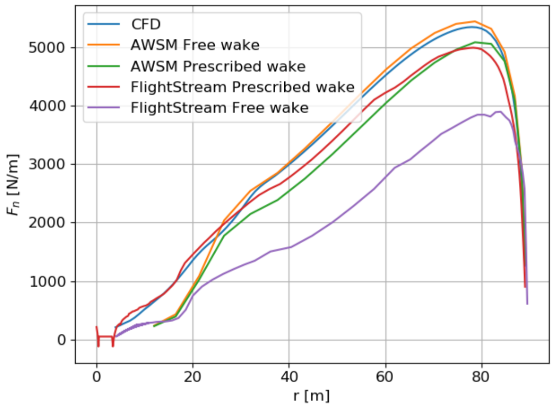

(a) Normal loads (b) Tangential loads

Figure 3.25: Comparison of loads for CFD, FlightStream and AWSM both for a free wake and prescribed wake

	CFD reference	AWSM free wake	AWSM prescribed wake	FlightStream prescribed wake	FlightStream free wake
C_P	0.491	0.497	0.381	0.569	0.118
C_T	0.834	0.823	0.737	0.788	0.536

Table 3.3: Integrated power and thrust coefficients from CFD, AWSM and FlightStream. The prescribed wakes for AWSM and FlightStream is expected to be approximately the same.

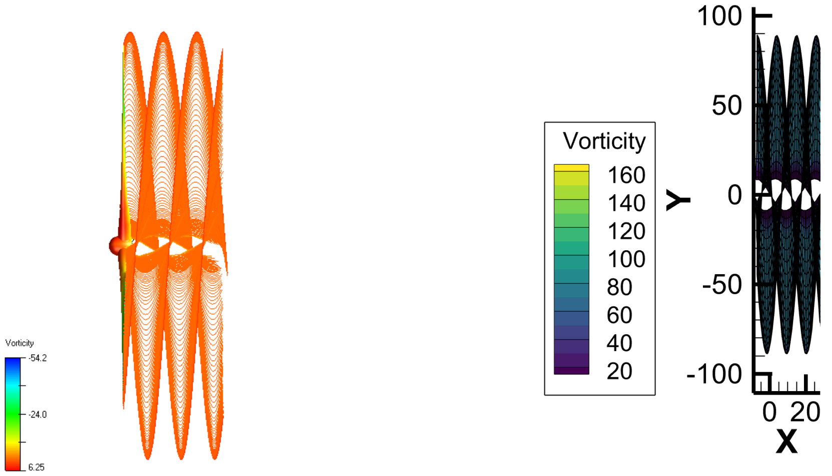

(a) FlightStream prescribed wake from FlightStream GUI (b) AWSM prescribed wake plotted in Tecplot

Figure 3.26: Wake for AWSM and FlightStream for $0 < x < 38m$ with $u_i = 3.511m/s$. The FlightStream GUI only shows the a small part of the wake.

3.4.2. Lifting line and panel codes

As discussed before, lifting line is theoretically a 2D model under the assumption that the extension of the geometry in the spanwise direction is predominant over the extension of the geometry in the chordwise and thickness direction. This assumption could have an effect on the loads in the normal and tangential direction. Sant et al. [76] investigated the difference in predictions for the axial and tangential velocities between experimental results using SPIV data, a panel code and lifting line (although not AWSM) for a horizontal axis wind turbine. Mean errors of 15% and 11% were found between lifting line and SPIV for the axial and tangential velocities at the blade's tip respectively. The difference between lifting line and SPIV became increasingly apparent closer to the tip. Panel codes performed better with mean errors of only 6 % and 2 % for the axial and tangential velocities respectively. This can be quite worrisome as the differences in induced velocities are what makes a winglet effective. It is difficult to conduct a similar study with AWSM and FlightStream, firstly, since reference CFD or experimental data, for the DTU10MW, for the velocities around the blade, is not available. Secondly, since there is a noticeable difference between the loads obtained from AWSM and FlightStream and it is unknown what the exact cause of this difference is.

3.5. Synthesis

This chapter concludes the load validation analysis for FlightStream and AWSM. It has been chosen to continue with AWSM for the optimisation part of this research. This has the disadvantage of going from 3D to 2D, meaning 3D effects on the rotor will not be modelled or modelled by correction factors instead. Another consequence is that only airfoils can be used for which polars are available. Still, AWSM is preferred, firstly and mainly, due to the free wake model, which has shown more reliable results in AWSM so far, as results are obtained that are in better agreement with the high fidelity CFD results. Secondly due to the inconsistency in the tangential forces obtained by FlightStream for different wind speeds and relatively large differences between FlightStream and reference results from CFD.

4

Optimisation setup

This chapter will discuss the optimisation setup used in this thesis, which includes the parameterisation, objectives optimised for and optimisation technique used.

As a winglet will change the loading on the blade, the blade will be optimised as well. For the optimisation, the blade first needs to be parameterised. How the blade is parameterised is explained in section 4.1. The parameterisation of the winglet itself is explained in section 4.2. The different objectives that will be maximised or minimised are explained in section 4.3. After the parameterisation and objectives are explained, a parameter study will be performed to determine the maximums and minimums of the winglet parameters, which will be done in section 4.4. In this thesis, for most optimisation cases, the loading on the blade will be optimised by optimising the blade's chord. The twist will be determined as a post-processing step, which will be explained in section 4.5. As it will be assessed in this thesis what influence different objectives have on the designs found by the optimiser, different combinations of objectives have been created. These combinations are termed optimisation cases from here on, which will be presented in section 4.6. The optimisation technique used in this thesis is called Bayesian Optimisation, which will be explained in section 4.7.

4.1. Blade parameterisation

Before the optimisation of a winglet, the DTU10MW blade's chord and twist distribution will first be optimised. When optimising using an aerodynamic analysis tool, the blade is essentially optimised for that tool. If another aerodynamic analysis tool than AWSM was used by the designers of the DTU10MW to optimise the blade design, optimising the blade for AWSM will likely result in an improvement in performance even without a winglet. To make sure the performance gain from the winglet could not also be achieved by simply optimising the blade only, the main blade ($0.3 < \frac{r}{R} < 1$) is first optimised, after which only the outer blade ($0.9 < \frac{r}{R} < 1$) is optimised. This is done in two separate steps because it is expected that the induced velocities at the tip can differ the most between aerodynamic analysis methods or experimental setups, as shown by Sant et al. [76]. Furthermore, the used geometry file from Bak et al. [59] is described for a BEM algorithm and is not described in much detail at the tip.

The blade's chord and twist are parameterised with Bézier curves, which were shortly described in section 2.2.1. Bézier are defined in equation form in eq. (4.1).

$$B(t) = \sum_{k=0}^{n} \binom{n}{k} (1-t)^{n-k} t^k P_k \tag{4.1}$$

Where k is the number of each control point from zero to n, where n is the number of control points, P_k is the x and y coordinate of each control point. The parameter t is the distance along the curve ranging from zero to one.

The user or optimiser is able to decide the locations of the control points. For the blade optimisation, a similar parameterisation as Sessarego et al. [37] has been taken, where also four control points are

used. The Bézier curve lies on the first and the last control points and the second and third control points work as 'attraction' points. In this work, the first control point is fixed in x and y location, the second point is free to move in y, the third point is free to move in x and y and the last point is free to move in y. An example of what twist and chord distributions can be obtained using this parameterisation is shown in fig. 4.2, where the example geometries are created with LHC using a sample size of five samples.
To decide the fixed y location of the first, second and last point and the fixed x location of the first point, the (Moore-Penrose) pseudo-inverse of $\sum_{k=0}^{n} \begin{pmatrix} n \\ k \end{pmatrix} (1-t)^{n-k} t^k$ from eq. (4.1), is taken with $n = 3$. The dot product is then taken between the pseudo-inverse and the x and y data of the baseline geometry, where t needs to have the same length as the baseline geometry data. The result is a 4x2 matrix with the x and y location of the four control points.

4.1.1. Main blade

Firstly, the blade is parameterised from $\frac{r}{R} > 0.3$. It is decided to only change the geometry from $\frac{r}{R} > 0.3$, firstly due to the complex curve shape of the chord and twist distribution, which is too difficult to represent with a Bézier curve using only four control points. Secondly, the blade design for $\frac{r}{R} < 0.3$ has relatively little influence on the torque of the rotor. The blade specifications for $\frac{r}{R} < 0.3$ are set to the baseline values and remain unchanged. The results for taking the pseudo-inverse dot product with the baseline geometry input is shown in fig. 4.1[1].

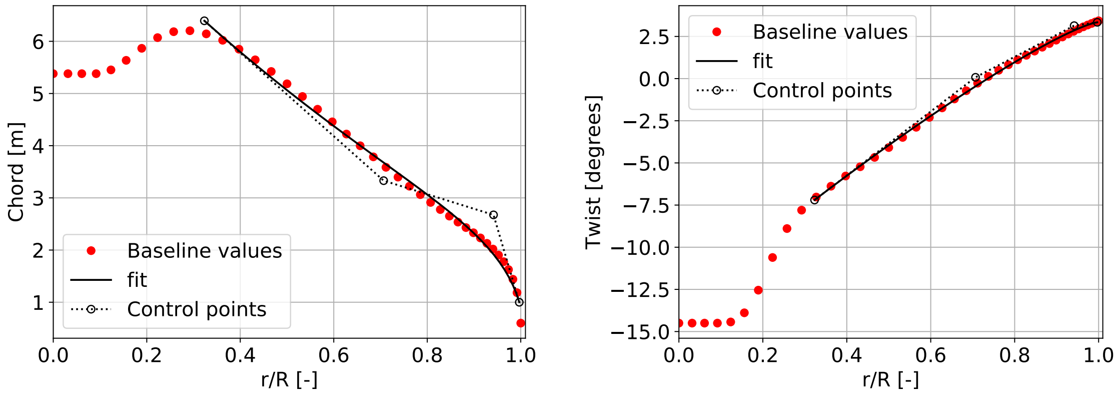

(a) Main blade chord

(b) Main blade twist

Figure 4.1: Fit for baseline geometry using the pseudo-inverse for $\frac{r}{R} > 0.3$

The blade was analysed with the geometry from the control points found and gave a similar integrated C_P and C_T with a difference of -0.67% for C_P and -0.24% in C_T. Although this is not a very large difference, improvements below one percent are expected and therefore the decrease is somewhat significant. However, with this parameterisation, the optimiser is able to change the chord and twist distribution quite freely as shown in fig. 4.2 while only controlling eights parameters. Besides that, Bézier curves also are more intuitive in the eyes of the author and might therefore lead to less nonphysical designs than, for example, polynomials.

4.1.2. Outer blade

The same parameterisation is used for the outer blade from $\frac{r}{R} > 0.9$. The initial x and y locations to fit the baseline blade design are determined using the pseudo-inverse again with the resulting curve and control points shown in fig. 4.3. The blade's geometry is set to the baseline design for $\frac{r}{R} < 0.9$.
An AWSM simulation is run for the blade with the Bézier curve parameterisation for the outer blade and a difference of -0.35% for C_P and -0.13% for C_T was found with the blade with baseline geometry.

---

[1] `https://stackoverflow.com/questions/12643079/bézier-curve-fitting-with-scipy`

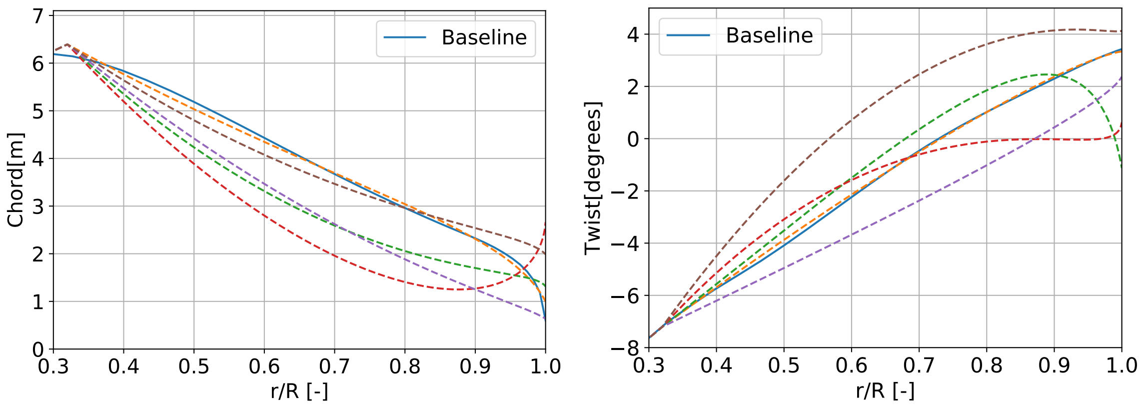

(a) Main blade chord

(b) Main blade twist

Figure 4.2: Bézier curve parameterisation of the blade's chord- and twist distribution for $\frac{r}{R} > 0.3$ where ten designs generated from LHC are shown. The domain is arbitrarily chosen in this plot.

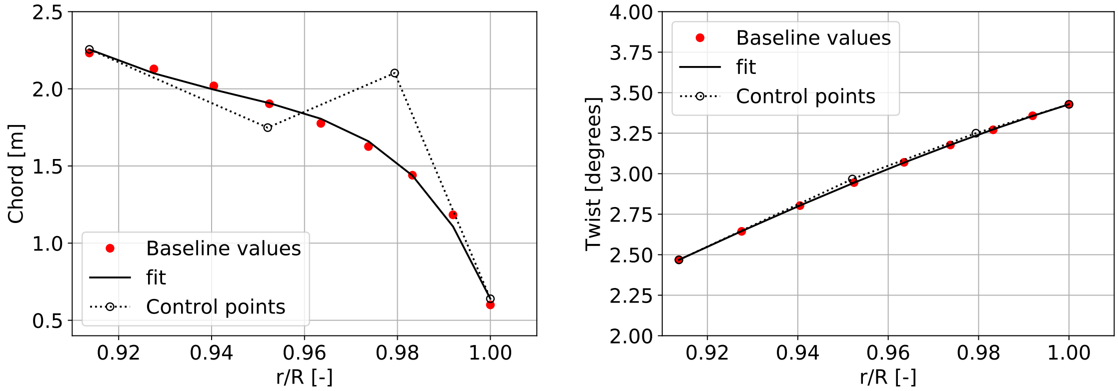

(a) Outer blade chord

(b) Outer blade twist

Figure 4.3: Fit for baseline geometry using the pseudo-inverse for $\frac{r}{R} > 0.9$

4.2. Winglet parameterisation

For this research, the winglet is parameterised in a similar manner as shown in fig. 2.1, this is done using slightly altered spherical coordinates defined as in eq. (4.2) and shown in fig. 4.5b.

$$x = h\,cos(\lambda) \tag{4.2a}$$

$$y = h\,cos(\phi)\,cos(\lambda) \tag{4.2b}$$

$$z = h\,cos(\phi)\,sin(\lambda) \tag{4.2c}$$

Where h is defined as the winglet height (h), which is the length from the winglet root to the winglet tip. This way the winglet parameters such as sweep (λ) and cant angle (ϕ), or winglet height and tip or root chord can be directly defined. The winglet is defined as a line from a point in x, y and z to another point. The line is representing the leading edge of the winglet. In FlightStream the leading edge of the airfoils is placed along this line. To find the points in AWSM, $\frac{c}{4}$ is added for each point as the points in AWSM are defined as the quarter-chord location of the airfoils.

Although it would have been more straightforward to set the definition of the winglet line as a line through the quarter-chord, this definition was more straightforward to create the geometry in ParaPy early in this research. Moreover, the parameterisation is tried to be kept as close as possible to the definition in fig. 2.1. The definition has been kept the same so FlightStream and AWSM could be compared easily. It has to be kept in mind that the angle for the sweep is the angle of the leading edge, leading

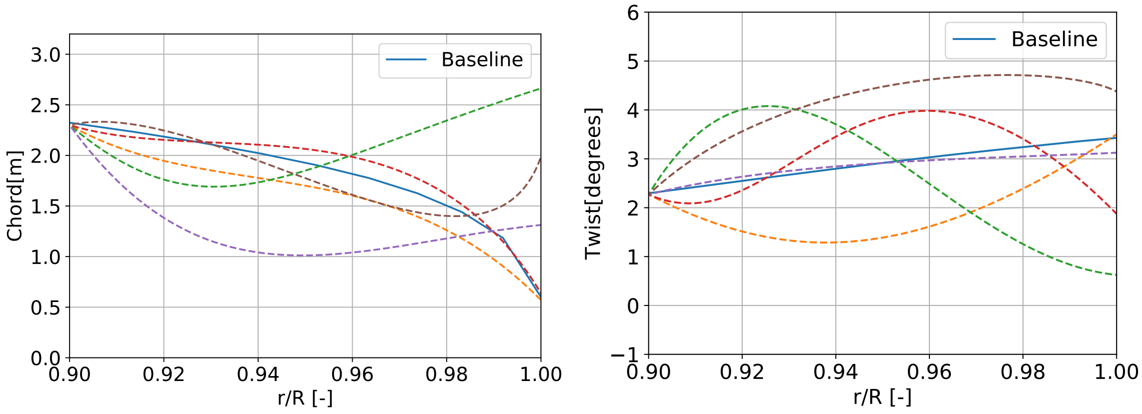

(a) Outer blade chord

(b) Outer blade twist

Figure 4.4: Bézier curve parameterisation of the blade's chord- and twist distribution for $\frac{r}{R} > 0.9$ where ten designs generated from LHC are shown. The domain is arbitrarily chosen in this plot.

to seemingly somewhat higher angles for sweep than the usual sweep definition through $\frac{c}{4}$, when the winglet's tip chord is smaller than the winglet's root chord.
Where the blade transitions into the winglet, the geometry has a curvature. The radius of this curvature is defined with another winglet parameter, called the winglet radius (r_w), which is shown in fig. 4.5a. The winglet curvature starts from the last point on the blade, with subscript $blade, end$, and ends at a location defined as in eq. (4.3), named the winglet root, with subscription w, r.

$$x_{w,r} = x_{blade,end} + r_w \, sin(\phi) \tag{4.3a}$$
$$y_{w,r} = y_{blade,end} + r_w \, cos(\phi) \tag{4.3b}$$

The origin of fig. 4.5b is the point w, r, which is from where λ, ϕ and h is defined. The point w, r has a chord length ($c_{w,r}$) and twist angle ($\gamma_{w,r}$). The tip chord point also has a a chord length ($c_{w,t}$) and twist angle ($\gamma_{w,t}$). The chord length and twist angle vary linearly between the winglet root and tip, which does only allow for a quite simple winglet definition. However, this does allow to say something about the winglet's taper ratio. The taper ratio will be defined as in eq. (4.4).

$$\tau_w = \frac{c_{w,t}}{c_{w,r}} \tag{4.4}$$

4.3. Objective parameters

This section will describe the objective parameters that will be maximised or minimised. Since this thesis concerns multi-objective optimisation, parameters such as thrust or bending moments are not constrained but minimised, as it is unknown if they can be constrained to the baseline value for thrust or bending moment for different optimisation cases.

4.3.1. Power

A parameter often optimised for is the C_P. Caution needs to be taken, however, whenever optimising for a winglet when no diameter constraint is set. As C_P is normalised by the radius this might give straight winglets an unfair advantage over tip extensions, as a winglet, in this case, would have a lower radius than a tip extension. Instead of maximising the C_P, the power ratio is maximised in this work. Where the power ratio is the ratio between the aerodynamic power of a design found by the optimiser and the baseline DTU10MW blade design.

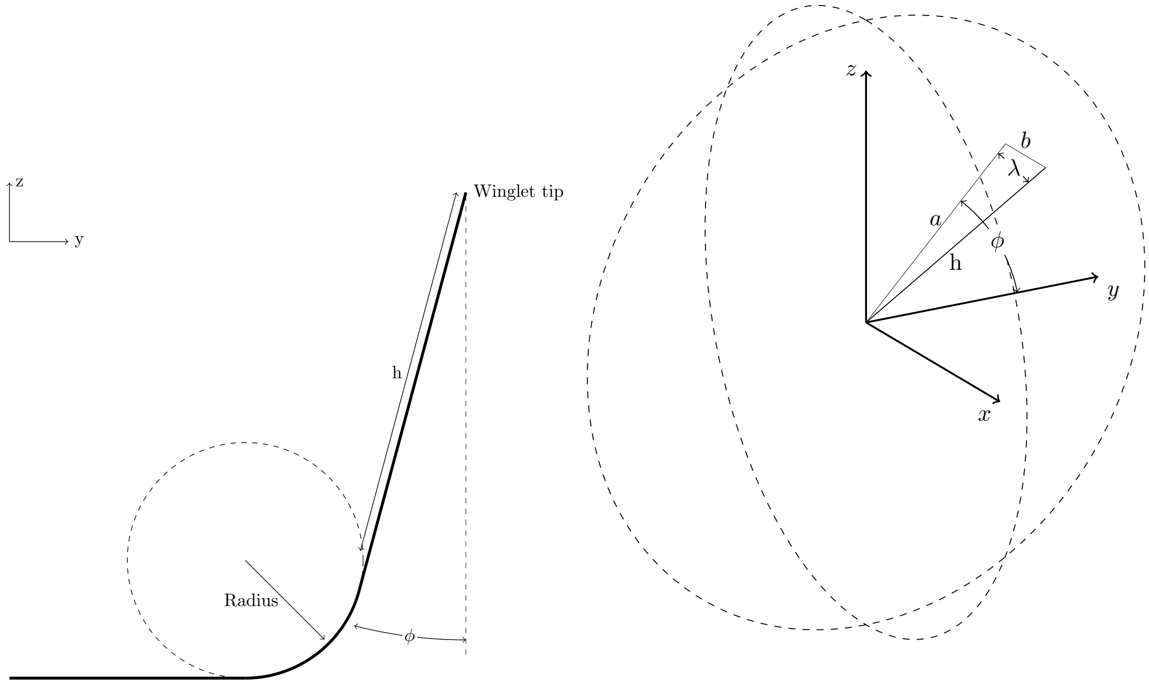

(a) Winglet radius

(b) Winglet cant (ϕ), sweep (λ) and height (h) spherical coordinates parameterisation

Figure 4.5: Winglet parameterisation used in this thesis

4.3.2. Annual Energy Production

The AEP is defined as eq. (4.5). Where $P(V)$ is the power curve of a wind turbine and $f(V)$ is the wind speed distribution.

$$\text{AEP} = \int_{V_{\text{min}}}^{V_{\text{max}}} P(V)f(V)dV \tag{4.5}$$

Optimising for the maximum power or C_P will not necessarily give the maximum AEP. The DTU10MW has a different tip speed ratio for lower wind speeds, for example at $6m/s$, as shown in table 3.2. Known from the Prandtl tip loss factor that the tip loss is lower for higher tip speed ratios. When optimising for power, the optimum winglet might look different when optimising for $6m/s$ than for $8m/s$. When optimising for the AEP, a winglet design will have to be investigated at all, or at least a number of, wind speeds, so the optimised design's power curve can be recreated, from which the AEP can be calculated.

4.3.3. Thrust

The thrust of a rotor is often constrained as this will give limit the loads on the tower of the turbine, therefore no redesign of the tower is needed. An optimised rotor where the thrust is constrained does not necessarily have the same (flapwise) bending moment along the radius of the blades, as shown by Loenbaek et al. [1]. An optimum, thrust constrained rotor might therefore still need a structural blade redesign.

The C_T is normalised by the radius of the blade as well, so the same caution needs to be taken when constraining C_T or thrust. As mentioned before, Loenbaek et al. [1] found that when constraining the thrust and optimising for power, the optimum rotor would be a very lightly loaded rotor with a radius tending to infinity. Although not the whole rotor is optimised in this study, this could have an influence on the optimum winglet as well, where the optimiser could prefer a lightly loaded tip extension over a winglet. Thrust is an available output of both AWSM and FlightStream. Instead of considering the C_T, the thrust ratio will be considered in this work. Where the thrust ratio is the ratio between the thrust of a design found by the optimiser and the thrust of the baseline DTU10MW blade design.

4.3.4. Flapwise bending moment

Root

The root bending moment is a common constraint in wing or winglet optimisations in aeroplanes, as it can be used as an indicator for the wing's structural weight. Although, as mentioned in section 2.2.2, Elham and Van Tooren [20] showed that for a winglet, the root bending moment is not a good indication for the wing weight as the bending moment ratio can be higher near the tip, while there is no increase at the root of the wing. For wind turbines, the same reasoning can be applied. The internal structure of a blade is designed for resistance against forces in the flapwise direction, while a blade often has enough strength in the edgewise direction. The root flapwise bending moment will therefore be tried as a minimisation objective to assess what the optimum winglet is under this objective. The root flapwise bending moment is an available output of both AWSM and FlightStream and will be called $m_{f,r}$ in this thesis.

At 90% of the total radius

As the blade's chord and twist distribution for $\frac{r}{R} > 0.9$ will be optimised for in the winglet optimisation, the flapwise bending moment at $\frac{r}{R} = 0.9$ will also be tried as a minimisation objective. The location where the flapwise bending moment is analysed is set the same as from where the blade's chord and twist distribution is optimised because that part of the blade would need a structural redesign due to the geometry change. It is expected that setting the location where the flapwise bending moment is analysed at $\frac{r}{R} = 0.9$, will yield to a higher change in bending moment than at the root, compared to the blade without winglet. If the flapwise bending moment at $\frac{r}{R} = 0.9$ is not increased, no or minimal structural redesign would be needed for $\frac{r}{R} < 0.9$. The flapwise bending moment at $\frac{r}{R} = 0.9$ is not an output of AWSM and therefore needs to be calculated. The calculation is explained and validated in appendix B.2.

The flapwise bending moment at 90% of the blade will be called $m_{f,0.9}$ in this thesis. For another optimisation case, the bending moment will also be constrained at 80% of the blade's radius. The bending moment at this location will be called $m_{f,0.8}$.

4.4. Winglet parameter study

To determine the bounds of the optimisation domain, a parameter study is done. It has to be noted that the results of this parameter study do not say anything about the optimum of the winglet parameters, as the parameters are highly dependent on each other. This is because changing a parameter can bring the loading on the blade and winglet further away, or closer, to the optimum loading. This study is done to determine at values of parameters the simulations diverge due to singularity problems, for example. This study can also show something about the effect of change on each objective, however, this is not definitive as there is no guarantee the blade and winglet are optimally loaded.

In this analysis, one parameter is varied while others are set to a fixed value. The fixed values are shown in table 4.1. Values for the blade's chord and are set to the chord length of the baseline blade design. The winglet root chord is not varied in this study, as it will be part of the Bézier curve that controls the blade's chord in the winglet optimisation. The power, thrust and root flapwise bending moment is taken from AWSM and is compared to the baseline blade of the same length without a winglet. The ratio between the blade with winglet and baseline blade is shown in figs. 4.6 to 4.8.

Symbol	Parameter	Quantity	Unit
ϕ	Cant	80	degrees
λ	Sweep	0	degrees
γ	Twist	0	degrees
h	Height	5	m
r_w	Radius	0.5	m
$c_{w,t}$	Tip chord	0.5	m
$c_{w,r}$	Root chord	1.3	m

Table 4.1: Fixed winglet values for the winglet parameter study

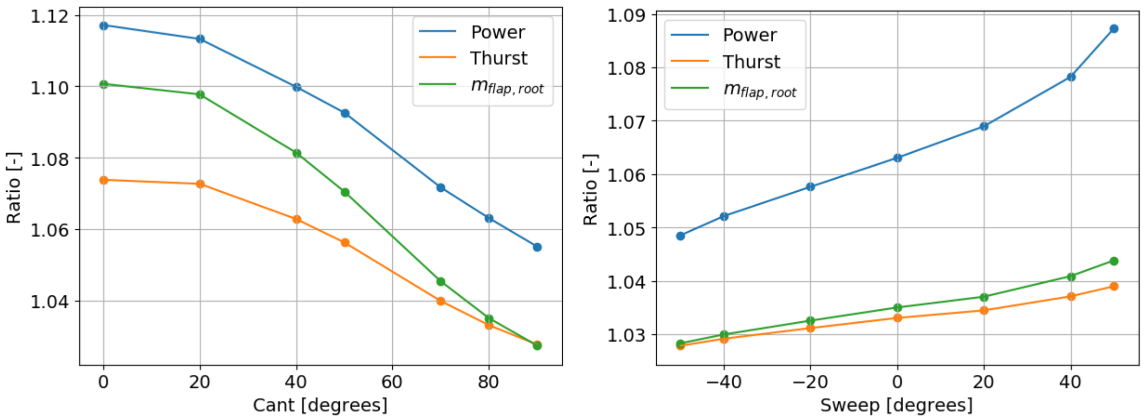

(a) Cant angle

(b) Sweep angle

Figure 4.6: Parameter study for the sweep and cant angle. The diameter is not constrained and thus does vary. The ratio is compared with the baseline geometry/

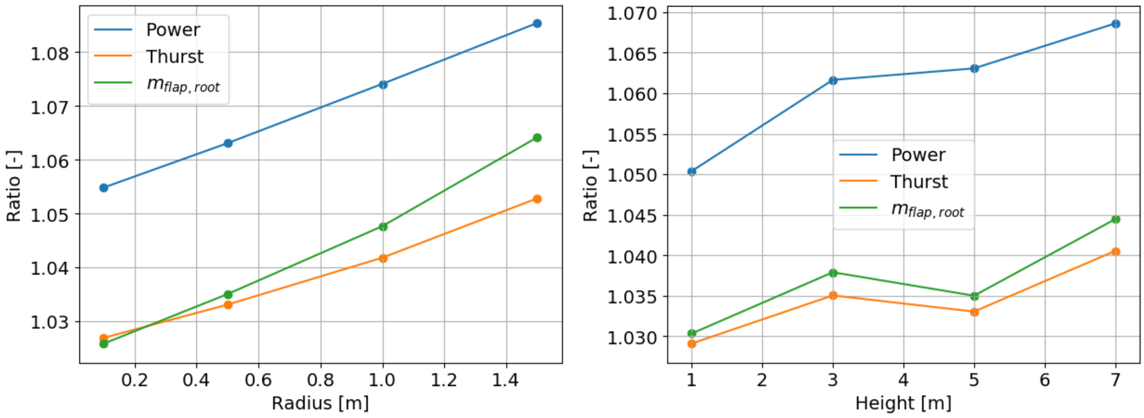

(a) Radius

(b) Height

Figure 4.7: Parameter study for the radius and height

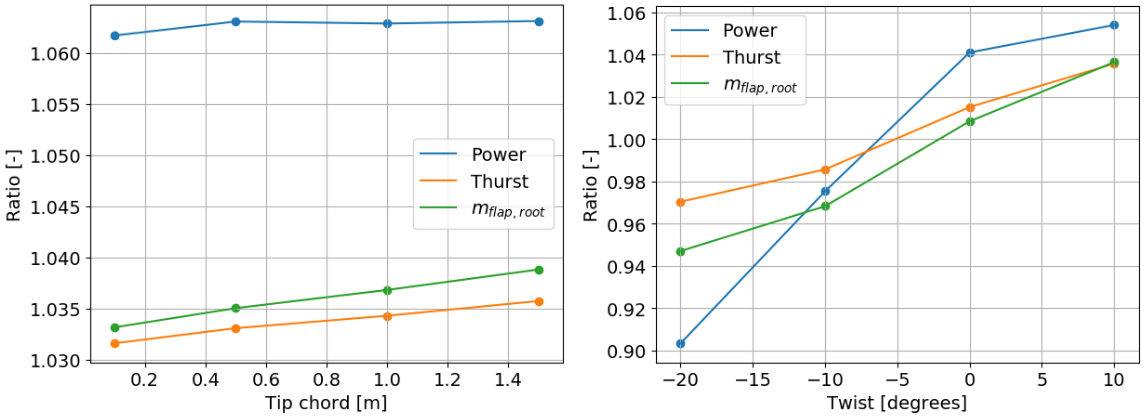

(a) Tip chord

(b) Twist

Figure 4.8: Parameter study for the tip chord and twist angle

Only the solutions for which AWSM converged are shown in the plot, values outside the range shown did not reach a converging solution in AWSM and are not shown in the plot. The limits on the x-axis are therefore taken as the domain, which is shown table 4.2. It should be noted that the value of $c_{w,t}$ in fig. 4.8a for which the simulations start to diverge is likely to be dependent on what value $c_{w,r}$ is set to. However, it was found in optimisation cases that the optimiser never preferred values close to $c_{w,t} = 1m$, but far lower values were preferred, so the maximum value of $c_{w,t}$ is kept at $1m$.

Symbol	Parameter	Lower limit	Upper limit	Unit
ϕ	Cant	0	90	degrees
λ	Sweep	-50	50	degrees
γ	Twist	-20	10	degrees
	Height	1	7	m
r_w	Radius	0.1	1.5	m
$c_{w,t}$	Tip chord	0.1	1.0	m
$c_{w,r}$	Root chord	0.3	3.0	m

Table 4.2: The domain of winglet parameters used for the optimisation

4.5. Predefined lift over drag ratio

During the research, it was decided to drop twist as an optimisation parameter when using AWSM. Instead, the C_l and C_d in the airfoil polars is set to a constant value corresponding to what the C_l and C_d would have been at a predefined angle of attack. The value for this angle of attack has to be chosen and is set to a value where the maximum lift-over-drag is obtained. The design point of maximum lift-over-drag is chosen as it is argued that for a given lift on a section of the blade, the drag should always be minimum. The blade's chord distribution can then be optimised for this predefined C_l. After the chord optimisation has been completed, a simulation of the optimised geometry is run with the actual C_l and C_d polars. Using the angle of attack obtained from the simulation, the blade's twist is modified such that the blade operates at the predefined angle of attack. This method is only applied at parts of the blade that are being optimised. Parts of the blade that are not optimised are not operating with the predefined C_l and C_d polars, but with the actual polars.

To determine the C_l and C_d the airfoil will be operating at, an angle of attack is chosen from the airfoil polars where $\frac{C_l}{C_d}$ is maximum. The $\frac{C_l}{C_d}$ as function of angle of attack is shown in fig. 4.9a. It can be seen that the DTU10MW 24.1% t/c airfoil is operating at optimum $\frac{C_l}{C_d}$ between an angle of attack of $8°$ and $10°$. AWSM will interpolate the coefficients as a function of angle of attack using a spline, so it might find a higher optimum α somewhere in between $8°$ and $10°$ for α, however, it is unknown to the author how exactly AWSM interpolates the coefficients. Therefore, an angle of attack of $8°$ is chosen as this value is a value with a high $\frac{C_l}{C_d}$ and furthest away from the stall angle of attack, where stall is estimated to occur around an angle of $14°$ as seen in fig. 3.8. The values for C_l and C_d at $\alpha = 8°$ in fig. 3.8 are now set in the predefined polar.

The blade's chord distribution can now be optimised for the chosen C_l. To validate this approach, a blade with a winglet is analysed using a predefined polar, after which the same blade with winglet is analysed with the actual polar, but with modified twist distribution. The twist is modified by simply taking the difference between the chosen predefined α, which is taken to be $8°$ for the FFA-W3-241 airfoil, and the actual angle of attack of the optimised section analysed with the actual polar. The difference in the integrated C_P and C_T is shown in table 4.3. The angle of attack and $\frac{C_l}{C_d}$ for the predefined polar and the actual polar before and after re-twisting the blade is shown in fig. 4.10 and the loads in the tangential and axial direction in fig. 4.11. The specifications for the blade with winglet are taken the same as table 4.1, except with a slightly modified twist of $5°$ and $c_{w,t}$ of $0.1m$. This was done as the loading on the winglet from table 4.1 was found to be quite far from optimum and required a re-twist of the blade with quite large angles, which would be hard to design in reality.

It can be seen that the integrated coefficients are fairly similar with a difference of 0.07 % in C_P and 0.01 % in C_T.

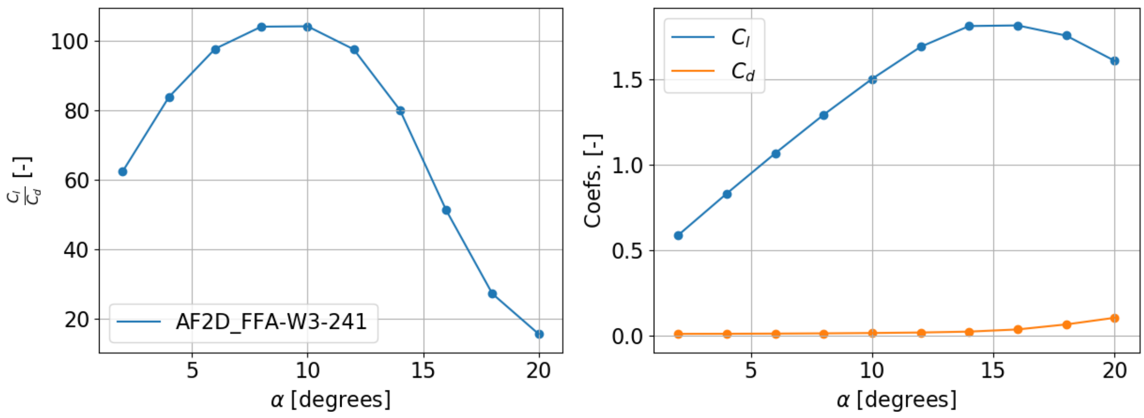

(a) Lift-over-drag ratio (b) C_l and C_d

Figure 4.9: Polars for the FFA-W3-241 airfoil

	C_P	C_T
Predefined polar	0.5228	0.8432
Actual polar	0.5257	0.8515
Actual polar, re-twisted twist	0.5224	0.8431

Table 4.3: Integrated C_P and C_T for simulation ran with predefined polar after which the angle of attack was used on a simulation performed with the actual to obtain retwist the blade from the which the coefficient are shown as well

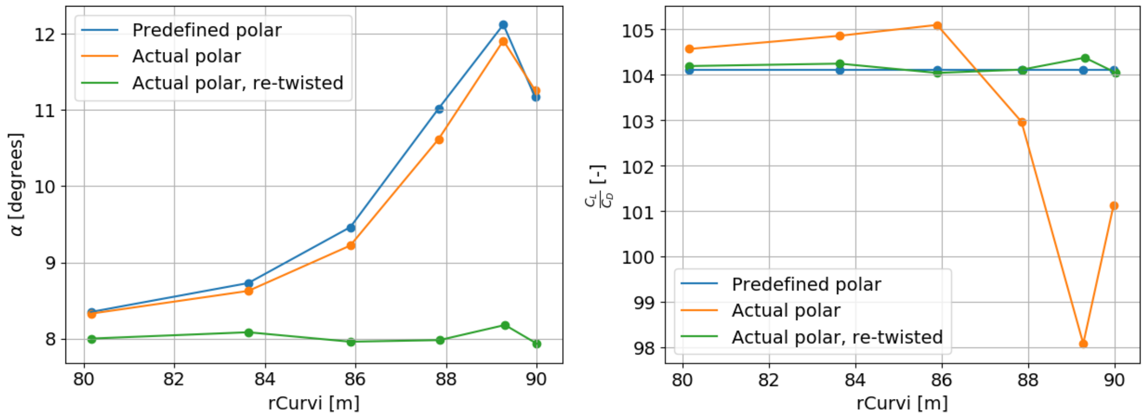

(a) Angle of attack (b) Lift-over-drag

Figure 4.10: The angle of attack and lift-over-drag ratio for a simulation with a predefined polar, actual polar and after the re-twist

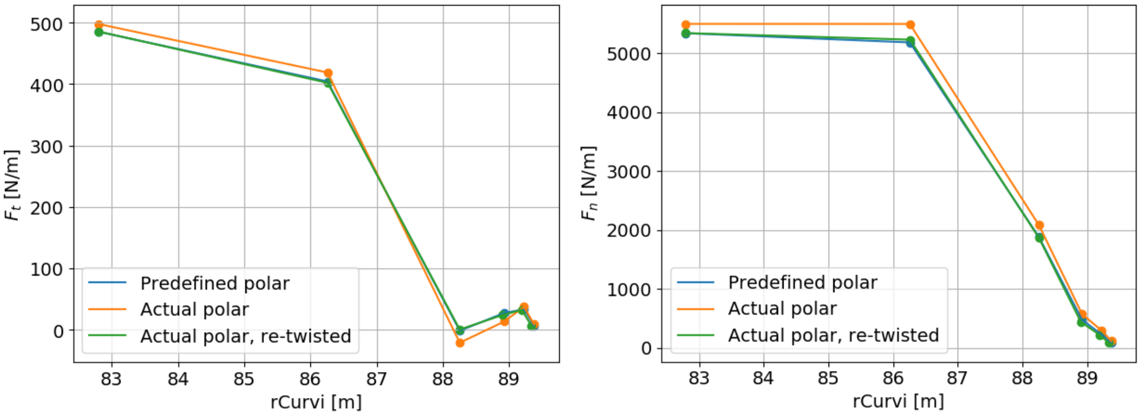

(a) (b)

Figure 4.11: Tangential and normal loads for a simulation with a predefined polar, actual polar and after the re-twist

The re-twisted blade is able to operate at approximately $8°$ ($\pm 0.2°$) as shown in fig. 4.10a. The $\frac{C_l}{C_d}$ is also fairly close to the predefined value of 104 (± 0.3), leading to matching forces for the predefined polar and actual polar after re-twist, as shown in fig. 4.11.

4.6. Optimisation cases

As it is expected different objectives will result in different optimum winglets, different optimisation cases are set up to investigate the effect of the different objectives.
Firstly, the blade optimisation without a winglet will be discussed. Secondly, the optimisation cases with a winglet will be shown. All optimisation cases for a blade with a winglet will separately be optimised for upwind and for downwind winglets.
This research concerns multi-objective optimisation, meaning multiple solutions, which lie on the Pareto front, can be chosen from by the blade designer. It is chosen to only consider solutions that have a higher or equal value for an objective that is maximised than the baseline blade value, such as power and a lower or equal value for an objective that is minimised than the baseline, such as thrust or flapwise bending moment. Therefore minimisation objectives are sometimes referred to as constraints. If an improved design from the blade optimisation case is obtained, this design will be set as the new baseline design to compare to during the winglet optimisation.

4.6.1. Main blade chord and twist

The blade's chord distribution will be optimised for $\frac{r}{R} > 0.3$ using the parameterisation described in section 4.1.1. The baseline design is added to the initial samples, which control points are shown in table 4.5. This table also shows what x and y locations of the control points are changed during the optimisation, denoted by var. The x location of the third chord and twist control points is optimised separately, which is perhaps not immediately obvious from table 4.5. At this point the blade is still optimised for twist as well as for chord, to make sure smooth twist distributions are obtained. A summary of the objectives and optimisation parameters is shown in table 4.4.

Objective	Maximize C_P Minimize C_T
Optimisation parameters	Chord $CP_{2,y}$ Chord $CP_{3,x}$ Chord $CP_{3,y}$ Chord $CP_{4,y}$ Twist $CP_{2,y}$ Twist $CP_{3,x}$ Twist $CP_{3,y}$ Twist $CP_{4,y}$

Table 4.4: Objective and optimisation parameters for main and outer blade optimisation

The bounds for the y chord control points for the main blade are set to a minimum value of $0.1m$ and maximum of $7m$. $CP_{3,x}$ was allowed to vary between $\frac{r}{R} = 0.7$ and $\frac{r}{R} = 0.995$.

4.6.2. Outer blade chord

The outer blade will also be optimised to see what improvement can be made by optimising the tip without using a winglet. This optimisation case is done separately as it is expected that with the current geometry optimisation using Bézier curves for the entire blade, the shape of the tip cannot reach its optimum shape. The optimisation parameters and objectives are shown in table 4.6. The control points' location is shown in table 4.5. Where the control points for the baseline blade are shown in the 'Outer blade baseline' columns, after which it's shown what control points are varied for the optimisation in the 'Outer blade opt' column, which are denoted by var. The control points that are not optimised are set at the same value as the baseline blade. A predefined polar will be used in this optimisation case, as only the chord is optimised.

CP	Main blade baseline			Outer blade baseline			Main blade opt			Outer blade opt		
i	x	y_{chord}	y_{twist}	x	y_{chord}	y_{twist}	x	y_{chord}	y_{twist}	x	y_{chord}	y_{twist}
1	0.3	6.39	-7.2	0.9	2.30	2.27	0.3	6.39	-7.2	0.9	2.30	2.27
2	0.70	3.33	0.08	0.93	1.80	2.88	0.70	var	var	0.93	var	var
3	0.94	2.67	3.14	0.995	2.18	3.23	var	var	var	var	var	var
4	1	1.00	3.34	1	0.60	2.15	1	var	var	1	var	var

Table 4.5: Overview of control points used to match the main blade and outer geometry and which control points x and y location are changed during the optimisation denoted by var

The bounds for the y chord control points for the outer blade are set to a minimum value of $0.1m$ and maximum of $3m$. $CP_{3,x}$ was allowed to vary between $\frac{r}{R} = 0.93$ and $\frac{r}{R} = 0.995$. These same bounds have been set for the control points during the winglet optimisation.

Objective	Maximize C_P Minimize C_T Minimize $m_{f,r}$ Minimize $m_{f,0.9}$
Optimisation parameters	Chord $CP_{2,y}$ Chord $CP_{3,x}$ Chord $CP_{3,y}$ Chord $CP_{4,y}$

Table 4.6: Objective and optimisation parameters for outer blade chord optimisation

4.6.3. Winglet thrust and diameter constrained

For the first winglet optimisation case, the thrust will be minimised, while the power will be maximised. The diameter of the rotor is constrained to the same diameter as the baseline blade. Therefore, a part of the blade will be removed and replaced by the winglet. If the winglet has a smaller cant angle a larger part of the blade will be removed. This way it is ensured the blade will always have the same diameter. The $c_{w,r}$ is not used as optimisation parameter and $CP_{4,y}$ is taken as $c_{w,r}$.

It should be noted that using this type of diameter constraint gives an advantage of a winglet over a blade extension since the winglet has a tapered chord distribution, where the chord length linearly decreases (or increases) from $c_{w,r}$ to $c_{w,t}$. An alternative approach would be to control the winglet and blade chord with one Bézier curve in the same manner as for the outer blade optimisation. This approach has been attempted but often led to a design that diverged in the simulations.
Since the diameter is constrained, optimising for C_P and C_T is the same as optimising for power and thrust in this case.
The objective and optimisation parameters are summarised in table 4.7, where the chord CPs are the same four parameters as shown in table 4.6.

Objective	Maximize C_P Minimize C_T
Optimisation parameters	Chord CPs Cant Sweep Height Radius Tip chord
Diameter constraint	Yes

Table 4.7: Objective and optimisation parameters for winglet with thrust and diameter constraint

4.6.4. Winglet thrust constrained, diameter free

A similar optimisation case as above will be performed, however, now a part of the blade will not be removed but the winglet will be attached to the blade. The optimiser is now free to extend the diameter of the blade using a tip extension or keep the diameter at about the same value as the baseline design using a straight winglet. The optimiser might prefer a lightly loaded tip extension, in this case, to minimise the thrust and still gain some power. The objective and optimisation parameters are summarised in table 4.8.

Objective	Maximize P Minimize T
Optimisation parameters	Chord CPs Cant Height Radius Tip chord
Diameter constraint	No

Table 4.8: Objective and optimisation parameters for winglet with thrust constraint and free diameter

4.6.5. Winglet root flapwise bending moment constrained

For this optimisation case, the root bending moment will be minimised. The diameter will also be constrained to be the same as the baseline value. For aircraft optimisation, it was already shown by Elham and Van Tooren [20] that a wing with a winglet can have the same root bending moment as a wing without a winglet, while having an increased bending moment closer to tip. It will be assessed if the same is true for a wind turbine. A summary of the objectives and optimisation parameters is shown in table 4.9.

Objective	Maximize C_P Minimize $m_{f,r}$
Optimisation parameters	Chord CPs Cant Sweep Height Radius Tip chord
Diameter constraint	Yes

Table 4.9: Objective and optimisation parameters for winglet with root flapwise bending moment constraint and constrained diameter

4.6.6. Winglet flapwise bending moment constrained at the blade

An optimisation case with a flapwise bending moment at $\frac{r}{R} = 0.9$ as constraint will be performed as well. It is expected from Elham and Van Tooren [20] and Zahle et al. [30] that whenever the bending moment at $\frac{r}{R} = 0.9$ is not exceeded, the bending moment at the rest of the blade is also not exceeded. The blade might therefore not need a structural redesign for $\frac{r}{R} < 0.9$ were an winglet added to the blade design.
A summary of the objectives and optimisation parameters is shown in table 4.10.

Objective	Maximize C_P Minimize $m_{f,0.9}$
Optimisation parameters	Chord CPs Cant Sweep Height Radius Tip chord
Diameter constraint	Yes

Table 4.10: Objective and optimisation parameters for winglet with $\frac{r}{R} = 0.9$ constraint and free diameter

To validate the setup in this thesis, it will be assessed if the same results are obtained as the research by Zahle et al. [30], who also constrained $m_{f,0.9}$, but did not use a diameter constraint. The optimisation case shown in table 4.11 will therefore be attempted as well. Sweep is not optimised for in this optimisation case, for which the reason will be given in section 5.5.

Objective	Maximize C_P Minimize $m_{f,0.9}$
Optimisation parameters	Chord CPs Cant Height Radius Tip chord
Diameter constraint	No

Table 4.11: Objective and optimisation parameters for winglet with $\frac{r}{R} = 0.9$ constraint and free diameter

An optimisation case where the bending moment is constrained $\frac{r}{R} = 0.8$ will be made as well, where sweep will also not be optimised for. The optmisation case is shown in table 4.12.

Objective	Maximize C_P Minimize $m_{f,0.9}$
Optimisation parameters	Chord CPs Cant Height Radius Tip chord
Diameter constraint	Yes

Table 4.12: Objective and optimisation parameters for winglet with $\frac{r}{R} = 0.9$ constraint and free diameter

4.7. Bayesian Optimisation

In this thesis, the method of optimisation that is chosen is Bayesian Optimisation. A short explanation was given in section 2.4. This section will describe BO in more detail.

In BO, an acquisition function is used to determine if a given candidate sample is worth evaluating with the objective function, which is the aerodynamic performance analysed by the aerodynamic analysis tool. To make use of the acquisition function to decide what point should be evaluated next, candidate points are generated and their predicted performances on the objectives are predicted by the surrogate model with their respective uncertainty. The acquisition function is then used to score each sample's predicted mean and standard deviation.

To get an idea of the design space, both the surrogate model and the acquisition function needs some initial samples. The surrogate model needs to be trained with these initial samples and the acquisition function needs to have information on the non-dominated points lie to generate candidate points close to the non-dominated points. How these samples are generated is explained in section 4.7.1. In multi-objective optimisation, the aim is to maximise the hypervolume, which concept is explained in section 4.7.2. For multi-objective optimisation, different acquisition functions are used. In this thesis EHVI, which is a multi-objective version of EI is used, which is explained in section 4.7.3. An alternative approach is to use a scalarising function on the objectives to convert the optimisation problem to a single objective optimisation. The scalarising function used in this thesis is HyPI, which is explained in section 4.7.4.

4.7.1. Initial Sampling

In this thesis, Latin HyperCube is used for initial sampling. LHC aims to cover the design space as efficiently as possible. For sampling a function with N variables, this is done by maxmising the distance between samples in all N dimensions. This is achieved by using stratified sampling for the inputs, which can be visualised the following way.

Consider a problem with three input parameters, x_1, x_2 and x_3. A LHC sample is shown in fig. 4.12a with a sample size of eight. The distribution of samples seems random, however, for each two dimensional projection, it can be seen that none of the samples are in the same rows or columns, for an eight by eight grid. This is shown for x_1 and x_2 in fig. 4.12b, for x_1 and x_3 in fig. 4.13a and for x_2 and x_3 in fig. 4.13b.

This way the input space is well presented with a small number of samples. As a rule of thumb in this thesis, the number of LHC samples is always taken to be the number of inputs multiplied by eight. As there are nine parameters to control the winglet design, as shown in table 4.2, the number of LHC samples is 78 for most winglet optimisation cases.

4.7.2. Hypervolume

In multi-objective optimisation, no single optimal solution exists due to the conflicting nature of the objectives. Instead, the optimums are a set of Pareto-optimal solutions. The designer can then choose one of the Pareto-optimal solutions depending on the designer's preferences. In order to find the Pareto front, the optimiser will try to find as many non-dominated points as possible. A non-dominated point is a design point that, has no other point performing better on all objectives. A visual example is shown in fig. 4.14. For each non-dominated point, there is no point to the lower right of that point, meaning the is no design with a higher C_P and lower C_T in this case. The goal of the optimiser is then to find as many designs as possible to the lower right of this plot. With two objectives, the surface area the

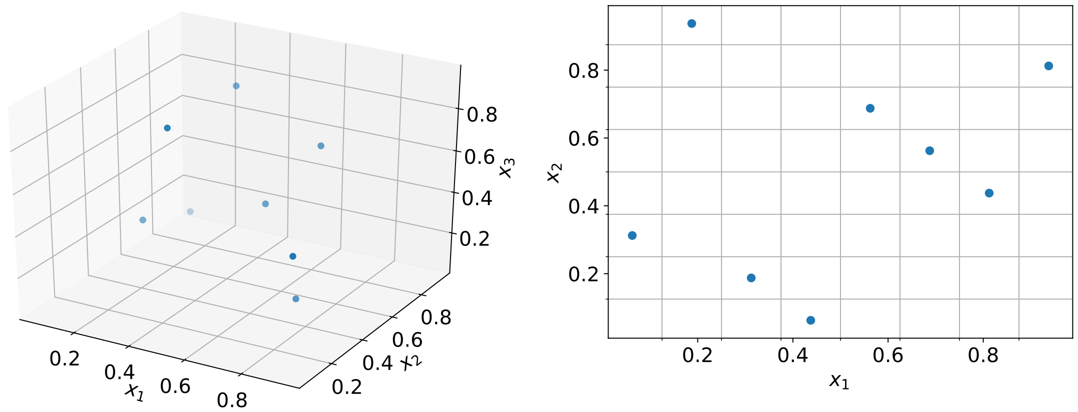

(a) Three dimensional LHC example

(b) Example of a LHC sample distribution

Figure 4.12: Projection on x_1 and x_2

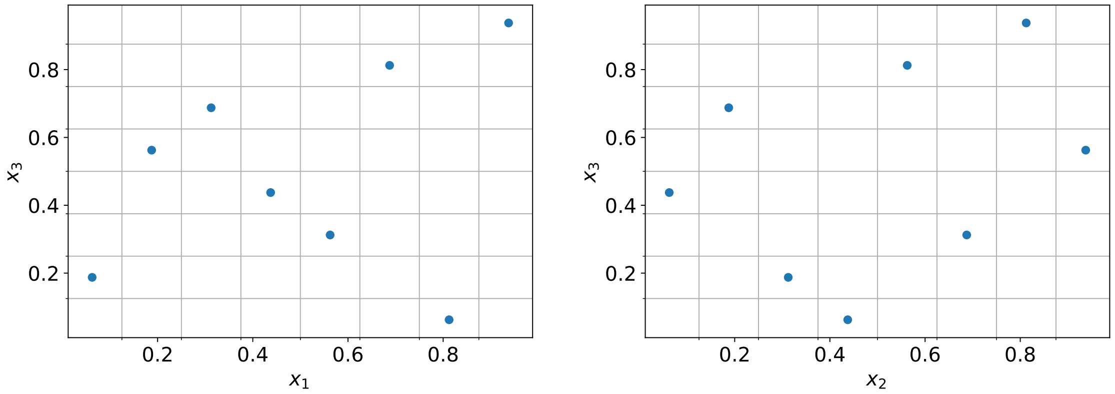

(a) Projection on x_1 and x_3

(b) Examples of projection of an LHC sample distribution

Figure 4.13: Projection on x_2 and x_3

non-dominated points make, can be calculated, which area then corresponds to the hypervolume. With three objectives this could be achieved by calculating the volume.

It can be desired to let the optimiser not explore designs with a very low C_T, for example, and therefore likely also a low C_P. To prevent this, a reference point can be set, from which the hypervolume is now calculated. In the example of fig. 4.14, any design with a C_P lower than 0.492 or a C_T higher than 0.83, will not contribute to the hypervolume and therefore the optimiser should be more likely to stay away from these designs.

When the optimiser cannot increase the hypervolume anymore, the optimiser is converged. To decide when optimisations can be stopped in this thesis, a stopping criterion has to be set. The stopping criterion is set to less than 2% increase for 30 constructive iterations.

4.7.3. Multi-surrogate EHVI

The EHVI is the expected increment of the hypervolume, which considers a Pareto front approximation. When using EHVI with GPs, a GP is trained for each objective. The outputs of the surrogate functions are used to calculate the EHVI. In the acquisition function, a number of N points close to an existing non-dominated point is generated, from which EHVI can then be evaluated by the surrogate model's prediction. A candidate point's EHVI is now optimised using a gradient optimiser. All N points are maximised for EHVI, after which the point with the highest EHVI is chosen to be evaluated by the objective function.

The training of separate GPs for different objectives and optimising the EHVI of N points for each iteration can take 50-100 seconds when N is ten, which is the chosen value for N in this thesis. As

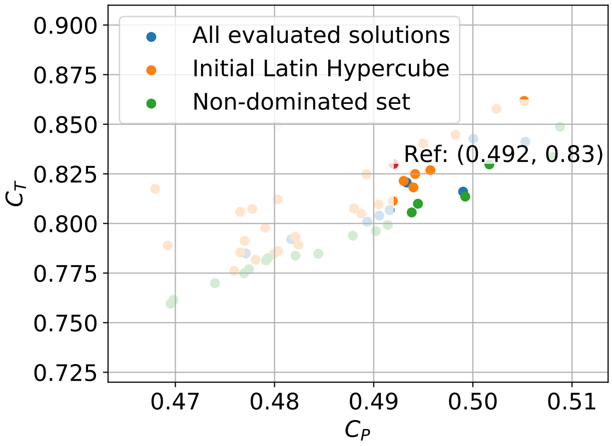

Figure 4.14: Example of scatter plot of found solutions of non-dominated set, initial latin hypercube and other solutions. The reference point is set to $C_P = 0.492$ and $C_T = 0.83$ meaning that only designs found with $C_P > 0.492$ and $C_T < 0.83$ will contribute to the total hypervolume

was found by Stock-Williams et al. [3], the EHVI acquisition function with GPs as a surrogate model led to the most improved designs. This combination of acquisition function and surrogate model will therefore be used for the optimisations in chapter 5 to make sure the results are obtained with a model that has been proven to work well. It will be in chapter 6 where different surrogate models, scalarising functions and acquisition functions will be compared.

4.7.4. Mono-surrogate HyPI

Scalarising functions can range from simple functions, such as taking the weighted sum, to more complicated scalarising functions such as HyPI, which is designing in a way that it uses Pareto dominance. Using HyPI the optimisation is now converted to a single-objective optimisation problem, meaning existing acquisition functions can now be used, for which in this thesis EI is used, and the large number and expensive integrations required for EHVI can be avoided. Although the HyPI mono-surrogate approach is faster than the multi-surrogate approach, it is not chosen to use for the optimisation of the winglets in chapter 5. The performance of HyPI, compared to the multi-surrogate approach, will be shown in chapter 6.

4.8. Synthesis

The parameterisation of the blade and winglet that is used during optimisation is presented in this chapter. A rather simple parameterisation of the winglet is chosen as this gives a clear overview of the effect of each winglet parameter. The different objectives which will be investigated for the optimisations are discussed and it is argued why these different objectives are considered. Using this parameterisation and objective set, different optimisation cases are set up, which can now be used to investigate what benefit a winglet can have with different objectives. Due to the long run times of one optimisation case, not all combinations of objectives can be tried. Furthermore, the basic principles that are used during optimisation in this thesis are explained, where it is chosen to run the optimisation cases with a multi-surrogate using the EHVI acquisition function.

5

Optimisation results

This chapter will show the results for the optimisation cases described in section 4.6. For each case, all found solutions are plotted against each other for two or more objectives as well as the hypervolume achieved against the iterations of the solver. The designs belonging to the initial samples set from LHC are plotted as well. It is assumed for now that all designs in the non-dominated set are 'optimised', meaning the chord distribution of the blade is (close to) optimally loaded.
For each case, all non-dominated solutions that have a higher value for the maximisation objective, for example, power, than the baseline case and a lower value for the minimisation objective, for example, thrust, than the baseline case, will be called the improved non-dominated solution from now on. From this subset of improved non-dominated solutions a table is created, which shows the design with the highest maximisation objective (power) for this subset, the design with the lowest value for the concerning minimisation objective (thrust or bending moments) for this subset, and a design intermediate between the two aforementioned cases. The mean (μ) and standard deviations (σ) of all parameters and objectives from the improved non-dominated improved subset are also shown. The differences between the improved non-dominated solutions will be shown and the causes of these differences will be discussed in chapter 7.

The baseline case is the original geometry for the blade optimisation cases. For the winglet cases, the baseline design replaced by is the design found from the blade optimisation case.
All optimisations done shown in this chapter are run with a wind speed of $8m/s$ and are run with a multi-surrogate approach using the EHVI acquisition function. The surrogate model used are GPs. For the sectional properties of each winglet design that is presented, the start of the winglet is shown by a dashed line, plotted in the same colour as the sectional property of the respective winglet. When no dashed line is shown, the design does not have a winglet.
Firstly, the optimisation cases without a winglet are shown in section 5.1 and section 5.2. Secondly, the cases for the winglet optimisation are presented in sections 5.3 to 5.5.

5.1. Main blade

In this work, the main blade is defined as the blade for which $0.3 < \frac{r}{R} < 1$. As first optimisation case, the main blade is optimised, using the parameterisation described in section 4.1. A summary of the optimisation case was shown in table 4.4.
The C_P is plotted against the C_T for all solutions in fig. 5.1a. The initial Latin hypercube solution is the initial sample size. Which are generated as discussed in section 4.7.1. All non-dominated solutions are the solutions for which no other design exists with a higher C_P and lower C_T, in the analysed designs for this case. The non-dominated solutions make up the Pareto front found by the optimiser. All solutions that are dominated and not part of the initial samples are termed 'all evaluated solutions' in this plot.
From fig. 5.1a it becomes apparent that the optimiser was able to find the Pareto front with fairly few iterations. In fig. 5.1b the calculated hypervolume over iterations is shown.

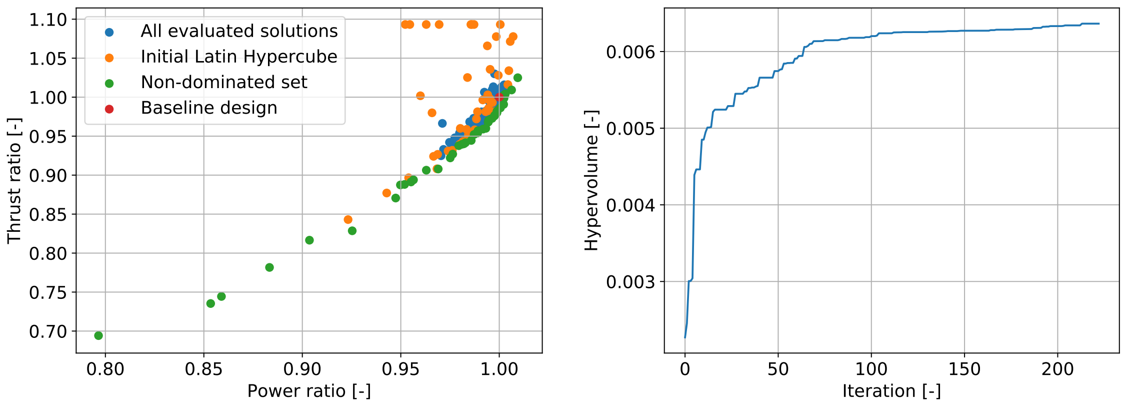

(a) C_P versus C_T for all solutions

(b) Hypervolume with increasing iterations

Figure 5.1: Optimisation for the blade for $0.3 < \frac{r}{R} < 1$ where the pareto front is shown and the hypervolume with increasing iterations

It can be seen that a few designs were found with a higher power and lower thrust than the baseline design. The design with the highest power and lower thrust than the baseline design and the design with the lowest thrust, but higher power than the baseline design, are chosen to display in the following figures. Their respective chord lengths are plotted in fig. 5.2a. It can be seen that the $Max(\Delta P)$ design has a decreased chord length for $0.3 < \frac{r}{R} < 0.8$ and a similar chord length closer to the tip. This resulted in a power increase of 0.22% and a decrease in thrust of 0.92%. The redesign led to an increase in normal and tangential loads at the outer part ($\frac{r}{R} > 0.75$) of the blade and decreased normal loads as shown in fig. 5.3.

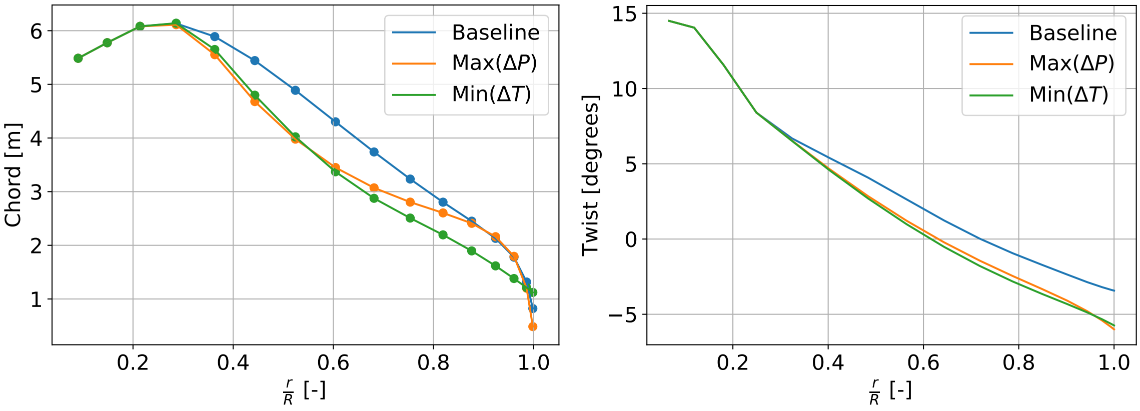

(a) Chord length

(b) Twist

Figure 5.2: Chord and twist for the design with the highest C_P that did not violate the thrust constraint and the design with the lowest C_T that did increase the blade's power, compared with the unmodified baseline blade

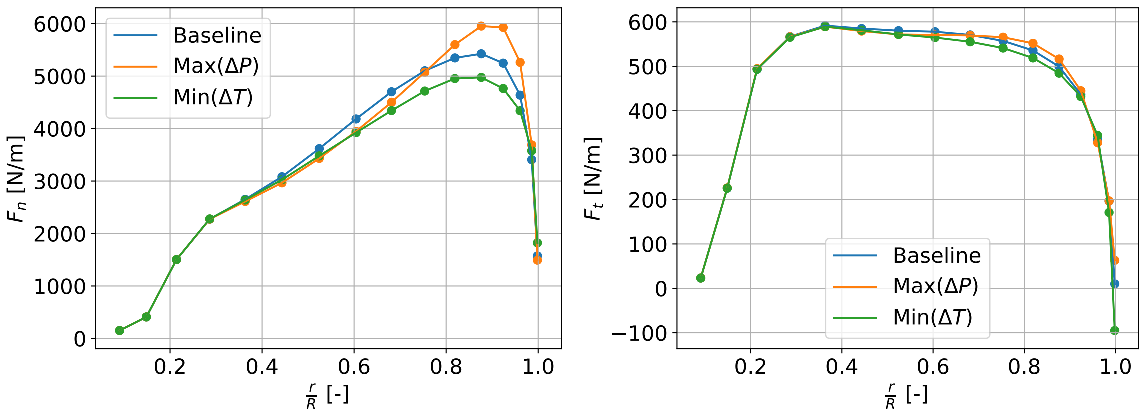

(a) Normal loads

(b) Tangential loads

Figure 5.3: Normal and tangential loads for the design with the highest C_P that did not violate the thrust constraint and the design with the lowest C_T that did increase the blade's power, compared with the unmodified baseline blade

The effect of the twist optimisation is seen in fig. 5.4a, where the result is simply causing the angle of attack of the blade to operate between $8°$ and $10°$. As this could also have been achieved without optimising for twist, but simply re-twisting the blade after optimisation for chord with a predefined polar, all optimisation will be run with a prescribed polar from here on and the twist will be modified as a post-processing step.

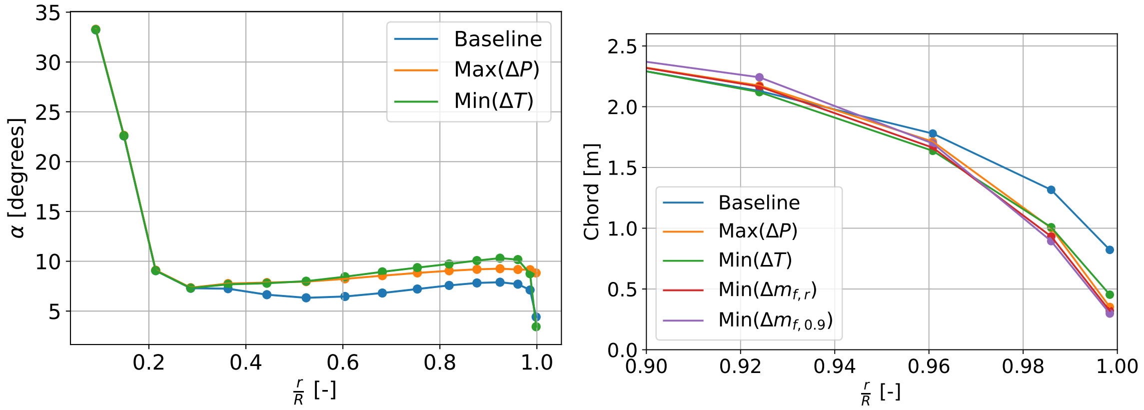

(a) Main blade optimisation angle of attack

(b) Outer blade optimisation chord lengths

Figure 5.4: Resulting angle of attack for the designs found from the main blade optimisation and the chord lengths for the outer blade optimisation

The lower C_T design has an overall decreased chord length and had an increase in power of 0.06%, with a decrease in thrust of 1.37%. Although difficult to see from the plot, the loads close to the tip were slightly higher for this design with lower normal loads over the whole blade. The baseline design is now replaced with the higher C_P design.

5.2. Outer blade

The outer blade is termed the blade for $0.9 < \frac{r}{R} < 1$. This optimisation case was maximised for power and minimised for thrust, flapwise bending moment at the root and at $\frac{r}{R} = 0.9$. A summary of the optimisation case was shown in table 4.6.

The optimiser was able to improve the power while reducing the other three minimisation objectives, however, the maximum power gain achieved was 0.3%. The Pareto fronts are seen in fig. 5.5 and fig. 5.6a. The modified chords are shown in fig. 5.4b, where it is observed that all found chord lengths are lower than the baseline chord length. The differences between the designs are minimal, with a

slightly higher chord length for the $Max(\Delta P)$ and $Min(\Delta T)$ design.
The hypervolume as function of iterations is shown in fig. 5.6b. The convergence criterion has not been met yet, with an increase of approximately 4% in the hypervolume the last thirty iterations, so it is possible more improved design could have been found.

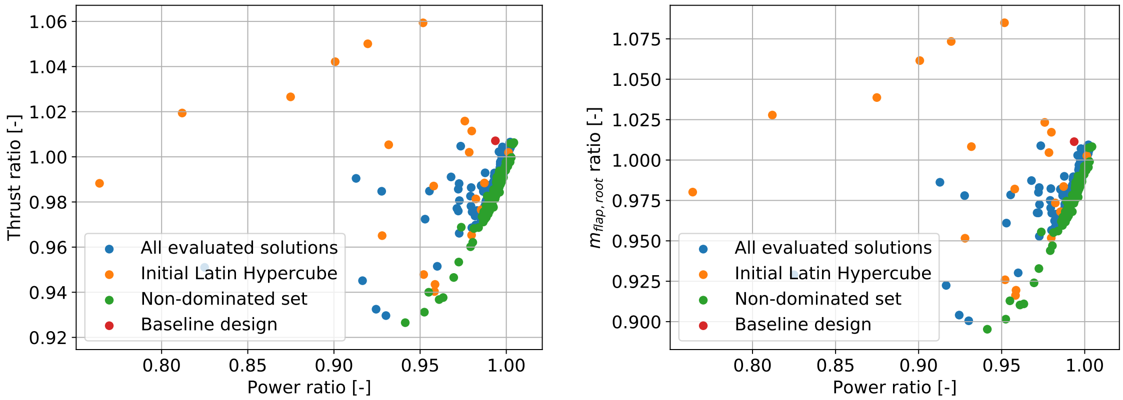

(a) Power ratio versus thrust ratio

(b) Power ratio versus root flapwise bending moment ratio

Figure 5.5: Optimisation for the blade for $0.9 < \frac{r}{R} < 1$ for the thrust and root flapwise bending moment versus power

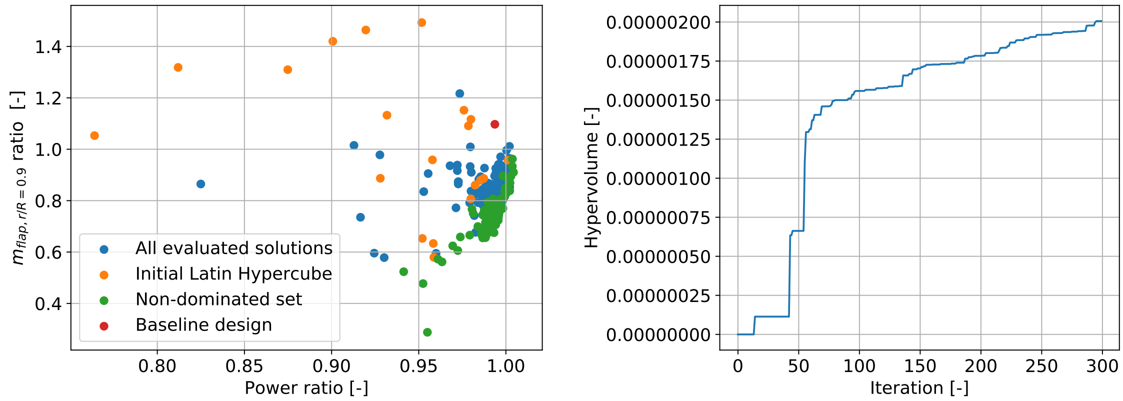

(a) C_P versus C_T for all solutions

(b) Hypervolume with increasing iterations

Figure 5.6: Optimisation for the blade for $0.9 < \frac{r}{R} < 1$ for $m_{f,0.9}$ versus power is shown as well as the hypervolume with increasing iterations

5.3. Thrust constrained

For this optimisation case, the power is maximised while the thrust is minimised. The diameter of the blade is kept the same regardless of the cant angle of the winglet as described in section 4.6.3 for the fixed diameter case. The thrust is a parameter that is output directly from AWSM. The increase or decrease of all objectives is compared with the optimum from the blade optimisation.
Optimisations are run for a downwind winglet first with and after without diameter constraint. For the upwind winglet only an optimisation is done with diameter constraint in section 5.3.2.

5.3.1. Downwind winglet

With fixed diameter

A summary of the design parameters and objectives for this optimisation case are shown in table 4.7. All evaluated designs for ΔP against ΔT for a blade design with a constrained diameter are shown in fig. 5.7a with the improved non-dominated subset designs in table 5.1.

The optimiser clearly prefers the highest sweep angle possible for the downwind winglet. The cant angles range from approximately $0°$ to $60°$, with the optimiser preferring the winglet to be somewhere in between a straight winglet and a straight blade. The winglet height is close to or at maximum value for all improved non-dominated designs. There is no clear optimum found for the winglet radius, where values range from its minimum to maximum for the improved non-dominated designs. Winglet taper ratios below 0.5 were mostly preferred by the optimiser, but also no clear optimum value is preferred.
It can be seen that the winglet with the highest power ratio has an increase of 9.10% at the flapwise bending moment at 90% of the blade and a slight increase in the root flapwise bending moment.
Figure 5.7b shows the increase of the hypervolume as a function of iterations, it can be seen that the optimisation stopping criteria has not yet been met and more optimum designs could still be found.

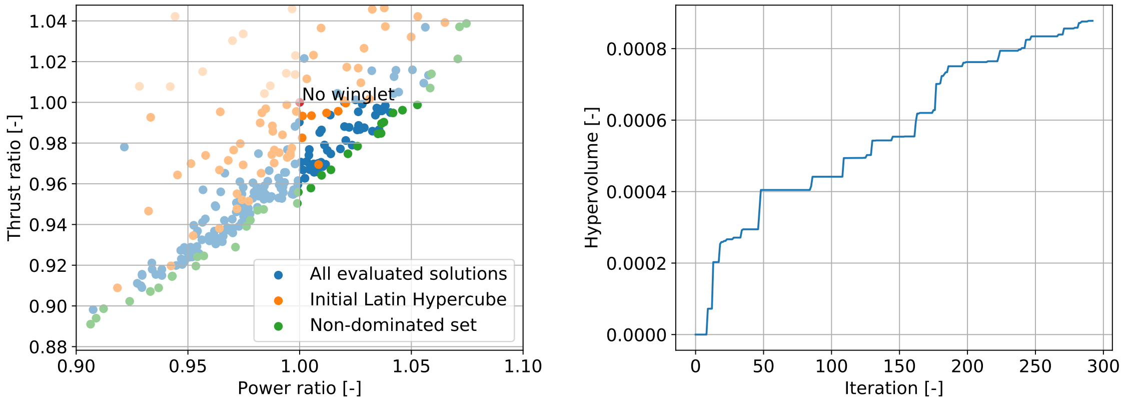

(a) Power ratio versus thrust ratio for all designs in optimisation case

(b) Hypervolume versus iteration

Figure 5.7: Pareto front and hypervolume for thrust minimisation with fixed diameter optimisation case for a downwind winglet

	ΔP [%]	ΔT [%]	$\Delta m_{f,0.9}$ [%]	$\Delta m_{f,r}$ [%]	τ_w [m]	λ [°]	h [m]	ϕ [°]	r_w [m]
Max (ΔP)	5.27	-0.12	9.10	0.25	0.40	55.0	7.99	51.56	0.30
Min (ΔT)	0.50	-4.21	-30.58	-5.71	0.07	55.0	7.74	53.72	0.99
Intermediate	3.51	-1.55	-7.90	-1.95	0.22	55.0	8.00	23.90	1.00
μ	3.02	-1.82	-9.59	-2.25	0.27	55.0	7.93	35.94	0.43
σ	1.49	1.34	11.01	1.91	0.23	0.0	0.18	22.22	0.31

Table 5.1: Downwind winglet optimisation for thrust minimisation with diameter constraint. From the improved non-dominated design the design with the highest power, the lowest thrust and a design with an intermediate increase in power and decrease in thrust, is shown. The mean μ and standard deviation σ of the design parameters and objectives is also taken from this subset and shown in this table.

For the downwind winglet optimisation, the normal and tangential loads are shown in fig. 5.8. The $Max(\Delta P)$ winglet and $Min(\Delta T)$ winglet have a cant angle of approximately $51°$ and $54°$ respectively, as shown in table 5.1. It can be seen in fig. 5.8a that there are some positive normal loads on the winglet itself for both cases, contributing to the integrated total thrust. Where the normal loads on the winglet are lower for the $Min(\Delta T)$ winglet than for the $Max(\Delta P)$ winglet. However, the normal loads on the blade close to the winglet are lower, due to the decreased chord length as shown in fig. 5.11a.
There is a positive tangential load on both winglets as seen in fig. 5.8b, where the $Max(\Delta P)$ has higher loads than the $Min(\Delta T)$ winglet, where the tangential loads on the blade close to the winglet are lower than on the baseline, due to the decreased chord again.
The tangential load on the main blade is also higher than the baseline, as seen in the zoomed-in figure for $35m < r < 75m$ is shown in fig. 5.8b. This increase in tangential loads is due to a decrease in negative axial induced velocity as shown in fig. 5.9b, where the winglet designs have a lower negative axial induced velocity, hence a higher effective axial velocity.

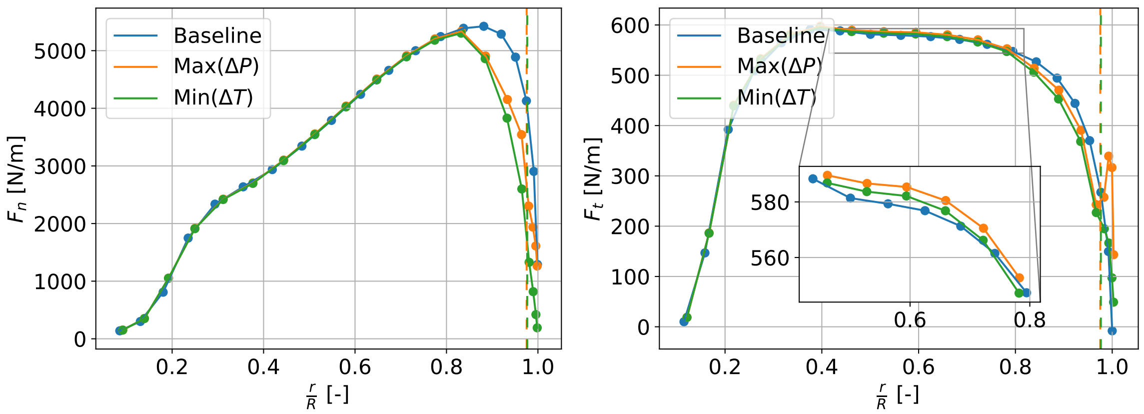

(a) Normal loads

(b) Tangential loads

Figure 5.8: Normal and tangential loads for $Max(\Delta P)$ and $Min(\Delta T)$ winglet designs from the downwind winglet thrust minimisation case

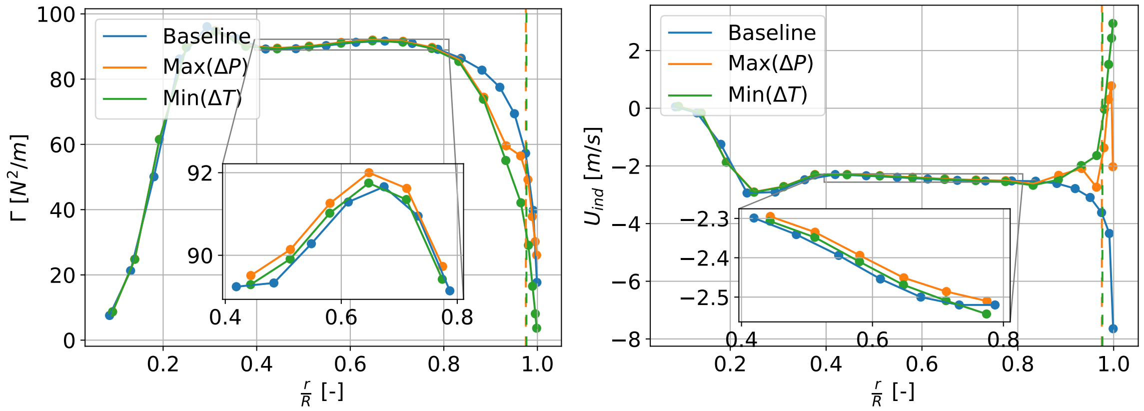

(a) Circulation

(b) Axial induced velocities

Figure 5.9: Circulation and axial induced velocity for $Max(\Delta P)$ and $Min(\Delta T)$ winglet designs from the downwind winglet thrust minimisation case

There is also a slightly increased circulation on the main blade shown in fig. 5.9a, where the circulation on the main blade is highest for the $Max(\Delta P)$ winglet design. Compared to the $Min(\Delta T)$ winglet, there is a slightly more positive radial induced velocity for the $Max(\Delta P)$ winglet as shown in fig. 5.10a, while the tangential forces on the winglet are higher. This is expected to be due to the higher circulation on the winglet as is shown in fig. 5.9a.

The downwind winglet designs found when maximising for power and minimising for thrust mostly serve to increase the tangential loading on the winglet itself, without increasing the tangential loads on the blade itself by a large amount. Still, an increase in power of approximately 5% can be achieved without increasing the rotor's thrust. However, this leads to a large increase in the flapwise bending moment at $\frac{r}{R} = 0.9$ and throughout a large part of the blade as shown in fig. 5.10b. Meaning a structural redesign of the main blade would probably be required for the DTU10MW design with the $Max(\Delta P)$ winglet design, or any other designs with higher power and lower thrust. This could lead to costs that might make the winglet no worthwhile addition to a winglet turbine design when considering the CoE.

The winglet height of the improved non-dominated winglet designs are always near or at the maximum and likely the optimiser would tend to even greater heights if higher winglet heights were allowed. This could in turn lead to even higher flapwise bending moments.

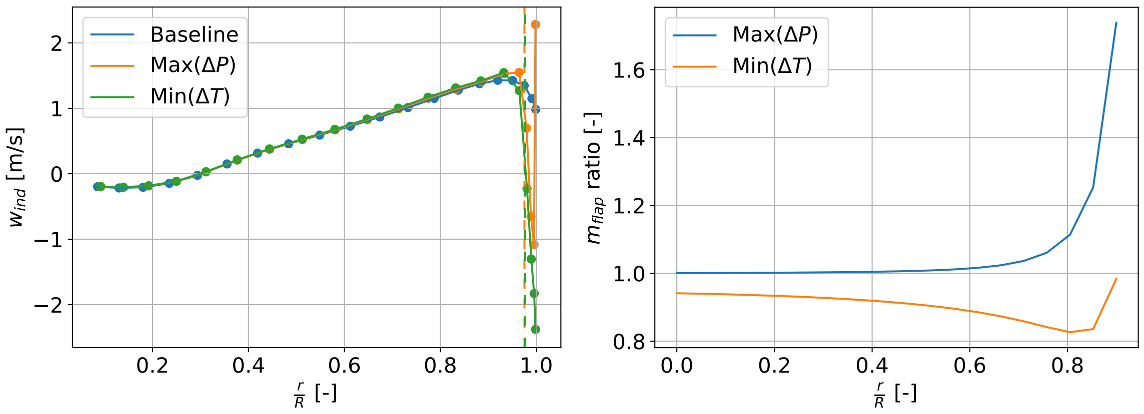

(a) Radial induced velocities

(b) Flapwise bending moment as a function of radial position

Figure 5.10: Radial induced velocity and flapwise bending moments for $Max(\Delta P)$ and $Min(\Delta T)$ winglet designs from the downwind winglet thrust minimisation case

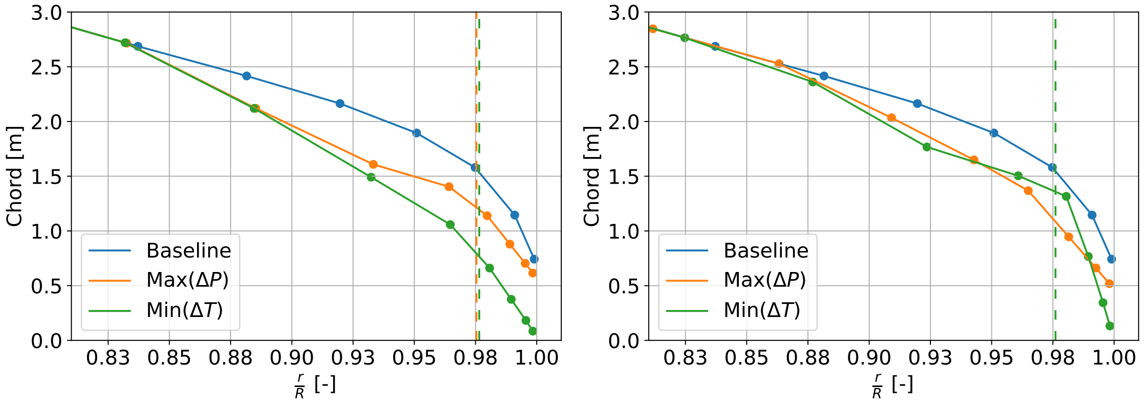

(a) Downwind winglet

(b) Upwind winglet

Figure 5.11: Chord lengths from thrust minimisation with fixed diameter cases for a downwind and upwind winglet

With variable diameter

For this optimisation case, the optimiser is free to change the blade's diameter and therefore either create a winglet or a tip extension. A summary of the optimisation case's objectives and design parameters was shown in table 4.8.

All evaluated designs for ΔP against ΔT are shown in fig. 5.12a and the tabular summary of the improved non-dominated design is shown in table 5.2. This optimisation case was run without varying the blade's sweep so it can be compared with the optimisation case that will be shown in table 5.8, in which section it will be explained why the sweep is not optimised for in this case.

It can clearly be seen that, when thrust is constrained and there is no diameter constraint, a tip extension is a better option than a winglet. Although not apparent from the table, it was found that every design with $\Delta P > 3\%$ had a $\phi < 25°$.

Figure 5.12 shows the chord length and tangential loads for the $Max(\Delta P)$ and $Min(\Delta T)$ designs, where it can be seen that the optimiser created designs with a lightly loaded outer part of the blade, by using a low chord length, where the $Min(\Delta T)$ shows the lowest chord length.

No other figures of the blade design's performance are shown for this case, as it is evident the increase in power is a result of the lightly loaded tip extension. It can also be seen from table 5.2 that although the improved non-dominated designs have a decreased thrust, the flapwise bending moment at $\frac{r}{R} = 0.9$ has been increased by 165%.

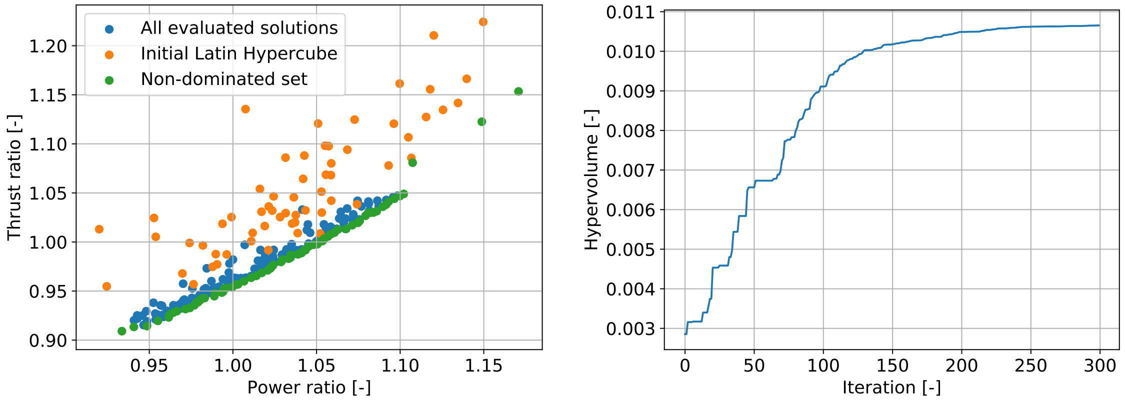

(a) Power ratio versus thrust ratio

(b) Hypervolume with increasing iterations

Figure 5.12: Pareto front and hypervolume for thrust minimisation with fixed diameter optimisation case for a downwind winglet

	ΔP [%]	ΔT [%]	$\Delta m_{f,0.9}$ [%]	$\Delta m_{f,r}$ [%]	τ_w [m]	λ [°]	h [m]	ϕ [°]	r_w [m]
Max (ΔP)	5.05	-0.22	165.53	0.76	0.01	5.0	7.66	0.10	0.31
Min (ΔT)	0.21	-4.33	59.19	-5.47	0.02	5.0	7.28	0.10	1.00
Intermediate	2.88	-2.03	119.71	-2.00	0.11	5.0	8.00	0.10	0.24
μ	2.73	-2.18	112.17	-2.18	0.09	5.0	6.79	1.59	0.37
σ	1.49	1.31	29.59	1.97	0.09	0.0	0.62	3.34	0.23

Table 5.2: The improved non-dominated set for downwind winglet optimisation with for thrust minimisation and variable diameter

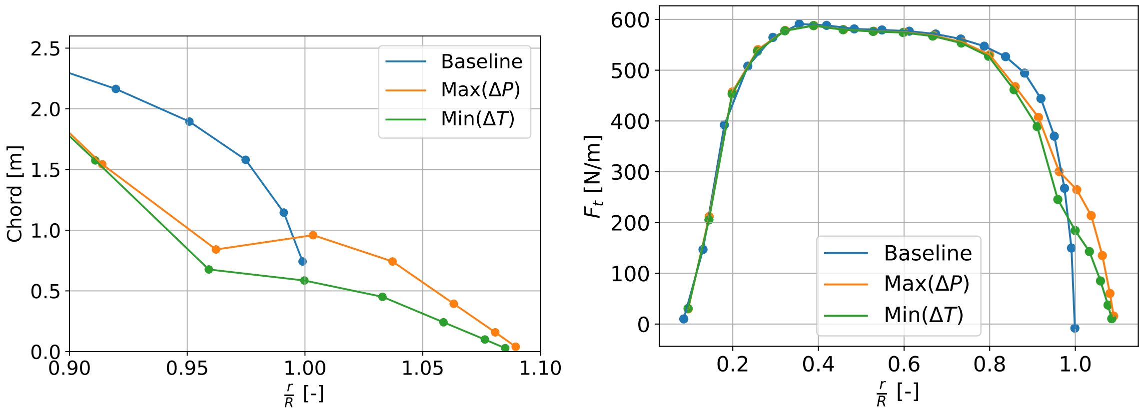

(a) Chord lengths

(b) Tangential loads

Figure 5.13: Tangential loads and chord lengths for thrust minimisation case with variable diameter

5.3.2. Upwind winglet

A summary of the design parameters and objectives was shown in table 4.7, where now an upwind winglet is considered.

The evaluated designs for the upwind winglet with diameter constraint with ΔP against ΔT are shown in fig. 5.14a where the improved non-dominated subset designs are shown in table 5.3.

For the upwind winglet, a high positive sweep is also preferred, as is for the downwind winglet case, with most improved non-dominated designs having sweep angles close to the bounds of the domain. However, the benefit of high sweep does not seem as pronounced as for the downwind winglet, with not all designs being at the upper bounds of the domain and a fairly high standard deviation of approximately

$25°$. Upon further investigation, however, this is was caused by one design with a negative sweep angle, with all other designs having a sweep of $50°$. The effect of sweep for upwind and downwind winglets will be investigated further in section 7.1.

Although not all part of the improved non-dominated designs, it was found when looking at designs that have relatively high power ($\Delta P > 2\%$), lower thrust than the baseline design ($\Delta T < 0\%$), that all designs with a negative sweep angle, also had a cant angle of approximately $90°$. This was found for five out of the thirteen designs in this subset. Meaning that for an upwind winglet with thrust constraint, a negative (upwind) sweep, could be beneficial for (nearly) straight winglets.

The mean preferred cant angle is lower than for the downwind winglet, with a mean cant angle of the design coming quite close to a straight wing. The maximum power design is a straight blade, so here the gain in power is expected to come from the sweep. Again for the upwind winglet, there is no clear optimum in the winglet radius with values ranging from its minimum to maximum.

A somewhat lower taper ratio for the winglet is preferred by the optimiser. The power increase for the maximum power design for this upwind optimisation case is lower than for the downwind case. Also, the thrust decrease for the minimum thrust case is also lower. Interesting to see is that the minimum thrust case has a relatively high cant angle, compared to other improved non-dominant designs, however, there were not many designs found with high positive sweep and $\phi > 60$, such as the minimum thrust design.

The hypervolume with increasing iterations is shown in fig. 5.14. The stopping criterion has been met with 1.7% increase in hypervolume the last thirty iterations, although the hypervolume is still slowly increasing. The maximum power design lies on the bounds of the sweep, cant and height, however, so it is expected that not many more optimum designs can be found.

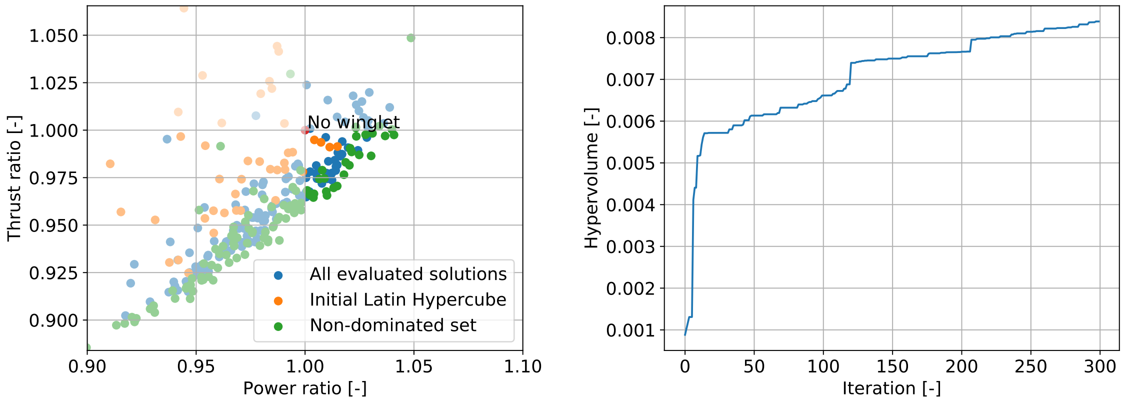

(a) Power ratio versus thrust ratio

(b) Hypervolume for increasing iterations

Figure 5.14: Pareto front and hypervolume for thrust minimisation optimisation case for an upwind winglet

	ΔP [%]	ΔT [%]	$\Delta m_{f,0.9}$ [%]	$\Delta m_{f,r}$ [%]	τ_w [m]	λ [°]	h [m]	ϕ [°]	r_w [m]
Max (ΔP)	4.08	-0.25	15.30	0.09	0.24	50.00	8.00	0.10	0.10
Min (ΔT)	0.38	-3.55	23.39	-4.36	0.05	47.01	6.50	60.62	0.89
Intermediate	2.04	-1.85	12.40	-2.06	0.24	50.00	7.37	12.69	0.52
μ	2.09	-2.12	10.65	-2.54	0.18	41.31	7.70	18.21	0.38
σ	1.25	1.27	30.80	1.81	0.09	24.97	0.51	33.45	0.31

Table 5.3: Upwind winglet optimisation improved non-dominated design set showing, from this set, the design with the highest power, the lowest thrust and a design with an intermediate increase in power and decrease in thrust

For the upwind winglet optimisation, the normal and tangential loads are shown in fig. 5.15. The $Max(\Delta P)$ design was found to have a cant angle of approximately $0°$, therefore the design will be called a straight tip instead of a winglet. The $Min(\Delta T)$ design was found to be a winglet with a cant angle of approximately $61°$. Both designs had a sweep angle of approximately $50°$, which is the maximum sweep angle allowed. The sweep angle led to an increase in tangential loads on the winglet or straight tip as seen in fig. 5.15, where the straight tip from the $Max(\Delta P)$ design has the largest tangential loads on the tip of the two designs. As expected for an upwind winglet, the tangential loads are decreased on the main blade compared to the baseline design. Where the decrease is smaller for the $Max(\Delta P)$ design compared to the $Min(\Delta T)$ design, which is not surprising as the $Max(\Delta P)$ is not a winglet, but a straight tip. The $Max(\Delta P)$ design has some slightly increased normal loads on the straight tip as seen from fig. 5.15a with decreased normal loads close to the straight tip ($0.85 < \frac{r}{R} < 0.95$), compared to the baseline blade, due to the decreased chord length as shown in fig. 5.11b. The $Min(\Delta T)$ design has relatively low normal loads on the winglet and also decreased loads on the blade close to the winglet, also due to the decreased chord length.

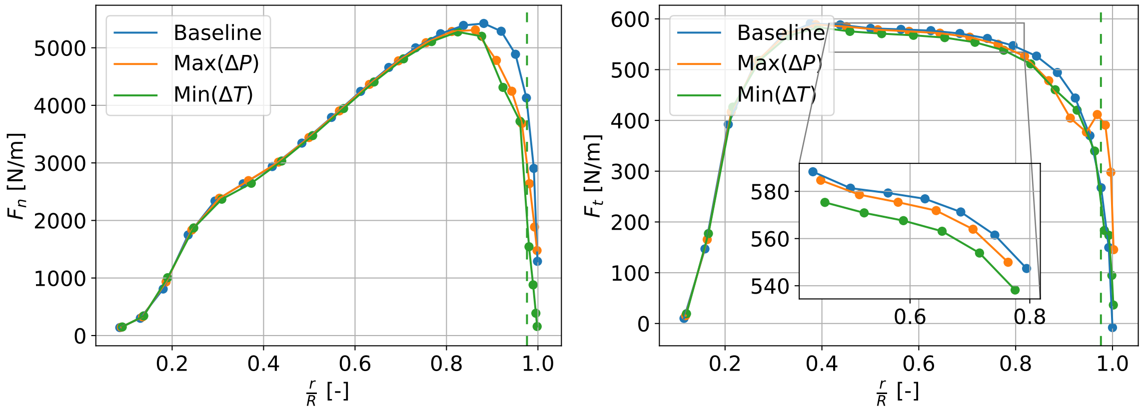

(a) Normal loads

(b) Tangential loads

Figure 5.15: Normal and tangential loads for $Max(\Delta P)$ and $Min(\Delta T)$ winglet designs from the upwind winglet thrust minimisation case

The circulation of the designs is shown in fig. 5.16a. The circulation is slightly higher on the blade for the $Max(\Delta P)$ design compared to the $Min(\Delta T)$ design. The tangential loads on the $Min(\Delta T)$ winglet are a result of the increase in positive radial induced velocity as shown in fig. 5.17a, where the $Max(\Delta P)$ straight tip does not show much change in the radial induced velocity. The increase in tangential loads at $\frac{r}{R} > 0.95$ for the $Max(\Delta P)$ design is expected to come from the less negative axial induced velocity as shown in fig. 5.16b, which gives a higher effective velocity on the straight tip. The increase in axial induced velocity is suspected to be a result of the downwind sweep of the straight tip.

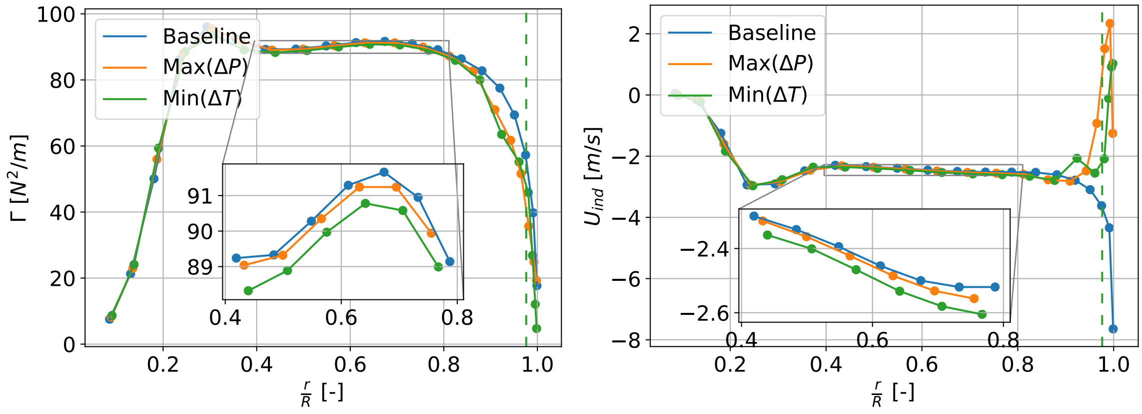

(a) Circulation

(b) Axial induced velocities

Figure 5.16: Circulation and axial induced velocities for $Max(\Delta P)$ and $Min(\Delta T)$ winglet designs from the upwind winglet thrust minimisation case

The flapwise bending moment ratio as a function of the radial location on the blade is shown in fig. 5.17b.

Where the ratio is the flapwise bending moment for the improved design divided by the flapwise bending moment of the baseline design. For the $Min(\Delta T)$ design the bending moment ratio is lower due to the lower normal loads along the blade, compared to the baseline design. Closer to the tip ($\frac{r}{R} > 0.8$) the flapwise bending moment ratio actually becomes larger as the influence from the radial loads on the winglet has a relatively larger influence compared to the normal loads.

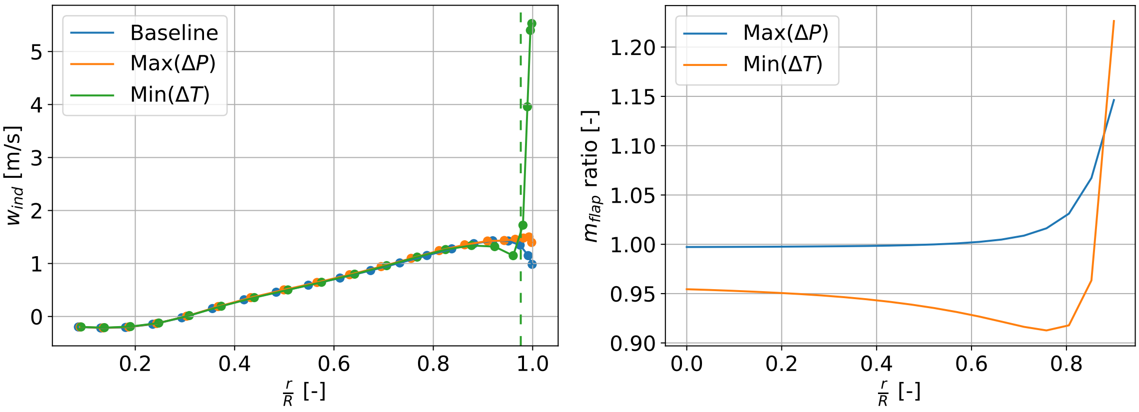

(a) Radial induced velocities

(b) Flapwise bending ratios as a function of radial position

Figure 5.17: Radial induced velocity and flapwise bending ratios for $Max(\Delta P)$ and $Min(\Delta T)$ winglet designs from the upwind winglet thrust minimisation case

5.4. Winglet root flapwise bending moment constrained

In this optimisation case, the power is maximised while the root flapwise bending moment is minimised. The diameter of the blade is kept constant. A summary of the design parameters and objectives was shown in table 4.9. The root flapwise bending moment is a parameter that is output directly from AWSM. The increase or decrease of all objectives is compared with the optimum from the blade optimisation. Optimisations are run separately for a downwind winglet in section 5.4.1 and upwind winglet in section 5.4.2.

5.4.1. Downwind winglet

The evaluated designs for ΔP and $\Delta m_{f,r}$ are shown in fig. 5.18a with the improved non-dominated subset table in table 5.4. Again, high positive sweep angles are preferred by the optimiser, just as winglet heights that are close to the maximum are preferred. Winglet cant angles are found to be somewhat higher on average than for the thrust minimisation case, which could indicate that a winglet design is slightly more beneficial to the design when the root flapwise bending moment is a constraint, instead of when the thrust is constrained. Again, the maximum winglet length is preferred by the optimiser for most winglet designs. It is suspected that the height of the winglet does not have a large effect on root flapwise bending moment as the effect of radial loads on the flapwise bending moment at the root is much smaller than the normal loads, as the normal loads have a much larger arm.

The taper ratio varies quite much again, with no clear optimum ratio. Interesting to see is that for the maximum power case, the winglet does decrease the root flapwise bending moment, but not the bending moment at $\frac{r}{R} = 0.9$. This was found to be the case for all designs with higher power ($\Delta P > 2\%$) and non increased $m_{f,r}$ ($\Delta m_{f,r} < 0\%$) compared to the baseline design, where ten out of ten designs did have a lower bending moment at the root, but not at $\frac{r}{R} = 0.9$.

Figure 5.18b shows the hypervolume as function of iterations. The hypervolume does not increase much anymore from iteration number 160, however most high power or improved non-dominated designs were found after iteration 260. The stopping criterion has been met with 0.97% increase in hypervolume the last thirty iterations. The chord length of the $Max(\Delta P)$ and $Min(m_{f,r})$ designs are shown in fig. 5.19a, where the chord lengths are found to be slightly lower than for the downwind thrust minimisation case.

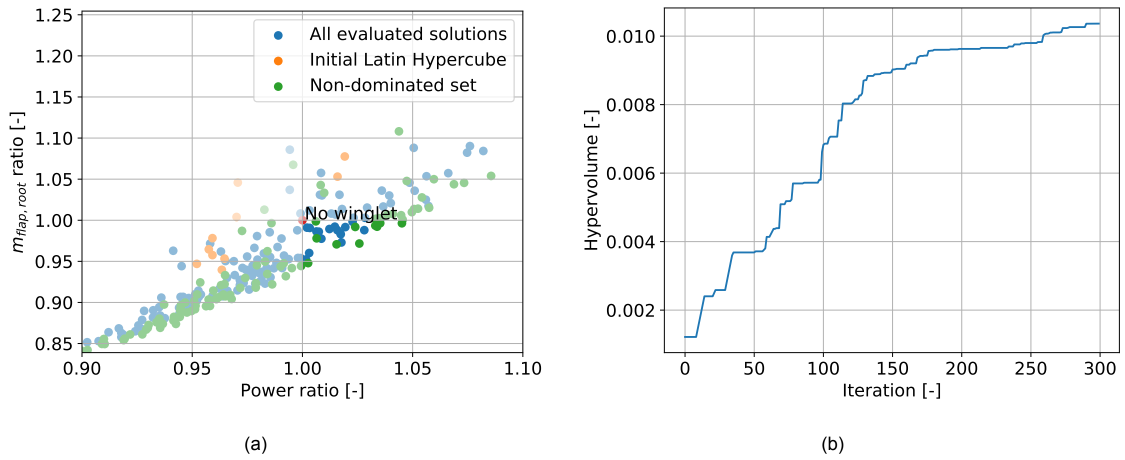

(a)

(b)

Figure 5.18: Pareto front and hypervolume for root flapwise bending moment minimisation optimisation case for a downwind winglet

	ΔP [%]	ΔT [%]	$\Delta m_{f,0.9}$ [%]	$\Delta m_{f,r}$ [%]	τ_w [m]	λ [°]	h [m]	ϕ [°]	r_w [m]
Max (ΔP)	4.51	-0.49	17.53	-0.37	0.22	55.00	7.53	42.31	0.21
Min ($\Delta m_{f,r}$)	0.26	-3.92	-25.19	-5.21	0.04	55.00	8.00	0.10	0.99
Intermediate	2.58	-2.13	9.66	-2.83	0.35	51.12	8.00	34.07	1.00
μ	2.20	-2.01	18.35	-2.47	0.10	45.30	7.34	37.16	0.69
σ	1.58	1.27	32.78	1.78	0.13	22.52	0.84	31.70	0.39

Table 5.4: Downwind winglet optimisation for the root flapwise bending moment minimisation case. Showing the improved non-dominated design.

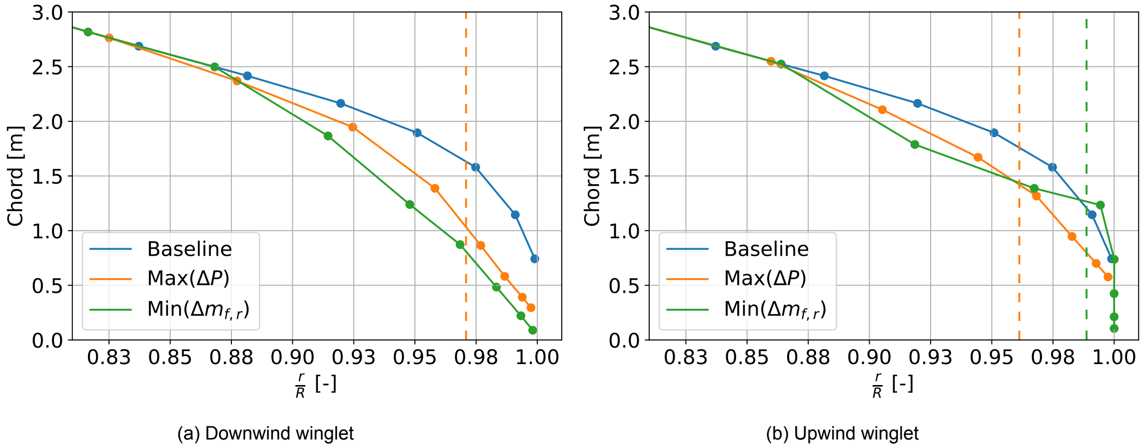

(a) Downwind winglet

(b) Upwind winglet

Figure 5.19: Chord length for root flapwise bending moment minimisation case for an upwind and a downwind winglet

For the downwind winglet optimisation, the normal and tangential loads are presented in fig. 5.20. The $Max(\Delta P)$ case is a winglet with a cant angle of approximately $42°$ and the $Min(\Delta m_{f,r})$ is a straight tip with a cant angle of $0°$. The tangential loads on the winglet are lower than for the thrust minimisation case, which is the main difference between the two optimisation cases for a downwind winglet. The tangential and normal loads are reduced for $0.85 < \frac{r}{R} < 0.95$ compared to the baseline design, due to the decreased chord length.

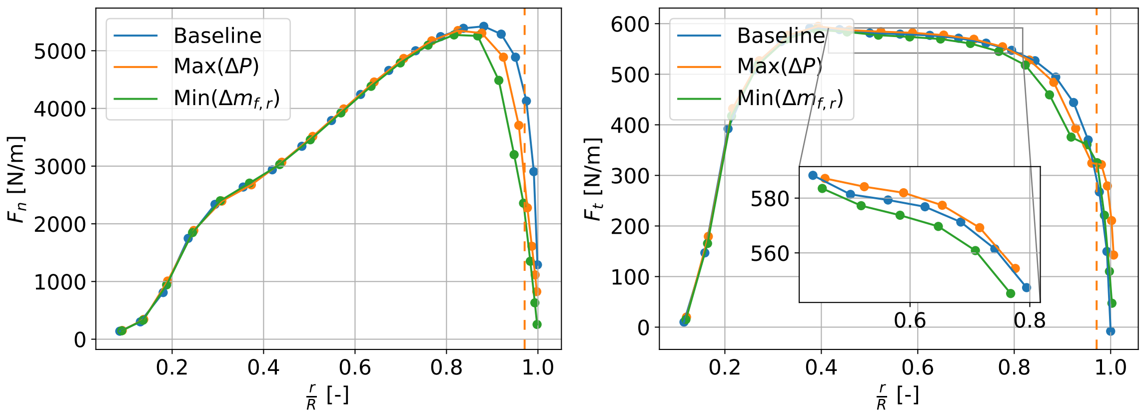

(a) Normal loads

(b) Tangential loads

Figure 5.20: Normal and tangential loads for the root flapwise bending moment minimisation case for a downwind winglet

The tangential loads on the main blade are somewhat higher for the $Max(\Delta P)$ design, compared to the baseline design, which is again the result of increased circulation and reduced negative axial induced velocity on the main blade, as seen in fig. 5.21a and fig. 5.21b respectively.

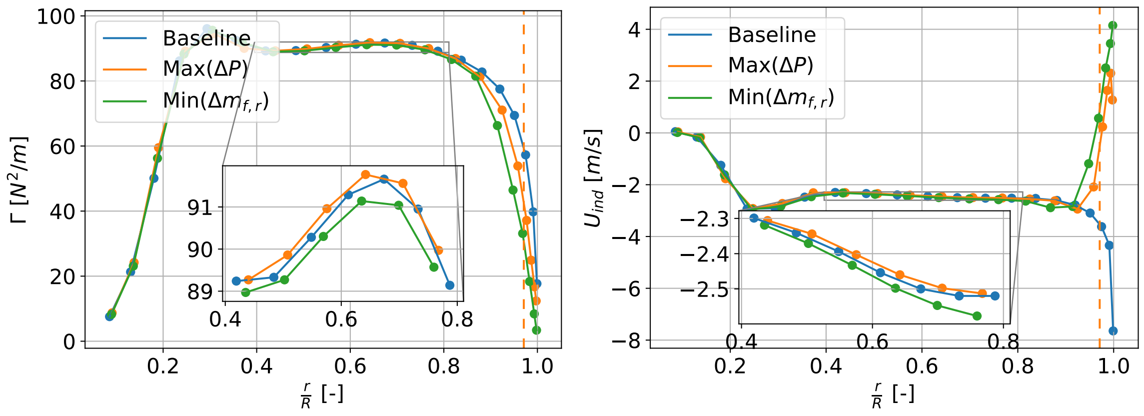

(a) Circulation

(b) Axial induced velocity

Figure 5.21: Circulation and axial induced velocity for the root flapwise bending moment minimisation case for a downwind winglet

For the $Min(\Delta m_{f,r})$ straight tip, the tip has higher tangential loads compared to the baseline design, however, the rest of the blade seems to have lower tangential loads as seen in fig. 5.20b. The power increase solely comes from the tip therefore for this design. It can be seen that the circulation and axial induced velocity are both lower for this design, which is the cause of the lower tangential loads. The higher tangential loads are expected to be from the less negative axial induced velocity on the tip as seen in fig. 5.21b, as the $Min(\Delta m_{f,r})$ is a straight tip, instead of a winglet. The positive axial induced velocity is expected to be the result of the high sweep of the straight tip.

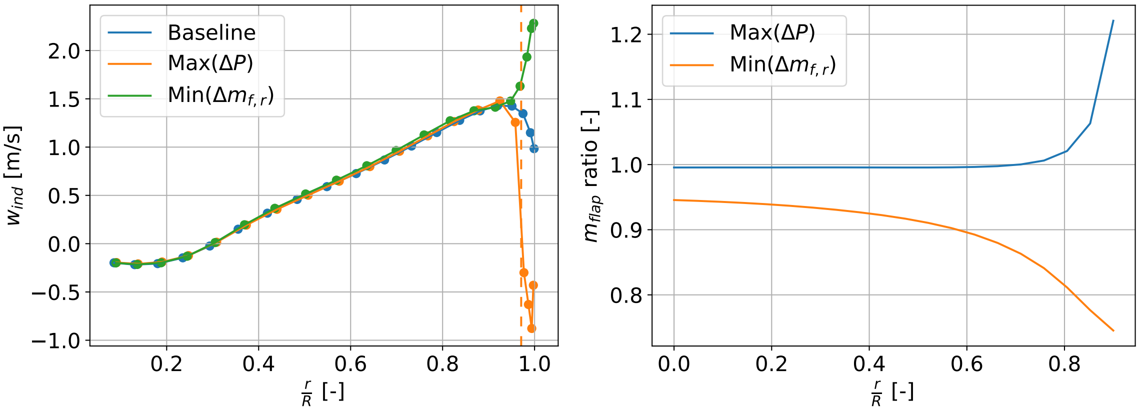

(a) Radial induced velocity (b) Flapwise bending ratios as a function of radial position

Figure 5.22: Radial induced velocity and flapwise bending ratios for the root flapwise bending moment minimisation case for a downwind winglet

For the $Max(\Delta P)$ design, the increased tangential loads on the winglet come from the negative radial induced velocity shown in fig. 5.22a, where the $Min(\Delta m_{f,r})$ straight tip actually has a positive radial induced velocity.

The flapwise bending ratio, where the ratio is the flapwise bending moment of the optimised design divided by the flapwise bending moment of the baseline design, is shown in fig. 5.22b. It can be seen that the bending moment only starts to increase from $\frac{r}{R} > 0.7$, with a ratio going to 1.22, which is lower than for the downwind winglet thrust minimisation case.

5.4.2. Upwind winglet

The evaluated designs for ΔP and $\Delta m_{f,r}$ are shown in fig. 5.23a with the improved non-dominated subset shown in table 5.5. The optimiser seems less conclusive on this optimisation case, the $Max(\Delta P)$ design was found for a straight tip with high sweep, however also a straight winglet ($\phi = 90°$ with an increase in power of 2.3% was found. A winglet height close to the maximum is preferred by the optimiser, but not at the maximum, as for the thrust minimisation cases. Also for the sweep, the maximum sweep is not always preferred in the improved non-dominated design. However, for all designs with a power increase of 2% and no increased $m_{f,r}$, a maximum sweep was generally preferred, with a mean sweep of approximately $52°$ and a standard deviation of $3.8°$. Again, there is no clear optimum on the taper ratio and winglet radius found. The chord length is shown in fig. 5.19b. Similar chord lengths as for the thrust minimisation case were found.

The hypervolume as a function of iterations is shown in fig. 5.23b, the stopping criterion has not been met yet, so a more optimum design likely could have been achieved.

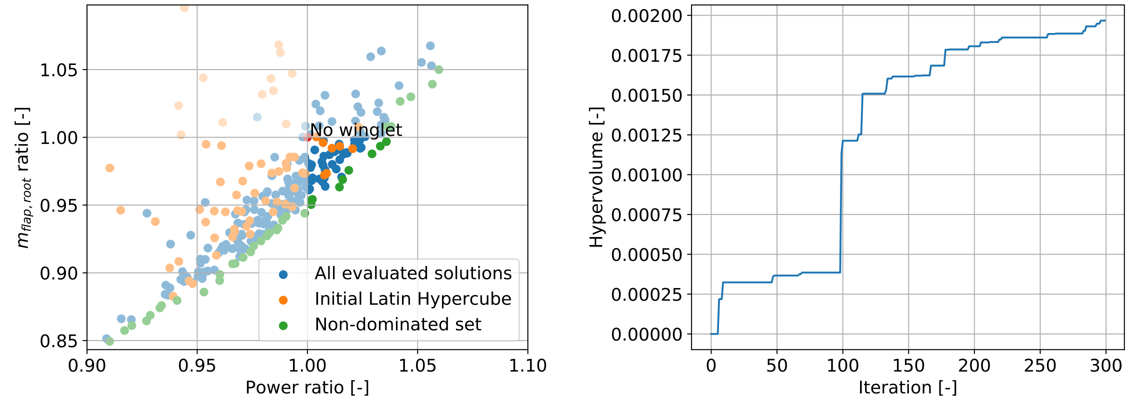

(a) Power versus $m_{f,r}$ for all designs

(b) Hypervolume versus iterations

Figure 5.23: Pareto front and hypervolume for root flapwise bending moment minimisation optimisation case for a upwind winglet

	ΔP [%]	ΔT [%]	$\Delta m_{f,0.9}$ [%]	$\Delta m_{f,r}$ [%]	τ_w [m]	λ [°]	h [m]	ϕ [°]	r_w [m]
Max (ΔP)	3.59	-0.54	20.69	-0.32	0.36	55.00	5.85	5.68	0.10
Min ($\Delta m_{f,r}$)	0.17	-3.87	45.64	-4.97	0.08	36.41	8.00	90.00	0.99
Intermediate	1.60	-2.53	1.20	-3.12	0.30	55.00	7.03	13.82	0.23
μ	1.70	-2.34	18.59	-2.84	0.20	35.68	7.18	33.19	0.46
σ	1.35	1.24	27.81	1.78	0.18	32.15	0.97	41.71	0.35

Table 5.5: Upwind winglet optimisation for $m_{f,r}$ minimisation showing the improved non-dominated design

The normal and tangential loads for this optimisation case are shown in fig. 5.24. The increase in power for the $Max(\Delta P)$ straight tip again comes from the increase in tangential loads due to the tip. Figure 5.24b shows a minimum decrease again in the tangential loads on the blade for the straight tip, compared to the baseline design. The increase in tangential loads on the tip seems to come from the increase in positive axial induced velocity again as shown in fig. 5.25b, leading to a higher effective velocity on the straight tip.

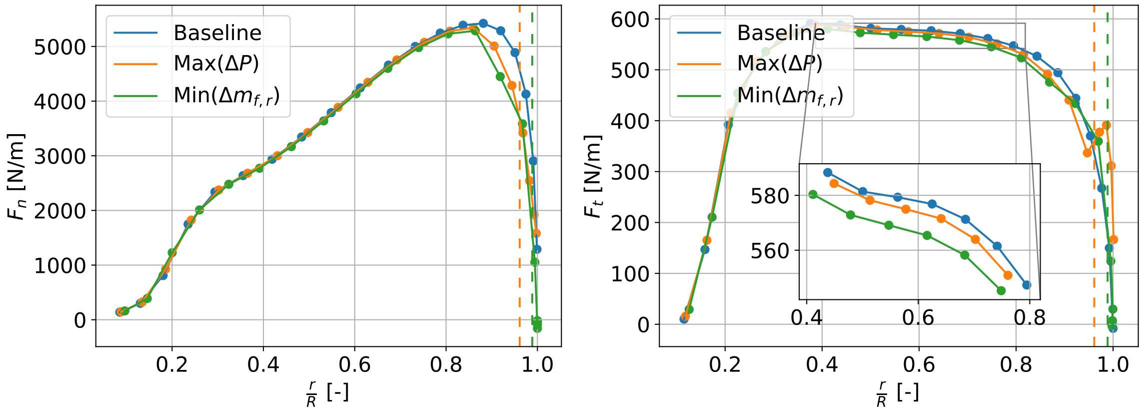

(a) Normal loads

(b) Tangential loads

Figure 5.24: Tangential and normal loads for the root flapwise bending moment minimisation case for an upwind winglet

For the $Min(\Delta m_{f,r})$ design, which is a straight winglet with, relatively to other improved non-dominated sets, moderate sweep downstream, the increase in power also seems to come from increased tangential loads on the winglet. The tangential loads on the main blade are decreased compared to the baseline blade, as expected from a straight upwind winglet. The decrease is the result of a more negative axial induced velocity on the main blade as shown in fig. 5.25b and lower circulation as shown in fig. 5.25a.

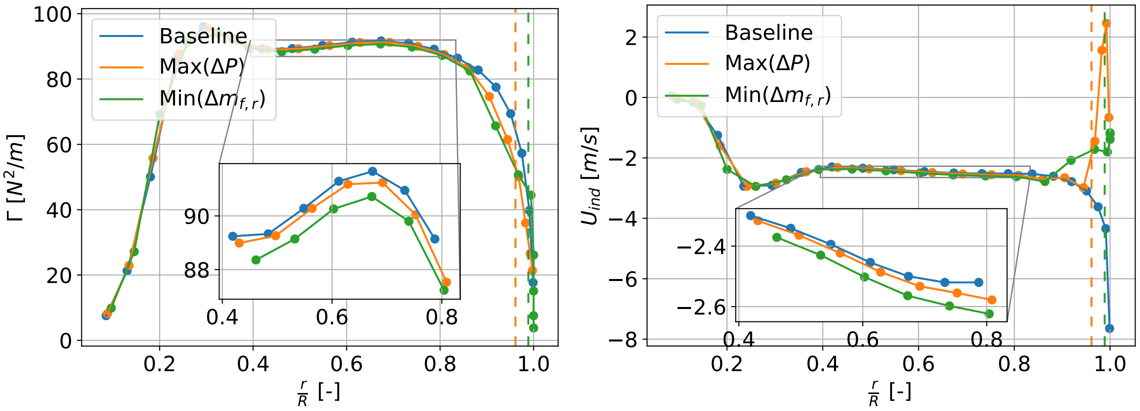

(a) Circulation

(b) Axial induced velocity

Figure 5.25: Circulation and axial induced velocity for the root flapwise bending moment minimisation case for an upwind winglet

The increased tangential loads on the winglet come from the positive radial induced velocity as seen in fig. 5.26a.

The flapwise bending moment ratio is shown in fig. 5.26b. Where the $Min(\Delta m_{f,r})$ design does have a decrease bending moment at the root and up to approximately $\frac{r}{R} = 0.85$, however, the bending moment for $\frac{r}{R} > 0.85$ is much higher due to the radial forces of the straight winglet. This ratio is much smaller for the $Max(\Delta P)$ design, as this is a straight tip, which has no, or at least small, radial loads.

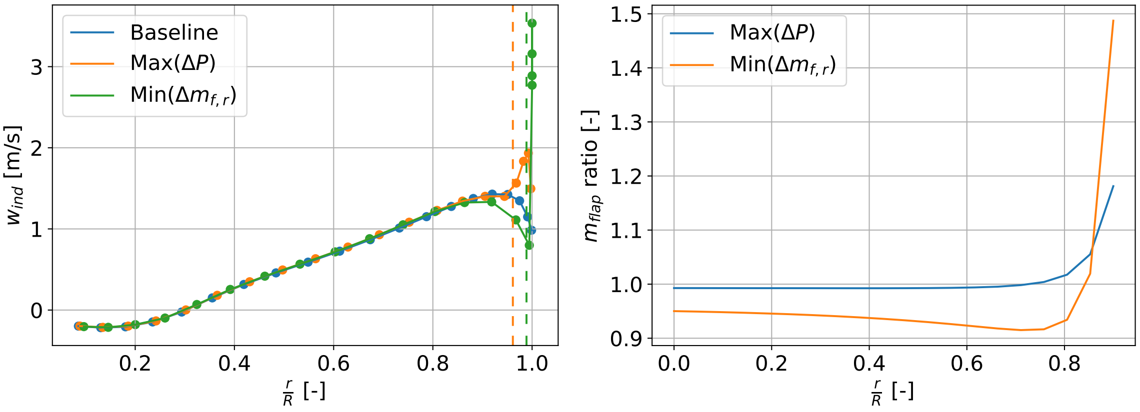

(a) Radial induced velocities

(b) Flapwise bending ratios as a function of radial position

Figure 5.26: Radial induced velocity and flapwise bending ratios for the root flapwise bending moment minimisation case for an upwind winglet

5.5. Winglet flapwise bending moment constrained on the blade

This section will show the results for minimising the flapwise bending moment at a location on the blade. This flapwise bending moment is not directly output from AWSM and has to be calculated using the loads given by AWSM, which calculation process is explained in appendix B.2. This might introduce some error in the results, so the actual values for $\Delta m_{f,0.9}$ might be off, however, it is assumed the trends are correct, meaning, for example, a positive $\Delta m_{f,0.9}$ is actually a positive $\Delta m_{f,0.9}$.

For this minimisation objective, three different cases are made for the downwind winglet and two different cases for the upwind winglet. The moment was minimised at $\frac{r}{R} = 0.9$ for one case $\frac{r}{R} = 0.8$

for another case for both the upwind and downwind winglet. For the downwind winglet also a case is performed without constraining the diameter, to match the research by Zahle et al. [30] as verification if similar results are obtained, although this research concerns an upwind winglet. Sectional plots are only shown for the moment constrained at $\frac{r}{R} = 0.8$.

5.5.1. Downwind winglet

At 90% of the blade's radius with a fixed diameter

A summary of the design parameters and objectives is shown table 4.10. The evaluated designs for ΔP and $\Delta m_{f,0.9}$ are shown in fig. 5.27a with the improved non-dominated subset shown in table 5.6. The cant angles of the improved non-dominated designs are all relatively low compared to previous optimisation cases, with all designs that were found having $\phi < 20°$. High values for the sweep are preferred by the optimiser, however, the optimum was not always the largest possible sweep angle. Relatively low taper ratios were preferred, likely due to all designs having a low cant angle. The winglet radius did not seem to have much effect on the results.

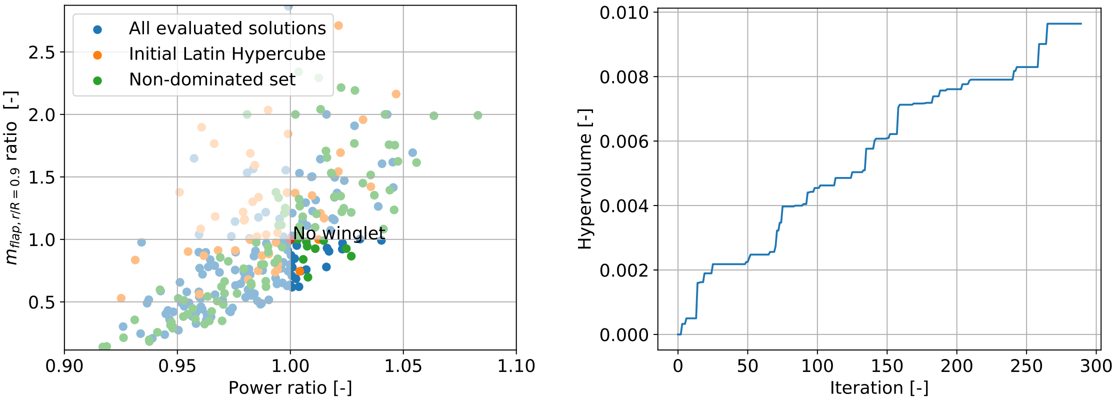

(a) Power versus $m_{f,0.9}$ for all designs

(b) Hypervolume versus iterations

Figure 5.27: Pareto front and hypervolume for flapwise bending moment $\frac{r}{R} = 0.9$ minimisation optimisation case for a downwind winglet

	ΔP [%]	ΔT [%]	$\Delta m_{f,0.9}$ [%]	$\Delta m_{f,r}$ [%]	τ_w [m]	λ [°]	h [m]	ϕ [°]	r_w [m]
Max (ΔP)	4.03	0.43	-0.78	0.81	0.30	55.00	6.96	16.01	0.51
Min ($\Delta m_{f,0.9}$)	0.07	-2.52	-38.30	-3.29	0.02	37.34	7.16	0.10	0.62
Intermediate	1.59	-2.37	-22.06	-3.15	0.16	46.73	8.00	7.78	0.18
μ	1.59	-1.75	-23.78	-2.28	0.17	45.50	7.48	12.94	0.46
σ	1.52	1.14	14.77	1.61	0.16	8.04	0.46	14.56	0.23

Table 5.6: Downwind winglet optimisation for the $m_{f,0.9}$ minimisation case, showing the improved non-dominated design set

Perhaps surprising, the improved non-dominated designs are not winglets, but straight tips. This is unexpected as this is contrary to the results found by Zahle et al. [30]. However, there are some differences between the research by Zahle et al. [30].

Firstly, Zahle's research concerned a tip extension with no diameter constraint, where the tip extension was free to move to the upwind direction, so the tip extension could be a winglet or straight tip extension. It was argued that the tip extension, in this research, could best be a lightly loaded winglet which itself does not contribute much to the power of the turbine, however does function to displace the tip vortex, increasing the tangential load on the main blade. This would be more beneficial than a tip extension which itself contributes to the power of the turbine, but would therefore also contribute to the flapwise bending moment at $\frac{r}{R} = 0.9$. The tip extension would have a longer arm to the $\frac{r}{R} = 0.9$ location than the radial force on the winglet. This is not the case for this research, where the radius of the blade is the same regardless of the cant angle. The radial loads on the blade of a winglet with a winglet height of 10% of the blade's radius, would have the same arm as the normal loads on a straight tip, for the optimisation in this thesis. In addition to these radial loads, the part of the blade close to the winglet still has some normal loads also contributing to the flapwise bending moment at $\frac{r}{R} = 0.9$, these loads added up could simply be too high to not exceed the bending moment constraint. This was seen in some of the winglet designs from other optimisation cases, such as in, for example, the $Min(\Delta T)$ winglet design in fig. 5.10b, where the flapwise bending moment sharply increases for $\frac{r}{R} > 0.85$, which is likely due to the influence of the radial loading being relatively high at $\frac{r}{R} > 0.85$ compared to the normal loads on the blade.

Secondly, as seen from previous optimisation cases, a high sweep of straight tip or winglets is always preferred by AWSM as it increases the tangential loads on the straight tip part or winglet with almost no normal loads, as will be elaborated on further in section 7.1. The optimiser could prefer a straight, swept-back tip as the best trade-off between maximising power and minimising $m_{f,0.9}$ and might not reach any design with a (nearly) straight winglet which performs as well in reducing $m_{f,0.9}$ and increasing power.

Thirdly, a different parameterisation is used in this research, with which it might be impossible, or very difficult, to reach a proper winglet design that can successfully increase the tangential loads on the main blade without increasing the flapwise bending moment at $\frac{r}{R} = 0.9$. However, winglet designs with $\phi > 45°$ were found with ΔP up to 2.71%, however, these designs all had a high downstream sweep angle, which mostly increased the power due to the tangential loads on the winglet itself with only small increased tangential loads on the blade.

Lastly, a different optimisation algorithm is used. Although Bayesian Optimisation has worked well in other researches, such as for Stock-Williams et al. [3], perhaps more iterations were needed than expected to reach a more optimised design which is actually a winglet.

At 80% of the blade's radius with a fixed diameter and fixed sweep

To find out if the cause of a winglet not being the preferred design by the optimiser is the location where the bending moment is analysed or an effect of the overestimated positive effect of downstream sweep, another optimisation case is created where the bending moment is analysed on $\frac{r}{R} = 0.8$ instead. The sweep is set to a constant value and is not optimised for. This constant value is chosen to be $\lambda = 5°$ as this leads to an approximately straight trailing edge. A summary of the objectives and optimisation parameters was shown in table 4.12.

The chord of the blade is still only optimised for $\frac{r}{R} > 0.9$. This is left unchanged to not give an unfair advantage to the optimiser compared to the previous optimisation cases, which would make it harder to compare results.

The results of this optimisation are shown in table 5.7, where only two designs were found to be part of the improved non-dominated subset. The optimiser did have a fairly clear preference for higher cant angles, however, struggled to find solutions with higher power and a lower $m_{f,0.9}$. When looking at the non-dominated set instead of the improved non-dominated set, for example, all designs with high power, for example, the two non-dominated designs shown in fig. 5.28a with a ΔP of 1.035 and 1.038 respectively and a $\Delta m_{f,0.8}$ ratio of 1.17 and 1.26 respectively, these were both straight winglet with a length of approximately $7m$. In fact, any non-dominated solutions found with $\Delta P > 0$, have a $\phi > 78°$ with most designs being a straight winglet. The non-dominated solutions with $\Delta m_{f,0.8} < 0$ were mostly straight tips, with an exception of a fairly short winglet ($h_w = 1.95m$) winglet with $\phi = 61$, which did not manage to increase the power, but decreased $m_{f,0.8}$ with approximately 32%. This shows that the optimiser has a preference to design a winglet to maximise power with only a minimal increase in the flapwise bending moment at $\frac{r}{R} = 0.8$.

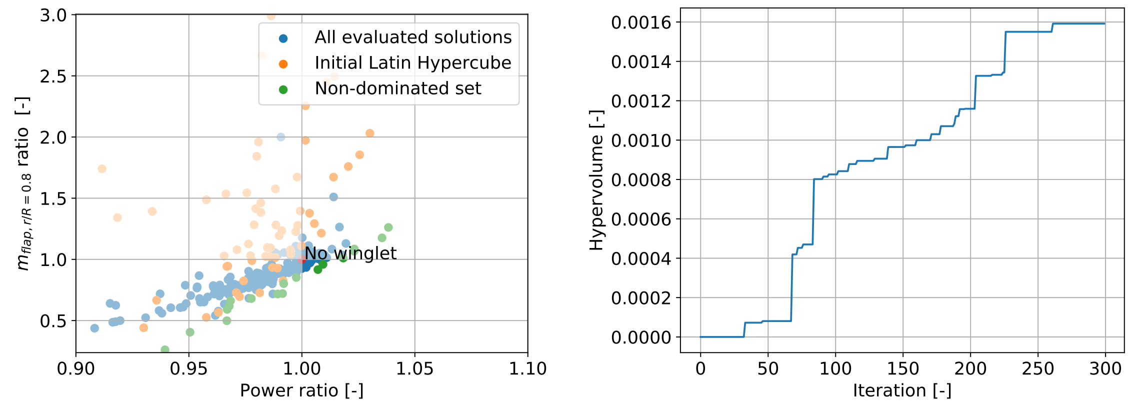

(a) Power versus $m_{f,0.8}$ for all designs

(b) Hypervolume versus

Figure 5.28: Pareto front and hypervolume for flapwise bending moment $\frac{r}{R}$ = 0.8 minimisation optimisation case for a downwind winglet

	ΔP [%]	ΔT [%]	$\Delta m_{f,0.8}$ [%]	$\Delta m_{f,r}$ [%]	τ_w [m]	λ [°]	h [m]	ϕ [°]	r_w [m]
Max (ΔP)	0.93	-0.73	-4.10	-1.28	0.12	5.0	5.94	66.99	0.34
Min ($\Delta m_{f,0.8}$)	0.71	-1.33	-8.35	-1.77	0.15	5.0	4.95	78.78	0.10

Table 5.7: Improved non-dominated design set for downwind winglet optimisation case for $m_{f,0.8}$ minimisation with constrained diameter

As seen from fig. 5.29, both winglets that are shown are able to increase the tangential loads on the blade, which is a result of increasing the effective axial velocity as seen in fig. 5.30a, with increased circulation as well as shown in fig. 5.30b. Contrary to the downwind winglet in the previous two downwind optimisation cases, the radial induced velocity is now positive as seen in fig. 5.31a, leading to a power decrease from the downwind winglet itself, which effect is seen especially for the $Max(\Delta P)$ winglet. This is probably a result of the increased circulation on the blade which results to a lower axial velocity in the axial direction in the wake, leading to a positive radial flow due to mass conservation. Figure 5.29a shows the reduced normal loads over the whole blade as well for both winglets.

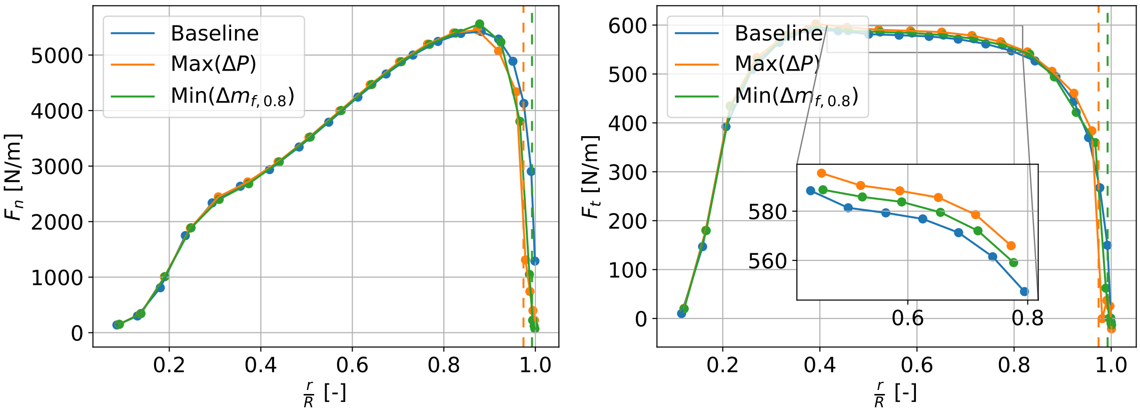

(a) Normal loads

(b) Tangential loads

Figure 5.29: Normal and tangential loads for the flapwise bending moment at $\frac{r}{R}$ = 0.8 minimisation case for a downwind winglet

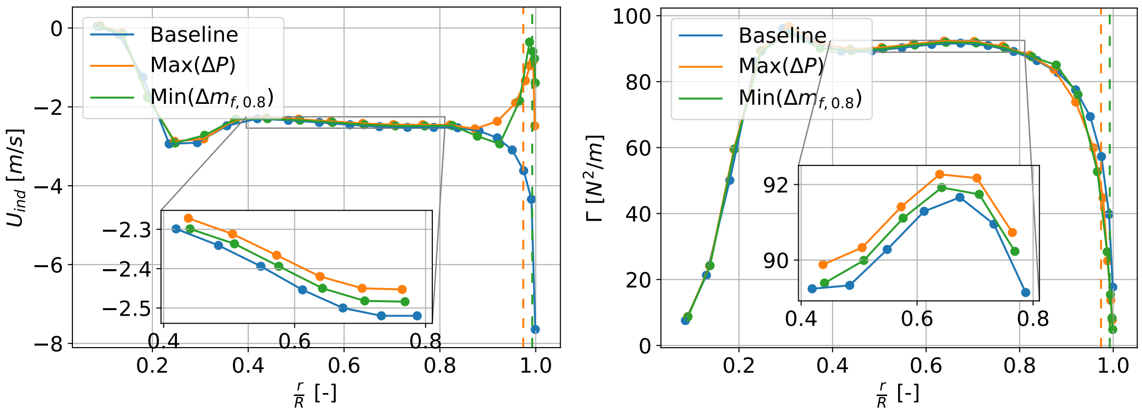

(a) Axial induced velocities

(b) Circulation

Figure 5.30: Circulation and axial induced velocity for the flapwise bending moment at $\frac{r}{R} = 0.8$ minimisation case for a downwind winglet

Both winglets found from this optimisation case do have a reduced bending moment at 80% of the radius, however, as seen from fig. 5.31b shows the bending moment is not reduced at 90% of the radius.

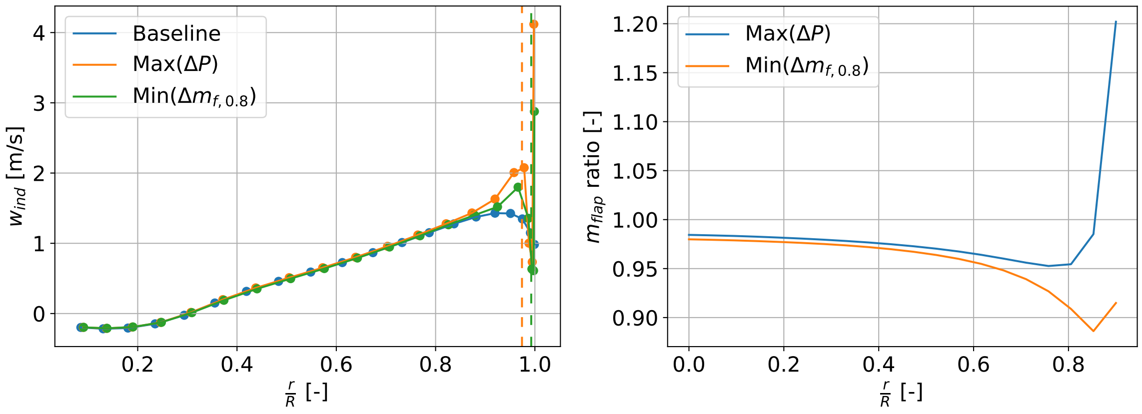

(a) Radial induced velocities

(b) Flapwise bending ratio as a function of radial position

Figure 5.31: Radial induced velocity and flapwise bending ratios for the flapwise bending moment at $\frac{r}{R} = 0.8$ minimisation case for a downwind winglet

At 90% of the blade's radius with variable diameter and fixed sweep
A similar optimisation case is also set up to the research by Zahle et al. [30], where the diameter constraint is removed and thus allows the optimiser to design a tip extension or a winglet. One difference between this optimisation case is that the sweep is not allowed to vary, due to the possible overestimation by AWSM in tangential loads as a result of sweep. Another difference is that the blade used in this research is the DTU10MW RWT and in Zahle's research the IEA 10MW RWT is used. Zahle's research also concerned an upwind winglet, instead of a downwind winglet.
The results are shown in fig. 5.32 and table 5.8.

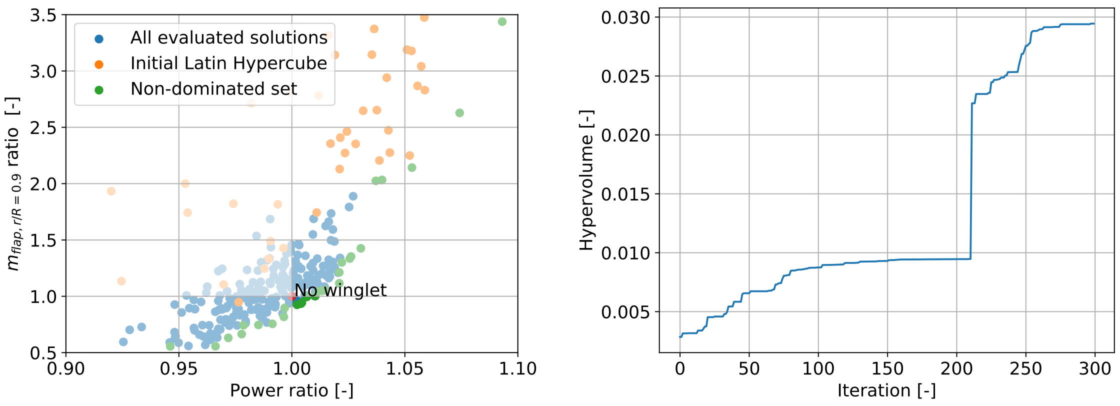

(a) Power versus $m_{f,0.9}$ for all designs

(b) Hypervolume versus iterations

Figure 5.32: Pareto front and hypervolume for downwind winglet optimisation without a diameter constraint

	ΔP [%]	ΔT [%]	$\Delta m_{f,0.9}$ [%]	$\Delta m_{f,r}$ [%]	τ_w [m]	λ [°]	h [m]	ϕ [°]	r_w [m]
Max (ΔP)	1.04	-0.93	0.13	-1.17	0.17	5.0	3.37	90.00	0.1
Min ($\Delta m_{f,0.9}$)	0.23	-1.65	-7.55	-2.08	0.20	5.0	1.94	1.69	0.1

Table 5.8: Improved non-dominated design set for the downwind winglet optimisation case minimising $m_{f,0.9}$ without diameter constraint

The optimiser found winglets to be most effective in increasing the power without increasing the flapwise bending moment at $\frac{r}{R} = 0.9$, as was found by Zahle et al. [30] as well. The winglet achieving the highest power increase, increased the power by 1.04% as seen from table 5.8. Although this design had a small bending moment increase of 0.13%, however, this is deemed an insignificant increase. Zahle et al. [30] did report a winglet increasing the power by 2.6%, which is significantly higher than the winglet found in this optimisation case. However, this is expected to be due to the aforementioned differences with this research, mainly due to not optimising for the sweep. The design most successful in reducing the flapwise bending moment at $\frac{r}{R} = 0.9$, while still increasing the power, was found to be a tip extension with a relatively low chord length. The tip extensions that did not increase $m_{f,0.9}$ compared to the baseline, had a lower ΔP in general.

5.5.2. Upwind winglet

At 90% of the blade's radius with a fixed diameter

A summary of the optimisation parameters and objectives for this optimisation case was shown in table 4.10. The evaluated designs for ΔP and $\Delta m_{f,0.9}$ are shown in fig. 5.33a with the improved non-dominated subset table in table 5.9. For this optimisation case, the improved non-dominated subset consists almost entirely of designs with the minimum cant angle. Interesting to see is that the $Max(\Delta P)$ design of the upwind optimisation case has approximately 0.6% less power than the $Max(\Delta P)$ downwind shown in table 5.6. This could mean some cant angle has a beneficial effect in this optimisation case for the downwind winglet, but not or less for upwind winglets.

However, although not shown in this table, there was a single design found in the improved non-dominated set which was a straight winglet ($\phi = 90°$) with a sweep of approximately $10°$ with a $\Delta P = 1.47\%$ and $\Delta m_{f,0.9} = -21.00\%$, showing that is at least possible to decrease the flapwise bending moment at $\frac{r}{R} = 0.9$ and still improve the turbine's power. However, an optimisation run for an upwind straight winglet would have to be done to see the possible increase in power without increasing the $m_{f,0.9}$.

Furthermore, high sweep angles were preferred in this optimisation case, however not the maximum sweep angles in most designs in the improved non-dominated set.

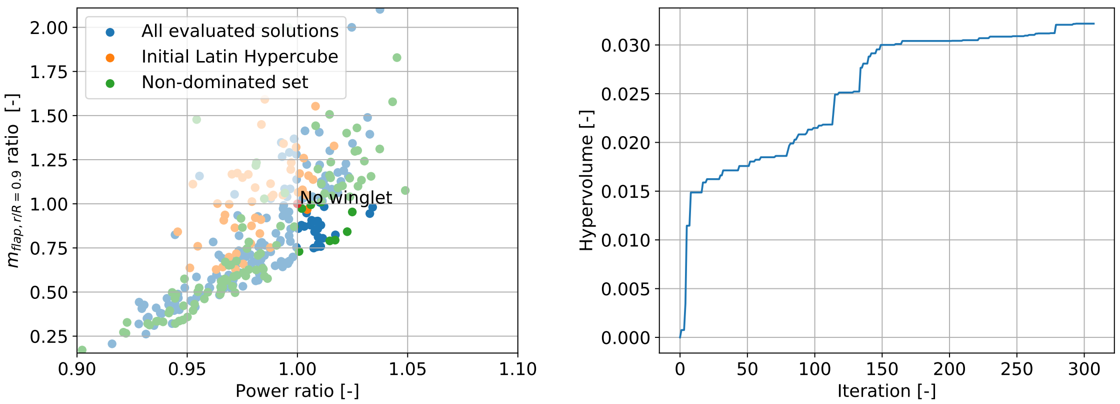

(a) Power versus $m_{f,0.9}$ for all designs

(b) Hypervolume versus iterations

Figure 5.33: Pareto front and hypervolume for flapwise bending moment $\frac{r}{R} = 0.9$ minimisation optimisation case for a upwind winglet

	ΔP [%]	ΔT [%]	$\Delta m_{f,0.9}$ [%]	$\Delta m_{f,r}$ [%]	τ_w [m]	λ [°]	h [m]	ϕ [°]	r_w [m]
Max (ΔP)	3.41	0.06	-1.93	0.42	0.00	49.38	8.00	0.10	0.53
Min ($\Delta m_{f,0.9}$)	0.07	-2.99	-27.02	-3.88	0.17	40.88	7.08	8.29	0.86
Intermediate	1.72	-0.77	-17.60	-0.96	0.01	54.50	5.23	0.10	0.81
μ	1.66	-1.85	-18.31	-2.39	0.24	44.11	7.02	11.50	0.67
σ	1.08	1.78	8.45	2.52	0.56	12.72	0.82	28.06	0.18

Table 5.9: Improved non-dominated set for upwind winglet optimisation for $m_{f,0.9}$ minimisation with diameter constraint

At 80% of the blade's radius with a fixed diameter and fixed sweep
A summary of the objectives and optimisation parameters for this case was shown in table 4.12.
As was found for the downwind winglet as well, the optimiser preferred an upwind winglet to maximise the power while minimising $m_{f,0.8}$. All solutions are shown in fig. 5.34a, with two designs from the improved non-dominated set shown in table 5.10. Slightly more power is actually achieved for the $Max(\Delta P)$ design from the upwind optimisation case, compared to the downwind case. The optimum upwind winglet found has a slightly lower winglet height and lower cant angle than the downwind winglet from the $m_{f,0.8}$ downwind case.
Another difference with the downwind winglet case is that the optimiser found a straight, thin winglet to achieve the greatest decrease in $m_{f,0.8}$ while still increasing the power, while for the downwind optimisation case, a straight tip was found to decrease $m_{f,0.8}$ the most, while still increasing the power.

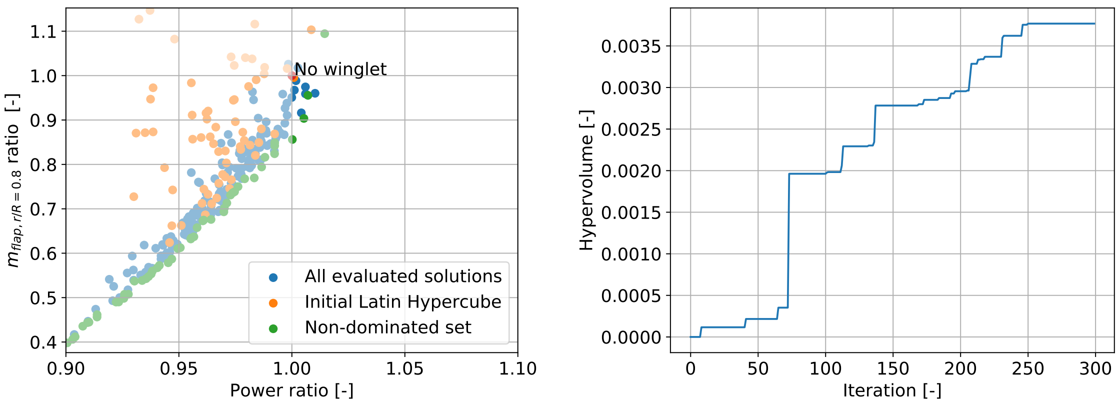

(a) Power versus $m_{f,0.8}$ for all designs

(b) Hypervolume versus iterations

Figure 5.34: Pareto front and hypervolume for for flapwise bending moment $\frac{r}{R}$ = 0.8 minimisation optimisation case for a upwind winglet

	ΔP [%]	ΔT [%]	$\Delta m_{f,0.8}$ [%]	$\Delta m_{f,r}$ [%]	τ_w [m]	λ [°]	h [m]	ϕ [°]	r_w [m]
Max (ΔP)	1.03	-1.35	-3.98	-1.59	0.04	5.0	4.03	80.21	0.32
Min ($\Delta m_{f,0.8}$)	0.02	-3.03	-14.39	-4.00	0.03	5.0	5.94	90.00	0.26

Table 5.10: Improved non-dominated set for an upwind winglet optimisation case for $\frac{r}{R}$ = 0.8 minimisation with a diameter constraint

As shown in fig. 5.35b, the increase in power production stems from the winglet itself for both the $Max(\Delta P)$ and $Min(\Delta m_{f,0.8})$, although lower power production from the winglet is found than was found for the other upwind optimisation cases. The tangential load on the main blade is decreased compared to the baseline design, which is more apparent for the $Max(\Delta P)$ design. This is a result of the lower effective axial velocity as seen in fig. 5.36a and lower circulation as seen in fig. 5.36b.

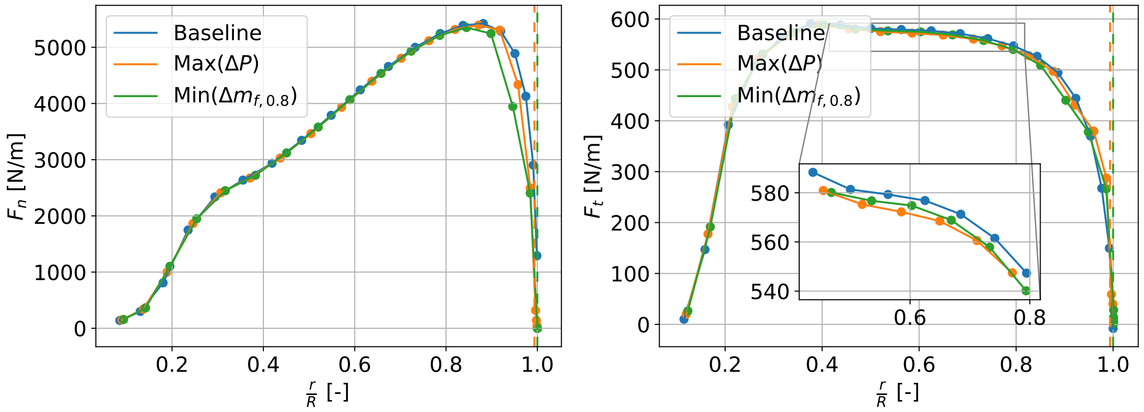

(a) Normal loads

(b) Tangential loads

Figure 5.35: Normal and tangential loads for the flapwise bending moment at $\frac{r}{R}$ = 0.8 minimisation case for an upwind winglet

The radial induced velocity seems to be lower for the $Max(\Delta P)$ case than for the $Min(\Delta m_{f,0.8})$ case as seen in fig. 5.37a, which is somewhat surprising as the power contribution from the $Max(\Delta P)$ is higher. The higher power production is expected to come from the high effective axial velocity as shown in fig. 5.36a, which is expected to result in some tangential loads as the $Max(\Delta P)$ is a not entirely straight winglet.

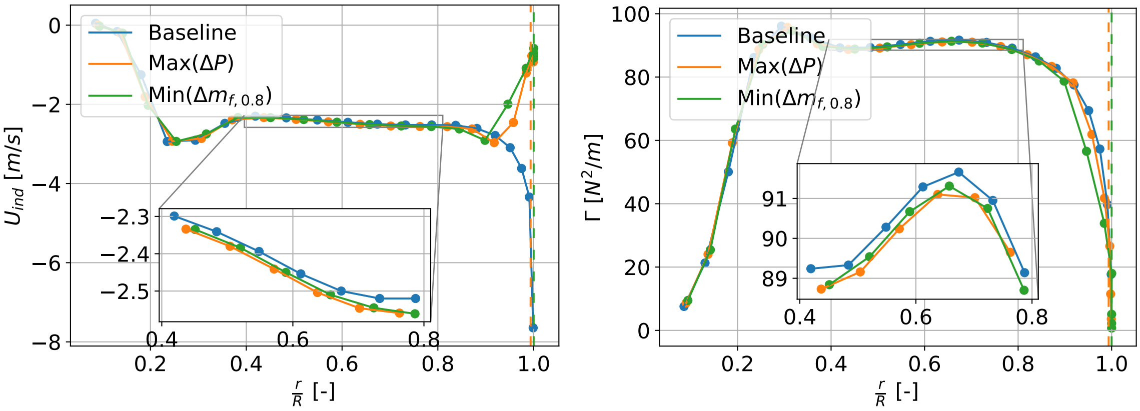

(a) Axial induced velocities

(b) Circulation

Figure 5.36: Circulation and axial induced velocity for the flapwise bending moment at $\frac{r}{R}$ = 0.8 minimisation case for an upwind winglet

As seen from fig. 5.37b, the $Max(\Delta P)$ does have a reduced flapwise bending moment at 80% of the radius but not at 90% of the radius. The $Min(\Delta m_{f,0.8})$ does have a decreased bending moment at 90% of the radius.

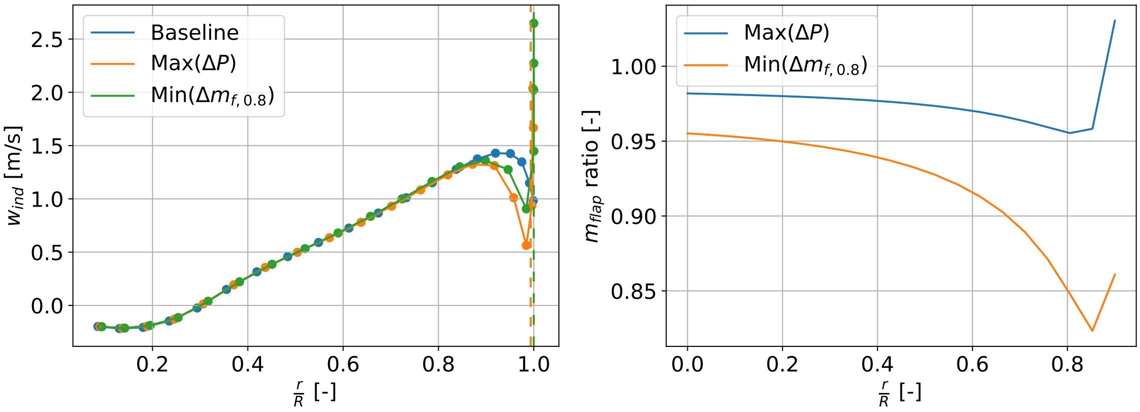

(a) Radial induced velocities

(b) Flapwise bending moments as function of radial position

Figure 5.37: Radial induced velocity and flapwise bending moment ratios for the flapwise bending moment at $\frac{r}{R}$ = 0.8 minimisation case for an upwind winglet

5.6. Synthesis

The results from the optimisation cases have been presented in this chapter. It was found that a winglet with a diameter constraint was not the most effective design to increase the power of the rotor without exceeding the flapwise bending moment at $\frac{r}{R} = 0.9$, however, a winglet was shown the be a more effective design than a straight tip to improve the power when the flapwise bending moment constraint was set to $\frac{r}{R} = 0.8$. Constraining the flapwise bending moment at $\frac{r}{R} = 0.8$ also resulted in the highest cant angles found by the optimiser, both for upwind and downwind winglet. Although this was more apparent for the upwind winglet, which was also able to increase the power more without exceeding the flapwise bending moment at $\frac{r}{R} = 0.8$. The winglets that were found from the $m_{f,0.8}$ minimisation optimisation case also had a decrease root flapwise bending moment and a decreased thrust.

6

Surrogate modelling

Even when using a fitting function for the power and thrust, a single aerodynamic simulation run takes around 300 seconds, with many optimisation cases, it can therefore be very expensive to evaluate a high number of designs. An approach to solve this issue is to create a simpler surrogate model which is optimised instead. A surrogate model must be able to accurately predict and provide a robust uncertainty estimation of the outputs of the aerodynamic analysis tool, such as the C_P or flapwise bending moment, with the given inputs, such as the winglet cant angle or location of the chord control points.

This chapter will explain the working of surrogate models used for optimisation. The data considered in this work is regression data, where the models should be able to predict the value of outputs such as the C_P or C_T. During optimisation, all data is used as training data for the models. In this section, however, data will be split into training and test data to evaluate the performance of the models on unknown data.

The three surrogate models that are investigated are Gaussian Processes in section 6.1, Random Forest in section 6.2 and Bayesian Artificial Neural Networks in section 6.3. Each surrogate model will be tested on its performance to predict values of the objectives of a chosen sample set in section 6.4. The surrogate models will also be compared in their performance during the optimisation process in their ability to find the Pareto front for a given optimisation problem in section 6.5. It should be noted that these machine learning models are very sensitive to hyperparameter tuning, where hyperparameters are the parameters that used to control the learning process. Some hyperparameter tuning will be performed in this work, however, it is not guaranteed that the most optimum parameters will be found.

6.1. Gaussian Processes

A GP is based on a Gaussian distribution, as the name suggests. As explained by Citi [77] the normal distribution can be generalised to a multivariate Gaussian distribution, which is a distribution of n-dimensional vectors ($x = \begin{bmatrix} x_1 & x_2 & \cdots & x_n \end{bmatrix}^T$). In GPs this multivariate Gaussian distribution is used, where the variable are distributed normally with a Gaussian joint distribution. This multivariate Gaussian distribution has a mean vector and covariance matrix, where the mean vector describes the mean of each corresponding dimension. The covariance matrix determines the variance along each direction in the n-dimensional space and how variables are correlated.

Two operations used in GPs are conditioning and marginalisation. With conditioning, one can determine the probability of one variable depending on another variable in a multivariate Gaussian distribution. Marginalisation is used to extract partial information from the distribution by summing over probabilities to get to the desired probabilistic quantity. The resulting distributions from conditioning and marginalisation are also Gaussian. This is a useful property as it means an uncertainty of the predictions made by the model can be obtained. A multivariate Gaussian distribution has a finite number of dimensions however, for a GP the covariance matrix mentioned before, is replaced by a kernel function and the mean is usually replaced by a zero vector. This is done so it is possible to use continuous values.

The choice of a Kernel function is an important choice for the GP, where, for example, Stock-Williams et al. [3] used the Matern 5/2 ARD kernel function from the Python package GPyOpt [78]. In this work, different kernel function are tested. The mean function, however, is set to zero and it is assumed that the output has no noise.

To test a GP, a set of samples is generated using LHC. These samples are separated into a training set and test set. Firstly, the GP is trained on the training set, where the GP has access to both the inputs and output to the model, X_{train} and y_{train}. After training is completed, the model is tested on the input variables from the testing set, X_{test} and is compared to the actual values y_{test}. In the beginning, the samples are randomly shuffled so the samples belonging to the train or test set differ every time. The root mean squared error (RMSE) is used as a performance measurement of how well the optimiser performs overall on a test set. The RMSE is chosen as the RMSE penalises high deviations from the actual value more. It is desired to use a model that predicts the overall trend of the data well, not exactly predict the value of one objective. The definition of the RMSE is shown in eq. (6.1).

$$RMSE = \sqrt{\frac{\sum_{i=1}^{N} (\text{ Predicted }_i - \text{ Actual }_i)^2}{N}} \tag{6.1}$$

6.1.1. Hyperparameter tuning

As for GPs, an important choice is the choice of kernel function, a few kernel functions will be compared here to select the most suited for GPs in this thesis. The kernels chosen to compare are the earlier mentioned Matern 5/2 kernel, the Matern 3/2 kernel, a linear kernel, an RBF kernel and a periodic kernel. All kernels are set with a variance of one and Automatic Relevance Determination (ARD) is used for every kernel, except the periodic kernel, for which ARD is not available.

To train and test the data, a dataset of LHC sampled data with a size of 80 samples is chosen. The input parameters are the $c_{w,t}$, h, ϕ, r_w and chord control points $CP_{2,y}$, $CP_{3,y}$, $CP_{4,y}$ and $CP_{3,x}$. The diameter is constrained in this case. The outputs are the power and thrust ratio, where the power and thrust of a blade design with a winglet are divided by the power and thrust of the baseline DTU10MW blade. Sixty-four samples are used for the training set and the remain sixteen samples for the test set. The model is created ten times where each model is trained with a randomly shuffled test and train set. The model is then tested on the test data for the power and thrust after which the RMSE is calculated. Table 6.1 shows the mean of the RMSE for the ten trained models and their corresponding standard deviation.

	mean($RMSE_P$) [-]	std($RMSE_P$) [-]	mean($RMSE_T$) [-]	std($RMSE_T$) [-]
Matern 5/2	0.0411	0.0226	0.0165	0.0097
Matern 3/2	0.0500	0.0223	0.0211	0.0096
RBF	0.0365	0.0114	0.0252	0.0118
Linear	0.2168	0.0218	0.1851	0.0146
Periodic	0.0553	0.0246	0.0172	0.0084

Table 6.1: RMSE for different kernels investigated. Subscript P indicates the RMSE on the power prediction and subscript T indicates the RMSE on the thrust prediction.

The power is best predicted by the RBF kernel, while the thrust is best predicted by the Matern 5/2 kernel. However, the difference between Matern 5/2 and RBF for power is lower than the difference between Matern 5/2 and RBF for thrust. The Matern 5/2 kernel is therefore chosen to continue with for this thesis.

A perhaps useful visualisation of the GP model is how the model predicts what the effect of certain input parameters is on the output while keeping other inputs constant. The winglet from table 4.1 is chosen as constant parameters, while two input parameters are varied independently. The result of the model's prediction on C_P is plotted in a landscape plot shown in fig. 6.1.

What can be seen from this plot is that, for example, the model predicts a high correlation between ϕ and the y locations of the chord control points. Which makes sense, as a winglet changes the loading on the blade, and therefore requires a change in chord length. Another observation that can be made is that the model predicts a poor performance for a high h and low ϕ, as with the diameter constraint a low cant angle and high height means a part of the blade is replaced with a straight tip. Plots for other objectives can be found in appendix D.

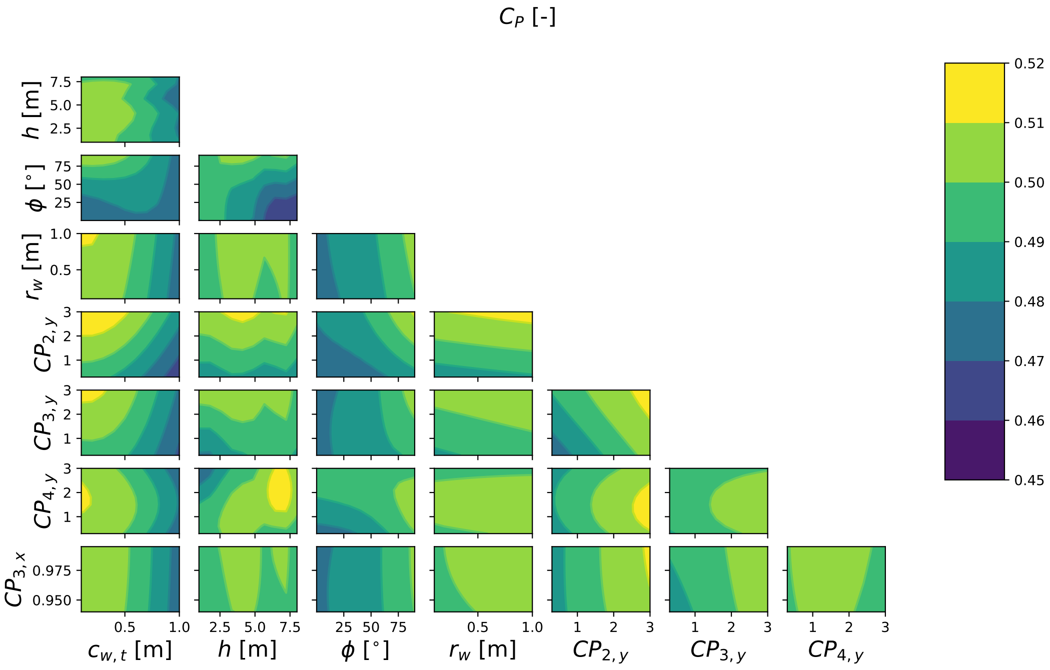

Figure 6.1: Landscape plot for prediction of the GP surrogate model on the C_P of a blade with winglet

6.2. Random Forest

Random Forest operates by constructing several decision trees. It then merges their predictions together to get a accurate and more stable prediction. Each tree in the random forest learns from a random sample from the training set. The number of trees can be controlled with the number of estimators hyperparameter. The RMSE error is calculated in the same manner as for GPs, where ten models are trained and the average RMSE is taken. The RSME is shown for different numbers of estimators in fig. 6.2. Where it is shown that a high number of estimators increases the test error.

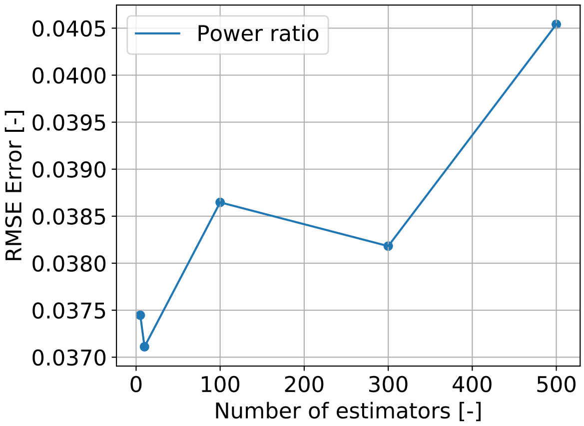

Figure 6.2: Hyperparameter study for different numbers of estimator in the RF

It is quickly observed that RF performs worse than a GP. It is therefore chosen to not spend much time on the theory of RFs and RF will not be used in the comparison of surrogate models for BO in section 6.5. The landscape plot for RF is shown in fig. 6.3.

A similar conclusion can be drawn from the RF landscape plot as was done for the GP landscape plot, where the model predicts a higher C_P for a higher ϕ and predicts an especially low C_P for a low ϕ with high h_w. A difference is that RF predicts virtually no influence of the r_w, where the GP model found

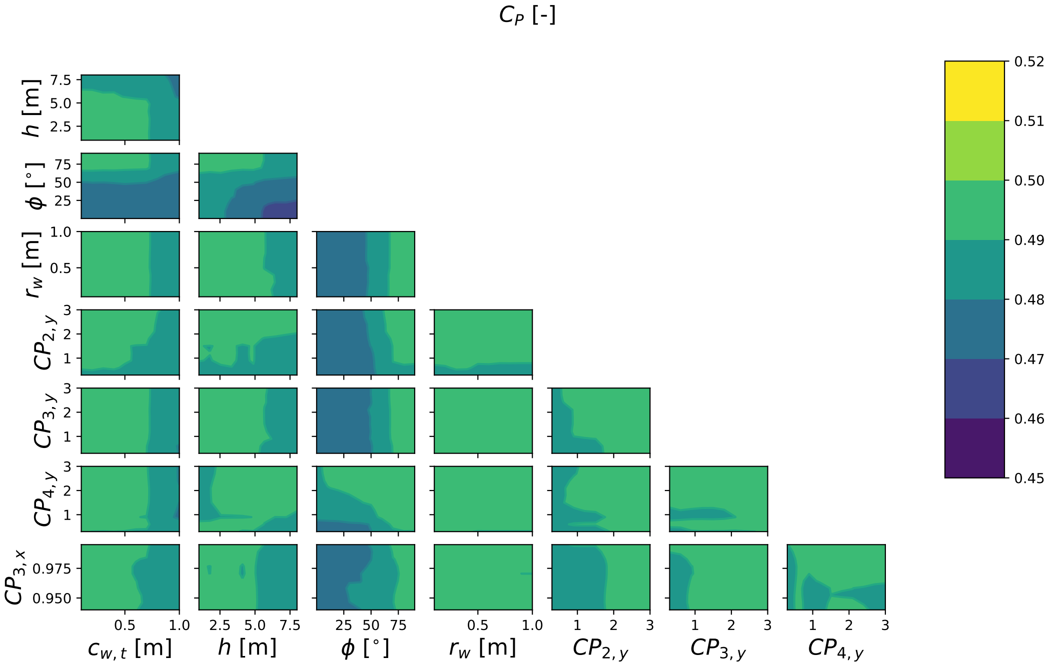

Figure 6.3: Landscape plot for prediction of the RF surrogate model on the C_P of a blade with winglet

some correlation between r_w and ϕ or the chord control points.

6.3. Bayesian Neural Networks

The implementation of a Bayesian Neural Network (BNN) in this work is taken from the package BLiTZ by Esposito [79]. As mentioned before, the standard used neural networks are deterministic, meaning the trainable parameters correspond directly to the weights used on the linear translation of the previous parameter. This can be written in equation form as in eq. (6.2).

$$a^{(i+1)} = W^{(i+1)} \cdot z^{(i)} + b^{(i+1)} \tag{6.2}$$

Where the output of each layer is denoted as a, the weights by W, the output of the previous layer as z and the bias as b for a neural network with i layers.
With BNNs, uncertainty is introduced on the network's layers by sampling the weights from a Gaussian distribution, which is parameterised by trainable variables. To do this, each feed-forward operation the weights and biases are samples with eq. (6.3) and eq. (6.4) respectively.

$$W^{(i)}_{(n)} = \mathcal{N}(0,1) * \log\left(1+\sigma^{(i)}\right) + \mu^{(i)} \tag{6.3}$$

$$b^{(i)}_{(n)} = \mathcal{N}(0,1) * \log\left(1+\sigma^{(i)}\right) + \mu^{(i)} \tag{6.4}$$

Where σ is the standard deviation and μ is the mean for each sample's linear transformation parameter. These trainable weights and biases can be optimised as well, which is used to minimise the variance of the predictions. This is done by minimising the loss of the predictions. The loss for a deterministic neural network is usually the residual sum of squares. This loss will be termed the fitting-to-data-cost. In BNN's another loss is added, called the complexity cost. The complexity cost is the sum of the probability density function of the sampled weights for each hidden layer. This way the variance of the network is minimised. To calculate this loss, the Kullback-Leibler Divergence function is used as proposed by Blundell et al. [80].

6.3.1. Hyperparameter tuning

Neural networks have a high amount of hyperparameters that can be tuned. Moreover, neural networks are, similarly to GPs, prone to overfitting. Overfitting is when a model fits well to the training set, but does not generalise to unknown data, or the test set. There are a few techniques that prevent overfitting, with the most straightforward one being early stopping, where the training is stopped at a certain point where the test error is minimum.
A hyperparameter study can be difficult to perform, as the hyperparameters often have a high correlation. The hyperparameters are therefore often tuned with Bayesian Optimisation. However, this will not be done for this work and the parameters will be varied independently, under the assumption that the correlation between the hyperparameters is small enough to show some insight into the effect of these hyperparameters. The hyperparameter that is expected to be quite correlated with the other hyperparameters, is the number of iterations done by the model during training. The results that are shown will therefore be plotted as a function of the number of iterations. As the result is dependent on how the test and training data are shuffled, the average of 10 runs is plotted for the hyperparameter analysis. The RMSE error shown in the plots is averaged over ten iterations, to avoid fluctuating plots.

Optimiser

Optimisers in NNs will try to update the weights of the neural network, which is done through backpropagation. Backpropagation is used to compute the gradient of weight space of the neural network, by simply using the chain rule. This is done by minimising the fitting-to-data cost. The effect of the optimiser for the complexity cost function is not investigated here. The default optimiser used in NNs is Stochastic Gradient Descent (SGD), which randomly picks a different point each iteration from the data, after which it computes the gradient to move in the direction of the minimum. SGD is compared against Adam from Kingma and Ba [81]. Adam is an optimiser which is an extension on SGD, which main advantages are that it maintains per-parameter learning rates and has few hyperparameters to tune. The test and training error is shown in fig. 6.4a. The testing error is the value that should be minimum, as it gives an indication of how well the optimiser performs on unknown data. It can be seen that the RMSE testing error is lower for Adam, so Adam will be chosen as an optimiser to minimise the fitting-to-data-cost function. What can also be seen from fig. 6.4a, that the test error start to increase after 200 iterations. The training will therefore be stopped at this number of iterations from here on.

Hidden layers

In section 6.4 some research in wind energy applications is discussed where neural networks are used. Some research reported improved results by using deep learning, where deep learning is simply a NN with more than one hidden layer. A NN with one hidden layer termed not deep is compared with a NN with two hidden layers, termed deep. The result of the training and test error is shown in fig. 6.4b. A lower test error is achieved with a deep NN. Therefore, a network architecture with two hidden layers is chosen. More layers than two have not been attempted.

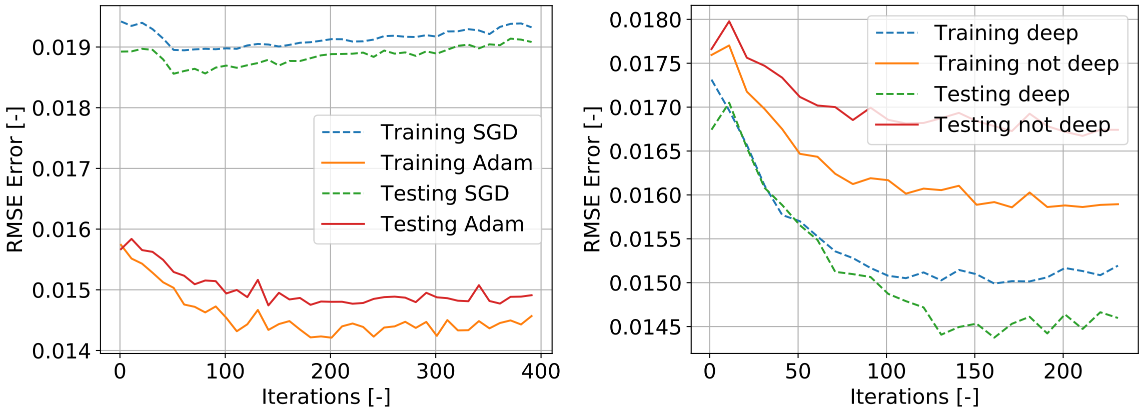

(a)

(b) two hidden-layer NN versus one hidden-layer NN

Figure 6.4: Hyperparameter study for difference fitting-to-data optimisers and different numbers of hidden layers

Features

The number of features is the number of neurons per hidden layer in the NN, which has a weight vector containing the weights of the connections between itself and the neurons it is connected to, an input and an activation function. The activation function is chosen the be ReLU in this work. The number of neurons per layer can be varied. More features potentially allow the model to learn more complicated functions, however, it might also cause overfitting when too many features are used on a simpler function. The number of features per layer tried is 128, 256, 512 and 1024. The test errors are shown in fig. 6.5a. It can be seen that the lowest test error is obtained for 256 features. Showing that more features is not always better and has likely caused the model to overfit.

Batch size

It is possible to supply a NN with multiple samples of inputs, called a batch, at the same time after which the NN outputs an output batch. An advantage of supplying the NN with a batch is the decreased training time of the NN. Training can therefore be much faster. A lower test error can also be obtained using batches. Figure 6.5b shows the test error for different batch sizes, where it can be seen that the error is lowest for a batch size of 64. The number of iterations is also lower as fewer iterations are done with lower batch size. A higher number for the batch size is not attempted as the initial sample size can be around 64 for some optimisation cases. Batch normalisation is applied as an improved performance was found by Ioffe and Szegedy [82].

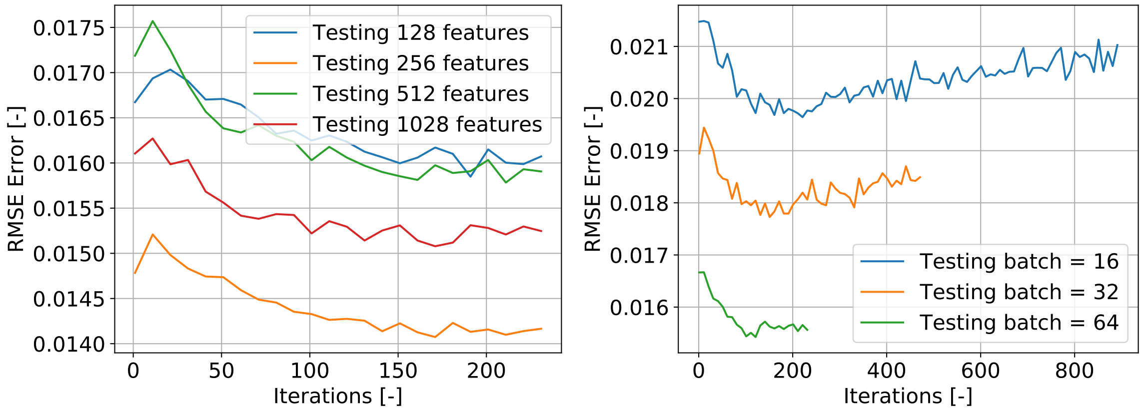

(a) Varying the number of features in the NN architecture

(b) Different training batch sizes

Figure 6.5: Hyperparameter study for different number of features in the NN architecture and different number of batch sizes used for training

Dropout

Dropout, by Hinton et al. [83], will dropout certain random weights in the network making the probability that the network will overfit a certain dataset smaller. Dropout, therefore, serves to decrease the test error, by preventing overfitting. Dropout is only applied during training. When testing the model, dropout is turned off. For this network architecture, dropout is only applied after the last layer of the network architecture. As can be seen from fig. 6.6a, the training error is higher when using dropout, however, the error on the unknown test set is lower, as is desired. Therefore dropout will be used in the architecture of the NN.

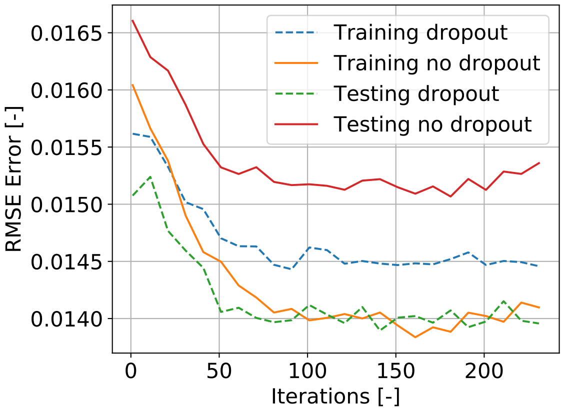

(a) Hyperparameter study with and without dropout for training

Figure 6.6: Hyperparameter study for dropout

A summary of the chosen hyperparameters is shown in table 6.2. An advantage of a NN is that its computation can be sped up by a computer's graphics processing unit (GPU), this is useful when a large number of computations need to be done simultaneously. NN can therefore be quickly trained with batches of samples as mentioned before. Another advantage is that a NN can have multiple outputs without the need to train another NN for different objectives.

Optimiser	Adam
Hidden layers	2
Features	256
Batch size	64
Dropout	Yes
Activation function	ReLU
Batch normalisation	Yes

Table 6.2: Summary of hyperparameters chosen for

The landscape plot for the BNN is shown in fig. 6.7, where it quickly can be seen that it is more difficult to draw conclusions from this plot than it was for the GP or RF models. The landscape from a NN does not show a clear correlation between different input variables and it is expected that it would be difficult for a gradient optimiser to find an optimum in this output space, as no clear peak in C_P can be found in any of the subplots for varying inputs.

6.4. Comparison of surrogate models for objective prediction

An example of a test of how well each model predicts the power and thrust is seen in fig. 6.8, where the power and thrust are shown as a ratio compared to the baseline DTU10MW power and thrust. It should be noted that this is only an example of how the model predicts the values from y_{test}, this analysis should be performed multiple times, from which a mean can be taken, which can say something about the ability of the model to predict unknown data.

Such an analysis is done in table 6.3. Where it can be seen that the lowest RMSE error is indeed obtained by the GP. The BNN's RMSE error is higher than the GP error, but still relatively low compared to the RF.

The GP seems to perform the best in predicting the values of objectives. This analysis only covers the predicted values by the surrogate models, however, the surrogate models also provide an uncertainty estimate for the predicted values. The quality of this uncertainty estimation is important for the EHVI acquisition function. It might be the case that the BNN outperforms the GP at estimating uncertainty, however, this is not quantified in this thesis. It was found that the uncertainty standard deviations predicted by the BNN were all lower than what was found by the GP.

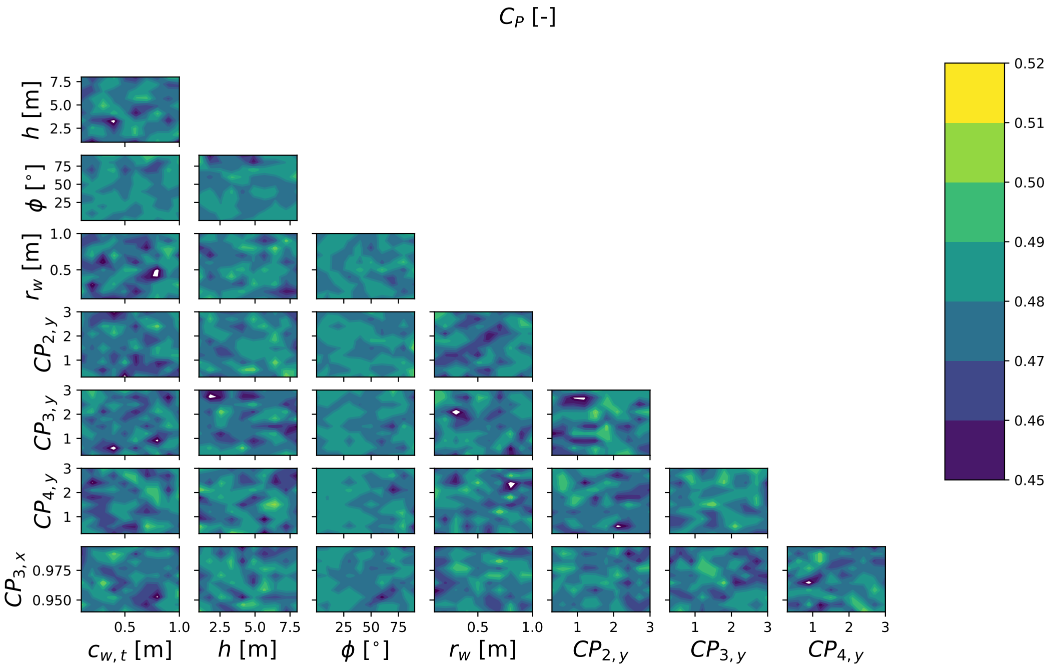

Figure 6.7: Landscape plot for prediction of the BNN surrogate model on the C_P of a blade with winglet

	$RMSE_P$	$RMSE_T$
GP	0.006 +- 0.0023	0.005 +- 0.0014
RF	0.025 +- 0.0051	0.035 +- 0.0045
BNN	0.015 +- 0.0045	0.019 +- 0.0041

Table 6.3: Average RMSE error and standard deviation of the RMSE for ten model optimisation runs

6.5. Comparison of surrogate models for Bayesian Optimisation

For comparison on the actual optimisation done in this thesis, three cases were tried. The first being a case with the HyPI scalarising function and a GP surrogate model. The second being a case with a multi-surrogate approach using a GP as the surrogate model and EHVI as the acquisition function. The third also using EHVI as the acquisition function, but a BNN as the surrogate model. A single surrogate model is only needed, however, as a BNN can have multiple outputs.

There is one more modification made to the third case, however. By default, the optimisation of the acquisition function was done using a gradient optimiser, which calculates the gradient for one sample, after which it evaluates another sample to get to the optimum step-by-step. A NN, however, is relatively slow when only evaluating one sample, but fast when evaluating a large batch of samples. Instead of optimising the acquisition function, a large number of random points close to other non-dominated solutions is generated for which all points their performance is estimated by the NN. The number of random points is chosen to be one thousand. The process of generating these points, evaluating them, and calculating the EHVI of each point, takes approximately the same time as optimising the acquisition function for ten points using a gradient optimiser and GPs. Another reason to choose this option is that a gradient optimiser is expected to not perform well on finding the optimum of the NN as was shown in fig. 6.7.

The three cases are run on a downwind winglet optimisation with C_P as maximisation objective and the flapwise bending moment at $\frac{r}{R} = 0.8$ as minimisation objective, where the design parameter were summarised in table 4.12. The results for the hypervolume per iteration is shown in fig. 6.9b. It can be seen that the hypervolume of the BNN case increase the fastest and is able to reach the highest

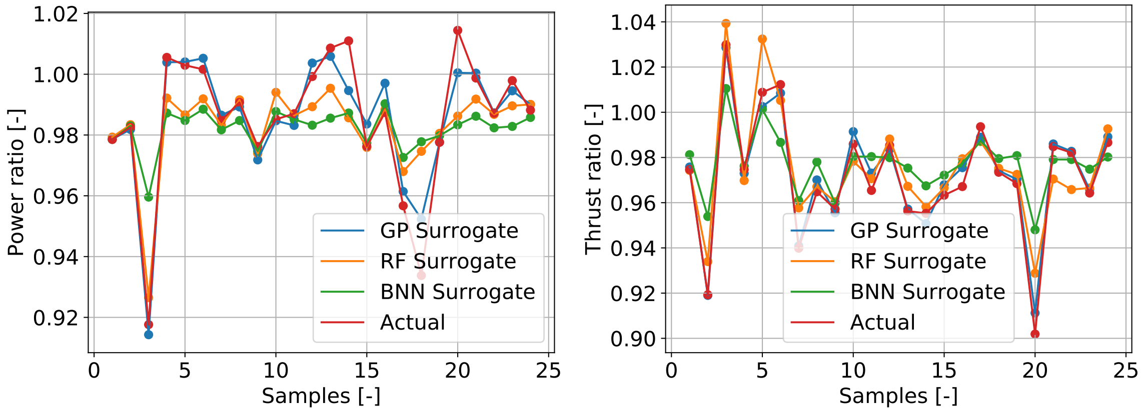

(a) $RSME_{GP}$ = 0.007, $RSME_{RF}$ = 0.026, $RSME_{BNN}$ = 0.018

(b) $RSME_{GP}$ = 0.004, $RSME_{RF}$ = 0.036, $RSME_{BNN}$ = 0.016

Figure 6.8: Example of predictions of the power ratio and the thrust ratio from different surrogate models. This figure serves illustrative purposes and no conclusions should be drawn from it.

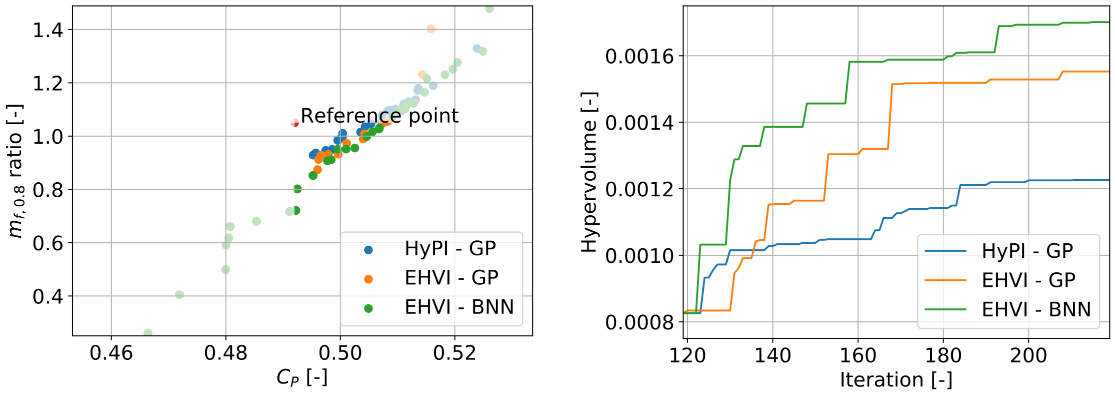

(a) C_P versus $m_{f,0.8}$ for non-dominated designs found by the objective function for all three optimisation cases

(b) Hypervolume versus iterations for the three different optimisation cases from this section

Figure 6.9: Analysis for different combinations of surrogate models and acquisition functions for which the found solutions and hypervolume as a function of iterations is shown

hypervolume. With the HyPI case reaching the lowest hypervolume. The BNN case also seems to outperform the other cases in finding the non-dominated solution as shown in fig. 6.9a, where only non-dominated designs are shown found from the three different optimisation cases explained in this section. The time needed to complete one iteration is shown in fig. 6.10a for each case, showing the shortest time for HyPI and a similar time for the GP and BNN in combination with EHVI.

The optimiser was able to find winglets with higher power that did not exceed the $m_{f,0.8}$ constraint. One of the winglet designs found has a $\Delta P = 1.64\%$ and $\Delta m_{f,0.8} = 0.996$, which is a significant increase for the downwind $m_{f,0.8}$ minimisation case. This winglet is, however, not included into the discussion as the upwind winglet is not optimised with the same optimisation technique, leading to an unfair comparison.

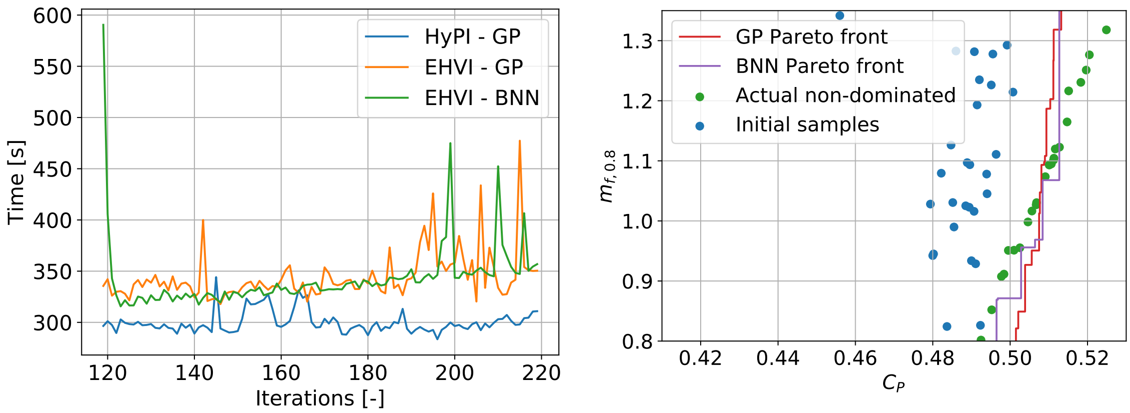

(a) Time it took to complete one iteration of the optimisation process for different combinations of surrogate models and acquisition functions

(b) Predicted Pareto front comparison. The actual designs are the actual C_P and $m_{f,0.8}$ given by the objective function where the Pareto fronts shown are the predicted Pareto fronts by the GP and BNN.

Figure 6.10: Time needed per iteration of the objective function and optimisation process and predicted Pareto fronts for surrogate models

The predicted Pareto fronts by a GP and BNN are shown in fig. 6.10b. This figure is made by training a GP and BNN on an initial sample set, with a size of 64 samples, created with LHC. The trained model is then tested on a high number of randomly generated test samples for which the model predicts the C_P and $m_{f,0.8}$ of each test sample. Only the non-dominated predictions are then taken and plotted in a line in fig. 6.10b. The predicted Pareto fronts by the models are compared with the actual non-dominated solutions found by the optimiser after optimisation has taken place with these initial samples. This optimisation was done with the BNN surrogate model, however, so it is unsurprising the BNN predicts the actual non-dominated designs more accurately in this case. It can be seen that the predictions by the BNN and GP are quite similar around $m_{f,0.8} = 1$, however, the GP predicts higher C_P for designs with lower $m_{f,0.8}$, while the BNN predicts higher C_P for a higher $m_{f,0.8}$ compared to the GP.

6.6. Synthesis

As seen from this chapter, GPs are performing better at predicting the objectives for this optimisation problem. However, optimisation using the BNN surrogate model led to a faster increase of the hypervolume. Significantly better performing winglets were found as well. The suspected reason for this increase is the change in acquisition function, where now a random search method is used, which can be performed in a short amount of time by a NN. To confirm this, the same methods should be used for the GP model, however, this has not been done in this thesis.

Another possible reason, which has not been discussed in this thesis, could be a more robust uncertainty prediction by the BNN. The BNN is trained to reduce the variance over the predictions as much as possible, which could lead to a better estimation of the EHVI, where a somewhat better estimation of the hypervolume was indeed obtained by the BNN as was shown in fig. 6.10b.

7

Discussion

This chapter will discuss the findings from this thesis and perform a more detailed analysis of those findings. Firstly, the effect of the winglet sweep on the winglet's power production is discussed in fig. 7.1. Secondly, the effect of the different objectives, such as power, thrust and bending moments as well as the effect of the diameter constraint will be discussed in section 7.2.1. Thirdly, the effect of upwind winglets or downwind winglets will be elaborated on in section 7.3. Finally, an optimum downwind and an optimum upwind winglet design will be analysed on different wind speeds in section 7.4.

7.1. The effect of winglet sweep

As seen for most optimisation cases, the optimiser found designs with more power production by sweeping winglets, usually downstream with positive sweep, but also sometimes upstream with a negative sweep. This section will attempt to explain why the optimiser prefers to sweep the winglet upstream or downstream.

The Munk [11] stagger theorem states that any system is equivalent to a simpler system having the same frontal view, in terms of total induced drag. Meaning that for a wing where the projected circulation stays constant, a swept wing with the same frontal view, from the freestream's perspective, should have the same lift and induced drag. Munk's stagger theorem is derived for the non-rotating case, so it does not necessarily hold for the rotating case, meaning C_P and C_T should not necessarily be the same with or without sweep.

There seems to be no clear consensus yet whether sweep on winglet has a beneficial effect for wind turbine winglet. Johansen and Sørensen [27] reported no positive effect using downstream sweep on winglets for wind turbines. Ferrer and Munduate [28] did notice a positive effect of sweeping a straight blade downstream. Also, Zahle et al. [30] noted a positive effect of sweeping a downwind winglet downstream. No explanation was found why.

7.1.1. Influence of sweep for a non-optimised winglet

To investigate the positive effect of sweep on the winglet, a straight winglet ($\phi = 90°$) is considered, with a prescribed polar to operate at the same maximum C_L C_D. The performance of this winglet is investigated for different angles of sweep. With the prescribed polars the circulation on the blade and winglet should stay approximately the same. The winglet height is changed in this analysis to keep the projected shape of the winglet the same on a plane perpendicular to the freestream. Meaning length a stays the same in fig. 4.5b. This length a has been set to a constant of $5m$. The relative integrated C_P and C_T compared to the zero sweep case, is shown in fig. 7.1.

As already found from some optimisation cases in chapter 5, downstream sweep does have a positive effect on the C_P of both downwind and upwind winglets. The C_T remains relatively unaffected in general, where some increase for C_T is seen for sweeping the winglet upstream. Something also seen in the optimisation cases is that upstream sweep has a negative effect on the downwind winglet, but a positive effect on the upwind winglet, however, the benefit from upstream sweep seems slightly less than for downstream sweep for the upwind winglet.

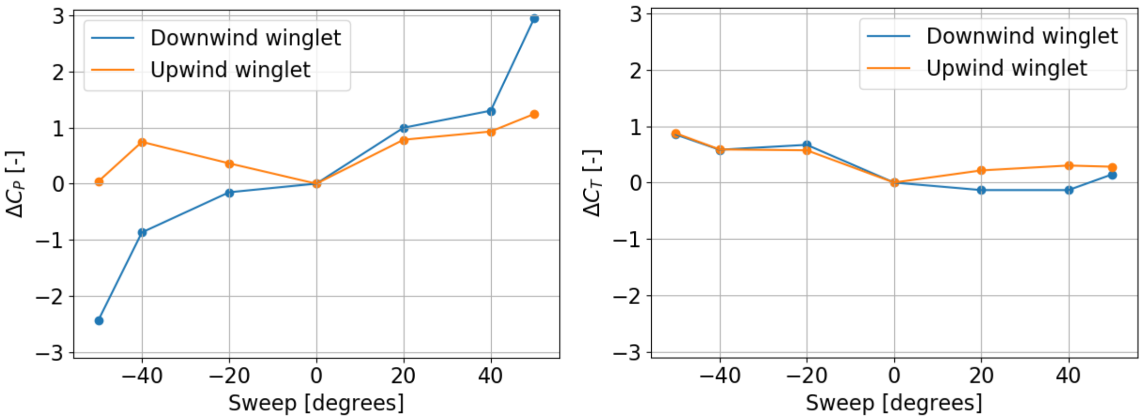

(a) Relative C_P compared to an unswept winglet

(b) Relative C_T compared to an unswept winglet

Figure 7.1: Non-optimised winglet's relative power and thrust with for different sweep angles compared to a zero sweep angle. The upwind winglet with zero sweep has $C_P = 0.508$ and $C_T = 0.821$. The downwind winglet with zero sweep has a $C_P = 0.512$ and $C_T = 0.839$.

7.1.2. Influence of sweep for an optimised winglet

In terms of performance, conclusions from the winglets in the analysis in fig. 7.1 cannot necessarily be taken, as all these designs were not optimised, so might not have an optimum loading. However, the results from fig. 7.1 seem to agree with the results the optimiser found in chapter 5. To make sure the performance gain actually comes from the sweep, both an unswept and swept, straight, downwind winglet are optimised for the chord with a predefined polar. The winglets are optimised for maximum power and minimum flapwise bending moment at $\frac{r}{R} = 0.8$. The integrated C_P and the $m_{f,0.8}$ are shown in table 7.1. $m_{f,0.8}$ is chosen as minimisation objective here as the objective was found to be the most beneficial for a winglet design as argued in chapter 5.
The designs shown here are the designs with non-increased $\Delta m_{f,0.8}$ and maximum power.

	C_P	$m_{f,0.8}$
$\lambda = 0°$	0.494	0.973
$\lambda = 40°$	0.505	0.998

Table 7.1: Swept and unswept downwind winglet with maximum C_P for chord using 110 iterations, for which the convergence criteria was met for both optimisation cases. Only designs with a lower $m_{f,0.8}$ than the baseline design are considered.

The optimiser was not able to improve the designs' power as both designs have a lower C_P than the non-optimised winglets, however, they have no increase in $m_{f,0.8}$. It can be seen that also between the optimised winglets there is an increase of 2.64% in power between the swept winglet compared to the unswept winglet, which is a higher increase found than for the non-optimised winglet as shown in fig. 7.1. So it is found for this analysis that the power increase due to the sweep is also the case for a load optimised design.

7.1.3. A possible explanation for the power increase from sweep

This subsection will attempt to explain a possible reason for the increase in power when using a swept winglet. Firstly, this will be explained for a downwind winglet. Secondly, the differences for the upwind winglet will be explained.

Downwind winglet

To investigate what the cause is for the increase in power using winglet sweep, firstly the tangential and normal loads are plotted in fig. 7.2. Which are the non-optimised $\lambda = 0$ and $\lambda = 40$ case from fig. 7.1. As seen from fig. 7.2b, the increase in power comes from the increase in tangential forces on the winglet. There seems to be no change in tangential forces on the blade itself, except for a relatively small decrease on the blade close to the winglet ($0.9 < \frac{r}{R} < 0.95$). As seen from fig. 7.2a there is also

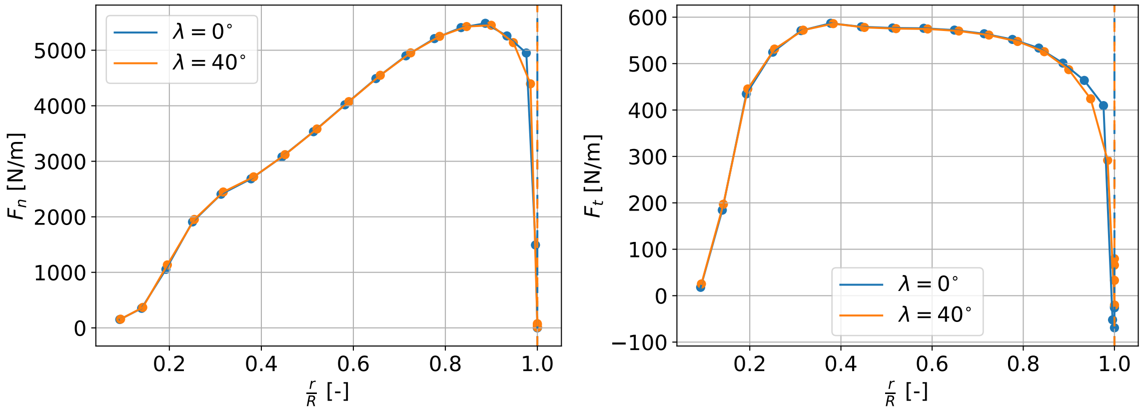

(a) Normal loads

(b) Tangential loads

Figure 7.2: Normal and tangential load for a downwind winglet with $\phi = 90°$ with winglet starting from $r = 83m$

a small increase in normal forces on the winglet with a small decrease in normal forces on the blade close to winglet, leading to no significant change in integrated C_T as seen in fig. 7.1.

The $\frac{C_L}{C_D}$ and circulation are shown in fig. 7.3. Both designs have the same $\frac{C_L}{C_D}$ as seen from fig. 7.3a, which is no surprise as predefined polars are used. As seen from fig. 7.3b, the circulation is virtually the same as well for the two designs, also on the winglet. So the frontal view and circulations are practically the same as required for Munk's stagger theorem. It should be noted that this is an attempt to transfer Munk's stagger theorem to the rotating case without having a justified theoretical foundation for doing so, as Munk's stagger theorem is derived for the non-rotating case. However, showing the circulation and lift-over-drag are equal for the two cases does show that this is not the reason for the difference in power production between the two cases.

The axial induced velocity for both designs can be seen in fig. 7.4a. As expected there are no large

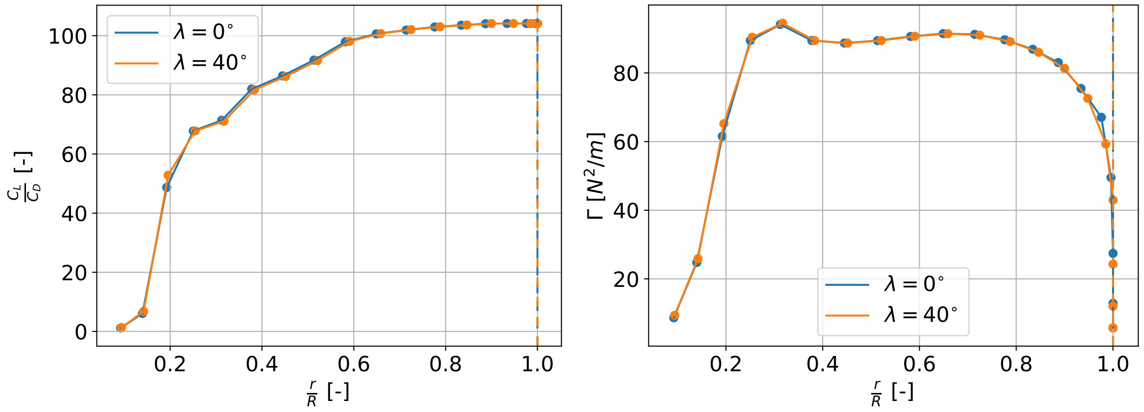

(a) Lift over drag

(b) Circulation

Figure 7.3: Lift over drag and circulation for no sweep and high winglet sweep, which are found to be approximately the same

differences on the blade itself, as the tangential loads are mostly the same on the blade. There is a small difference on the winglet, however, this does not affect the tangential forces much. The difference in tangential loads on the winglet is expected to come from the difference in radial induced velocity shown in fig. 7.4b. With relatively high negative induced radial velocity for the high sweep design compared to the zero sweep design. The larger the winglet's sweep angle, the larger the negative radial velocity, as is seen in fig. 7.5b for increasing sweep angle.

To investigate where this change in radial velocity comes from, an external velocity field analysis is done in AWSM, which gives the induced velocity in x, y and z at chosen locations. From this, the

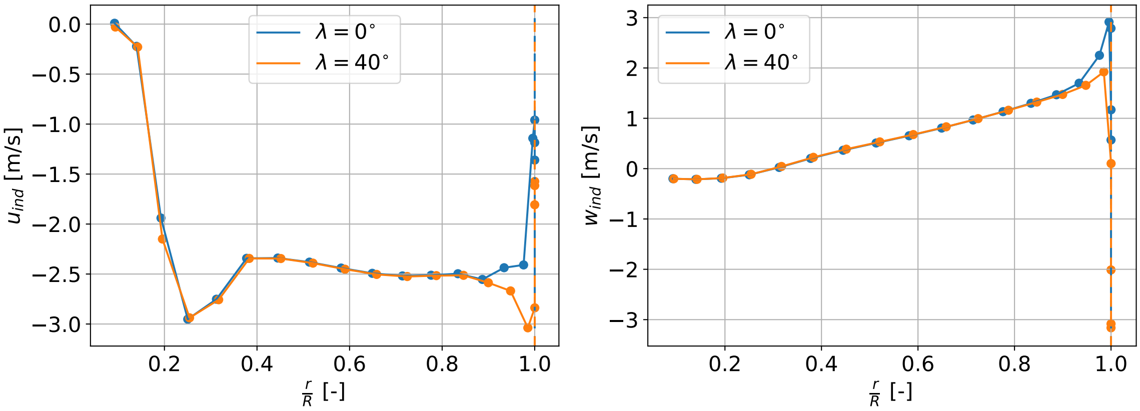

(a) Axial induced velocities

(b) Radial induced velocities

Figure 7.4: Axial and radial induced winglet for the different winglet sweeps

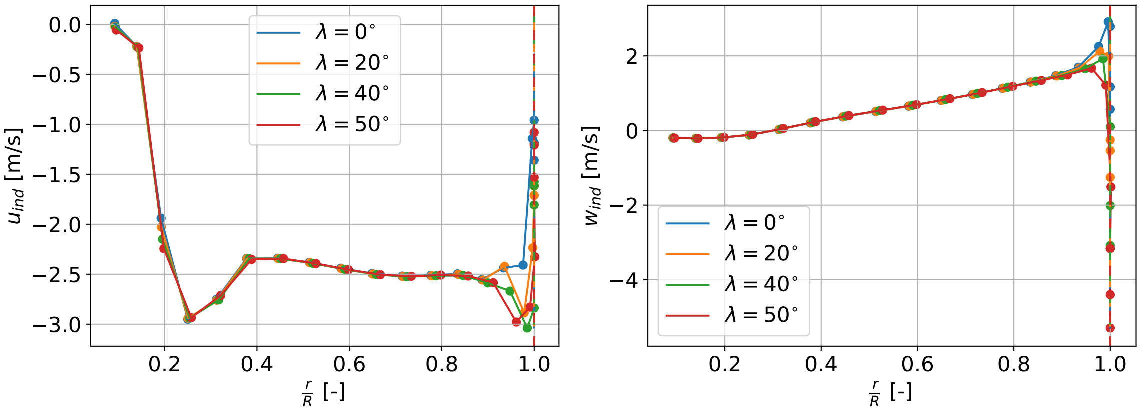

(a) Induced axial velocities

(b) Induced radial velocities

Figure 7.5: Induced axial and radial velocities on the blade for different sweep angles for designs shown in fig. 7.1

radial induced velocity can be calculated. This is done for various locations upwind and downwind of the blade. Shown in fig. 7.6a is the radial velocity field for $7.5m$ downwind of the rotor for the baseline DTU10MW design, without winglet. It can be seen that there is an area downstream of the rotor where there is a more negative (inward) radial induced velocity component. As this radial induced velocity results in tangential loads on the winglet, leading to increased power, it is expected that the optimiser wants to sweep the winglet in this area of inward induced radial velocity.

When the blade and winglet design is changed, this could lead to a change in the external velocity field behind the rotor. The external field is therefore analysed again for the winglet with $\lambda = 40°$ and shown in fig. 7.6b. The absolute difference in radial induced velocity between the two external fields are plotted in fig. 7.7. It can be seen that the external radial induced velocity does slightly change, however, there is no large change ($< 1m/s$) at the location close to the winglet. It is expected that this is the reason the optimiser prefers downstream sweep for downwind winglets.

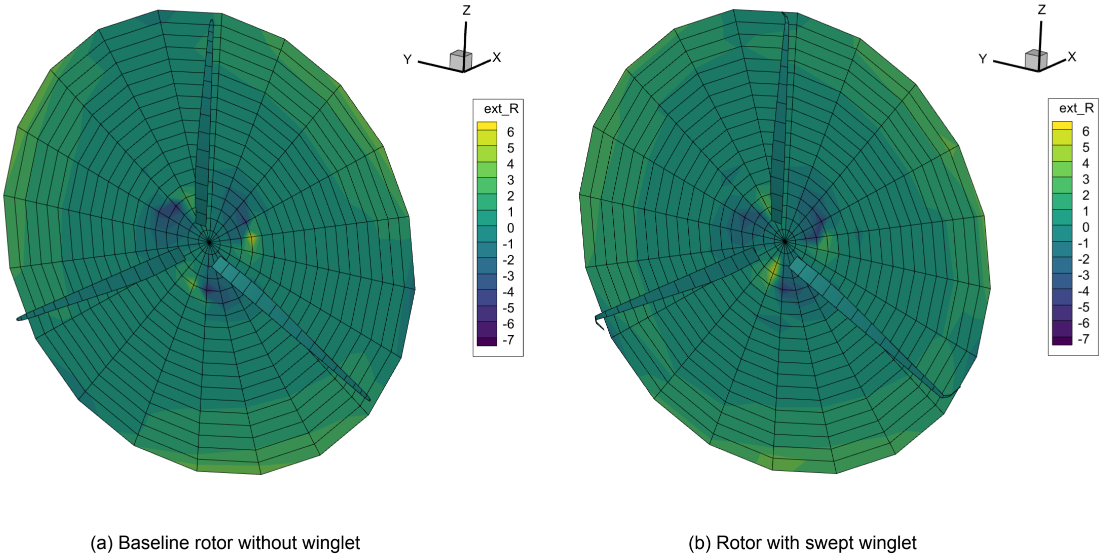

(a) Baseline rotor without winglet (b) Rotor with swept winglet

Figure 7.6: Induced radial velocity field $7.5m$ downwind of the baseline rotor and a rotor with a swept winglet. The freestream is in the positive x-direction and the rotation is clockwise around the x-axis. A positive ext_R corresponds to an induced velocity outwards from the centre of the rotor. Units of ext_R are in m/s.

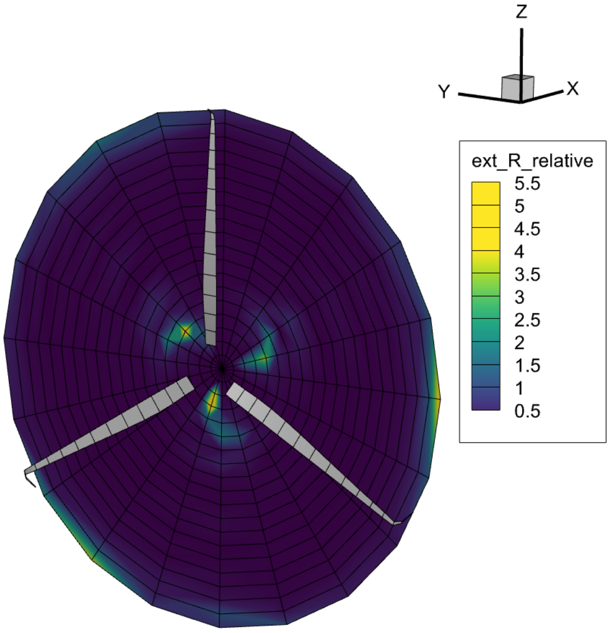

Figure 7.7: Absolute difference in radial induced velocity between the two external wake shown in fig. 7.6. Units of ext_R are in m/s.

Upwind winglet

For upwind winglets, it was seen that both upstream and downstream sweep could be beneficial in this design. A similar analysis is therefore done for the upwind winglet as was done for the downwind winglet. For the upwind winglet, the findings were slightly different. An upwind winglet is analysed with no sweep, upstream sweep and downstream sweep. The tangential loads for these three cases are shown in fig. 7.8a. A positive tangential load is seen on the downstream swept winglet, as expected for an upwind winglet. The tangential force is slightly higher for the downstream swept winglet when compared to the straight winglet. However, for the upstream swept winglet, the tangential loads on the winglet are negative. The blade close to the winglet ($0.92 < \frac{r}{R} < 0.98$) seems to have higher tangential loads.

Figure 7.8b shows the radial induced velocity on the blade, where the induced velocity is positive for the downstream swept winglet, leading to positive tangential loads on the winglet for the upwind winglet case. For the upstream swept winglet, the radial induced velocities are negative, as expected from the tangential loads. However, a radial induced velocity higher than U_∞ is shown at the winglet tip point, which might indicate AWSM is not suited to deal with upstream winglet sweep.

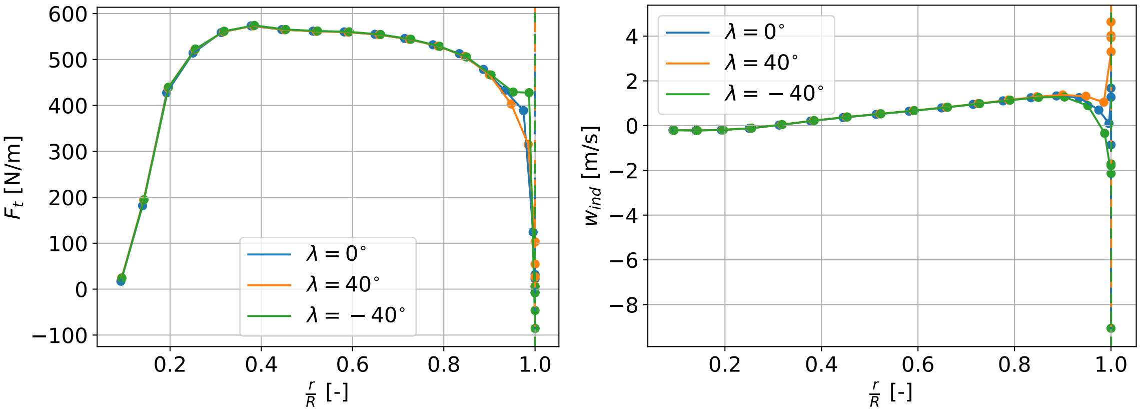

(a) Tangential loads

(b) Radial induced velocities

Figure 7.8: Tangential loads and radial induced velocity on the winglet and the blade close to the winglet for no sweep, upstream sweep and downstream sweep on an upwind winglet

The circulation for the three cases is shown in fig. 7.9a, which shows only minor differences for all cases. A more apparent difference is seen in the axial induced velocity shown in fig. 7.9b. The upstream sweep leads to a lower axial induced velocity on the blade close to the winglet, which could be the cause for the higher tangential loads on the blade.

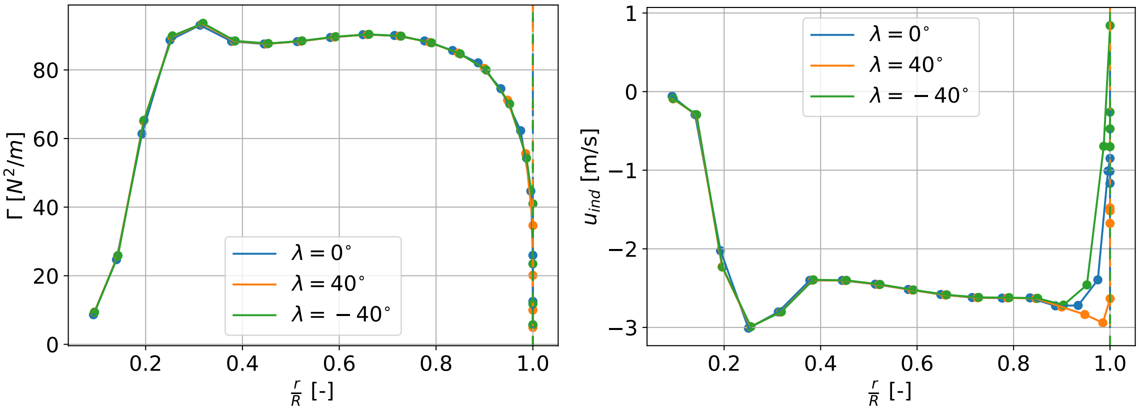

(a) Circulation

(b) Axial induced velocities

Figure 7.9: Circulation and axial induced velocity on the winglet and the blade close to the winglet for no sweep, upstream sweep and downstream sweep on an upwind winglet

The same analysis is done for the external velocity field upwind of the rotor. The radial induced velocity field is analysed $5m$ upstream, which corresponds to approximately the x-location of the tip of the winglet. From fig. 7.10a the baseline blade seems to induce a positive external radial induced velocity at the downstream location where an upwind winglet would be. In fig. 7.10b it can be seen that with an upwind winglet swept downstream, the induced radial velocity is even larger.

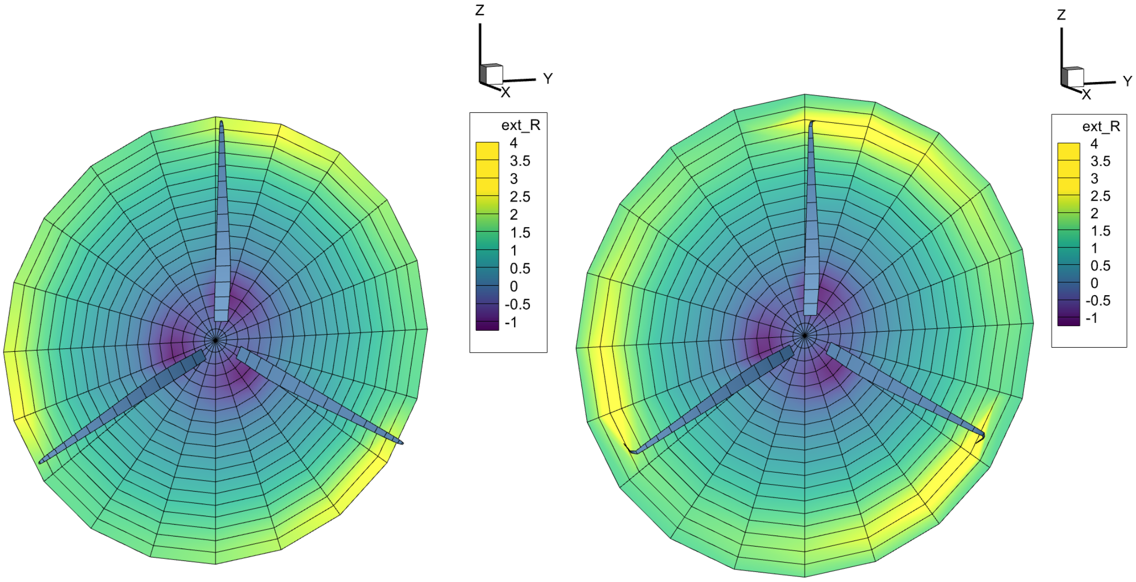

(a) Baseline rotor (b) Rotor with upwind winglet swept downstream with $\lambda = 40°$

Figure 7.10: Induced radial velocity field $5m$ upwind of a rotor with an unswept and swept winglet. The freestream is in the positive x-direction and the rotation is clockwise around the x-axis, or counter-clockwise from the viewer's perspective.

Concluding, for both the downwind and upwind winglet, sweeping the winglet downstream gives higher tangential loads on the winglet, loading to more power. Sweeping the winglet upstream gives negative tangential loads on the winglet, but reduces the axial induced velocity on the blade close to the winglet. The negative tangential loads were also observed for sweeping the downwind winglet upstream, however, the reduction in axial induced velocity on the blade was not as pronounced for the downwind winglet as it was for the upwind winglet. A possible explanation might be that as the downwind winglet already serves to reduce the axial induced velocities, the reduction is relatively smaller than for the upwind winglet, leading to a lower C_P for the upstream sweep with a downwind winglet as shown in fig. 7.1. It is unknown why exactly an upwind winglet swept upstream reduces the negative axial induced velocities on the blade close to the winglet, but an attempted explanation is that it is a consequence of the negative radial induced velocity on the winglet, which leads to a higher velocity on the blade close to the winglet due to mass conservation, hence the lower axial induced velocity.

From this analysis on sweep for the winglet, at least downstream sweep, seems to improve the winglet by a quite significant amount, with an increase as high as 3% for $\lambda = 50°$. Yet, winglet sweep is expected to not increase a winglet's performance for subsonic speeds, according to Munk's stagger theorem, showing that, perhaps, Munk's stagger theorem does not hold for the rotating case.

In the non-rotating case, a winglet swept downstream will also have a higher side-force component, which would lead to a lower induced drag for the aircraft wing, however, in reality, the induced drag with and without the winglet sweep is the same.

The difference in the rotating case might be due to the higher inductions in the wind turbine case, which are quantified in the external velocity field analysis in this section, however, this analysis should be done with higher fidelity methods, such as CFD, to have more certainty the external velocity field actually looks like it does in this analysis.

The results that are shown in fig. 7.1 would need validation with higher fidelity methods as well, to see if the tangential forces on the winglet indeed increase with increasing sweep, without any decrease of tangential forces on the blade. In this thesis, quite high sweep angles were used for the winglet, which might lead to aerodynamic phenomena not captured by a lifting line code. As a final note, FlightStream also preferred maximum sweep for single-objective optimisation of the power as is shown in appendix C.2.

7.2. The effect of different objectives and constraints

In this section, the effect of different loads minimisation cases and the effect of constraining the diameter are compared between different optimisation cases. A few designs that are considered to be optimised, are chosen to present as results of the optimisation cases. The load minimisation cases are compared in section 7.2.1 for downwind and upwind winglets separately, while the diameter constraint its effect is discussed in section 7.2.2.

7.2.1. Load minimisation comparison

All designs from optimisation cases shown in this subsection are with a diameter constraint. Firstly, the downwind winglet optimisations are shown. Secondly, the upwind winglet optimisations are shown. The $Max(\Delta P)$ designs found from the optimisation cases will be shown here. They are, however, termed $Min(T)$, $Min(m_{f,r})$ and $Min(m_{f,0.8})$ for the thrust minimisation case, root flapwise bending moment minimisation case and $\frac{r}{R} = 0.8$ flapwise minimisation case respectively. This should not be confused with the $Min(\Delta T)$, $Min(\Delta m_{f,r})$ and $Min(\Delta m_{f,0.8})$ designs.

Downwind

In this research, a downwind winglet has proven to be more beneficial to the design than a straight tip for all different loading minimisation objectives. However, the different minimisation objectives led to different winglet designs which improved the power for different reasons. The $Max(\Delta P)$ designs for the three different minimisation objectives are repeated in table 7.2 and are used for the plots that follow in this subsection. Note that the $Min(m_{f,0.8})$ design has not been optimised for the sweep, resulting in lower power than the other designs. The normal loads are shown in fig. 7.11a. It can be seen that for the minimum thrust design the normal loads on the winglet are the highest. This is partly a result of a large chord length over the tip as seen in fig. 7.12a, which also leads to the highest tangential loads on the winglet as seen in fig. 7.11b. As for this case, the thrust is constrained, it does not matter for the optimiser where the normal loads are increased or decreased, as long as the integrated total of the normal loads, the thrust, is minimised or lower than the constraint. The optimiser found that the best way to do that was to create a winglet that was quite heavily loaded and reduce the chord length on the blade close to the winglet, as can be seen in fig. 7.12a, where the smallest chord length is found by the $Min(T)$ design. The radial induced velocity is the most negative on the winglet for the $Min(T)$ design as shown in fig. 7.13a as well as the circulation as seen in fig. 7.13b, which is what results in the highest tangential and normal loads on the $Min(T)$ winglet.

	ΔP [%]	ΔT [%]	$\Delta m_{f,0.8}$ [%]	$\Delta m_{f,r}$ [%]	τ_w [m]	λ [°]	h [m]	ϕ [°]	r_w [m]
$Min(T)$	5.27	-0.12	9.10	0.25	0.40	55.0	7.99	51.56	0.30
$Min(m_{f,r})$	4.51	-0.49	17.53	-0.37	0.22	55.0	7.53	42.31	0.21
$Min(m_{f,0.8})$	0.93	-0.73	-4.10	-1.28	0.12	5.0	5.94	66.99	0.34

Table 7.2: Repeated $Max(\Delta P)$ designs for the thrust minimisation case, root flapwise bending moment minimisation cases and flapwise bending moment at $\frac{r}{R} = 0.8$ minimisation case on a downwind winglet

For the $Min(m_{f,r})$ case the location of the normal loads does matter to the minimisation objective, contrary to the $Min(T)$ case. A highly loaded tip affects more to the root bending more than a load closer to the root, due to the larger arm from the loads on the tip.

The $Min(m_{f,r})$ winglet design is somewhat similar to the $Min(T)$ design, with a maximum sweep, close to maximum winglet height and a similar cant angle. Its winglet chord length, however, is lower, as seen in fig. 7.12a. This results in a somewhat lower normal and tangential load on the winglet as seen in fig. 7.11, which is seen back in the slightly lower circulation in fig. 7.13b and slightly less negative radial induced velocity in fig. 7.13a. The optimiser does seem to prefer a winglet slightly less loaded than for the $Min(T)$ case as expected.

It was, however, expected that the winglet from this minimisation case would be more successful in creating a less negative induced velocity on the blade, resulting in high tangential loads on the blade, however, as seen in fig. 7.12b, this is not really the case. A possible explanation was that the optimiser found loading the winglet just enough to not exceed the $m_{f,r}$ was more beneficial than creating a winglet

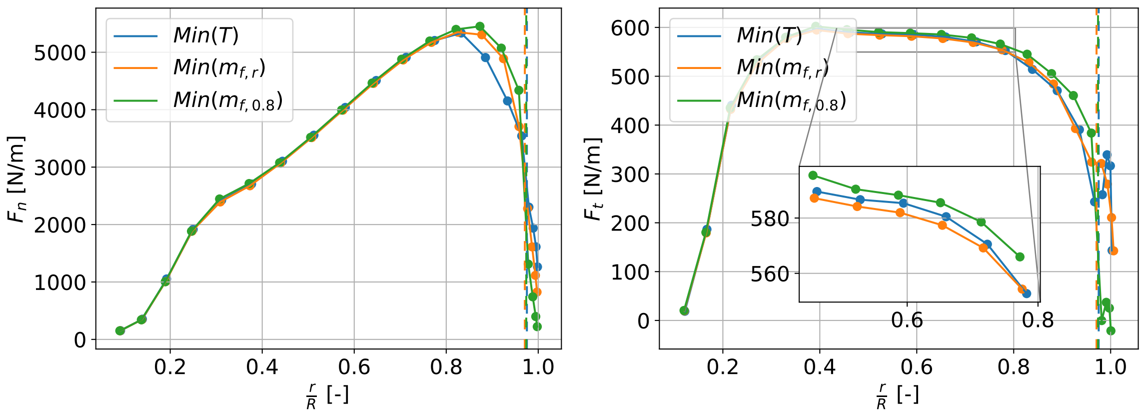

(a) Tangential loads

(b) Normal loads

Figure 7.11: Tangential and normal load comparison for the three minimisation cases on a downwind winglet

design that reduced the negative axial induced velocity on the main blade.

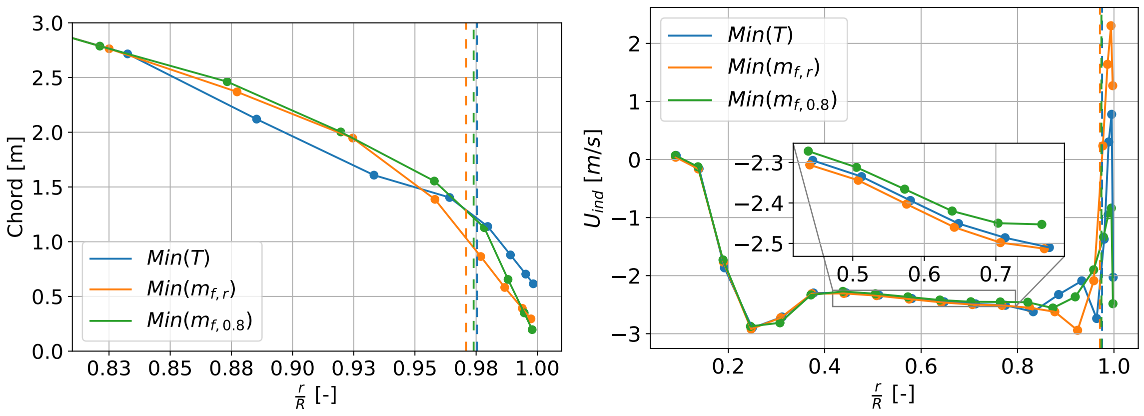

(a) Chord length

(b) Axial induced velocities

Figure 7.12: Chord length and axial induced velocity for the three downwind optimisation cases

Finally, the $Min(m_{f,0.8})$ design does seem to be able to reduce the negative axial induced velocity on the blade as seen in fig. 7.12b. This does lead to relatively low normal and tangential loads on the winglet, but the highest increase in loads on the main blade as seen in fig. 7.11b. Also on the blade close to the winglet ($0.9 < \frac{r}{R} < 0.95$), the tangential loads are higher for the $Min(m_{f,0.8})$ compared to the $Min(m_{f,r})$ design, even though circulation and chord length are approximately the same. The increase in tangential loads is expected to come from the less negative axial induced velocity in fig. 7.12b. The reduction in axial velocity at this location could be due to the higher winglet radius, higher cant angle or absence of winglet sweep.

As seen from this analysis, the $Min(m_{f,0.8})$ downwind winglet serves to displace the tip vortex and therefore reduce the negative axial velocity on the main blade, while the other two minimisation cases let to a winglet which itself contributes to the power increase of the design, but only led to small increases in tangential loads on the blade. The difference between the two cases is that the winglet was even more loaded in the $Min(T)$ case, as the location of normal loads does not influence the thrust minimisation objective, whereas for the $Min(m_{f,r})$ case a highly loaded winglet does contribute more the root bending moment than an increase of loads on the blade.
Although this comparison is not completely fair, as the optimiser in the $Min(m_{f,0.8})$ case was not allowed to change the winglet sweep, the same trends are expected if the two other cases would have

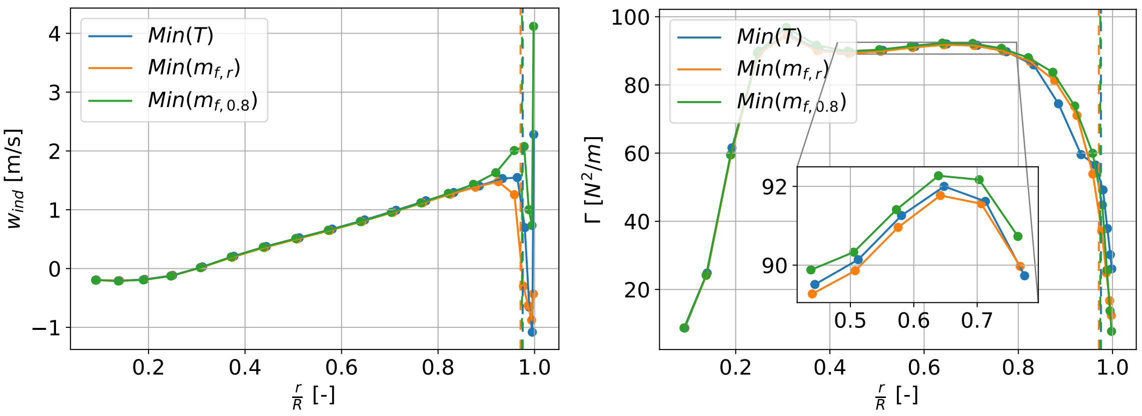

(a) Radial induced velocities

(b) Circulation

Figure 7.13: Radial induced velocities and circulation for the three minimisation cases on a downwind winglet

a constant sweep, where the optimiser would find other ways, such as increased winglet chord length and high winglet height, to increase the loads on the winglet itself. Optimisation cases for the $Min(T)$ and $Min(m_{f,r})$ with a fixed sweep might still be able to get a higher ΔP, with a high flapwise bending moment through the blade, as seen as well for the current cases in fig. 7.14a.

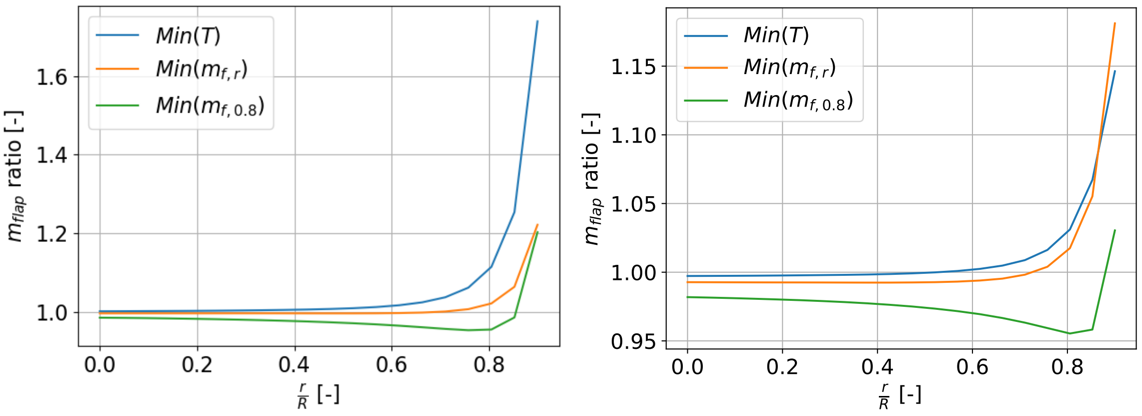

(a) Downwind

(b) Upwind

Figure 7.14: Flapwise bending moment ratios as a function of radial position for the downwind optimisation cases and upwind optimisation cases

Upwind

Again, the $Max(\Delta P)$ designs are plotted for the upwind winglet optimisation cases, which are repeated in table 7.3. However, for the $Min(T)$ and $Min(m_{f,r})$ cases, a straight tip was found to be the preferred design by the optimiser for those minimisation objectives. The $Min(T)$ and $Min(m_{f,r})$ designs are fairly similar, with similar sweep angles, both are straight tips instead of winglets and have a similar chord length plotted in fig. 7.16a. The winglet height is different, however, this does not really affect design

	ΔP [%]	ΔT [%]	$\Delta m_{f,0.8}$ [%]	$\Delta m_{f,r}$ [%]	τ_w [m]	λ [°]	h [m]	ϕ [°]	r_w [m]
$Min(T)$	4.08	-0.25	15.30	0.09	0.24	50.0	8.00	0.10	0.10
$Min(m_{f,r})$	3.59	-0.54	20.69	-0.32	0.36	55.0	5.85	5.68	0.10
$Min(m_{f,0.8})$	1.03	-1.35	-3.98	-1.59	0.04	5.0	4.03	80.21	0.32

Table 7.3: Repeated $Max(\Delta P)$ designs for the thrust minimisation case, root flapwise bending moment minimisation cases and flapwise bending moment at $\frac{r}{R} = 0.8$ minimisation case on an upwind winglet

as there is a diameter constraint, meaning more of the blade's radius is removed.
Between the $Min(T)$ and $Min(m_{f,r})$ cases, similar trends are seen as were seen for the downwind winglet cases. The tangential loads on the straight tip are slightly higher for the $Min(T)$ design as seen in fig. 7.15b, where also the normal loads on the straight tip are slightly higher as shown in fig. 7.15a. The slight decrease in tangential loads is expected to be the result of the slightly higher cant angle, as the chord lengths are almost identical as shown in fig. 7.16a. Although, a higher cant angle is expected to give higher tangential loads on an upwind winglet from fig. 4.6a.
Both designs have approximately the same effect on the axial induced velocity and circulation on the main blade as seen in fig. 7.16b and fig. 7.17b respectively. A slightly higher radial induced velocity component is observed for the $Min(m_{f,r})$ shown in fig. 7.16b, due to the larger cant angle.

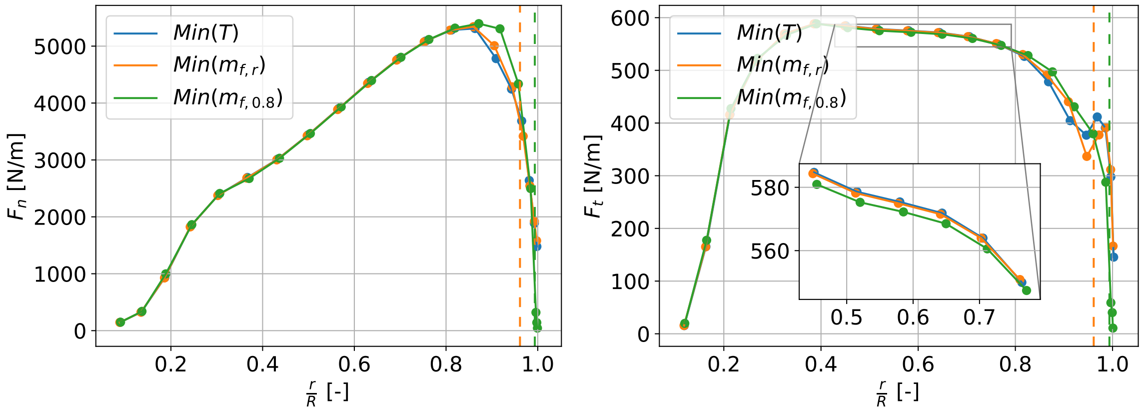

(a) Normal loads

(b) Tangential loads

Figure 7.15: Normal and tangential loads for the three upwind optimisation cases

As the design resulting from $Min(m_{f,0.8})$ is the only winglet design in this comparison, the winglet does decrease the tangential loads on the main blade and gets its increased power production from the loads on the winglet, which are smaller than the loads on the swept-back straight tips from the $Min(T)$ and $Min(m_{f,r})$ cases. The blade close to the winglet $0.85 < \frac{r}{R} < 0.98$ does have higher tangential loads than the other two designs, however.

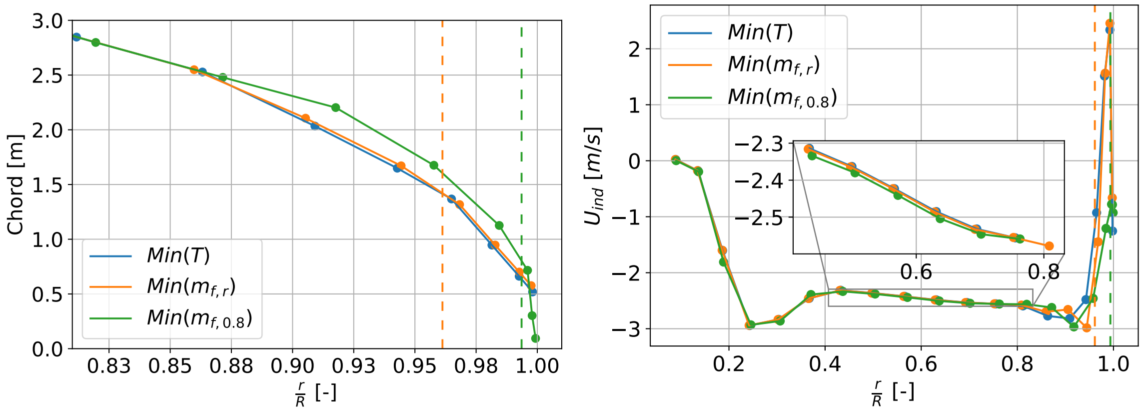

(a) Chords length

(b) Axial induced velocities

Figure 7.16: Chord lengths and axial induced velocities for the three upwind optimisation cases

Similar conclusions about the differences between the optimisation cases can be drawn for upwind winglets as for downwind winglets.

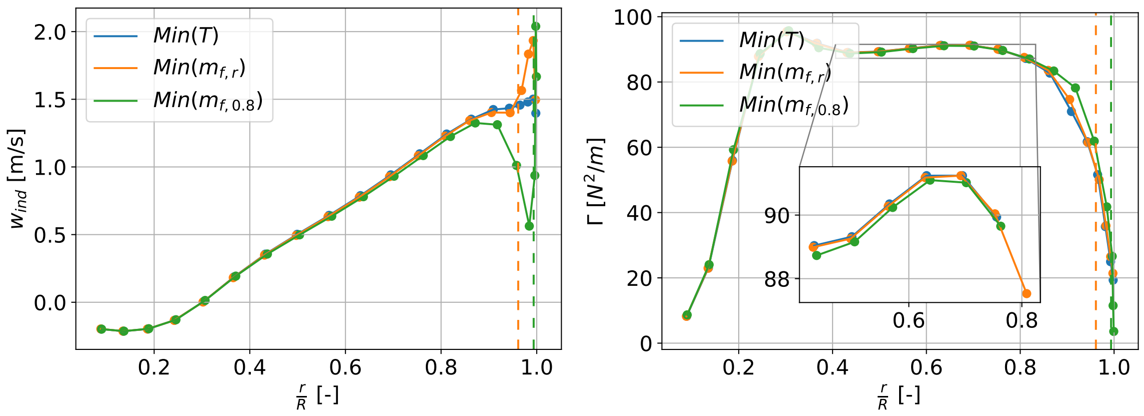

(a) Radial induced velocity

(b) Circulation

Figure 7.17: Radial induced velocity and circulation for the three upwind optimisation cases

7.2.2. Diameter constraint

Only two optimisation cases without diameter constraints were performed. However, this is suspected to be enough to draw conclusions about the diameter constraint. Section 5.3 has shown that, for the downwind optimisation case, with diameter constraint and thrust constraint, a winglet can still be beneficial to a blade design, however, when removing the diameter constraint, a tip extension proved to be more effective than a winglet. The found tip extensions did in most cases not have an increased root flapwise bending moment either. The designs did have an increase flapwise bending moment at $\frac{r}{r} = 0.9$, however. So when constraining the bending moment at this location, a winglet was found to be more beneficial in increasing the power as was shown in table 5.8.

Concluding, without a diameter constraint, a tip extension seems to be more beneficial to the blade design than a winglet, except when the flapwise bending moment is constrained at $\frac{r}{R} = 0.9$. Only downwind winglets were investigated without the diameter constraint, however, it is expected the same conclusions can be drawn for upwind winglets, as for the upwind optimisation cases a straight tip was preferred for the $Max(\Delta P)$ designs already, but winglets were preferred for the $m_{f,0.8}$ minimisation case.

7.3. The effect of up or downwind winglets

As already discussed in section 3.3.6, a downwind winglet serves to reduce the negative axial velocities on the main blade, which increases the tangential loads on the blade, whereas an upwind winglet serves to increase the tangential loads on the winglet itself, however, reduces the tangential loads on the blade.

As found from the optimisation cases in this work, downwind winglets were a better alternative than a straight tip, where having a flapwise bending moment constraint at 80% was the most beneficial for a winglet design as it led to the highest cant angle. For the upwind winglet cases, however, a straight tip gave a higher power increase with a thrust or root flapwise bending moment constraint, than an upwind winglet. Although these results are affected by the sweep, which seems to give a high increase in tangential loads on the winglet or straight tip, without influencing the minimisation objectives much. If the optimisation cases with thrust and root flapwise bending moment constraint would have not been optimised with a fixed sweep, winglets might have been a better alternative than a straight tip as, for example, during the upwind winglet thrust minimisation case a straight winglet with almost no sweep was found which increased the power by 2.8% and decreased the thrust by 0.2%. Similarly, a similar straight, unswept winglet design was found for the $m_{f,r}$ minimisation case which increased the power by 1.6% and decreased $m_{f,r}$ by 3%. Both designs are shown in table 7.4.

This shows that without sweep considered, a winglet might have been preferred by the optimiser over a straight tip, as without sweep considered, the optimiser was not able to increase the power by a significant amount as was shown in section 5.2. However, these upwind winglet designs have a high increase in flapwise bending moment at 90% of the blade. As an upwind winglet reduces the tangential loads on the main blade and can gain an increase in power for the rotor design from tangential loads on the winglet itself, high flapwise bending moments closer to the tip are expected to occur for any power

	ΔP [%]	ΔT [%]	$\Delta m_{f,0.9}$ [%]	$\Delta m_{f,r}$ [%]	τ_w [m]	λ [°]	h [m]	ϕ [°]	r_w [m]
$Min(T)$	2.78	-0.24	116.23	0.56	0.07	-3.13	6.68	85.78	0.73
$Min(m_{f,r})$	1.55	-2.57	83.06	-2.93	0.01	-5.61	7.18	88.34	0.27

Table 7.4: Selection of upwind winglet designs found in the thrust minimisation case and the root flapwise bending moment minimisation case

optimised upwind winglet with thrust or $m_{f,r}$ as the constraint. Power optimised downwind winglets were found to increase the flapwise bending moment close to the tip of the blade by a lower amount.

The optimiser was able to achieve higher power designs for downwind winglets compared to upwind winglets for the thrust and $m_{f,r}$ constraint. Where downwind winglets received a higher power increase from a downstream sweep. The suspected reason for this is that the higher difference between the negative radial velocity in the wake downwind at the unswept and downstream swept position winglet than is observed for the difference in the positive radial velocity in the wake upwind between the unswept and downstream swept position as argued in section 7.1.

However, for the $m_{f,0.8}$ constraint, an upwind winglet has slightly more power, the optimiser was also able to find more improved winglet designs for the upwind optimisation case. This is an unexpected result, as upwind winglets generally had less power in other optimisation cases, but also in simpler comparisons, such as was done for the sweep.

A possible explanation for the higher power of the upwind winglet is that the upwind winglet requires less radial loads to be effective, as the change in tangential induced velocities compared to the baseline design is lower for the upwind case, leading to lower radial loads on the winglet. This would mean a lower flapwise bending moment at 80% of the blade. The tangential induced velocities for the $Min(m_{f,0.8})$ optimisation cases for the upwind and downwind winglet are shown in fig. 7.18b.

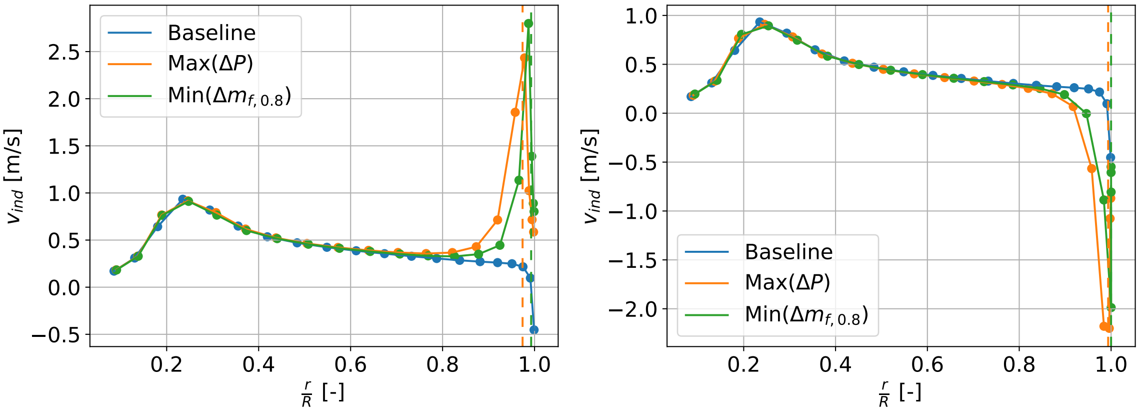

(a) Downwind winglets from $m_{f,0.8}$ minimisation case

(b) Upwind winglets from $m_{f,0.8}$ minimisation case

Figure 7.18: Tangential induced velocities for the optimum found from the flapwise bending moment at $\frac{r}{R} = 0.8$ optimisation cases

It can be seen that the difference between the tangential induced velocity is slightly bigger for the downwind winglet, compared to the baseline case, while the power increase is smaller for the downwind winglet. This could be an explanation why the radial loads are higher in general for downwind winglets. It is unknown why the difference in tangential induced velocity would be higher for the downwind winglet. A possible explanation could be found by doing an external velocity field analysis for the tangential induced velocity, as was done in fig. 7.6 for the radial induced velocity.

In this research, upwind winglets are only considered on upwind rotors and downwind winglets on downwind rotors. A downwind rotor will have a decreased performance in power compared to an upwind rotor, however. This effect is not quantified as lifting line is not a suitable method to do so, which is thus left as future work. Another option would have been to consider downwind winglets on upwind rotors. This would limit the winglet height, however, and require an aeroelastic analysis, even when the bending moment throughout the blade is not increased. This research did not consider the increase in torsion on the blade or displacement of the elastic axis due to the winglet and might result in different aeroelastic behaviour. A downwind winglet on an upwind rotor might require more prebend on the blades which might decrease the performance as well.

7.4. Optimised winglets operational performance

In this work, winglets have been optimised for a single wind speed, which was set to $8m/s$. It was at this wind speed where all objectives were analysed during optimisation without considering another wind speed, and thus the effect the tip speed ratio or pitch would have on these objectives. This section will analyse the performance of the optimised upwind and downwind winglet for the design case which minimised the flapwise bending moment at $\frac{r}{R} = 0.8$.

For the $Max(\Delta P)$ downwind winglet from this optimisation case, the ratios of all objectives analysed compared to the baseline design, are shown in fig. 7.19a. It can be seen that the ratio of every objective is almost constant for the range of wind speeds with a constant tip speed ratio ($8m/s$ - $11m/s$). Where $7m/s$ is not analysed here as no validation results were present for this research. Although the power ratio is slightly lower (approximately 0.1%) for $8m/s$. It is therefore expected that, were another wind speed chosen in chapter 5 for the optimisations, the results would have looked the same.

Furthermore, it can be seen that the power ratio is higher for lower wind speeds and lower for high wind speeds. Showing that this winglet is more beneficial to the power at lower wind speeds. The power is, however, also increased for wind speeds above rated ($> 11.4m/s$), meaning the blades should pitch accordingly to keep the power below rated. It should be noted that the validation results for $5m/s$ and $6m/s$ were not matching as well to the CFD reference results, compared to the other wind speeds analysed, as is shown in fig. B.6 and fig. B.7. However, the result of a higher increase in power for lower wind speeds matches with the finding of Zahle et al. [30].

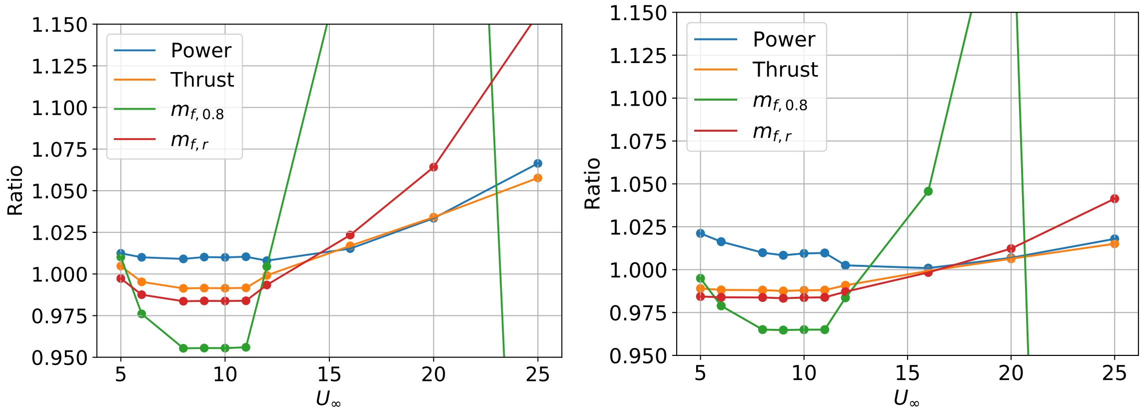

(a) Downwind winglet

(b) Upwind winglet

Figure 7.19: Ratios of all objectives between optimised winglet designs from the $m_{f,0.8}$ optimisation cases and the baseline blade design. Results were obtained with actual polars instead of prescribed polars. High flapwise bending moments are outside the y limits of this plot as the absolute results will be shown in fig. 7.20.

An especially high increase in the ratio is seen for $m_{f,0.8}$ for wind speeds above rated. The absolute values of the optimised design and baseline design are shown in fig. 7.20a. This shows that the absolute flapwise bending moment does not go above its maximum, which is at $11m/s$. However, the value is noticeably higher than for the baseline design. This could lead to an increase in fatigue and extreme loads.

The same was observed for $m_{f,r}$, however, the ratio between the blade with winglet and the baseline blade was smaller as was seen from fig. 7.19a. The sharp decrease in the $m_{f,0.8}$ ratio at $25m/s$ is due to the normal and tangential loads being negative for at this wind speed, as is seen in fig. B.15.

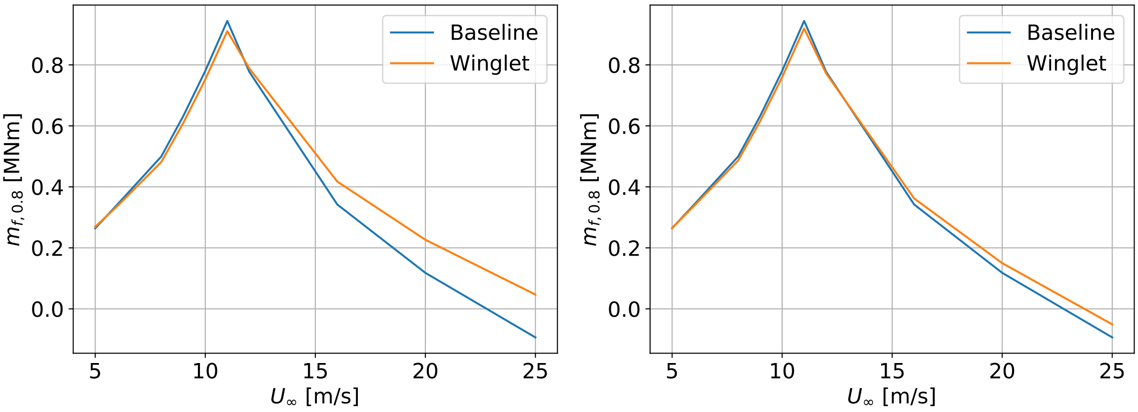

(a) Downwind winglet

(b) Upwind winglet

Figure 7.20: Absolute values for the optimised winglet designs from the $m_{f,0.8}$ optimisation cases and the baseline blade design. Results obtained with actual polars.

Approximately constant ratios of the objectives are seen for the optimised upwind winglet as well as seen in fig. 7.19b, with a slightly higher power ratio at $11m/s$ compared to $8m/s$. The difference is still small with 0.3%, however. The increase in $m_{f,0.8}$ is smaller for the upwind winglet, however, as seen in fig. 7.20b.

Would the winglet designs have been optimised for AEP instead of C_P, the winglet designs are expected to look very similar. When optimising for AEP, an objective function would have to be created that weights the power ratio at the evaluated wind speeds. As the DTU10MW RF is designed for wind class IA, the power production at $5m/s$ and $6m/s$ does not contribute much to the AEP and low weight would therefore be given to these wind speeds.

8

Conclusion and Recommendations

This chapter will provide an overview of the conclusions that are drawn from this work in section 8.1. Additionally, in section 8.2 recommendations for further work will be given which will consist of recommendations for validation of the work or ideas that can be interesting to pursue given the conclusions in this work.

8.1. Conclusion

This work aimed to contribute to the understanding of winglet optimisation for a wind turbine. Multi-objective optimisation was used to maximise or minimise different objectives to investigate how these different objectives influenced the winglet design. Multi-objective Bayesian optimisation was used for this purpose which uses an acquisition function, which effectively searches a surrogate model, to determine what winglet design should be analysed by the aerodynamic analysis method. Two aerodynamic analysis methods were considered for this purpose, where eventually the lifting line code, AWSM, was chosen. AWSM, as lifting line code, allowed to reduce the number of design variables, as predefined polars were used during the optimisation. The twist optimisation was then done as a post-processing step. FlightStream was found to be not usable for this type of analysis in its present version.
Multi-objective optimisation served to find multiple winglet designs with a trade-off between different objectives. The goal for the optimiser was to find designs that performed better, if possible, on two or more objectives than a baseline turbine, which was chosen to be the DTU 10MW Reference Turbine. In most cases, the optimiser was able to do so.

From optimisation runs, it quickly became apparent that the aerodynamic analysis method tended to design winglets with a downstream sweep to increase the rotor's aerodynamic power, where increases in power up to 3% were obtained, compared to having an unswept winglet. This was found for both downwind and upwind winglets, however, the increase in power was larger for a downwind winglet. Upwind winglets were also found to achieve some benefit from upstream sweep.
It was found by an external field analysis that downwind in the wake, just downstream of the blade's tip, there is a region with a more negative radial induced velocity, this was found to be true for a blade without a winglet and for a blade with a winglet. Whenever the downwind winglet is swept into this area of reduced induced radial velocity, this would create more tangential loads on the winglet and thus increase the rotor's power. Similarly, for the upwind winglet, just upwind and downstream of where an upwind winglet would be, a zone with increased positive radial induced velocity was found, also leading to increased tangential loads on the winglet, whenever a winglet is swept into this zone. This was found to be a possible explanation for the benefit of downstream sweep on a winglet. Upstream sweep for an upwind winglet, reduced the negative axial velocities on the blade close to the winglet, also leading to increased power production.
Although reasons were found for the benefit of winglet sweep, it has been proven by Munk [11] that for the non-rotating case sweep does not improve the performance of a wing, as long the projected shape and projected circulation, on a plane perpendicular to the freestream, do not change. This does not necessarily mean this theorem holds for the rotating case, but perhaps a disadvantageous effect

that occurs in reality, which cancels out the beneficial effect of winglet sweep, is missing in the lifting line code used. The beneficial effect of the winglet sweep, whether realistic or not, did influence the resulting optimum designs in this work, as the independent change of no other winglet parameter did achieve as high increases in power as the winglet sweep did.

Without the power contribution of the sweep, winglets were still able to increase the power by approximately 1% without exceeding the flapwise bending moment at $\frac{r}{R} = 0.8$. It was found that a winglet was more beneficial to the design than a straight tip for both an upwind and downwind winglet, when constraining the bending moment at $\frac{r}{R} = 0.8$. The optimum upwind and downwind winglets obtained from this optimisation case were analysed at different wind speeds as well.
For both winglets, it was found that there was no significant change in values of the objectives for a constant tip speed ratio. It would therefore not be necessary, for this work, to optimise a winglet for different wind speeds below rated, where the tip speed ratio is constant. It was also found that these winglets gave a higher increase in power for low wind speeds, where the rotor operates at a higher tip speed ratio. Besides that, the winglet had a lower power increase for the higher wind speeds below rated, which had a lower tip speed ratio. For wind speeds above rated, the power increase was even higher, so the pitch settings of the blades would have to be changed when using a winglet.

The aerodynamic power of the rotor was the objective maximised for and the different minimisation objectives tried were the thrust on the rotor, the flapwise bending moment at the root and the flapwise bending moment closer to the tip. It was found that the design of the winglet did change depending on the objectives and on the winglet direction, upwind or downwind.
When constraining the thrust, a winglet was able to increase the rotor's aerodynamic power for both an upwind and downwind winglet, although, for the upwind case, the optimiser was able to achieve a higher power by designing a swept-back straight blade, than it was by designing a winglet. The winglet designs that were found for the constrained thrust case, mostly increased the power contribution from the winglet itself, also for the downwind case, which was mostly achieved by winglet sweep. The optimised downwind winglets from this case, barely influenced the power contribution from the blade. This resulted in high flapwise bending moments near the tip. The optimiser also preferred a high load on the winglet for the upwind winglet optimisation without influencing the loads on the blade much. It was found by the optimiser that the best way to do this was with a swept-back straight tip instead of an upwind winglet. Although an unswept upwind winglet was also able to increase the rotor's power without increasing the thrust, again with large increases in the bending moment close to the tip.
Similar downwind winglet designs when constraining the flapwise bending moment at the root were found, where the increase in the rotor's aerodynamic power mainly came from the loads on the winglet. However, lower loads on the winglet were found compared to the thrust constrained winglets. The optimised designs found from this optimisation case did, however, often have a lower increase in power contribution from the blade, compared to the thrust constrained winglets. The optimiser again preferred to design a power contributing winglet over designing a winglet that increases the power by increasing the loads on the blade, where the loads on the winglet were somewhat lower to not exceed the bending moment at the root. The results from the optimiser showed that designing a highly loaded winglet was more beneficial than designing a winglet that increases the power contribution from the blade. For the upwind optimisation case, a straight, swept-back tip was again preferred by the optimiser over an upwind winglet with, however, a lower increase in power than for the thrust minimisation case.
Constraining the bending moment at 90% of the radius resulted in the optimiser not finding an upwind or downwind winglet design that was able to improve the power. The optimiser instead preferred a swept-back straight tip. Constraining the bending moment at 80% and while not optimising for the sweep, but setting the sweep to a constant value, however, did result in a winglet being the better alternative than a straight tip. A winglet was found to be most beneficial to the design for this constraint, where also the highest winglet cant angles were found in this optimisation case. For this optimisation case, upwind winglets were able to increase the power slightly more without increasing the bending moment at 80% of the rotor radius. A possible explanation could be that upwind winglets require a lower radial load to be effective than downwind winglets. However, this could also be due to other reasons such as the parameterisation used.

Different surrogate models have also been compared in this work to investigate which surrogate model is most suited for this optimisation problem. Although GPs were better able to predict the values of the

different objectives than RF and BNNs, A BNN was able to find designs lying on the Pareto front faster than GPs, without any sacrifice in running time for the optimiser.
A reason for this increase is believed to be due to the modified acquisition function. Where the acquisition function using GPs as a surrogate model was presented with ten candidate designs which were all optimised, using a gradient optimiser, for maximum EHVI. The acquisition function with a BNN as a surrogate model was presented with a much higher number of candidate designs, randomly generated close to a non-dominated design, which were not optimised. The candidate design with the highest EHVI was picked from these designs. This method was chosen due to a NN being able to evaluate a high number of samples at the same instant in a short time. Therefore, BNNs were not able to predict the values of the objectives better than GPs but were able to increase the hypervolume more effectively for the optimisation problem in this work. Another possible reason for the better performance of the BNN surrogate model could be a more robust uncertainty estimation.

All the findings in this work and any conclusions that can be taken from it are dependent on various assumptions done in this work. The beneficial effect of the sweep influenced the results found by the optimiser. Different optima may have been found if sweep happens to be not as beneficial as found by the lifting line code. Results from an optimiser are also very dependent on the parameterisation method used for the blade and winglet. It is possible that with another parameterisation method the optimum winglet would have looked different. It is also assumed the optimisation method used can find optimised designs that are optimally loaded, however, perhaps different optimisation methods could have found better designs.

8.2. Recommendations

Based on the results found in this thesis, recommendations can be made for future research.

As mentioned before, the increase in power on the winglet from sweeping the winglet downstream, is quite significant with increases up to 3% for sweeping a straight winglet downstream, which could be too high to be realistic. These findings would have to be validated with higher fidelity methods such as Navier-Stokes solvers. The finding of the change in radial induced velocities in the wake would have to be validated by methods more suitable to do so, such as Large-Eddy Simulations.
A non-rotating case in AWSM with winglets could also give more insight into the reason for the increased performance of the winglet with sweep. If no increase in power is found for a non-rotating case by AWSM, the reason for the increase might indeed be that Munk's stagger theorem is not valid for the rotating case. If an increase is still found for the non-rotating case, however, AWSM might not be suited to analyse winglet sweep with the setup used in this thesis.
The winglet designs themselves would have to be validated by higher fidelity methods as well. As the effect of thickness or displacement effects are not taken into account by a lifting line code. Navier-Stokes solvers with turbulence modelling might show that the high winglet sweep angles used in this work are unfeasible. Turbulence modelling might give more insight into what winglet radius should be used, wherein in this work the radius used did not affect the results by a large amount.

The effect of the winglet radius and taper ratio have been mostly left out of the discussion in this work, as no clear effect was observed on the objectives. It is assumed that these parameters mostly served to optimise the loading of the winglet, but more investigation could be done on the effect of these winglet parameters.

In this work, the structural design of the winglet is not considered. Chord lengths of winglets might be too small to design a structure that would be able to withstand the loads on the winglet itself. Wind turbine designs are often considered by load cases that are linked with extreme, unsteady, or non-normal operational events, such as extreme turbulence, gusts, emergency shutdowns, subsystem faults, or parked conditions as argued by Loenbaek et al. [1], which are not considered in this thesis.
Also, aeroelastic behaviour has not been modelled in this thesis. Winglet placement is largely behind the wing's elastic axis which can give unwanted frequencies, which is not analysed in this work. The high tangential loads on the winglet might introduce high torsion on the blade, which is not analysed. The changed loads due to the winglet might also lead to larger tip displacements, which might lead to violated tower clearances in the upwind rotor with upwind winglet case or might lead to decreased performance of the blade in both the upwind or downwind rotor cases. If the downwind winglet were

fitted on an upwind rotor, the prebend of the blades might have to be increased after an aeroelastic analysis is done, which could decrease the performance of the blade as well.

The assumption of using a downwind rotor with a downwind winglet would have to be checked as well. Using a downwind rotor would decrease the performance of the turbine, as the blades will pass through the tower shadow. The DTU10MW Reference Turbine is not designed as a downwind rotor and might need a significant redesign to be used as a downwind rotor. In the end, a downwind winglet on either a downwind rotor or also on an upwind rotor could lead to a large loss of performance due to these reasons, compared to an upwind winglet rotor on an upwind winglet. This would make an upwind winglet preferable over a downwind winglet.

A winglet can reduce the noise that is generated by the tip as was found by Ebrahimi and Mardani [84]. The noise reduction that can be obtained with a winglet can be another minimisation objective if an aeroacoustic analysis would be done for the turbine with a winglet.

Firstly, although BNN was found to find the Pareto front more quickly than GPs, the reason is not that BNNs are better estimators of the objectives for this optimisation problem, but likely due to the modified acquisition function, which is better suited for NNs. The same acquisition function should be tried with GPs to investigate if the modified acquisition function is really the reason for the better performance of the BNN. This would increase the optimisation time by a large amount, however, a GP would have to evaluate the thousand candidate designs for each objective that is optimised for. Due to this long-running time, this has not been attempted. Secondly, a GP and BNN have only been compared on one optimisation case, more optimisation cases would have to be tried to prove the BNN would really be the better alternative as a surrogate model for this work. Lastly, the problem with a comparison between machine learning models is that they are very dependent on the hyperparameter tuning, setup or sub-methods used in the models. The author of this thesis is more experienced with the usage of NNs than with GP or RF, which may have influenced the outcome of the results and led to unfair comparison.

In this thesis, only a fairly simple parameterisation technique has been used for the winglet and blade. The parameterisation gave a clear overview of the effect of each parameter, however, this parameterisation method may have limited the ability of the optimiser to cover the design space to the highest degree, preventing it from finding non-traditional shapes to be found. More complicated parameterisation techniques could have been used which make use of Bézier curves or B-Splines, which might also be able to decrease the number of design parameters.

Bibliography

[1] Kenneth Loenbaek et al. “Optimal relationship between power and design-driving loads for wind turbine rotors using 1-D models”. In: *Wind Energy Science* 5.1 (2020), pp. 155–170. ISSN: 23667451. DOI: `10.5194/wes-5-155-2020`.

[2] Guillaume Briffoteaux et al. “Parallel surrogate-assisted optimization: Batched Bayesian Neural Network-assisted GA versus q-EGO”. In: *Swarm and Evolutionary Computation* 57.October 2019 (2020), p. 100717. ISSN: 22106502. DOI: `10.1016/j.swevo.2020.100717`. URL: `https://doi.org/10.1016/j.swevo.2020.100717`.

[3] Clym Stock-Williams et al. “What Makes an Effective Scalarising Function for Multi-Objective Bayesian Optimisation ?” In: *Machine Learning* (2020).

[4] Thomas H. Hansen and Franz Mühle. “Winglet optimization for a model-scale wind turbine”. In: *Wind Energy* 21.8 (2018), pp. 634–649. ISSN: 10991824. DOI: `10.1002/we.2183`.

[5] Jospeh Katz and Allen Plotkin. *Low-Speed Aerodynamics*. Second Edi. 2001. ISBN: 978-0-521-66552-0.

[6] J. D. Anderson. “Fundamentals of Aerodynamics — Fifth edition, J. D. Anderson, McGraw-Hill, Shoppenhangers Road, Maidenhead, Berkshire, SL6 2QL, UK. 2011. 1098pp. Illustrated. £47.99. ISBN 978-007-128908-5.” In: *The Aeronautical Journal* 116.1176 (Feb. 2012), pp. 222–223. ISSN: 0001-9240. DOI: `10.1017/S000192400000676X`. URL: `http://arxiv.org/abs/1011.1669%20http://dx.doi.org/10.1088/1751-8113/44/8/085201%20https://www.cambridge.org/core/product/identifier/S000192400000676X/type/journal_article`.

[7] L Prandtl. “APPLICATIONS OF MODERN HYDRODYNAMICS to Aeronautics”. In: (1923).

[8] Ilan Kroo. “DRAG DUE TO LIFT: Concepts for Prediction”. In: *Annual Review of Fluid Mechanics* (2001), pp. 587–617. ISSN: 0066-4189.

[9] W. F. Phillips and D. F. Hunsaker. “Designing wing twist or planform distributions for specified lift distributions”. In: *Journal of Aircraft* 56.2 (2019), pp. 847–849. ISSN: 15333868. DOI: `10.2514/1.C035206`.

[10] C. W. Burkett. “Reductions in induced drag by the use of aft swept wing tips”. In: *Aeronautical Journal* 93.930 (1989), pp. 400–405. ISSN: 00019240.

[11] Max M. Munk. “The Minimum Induced Drag of Airfoils”. In: *NACA Report 121* (1923).

[12] P.J. Gage. “New Approaches to Optimisation in Aerospace Conceptual Design”. In: *nasa.gov* March (1994).

[13] R. T. Whitcomb. “A design approach and selected wind tunnel results at high subsonic speeds for wing-tip mounted winglets”. In: *Nasa Tn D-8260* July (1976), pp. 1–33. URL: `https://ntrs.nasa.gov/archive/nasa/casi.ntrs.nasa.gov/19760019075.pdf`.

[14] Joel Guerrero, Marco Sanguineti, and Kevin Wittkowski. “CFD Study of the Impact of Variable Cant Angle Winglets on Total Drag Reduction”. In: *Aerospace* 5.4 (2018), p. 126. ISSN: 2226-4310. DOI: `10.3390/aerospace5040126`.

[15] Shaun N. Skinner and Hossein Zare-Betash. “Aerodynamic design optimisation of non-planar lifting surfaces”. In: *57th AIAA/ASCE/AHS/ASC Structures, Structural Dynamics, and Materials Conference* January (2015), pp. 1–21. DOI: `10.2514/6.2016-0164`.

[16] James E. Hackett. *Vortex Diffuser patent*. 1980. URL: `https://patents.google.com/patent/US4190219A/en`.

[17] Jeffrey A. Jupp and Peter H. Rees. *US Patent Application for:”Aircraft Wing and Winglet Arrangment*. 1987.

[18] I. Whitehouse. “Wing Tip Fences to Sharks: The Development of Airbus Winglets”. In: *Wing Aerodynamic Design, Airbus Operations Ltd.* 5 (2014), pp. 1–8.

[19] P. Panagiotou, P. Kaparos, and K. Yakinthos. “Winglet design and optimization for a MALE UAV using CFD”. In: *Aerospace Science and Technology* 39 (2014), pp. 190–205. ISSN: 12709638. DOI: `10.1016/j.ast.2014.09.006`. URL: `http://dx.doi.org/10.1016/j.ast.2014.09.006`.

[20] Ali Elham and Michel J.L. Van Tooren. “Winglet multi-objective shape optimization”. In: *Aerospace Science and Technology* 37 (2014), pp. 93–109. ISSN: 12709638. DOI: `10.1016/j.ast.2014.05.011`. URL: `http://dx.doi.org/10.1016/j.ast.2014.05.011`.

[21] Harry H Heyson, Gregory D Riebe, and Cynthia L Fulton. “Theoretical parametric study of the relative advantages of winglets and wing-tip extensions”. In: (1977).

[22] Mark D. Maughmer. “Design of winglets for high-performance sailplanes”. In: *Journal of Aircraft* 40.6 (2003), pp. 1099–1106. ISSN: 15333868. DOI: `10.2514/2.7220`.

[23] Carlos Simão Ferreira. *AE4135: Rotor and Wake Aerodynamics slides*. 2020.

[24] Mac Gaunaa and Jeppe Johansen. “Determination of the maximum aerodynamic efficiency of wind turbine rotors with winglets”. In: *Journal of Physics: Conference Series* 75.1 (2007). ISSN: 17426596. DOI: `10.1088/1742-6596/75/1/012006`.

[25] R. Muller. “The Influence of Winglets on Rotor Aerodynamics”. In: (1986).

[26] Jeppe Johansen and Niels N Sørensen. “Aerodynamic investigation of Winglets on Wind Turbine Blades using CFD”. In: *Risø National Laboratory* 1543.February (2006), pp. 1–17. ISSN: 0021-8790.

[27] Jeppe Johansen and Niels N. Sørensen. “Numerical analysis of winglets on wind turbine blades using CFD”. In: *European Wind Energy Conference and Exhibition 2007, EWEC 2007* 2.February (2007), pp. 1184–1189.

[28] E. Ferrer and X. Munduate. “Wind turbine blade tip comparison using CFD”. In: *Journal of Physics: Conference Series* 75.1 (2007). ISSN: 17426596. DOI: `10.1088/1742-6596/75/1/012005`.

[29] Mohamed Khaled et al. “Investigation of a small Horizontal–Axis wind turbine performance with and without winglet”. In: *Energy* 187 (2019), p. 115921. ISSN: 03605442. DOI: `10.1016/j.energy.2019.115921`. URL: `https://doi.org/10.1016/j.energy.2019.115921`.

[30] Frederik Zahle et al. “Computational fluid dynamics-based surrogate optimization of a wind turbine blade tip extension for maximising energy production”. In: *Journal of Physics: Conference Series* 1037.4 (2018). ISSN: 17426596. DOI: `10.1088/1742-6596/1037/4/042013`.

[31] Sohail R. Reddy et al. “Bladelets-Winglets on Blades of Wind Turbines: A Multiobjective Design Optimization Study”. In: *Journal of Solar Energy Engineering, Transactions of the ASME* 141.6 (2019). ISSN: 15288986. DOI: `10.1115/1.4043657`.

[32] Monier A. Elfarra, Nilay Sezer-Uzol, and I. Sinan Akmandor. “NREL VI rotor blade: numerical investigation and winglet design and optimization using CFD”. In: *Wind Energy* February 2013 (2013), pp. 605–626. DOI: `10.1002/we.1593`.

[33] K. C. Giannakoglou. “Design of optimal aerodynamic shapes using stochastic optimization methods and computational intelligence”. In: *Progress in Aerospace Sciences* 38.1 (2002), pp. 43–76. ISSN: 03760421. DOI: `10.1016/S0376-0421(01)00019-7`.

[34] Damir Vučina, Ivo Marinić-Kragić, and Zoran Milas. “Numerical models for robust shape optimization of wind turbine blades”. In: *Renewable Energy* 87 (2016), pp. 849–862. ISSN: 18790682. DOI: `10.1016/j.renene.2015.10.040`.

[35] Mads H.Aa Madsen et al. “Multipoint high-fidelity CFD-based aerodynamic shape optimization of a 10 MW wind turbine”. In: *Wind Energy Science* 4.2 (2019), pp. 163–192. ISSN: 23667451. DOI: `10.5194/wes-4-163-2019`.

[36] A. F.P. Ribeiro, A. M. Awruch, and H. M. Gomes. “An airfoil optimization technique for wind turbines”. In: *Applied Mathematical Modelling* 36.10 (2012), pp. 4898–4907. ISSN: 0307904X. DOI: `10.1016/j.apm.2011.12.026`. URL: `http://dx.doi.org/10.1016/j.apm.2011.12.026`.

[37] Matias Sessarego et al. “Aerodynamic wind-turbine rotor design using surrogate modeling and three-dimensional viscous-inviscid interaction technique”. In: *Renewable Energy* 93 (2016), pp. 620–635. ISSN: 18790682. DOI: `10.1016/j.renene.2016.03.027`.

[38] Benjamin T Bertka. “An Introduction to Bezier Curves , B-Splines , and Tensor Product Surfaces with History and Applications”. In: *History* (2008), pp. 1–13.

[39] G. Sieros et al. “Upscaling wind turbines: theoretical and practical aspects and their impact on the cost of energy”. In: *Wind Energy* 15.1 (Jan. 2012), pp. 3–17. ISSN: 10954244. DOI: `10.1002/we.527`. URL: `http://doi.wiley.com/10.1002/we.527`.

[40] Matias Sessarego, Néstor Ramos-Garcia, and Wen Zhong Shen. “Analysis of winglets and sweep on wind turbine blades using a lifting line vortex particle method in complex inflow conditions”. In: *Journal of Physics: Conference Series* 1037.2 (2018). ISSN: 17426596. DOI: `10.1088/1742-6596/1037/2/022021`.

[41] Martin Hansen. *Aerodynamics of Wind Turbines, 2nd edition*. Routledge, May 2013. ISBN: 9781849770408. DOI: `10.4324/9781849770408`. URL: `https://www.taylorfrancis.com/books/9781136572265`.

[42] E. Branlard and M. Gaunaa. “Cylindrical vortex wake model: right cylinder”. In: *Wind Energy* 18.11 (Nov. 2015), pp. 1973–1987. ISSN: 10954244. DOI: `10.1002/we.1800`. URL: `https://onlinelibrary.wiley.com/doi/10.1002/we.1800`.

[43] Ryan Barrett and Andrew Ning. “Comparison of airfoil precomputational analysis methods for optimization of wind turbine blades”. In: *IEEE Transactions on Sustainable Energy* 7.3 (2016), pp. 1081–1088. ISSN: 19493029. DOI: `10.1109/TSTE.2016.2522381`.

[44] B Mutlu Sumer. *Lecture Notes on Turbulence Technical University of Denmark*. Technical University of Denmark, 2013.

[45] M. Drela. “XFOIL: an analysis and design system for low Reynolds number airfoils.” In: *Low Reynolds Number Aerodynamics. Proc. Conf., Notre Dame, U.S.a., June 5-7, 1989 Edited By T.J. Mueller* 54, Berlin, Germany, Springer-Verlag, 1989 (1989), pp. 1–12. DOI: `10.1007/978-3-642-84010-4-1`.

[46] Research in Flight. *Flightstream*. 2018. URL: `https://www.researchinflight.com/`.

[47] Matias Sessarego, Néstor Ramos-García, and Wen Zhong Shen. “Development of a Fast Fluid-Structure Coupling Technique for Wind Turbine Computations”. In: *Journal of Power and Energy Engineering* 03.07 (2015), pp. 1–6. ISSN: 2327-588X. DOI: `10.4236/jpee.2015.37001`.

[48] Matias Sessarego et al. “Design optimization of a curved wind turbine blade using neural networks and an aero-elastic vortex method under turbulent inflow”. In: *Renewable Energy* 146 (2020), pp. 1524–1535. ISSN: 18790682. DOI: `10.1016/j.renene.2019.07.046`.

[49] Andy Keane, Alexander Forrester, and Andras Sobester. *Engineering Design via Surrogate Modelling: A Practical Guide*. 2008. ISBN: 9780470060681. DOI: `10.2514/4.479557`.

[50] Tinkle Chugh. “Scalarizing functions in Bayesian multiobjective optimization”. In: *arXiv* (2019).

[51] Eric Brochu, Vlad M. Cora, and Nando de Freitas. “A Tutorial on Bayesian Optimization of Expensive Cost Functions, with Application to Active User Modeling and Hierarchical Reinforcement Learning”. In: (2010). URL: `http://arxiv.org/abs/1012.2599`.

[52] Gregor Urban et al. “Do deep convolutional nets really need to be deep and convolutional?” In: *5th International Conference on Learning Representations, ICLR 2017 - Conference Track Proceedings* 2014 (2017), pp. 1–13.

[53] D. A. Fadare. “The application of artificial neural networks to mapping of wind speed profile for energy application in Nigeria”. In: *Applied Energy* 87.3 (2010), pp. 934–942. ISSN: 03062619. DOI: `10.1016/j.apenergy.2009.09.005`. URL: `http://dx.doi.org/10.1016/j.apenergy.2009.09.005`.

[54] Laurent Valentin Jospin et al. “Hands-on Bayesian Neural Networks - a Tutorial for Deep Learning Users”. In: *arXiv* 1.1 (2020), pp. 1–35. ISSN: 23318422.

[55] Nicolas Durrande et al. *Introduction to Gaussian Process Surrogate Models*. 2017.

[56] J E Smith. *Introduction toEvolutionaryComputing*. 2015, pp. 1–294. ISBN: 9783662448731. URL: `papers2://publication/uuid/F189C4FB-EB51-43FE-B6FC-17BAF1BF36C8`.

[57] Z. Lyu, Z. Xu, and J.R.R.A. Martins. “Benchmarking Optimization Algorithms for Wing Aerodynamic Design Optimization”. In: *The Eighth International Conference on Computational Fluid Dynamics* (2014), p. 18.

[58] Changping Liang and Huaxing Li. “Effects of optimized airfoil on vertical axis wind turbine aerodynamic performance”. In: *Journal of the Brazilian Society of Mechanical Sciences and Engineering* 40.2 (2018), pp. 1–9. ISSN: 18063691. DOI: `10.1007/s40430-017-0926-2`. URL: `https://doi.org/10.1007/s40430-017-0926-2`.

[59] C. Bak et al. “Description of the DTU 10 MW Reference Wind Turbine Department of Wind Energy I-Report”. In: July (2013), pp. 1–138. URL: `https://dtu-10mw-rwt.vindenergi.dtu.dk`.

[60] F. Grasso. “Modeling and effects of base drag on thick airfoils design”. In: *32nd ASME Wind Energy Symposium* January (2014), pp. 1–9. DOI: `10.2514/6.2014-0168`.

[61] Neal J. Pfeiffer. “Numerical winglet optimization”. In: *AIAA Paper* (2004), pp. 1960–1963. DOI: `10.2514/6.2004-213`.

[62] Vivek Ahuja and R. J. Hartfield. “Aerodynamic loads over arbitrary bodies by method of integrated circulation”. In: *Journal of Aircraft* 53.6 (2016), pp. 1719–1730. ISSN: 15333868. DOI: `10.2514/1.C033619`.

[63] Vivek Ahuja. *Personal Communication*.

[64] Xiaofan Fei. “Evaluation of a commercial surface vorticity flow solver for the modeling of propeller-wing interaction”. In: *AIAA Scitech 2019 Forum* (2019), pp. 1–19. DOI: `10.2514/6.2019-1046`.

[65] ParaPy B.V. *ParaPy*. Delft, 2021.

[66] Groupe Dassault. *CATIA*.

[67] NASA. *Induced Drag Coefficient*. 2021. URL: `https://www.grc.nasa.gov/www/k-12/airplane/induced.html`.

[68] Georgios Martinopoulos and Dimitris Missirlis. “Investigation of the Performance of a Horizontal Axis Wind Turbine With the Use of Blade Element Momentum Theory and Cfd Computations”. In: March (2014).

[69] Rajesh Vaithiyanathasamy et al. “A double wake model for interacting boundary layer methods”. In: *Wind Energy Symposium, 2018* 210029 (2018), pp. 1–15. DOI: `10.2514/6.2018-0516`.

[70] Kenneth Loenbaek. “Preliminary Wind Turbine Rotor Design”. PhD thesis. DTU Wind Energy. ISBN: 0000000000000.

[71] Arne Van Garrel. “Development of a Wind Turbine Aerodynamics Simulation Module”. In: *ECN Wind Energy* August (2003), p. 106.

[72] C Lindenburg. “Investigation into Rotor Blade Aerodynamics Analysis of the stationary measurements on the UAE phase-VI rotor in the NASA-Ames wind tunnel”. In: *Ecnnl* July (2003), p. 114. URL: `http://www.ecn.nl/docs/library/report/2003/c03025.pdf`.

[73] Jensen B O.G. Montgomerie et al. *Three-dimensional effects in stall*. Tech. rep. Petten, 1997.

[74] K Boorsma and M Caboni. “TNO report ECN Aero Module”. In: (2020).

[75] Hugh D. Currin, Frank N. Coton, and Byard Wood. “Dynamic prescribed vortex wake model for AERODYN/FAST”. In: *Journal of Solar Energy Engineering, Transactions of the ASME* 130.3 (2008), pp. 0310071–0310077. ISSN: 01996231. DOI: `10.1115/1.2931503`.

[76] T. Sant et al. “Evaluation of the lifting line vortex model approximation for estimating the local blade flow fields in horizontal-axis wind turbines”. In: *Journal of Renewable and Sustainable Energy* 8.2 (2016). ISSN: 19417012. DOI: `10.1063/1.4942785`.

[77] Luca Citi. “Introduction to Machine Learning and Data Mining”. In: 802 (2013), pp. 1–47.

[78] The GPyOpt Authors. *GPyOpt: A Bayesian Optimization framework in python*. 2016.

[79] Piero Esposito. “BLiTZ - Bayesian Layers in Torch Zoo (a Bayesian Deep Learing library for Torch)”. In: *GitHub repository* (2020). URL: `https://github.com/piEsposito/blitz-bayesian-deep-learning/`.

[80] Charles Blundell et al. “Weight uncertainty in neural networks”. In: *32nd International Conference on Machine Learning, ICML 2015* 2 (2015), pp. 1613–1622.

[81] Diederik P. Kingma and Jimmy Lei Ba. “Adam: A method for stochastic optimization”. In: *3rd International Conference on Learning Representations, ICLR 2015 - Conference Track Proceedings* (2015), pp. 1–15.

[82] Sergey Ioffe and Christian Szegedy. “Batch normalization: Accelerating deep network training by reducing internal covariate shift”. In: *32nd International Conference on Machine Learning, ICML 2015* 1 (2015), pp. 448–456.

[83] Geoffrey E. Hinton et al. “Improving neural networks by preventing co-adaptation of feature detectors”. In: (2012), pp. 1–18. URL: `http://arxiv.org/abs/1207.0580`.

[84] Abbas Ebrahimi and Ramin Mardani. “Tip-Vortex Noise Reduction of a Wind Turbine Using a Winglet”. In: *Journal of Energy Engineering* 144.1 (2018), p. 04017076. ISSN: 0733-9402. DOI: `10.1061/(asce)ey.1943-7897.0000517`.

A

Power and thrust curve fitting

Although AWSM supports parallel computing, which speeds up computations, all simulations were run on a personal desktop PC using a 6-core (12 Threads) Ryzen 2600. Running full simulations, using 26 points and running for a simulation time corresponding to six rotor diameters wake convected, takes about 600 actual seconds (or 6430 seconds in CPU time) per simulation. Looking at fig. 3.14a, for $t > 20s$ the unsteady solution converges to an asymptotic value, which is the steady value. An attempt will be made to estimate this value by only using a part of the simulation length. Two equations were suggested to estimate this value. The equations are shown in eq. (A.1) and eq. (A.2).

$$C_P = a + b \cdot \exp(-c \cdot t) \qquad \text{(A.1)} \qquad C_P = a + b \cdot \left(1 - \frac{c \cdot t}{\sqrt{1 + c^2 t^2}}\right) \qquad \text{(A.2)}$$

Both equations have to be fit from some starting point in time and up until some ending point in time. The lower the ending point, the lower the computational time of each simulation. Time t is non-dimensionalised by converting t to convected wake lengths in rotor diameters in the following plots. This is done to determine the starting and ending point, which should work for each U_∞. Firstly, the starting point of the functions are determined, meaning the functions are fit between $t_{start} < t < 6\,D_{wake}$. The values for C_P from the simulation are removed below t_{start} and the remaining values are fit using $curve\_fit$ from Python's $SciPy$ package. Once the function is fit, the quality of the fit is determined by evaluating the fitted curve at $t = 6D_{wake}$. The error is then defined as in eq. (A.3).

$$Error = \frac{C_{P,pred} - C_{P,actual}}{C_{P,actual}} \qquad \text{(A.3)}$$

First t_{start} is chosen, after which the chosen value for t_{start} is used to for fitting t_{end}. It is assumed that t_{start} and t_{end} are independent of each other for this analysis. The error as function of t_{start} is shown in fig. A.1a for both functions. Equation (A.1) shows an error close to 0% at approximately $t_{start} = 1.6\,D_{wake}$, while eq. (A.2) shows an error close 0% at approximately $t_{start} = 1\,D_{wake}$. These are the values chosen for t_{start} for the respective functions. The same procedure is done to determine t_{end}. The errors as a function of t_{end} are shown in fig. A.3b. The error generally seems to be lower for eq. (A.2), which function is chosen as fitting function for the optimisation cases.

Simulations are chosen to be run until $3D_{wake}$ to have a fair trade-off between accuracy and simulation speed.

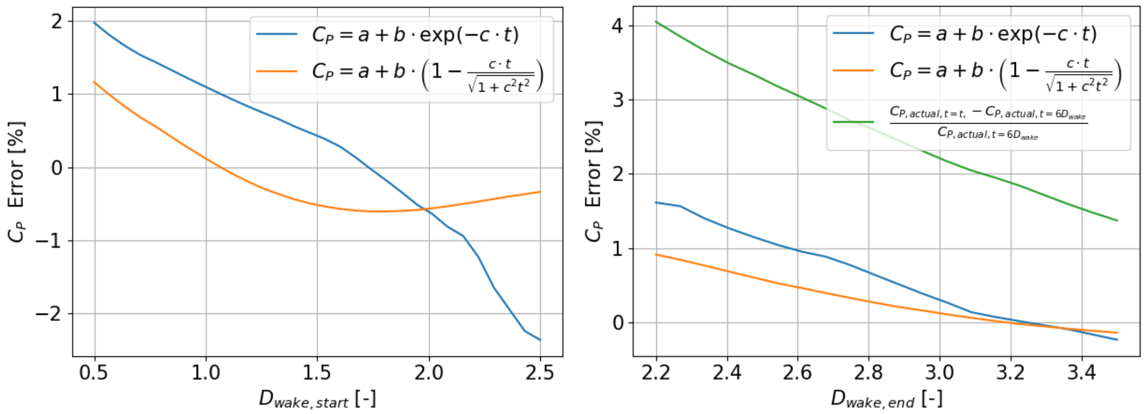

(a) Fitting t_{start}

(b) Fitting t_{end}. The green line corresponds to what error would be obtained if the no fitting is performed.

Figure A.1: Fitting t_{start} and t_{end} for a $U_\infty = 8m/s$

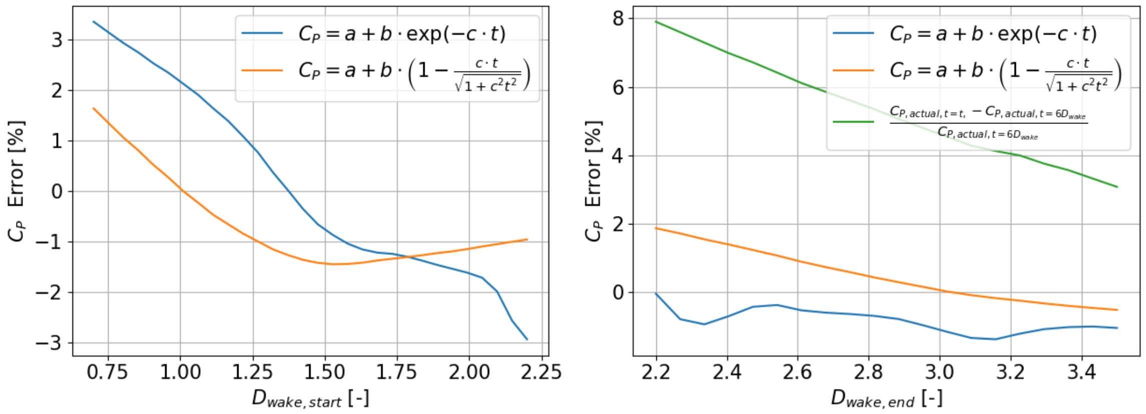

(a) Fitting t_{start}

(b) Fitting t_{end}. The green line corresponds to what error would be obtained if the no fitting is performed.

Figure A.2: Fitting t_{start} and t_{end} for a $U_\infty = 6m/s$

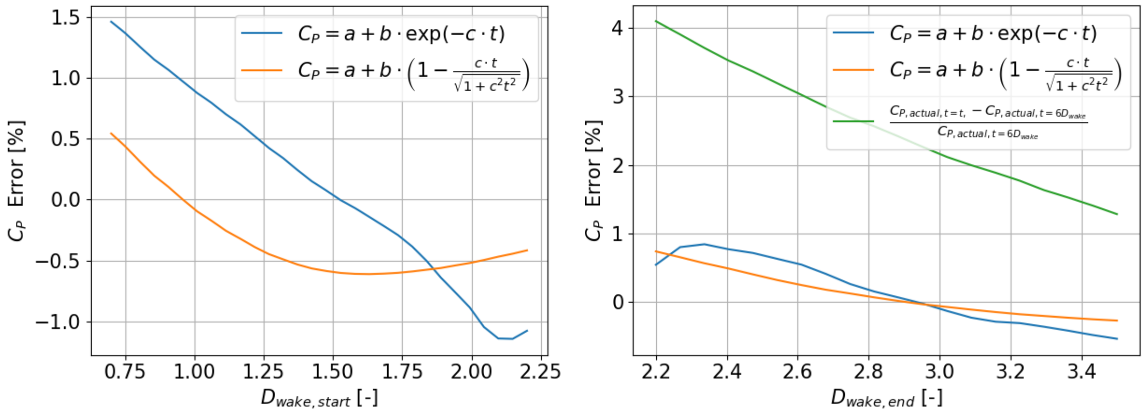

(a) Fitting t_{start}

(b) Fitting t_{end}. The green line corresponds to what error would be obtained if the no fitting is performed.

Figure A.3: Fitting t_{start} and t_{end} for a $U_\infty = 11m/s$

B

AWSM settings

B.1. Coordinate system

The coordinate system used by AWSM is shown in fig. B.1.

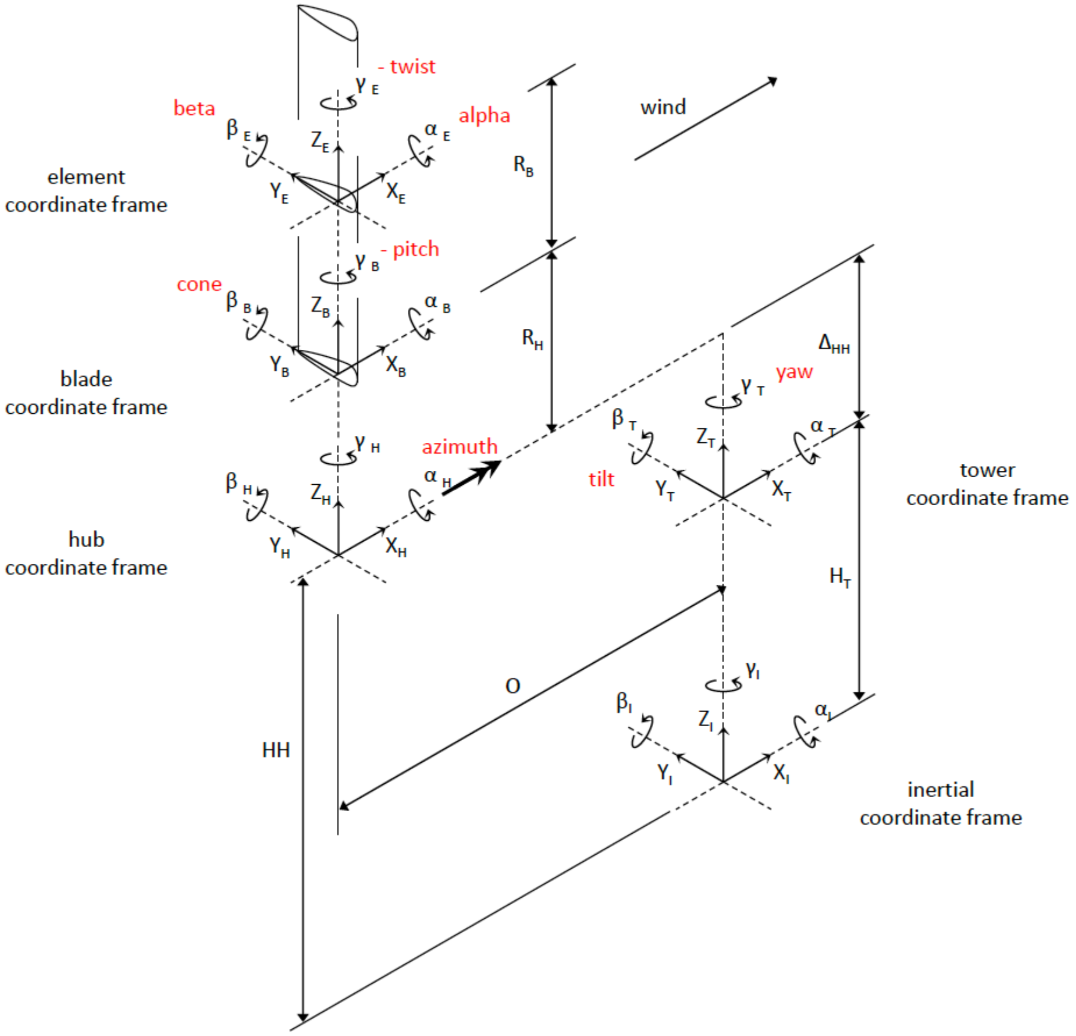

Figure B.1: Coordinate system for AWSM

B.2. Bending moment calculation

The flapwise bending moment is given as output by AWSM at the root. However, in this research, it is desired to know the bending moment at different locations on the blade. The calculate the flapwise bending moment, the $aeroresultsout$ file from AWSM is used. The $aeroresultsout$ gives the x, y and z location at which the loads on the blade are analysed and the resulting loads in the inertial frame. The loads in N/m in the x-direction, which are the loads in the out-of-plane direction are taken and are multiplied by the length along which the load acts to convert the loads into point equivalent loads. The length is calculated from the curvilinear radius, which is calculated using

$$r_{curvi_k} = \sum_{i=2}^{k} \sqrt{(x_{i-1} - x_i)^2 + (y_{i-1} - y_i)^2 + (z_{i-1} - z_i)^2} \tag{B.1}$$

Where the length dr along which a load is acting is calculated with eq. (B.2).

$$dr = < r_1, \frac{(r_2, ...r_n) + (r_1, ...r_{n-1})}{2}, r_n > \tag{B.2}$$

For each point from the $aeroresultsout$ file, the location on the blade's axis can be determined (zB in fig. B.1) using the azimuth angle of that blade from the $AeroPower$ file. The distance along the zB axis to the $\frac{r}{R}$ location the out-of-plane bending moment is analysed on is taken as the arm (l_r) for the moment calculation.

When the blade design includes a winglet, the radial forces from the winglet could become a significant contribution to the out-of-plane bending moment. The radial forces a therefore calculated from the forces in y and z using the blade azimuth angle a the time-step the moment is calculated. The x location of the blade at the given $\frac{r}{R}$ at which the at which the moment is calculated is determined, from which the arm (l_x) of the forces can be taken as the length distance from that point in x. The moment at any location on the blade can now simply be calculated by multiplying the point equivalent loads by their corresponding arm. The total equation for the out-of-plane bending moment is shown in eq. (B.3) with $0 < s < 1$.

$$m_{OOP}(s) = \sum F_{x_{i(\frac{r}{R}>s)}} \cdot dr_{(\frac{r}{R}>s)} l_{r_{(\frac{r}{R}>s)}} + F_{r_{i(\frac{r}{R}>s)}} \cdot dr_{(\frac{r}{R}>s)} l_{x_{(\frac{r}{R}>s)}} \tag{B.3}$$

The flapwise bending moment can now be calculated using

$$m_{flap} = m_{OOP}\, cos(\theta) + m_{tan}\, sin(\theta) \tag{B.4}$$

Where θ is the pitch of the blade and m_{tan} is the tangential moment.

Since the root flapwise bending moment is an output from AWSM, the calculation can be validated by setting $s = 0$. For the validation, a blade design with winglet will where the winglet parameters will varied independently, while keeping the other winglet parameters the same. The winglet parameters that are used are shown in table 4.1, the same parameters for the winglet parameter study. The error from eq. (B.3) can be determined by eq. (B.5).

$$Error = \frac{m_{flap,ref} - m_{flap}}{m_{flap,ref}} \cdot 100\% \tag{B.5}$$

Where $m_{flap,ref}$ is the value of the root flapwise bending moment as output from AWSM. The error is shown for the variation of different winglet parameters in figs. B.2 to B.4.

The errors do not exceed 0.4% for almost all cases. However, as the error seems to change when only changing winglet parameters, this error could be more significant when evaluated at locations closer to the tip. The root flapwise bending moment at the root of the baseline DTU10MW is $15.31MNm$ and only $66.41kNm$ at $\frac{r}{R} = 0.9$, using the calculation explained in this section, which is a factor of about 230, meaning the error could be as big as 46% for a $90°$ cant angle. However, the error is suspected to come from the calculation of the curvilinear radius in eq. (B.1). It is known that AWSM calculates this length slightly different, but it is unknown how exactly. The calculation using eq. (B.1) was found to be fairly accurate when no winglet is used, however seemed to differ more when the x coordinate changed of points on the blade, thus when a winglet is added to the design. Besides that, an error

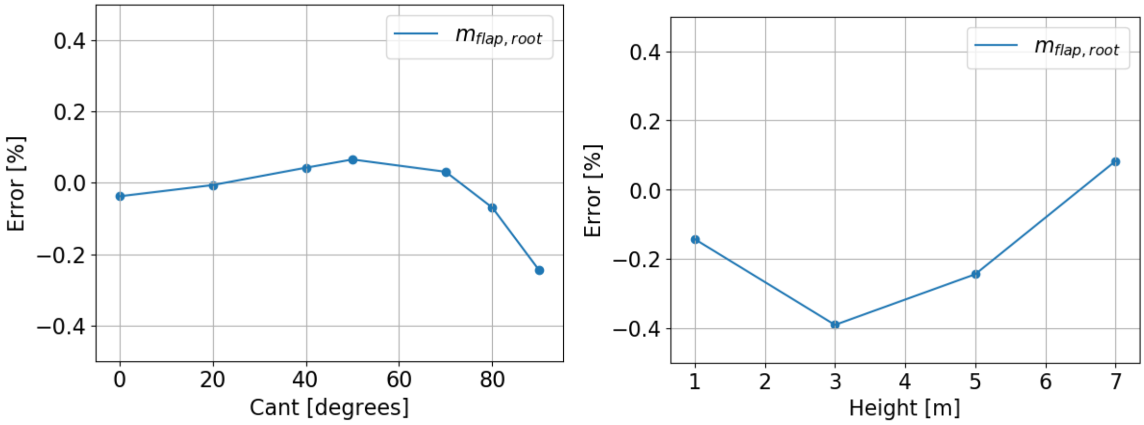

(a) Cant angle (b) Winglet height

Figure B.2: Out-of-plane bending moment calculation validation for cant angle and winglet height at $U_\infty = 8m/s$ and no pitch angle

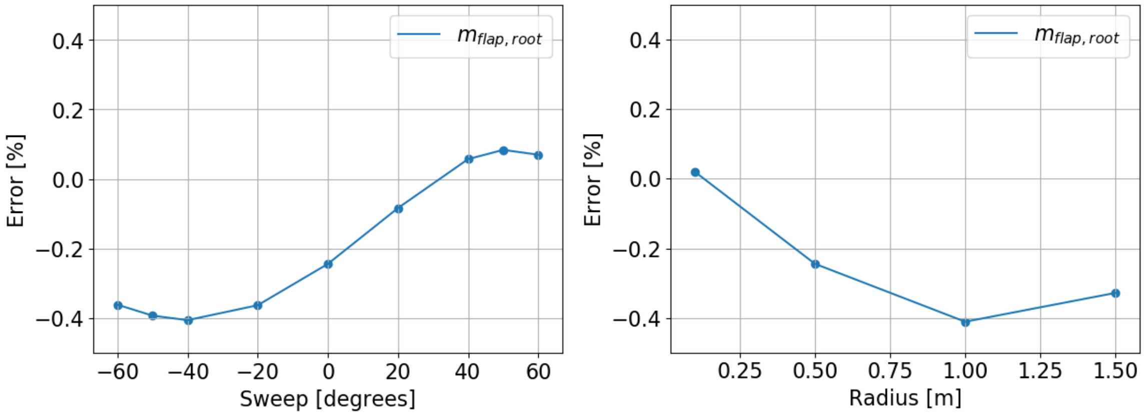

(a) (b)

Figure B.3: Out-of-plane bending moment calculation validation for sweep angle and winglet radius at $U_\infty = 8m/s$ and no pitch angle

is expected to come from using point equivalent loads, where it is expected AWSM is integrating the loads internally in the program, leading to some increase in error.

B.3. Loads for all wind speeds

This section contains the operational curves for the power and thrust as well as the normal and tangential loads for all different wind speeds analysed.
Overal, a good match was obtained for all wind speeds, with the biggest offset in tangential forces for $5m/s$ and $6m/s$ as shown in fig. B.6 and fig. B.7.

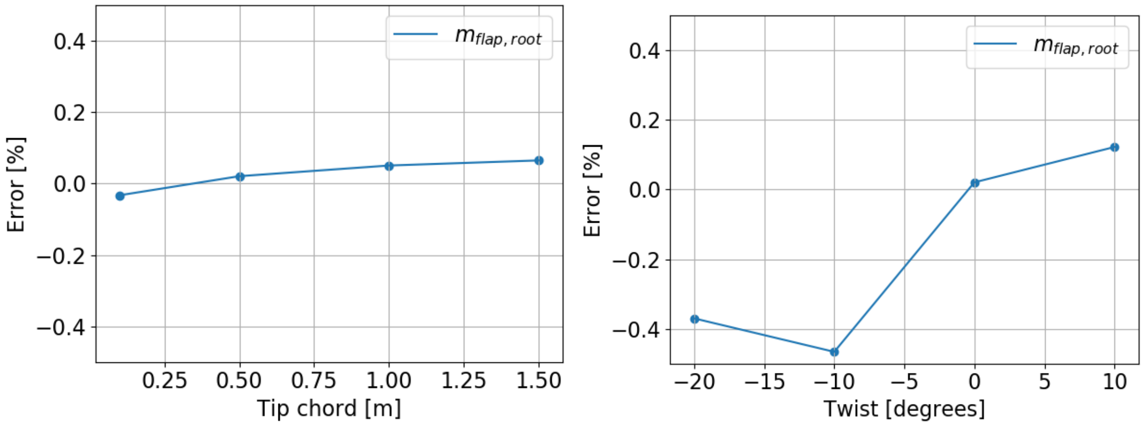

(a)

(b)

Figure B.4: Out-of-plane bending moment calculation validation for winglet tip chord and winglet twist at $U_\infty = 8m/s$ and no pitch angle

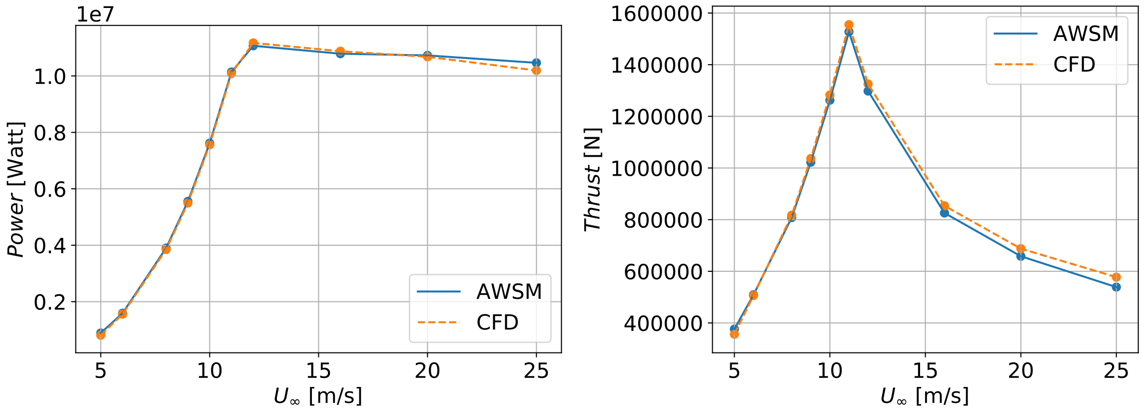

(a) Power versus wind speed

(b) Thrust versus wind speed

Figure B.5: Operational curve for power in Watt and thrust in N

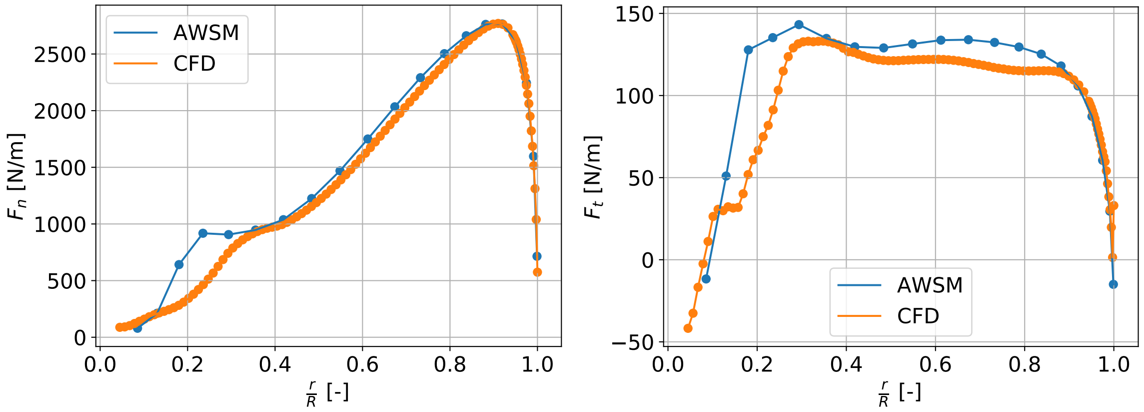

(a)

(b)

Figure B.6: Validation of loads for $U_\infty = 5m/s$

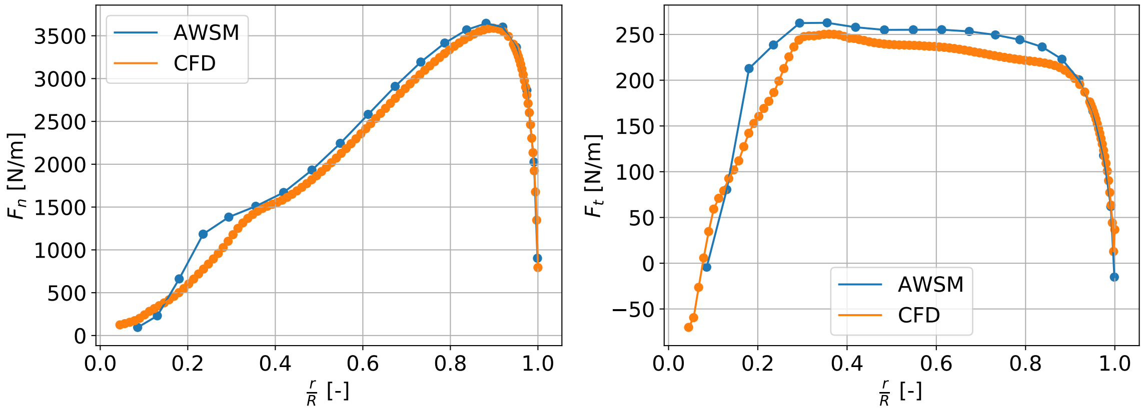

(a)

(b)

Figure B.7: Validation of loads for $U_\infty = 6m/s$

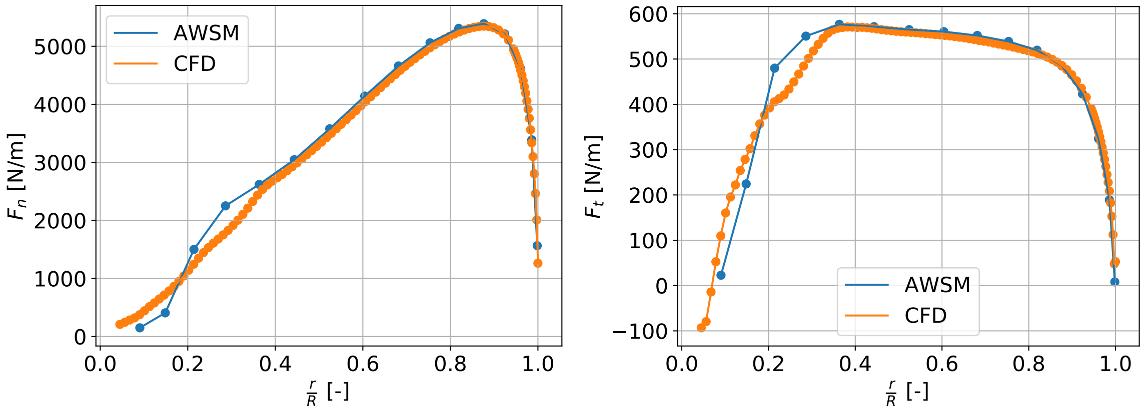

(a)

(b)

Figure B.8: Validation of loads for $U_\infty = 8m/s$

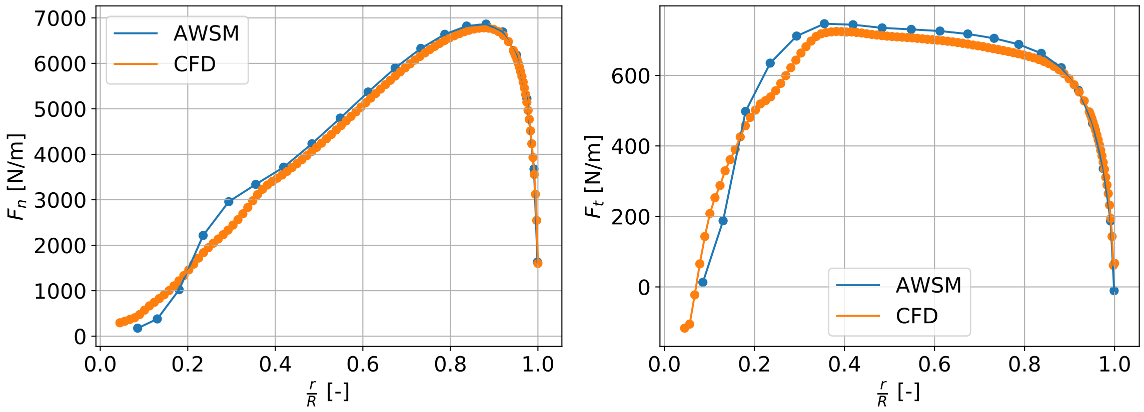

(a)

(b)

Figure B.9: Validation of loads for $U_\infty = 9m/s$

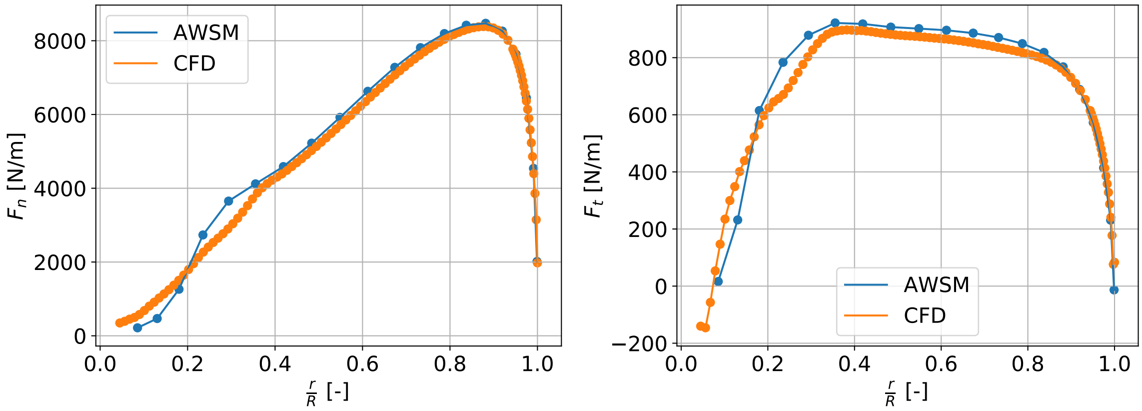

(a)

(b)

Figure B.10: Validation of loads for $U_\infty = 10m/s$

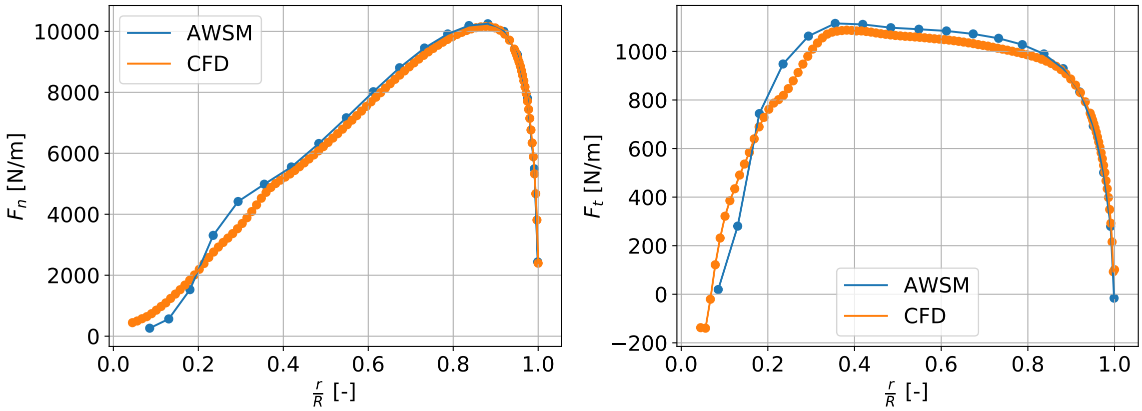

(a)

(b)

Figure B.11: Validation of loads for $U_\infty = 11m/s$

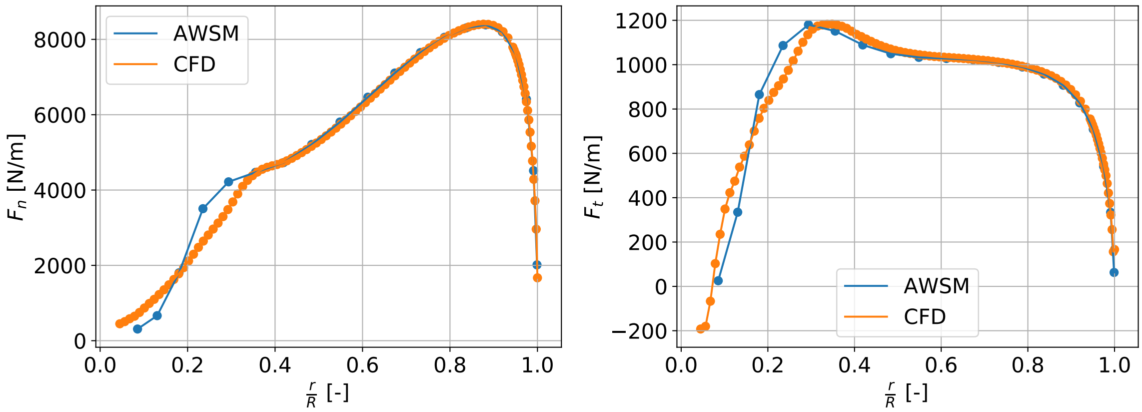

(a)

(b)

Figure B.12: Validation of loads for $U_\infty = 12m/s$

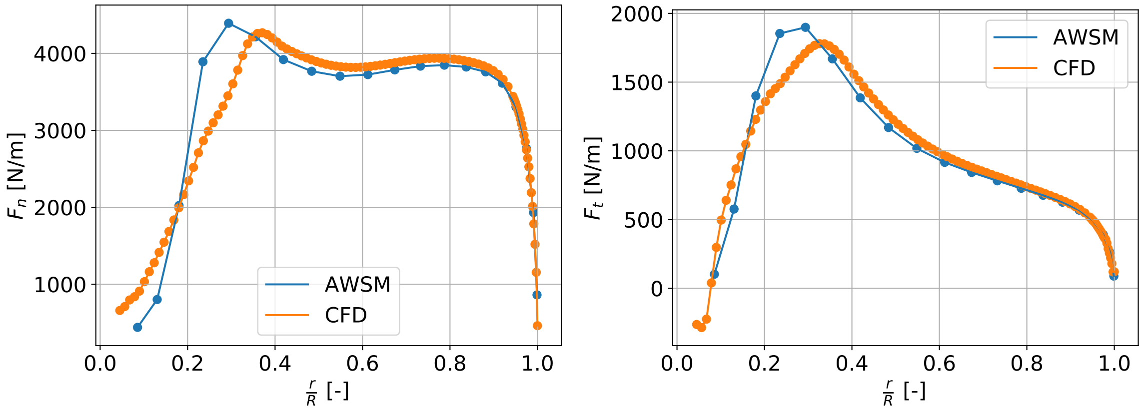

(a)

(b)

Figure B.13: Validation of loads for $U_\infty = 16m/s$

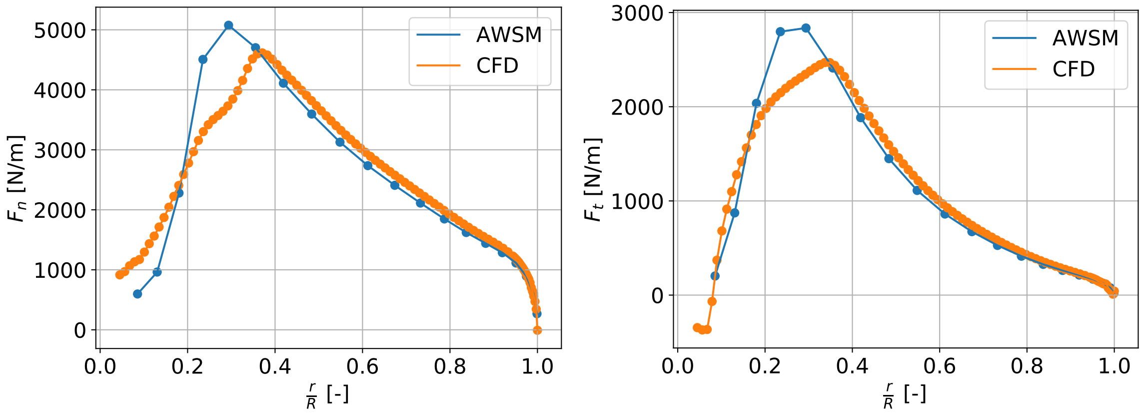

(a)

(b)

Figure B.14: Validation of loads for $U_\infty = 20m/s$

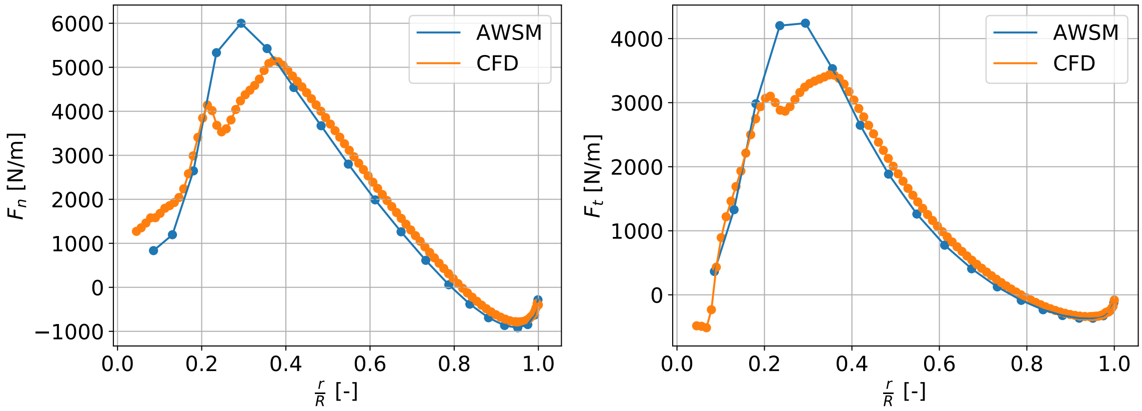

(a)

(b)

Figure B.15: Validation of loads for $U_\infty = 25m/s$

C

FlightStream plots

C.1. Spanwise panels for 2D mesh convergence

To justify the number of spanwise panels needed for the 2D mesh convergence in FlightStream, the C_l and C_d of the FFA-W3-241 airfoil was analysed for different numbers of panels in fig. C.1b. It can be seen there is no noticeable change for different numbers of spanwise panels.

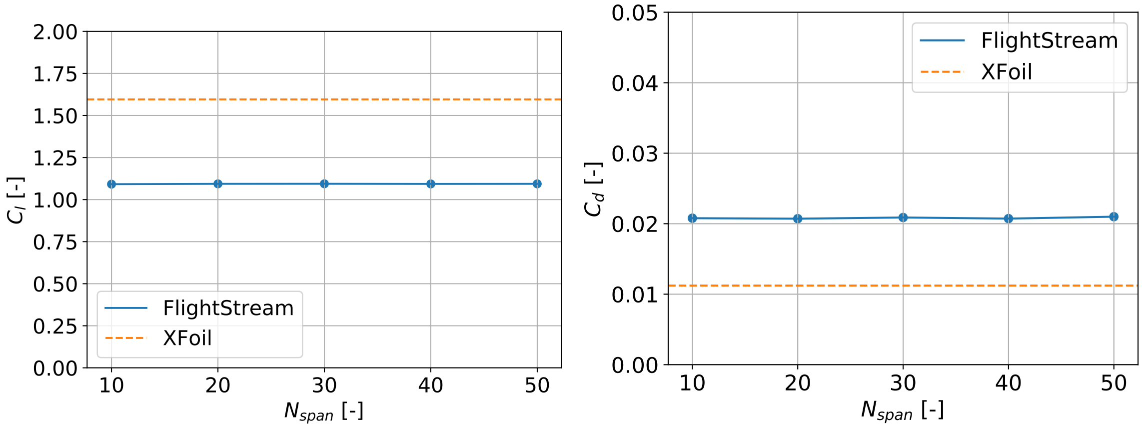

(a)

(b)

Figure C.1: Spanwise panels 2D mesh convergence

C.2. Single-objective optimisation for sweep and twist

As a test case, a single-objective Bayesian optimisation has been performed for a winglet in FlightStream. The parameters optimised for were the twist and sweep of the winglet. The initial samples are shown in fig. C.2a and the final samples after optimisation are shown in fig. C.2b. It can be seen the optimiser finds the highest C_P for a high sweep and twists between $0°$ and $5°$

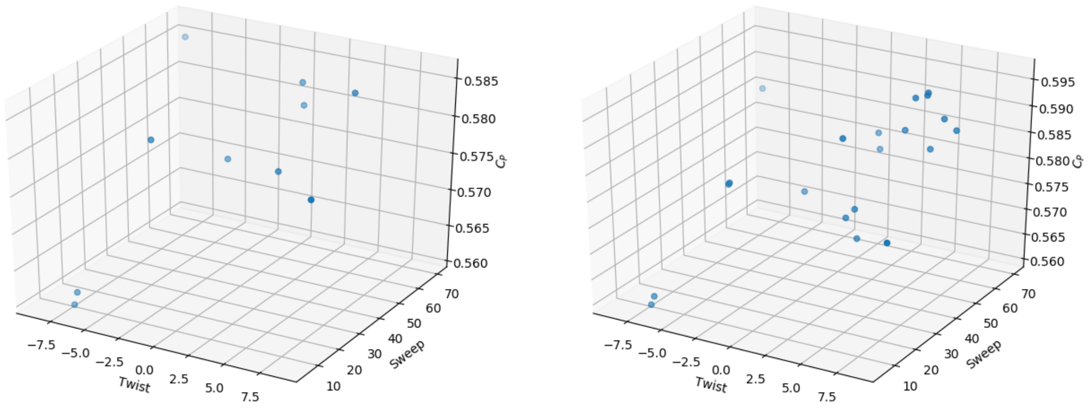

(a) Initial samples

(b) Final results

Figure C.2: Twist and sweep power optimisation for FlightStream

D

Landscape plots

This appendix shows the landscape plots for Gaussian processes, Random Forest and Bayesian Neural Networks. The plots can show some insight in what the impacts different combinations of parameters is as predicted by the surrogate models.

D.1. Gaussian Process

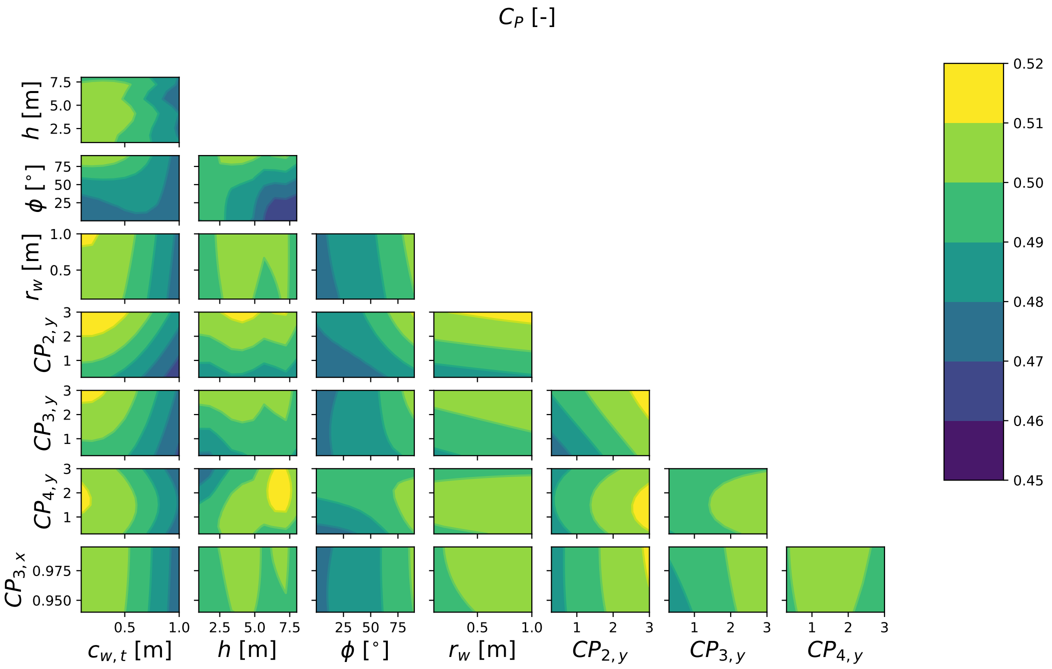

Figure D.1: Landscape plot for C_P of a GP

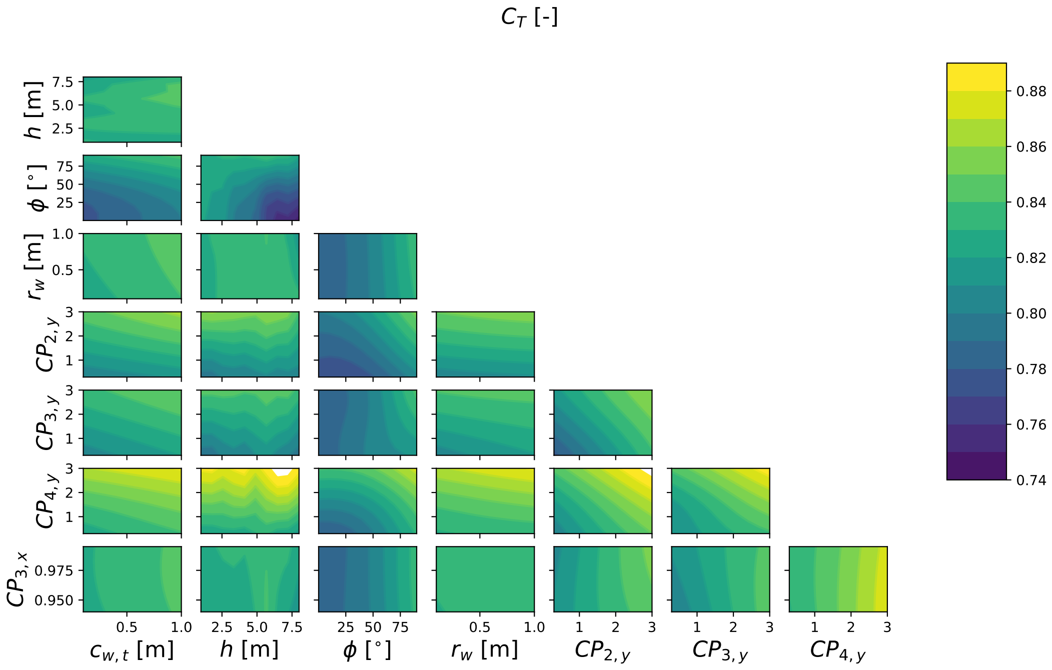

Figure D.2: Landscape plot for C_T of a GP

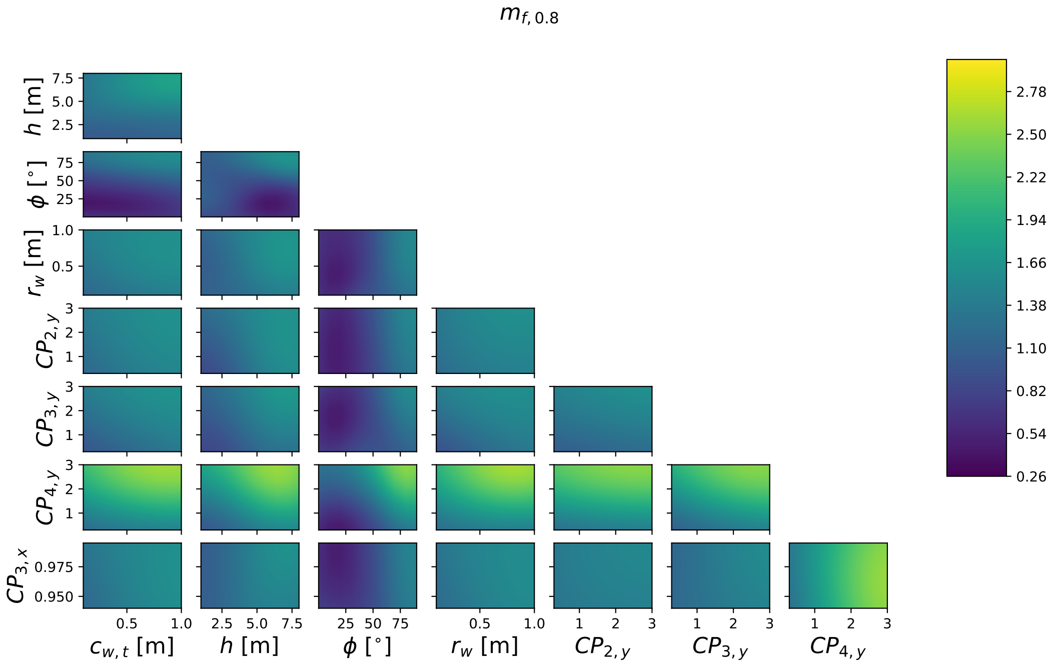

Figure D.3: Landscape plot for $m_{f,0.8}$ of a GP

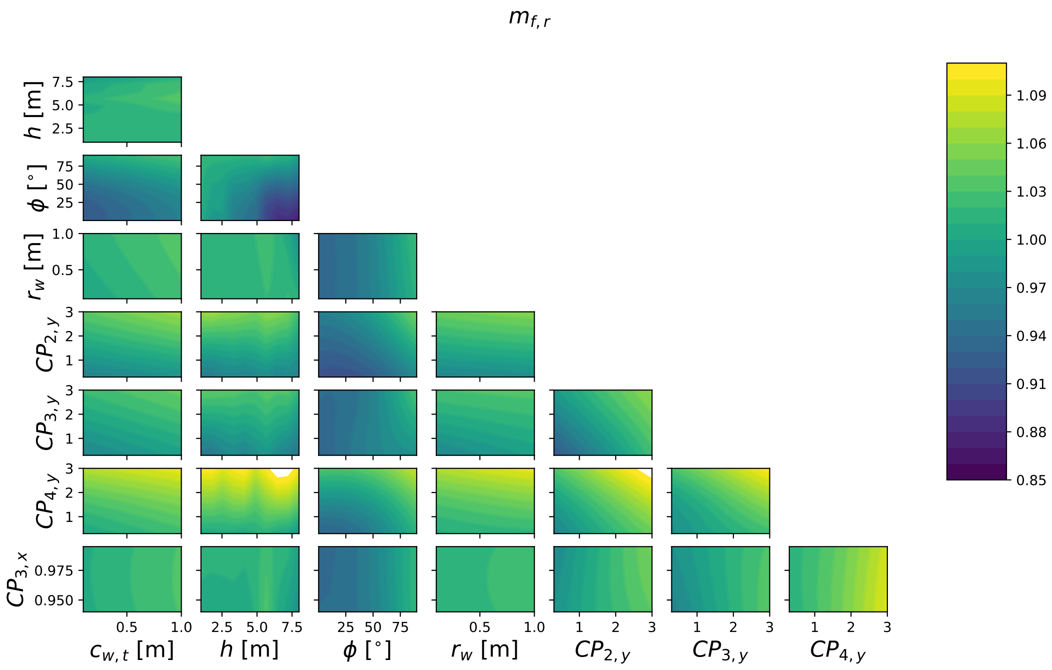

Figure D.4: Landscape plot for $m_{f,r}$ of a GP

D.2. Random Forest

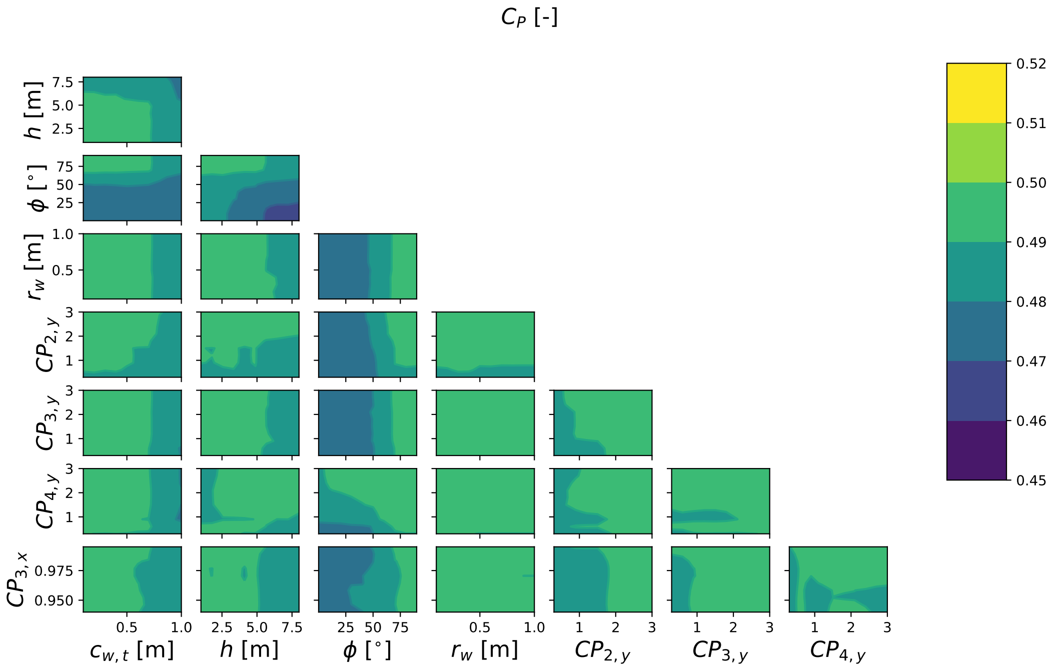

Figure D.5: Landscape plot for C_P of a RF

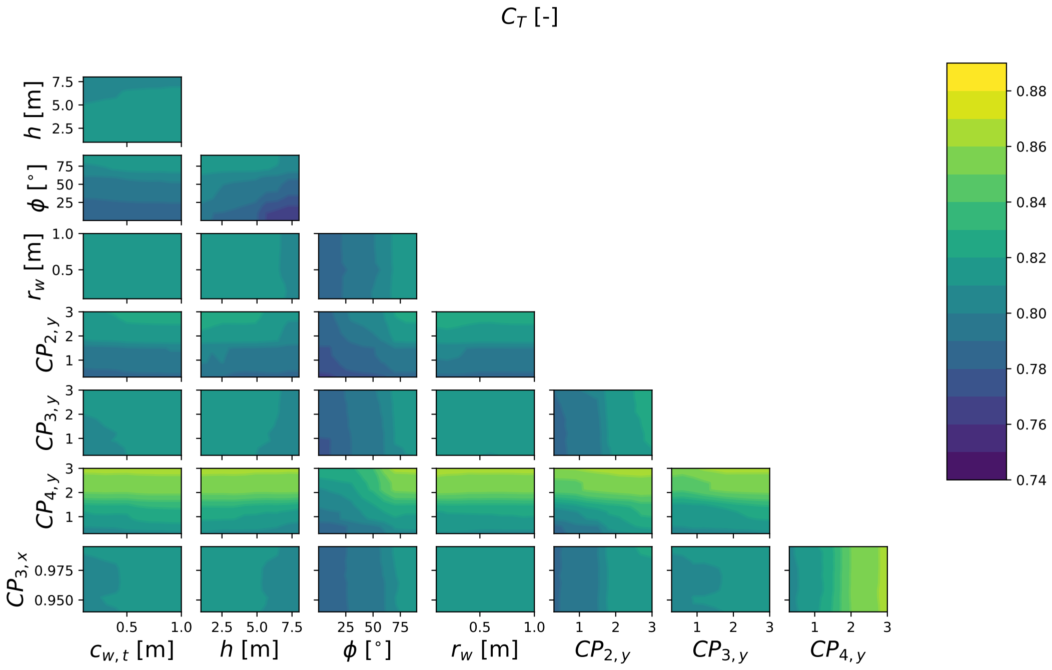

Figure D.6: Landscape plot for C_T of a RF

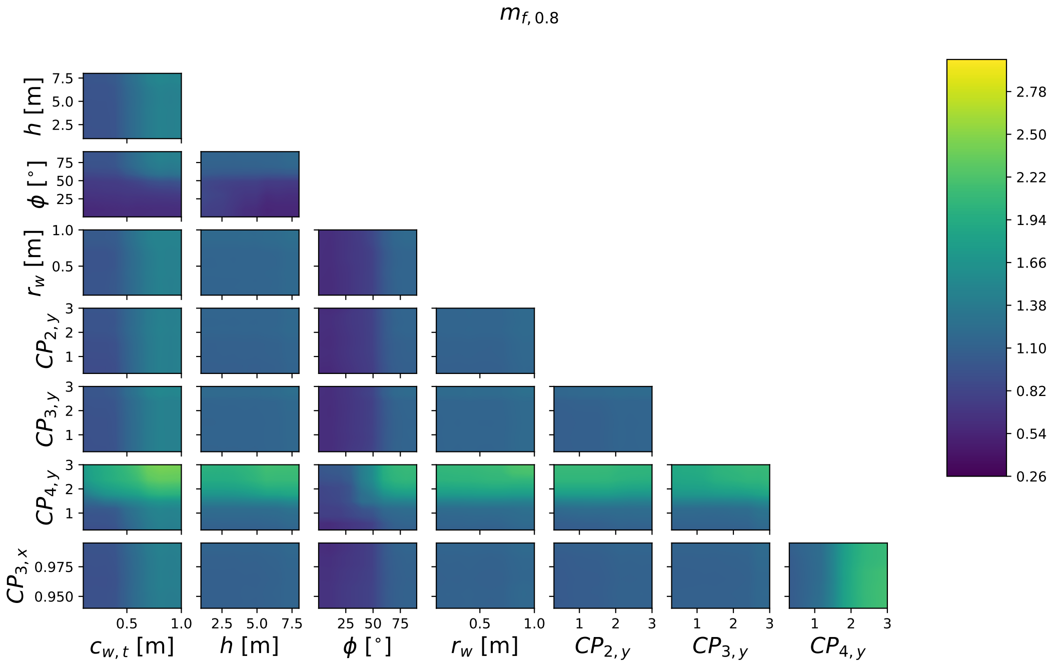

Figure D.7: Landscape plot for $m_{f,0.8}$ of a RF

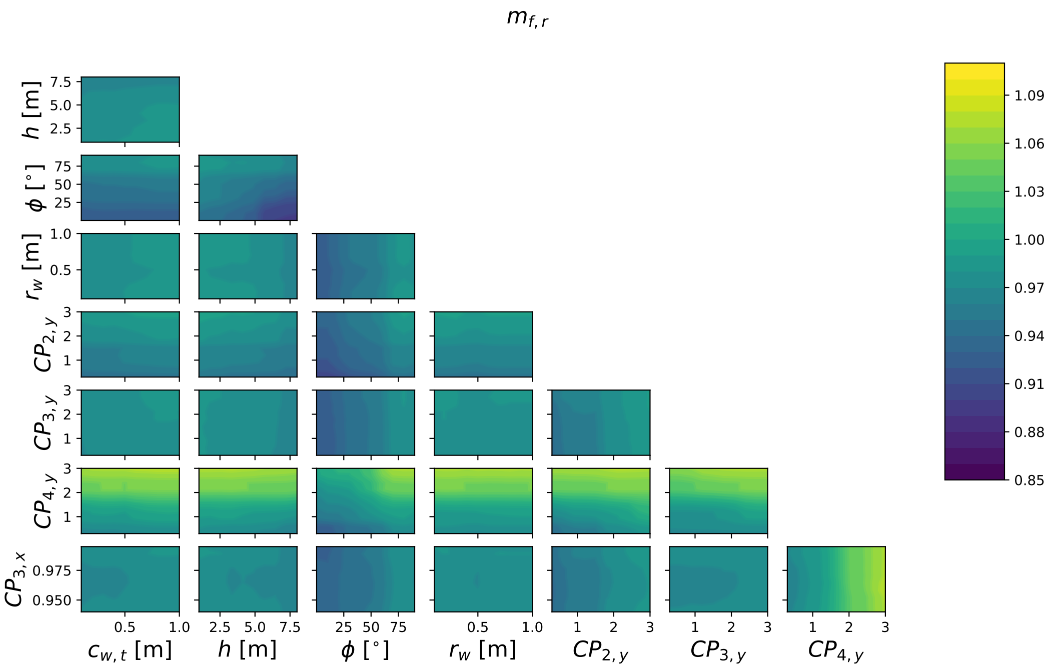

Figure D.8: Landscape plot for $m_{f,r}$ of a RF

D.3. Bayesian Neural Network

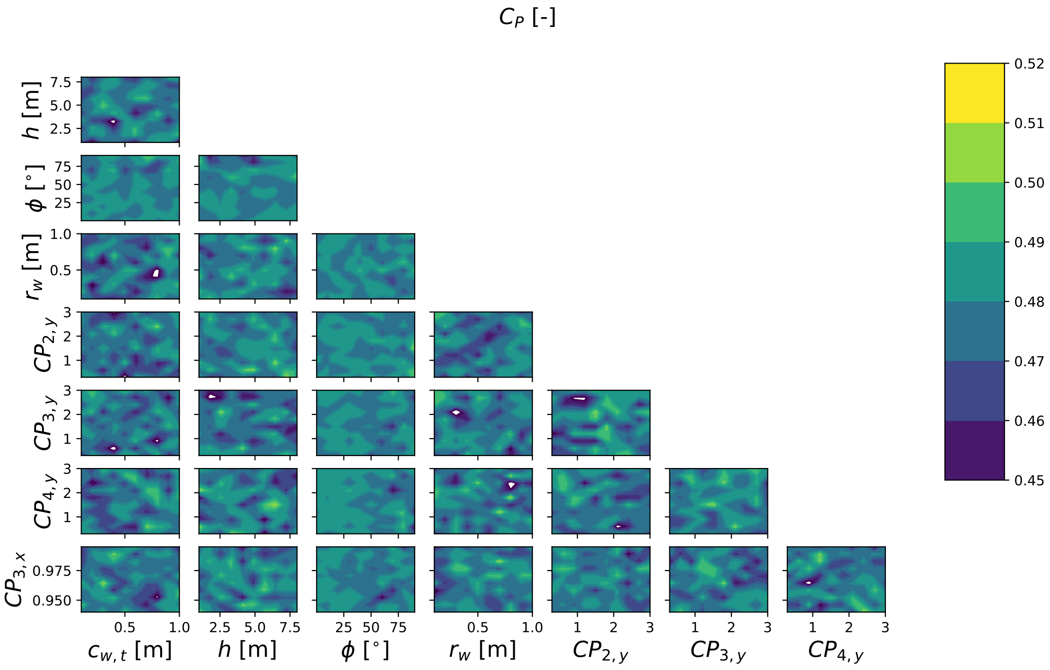

Figure D.9: Landscape plot for C_P of a BNN

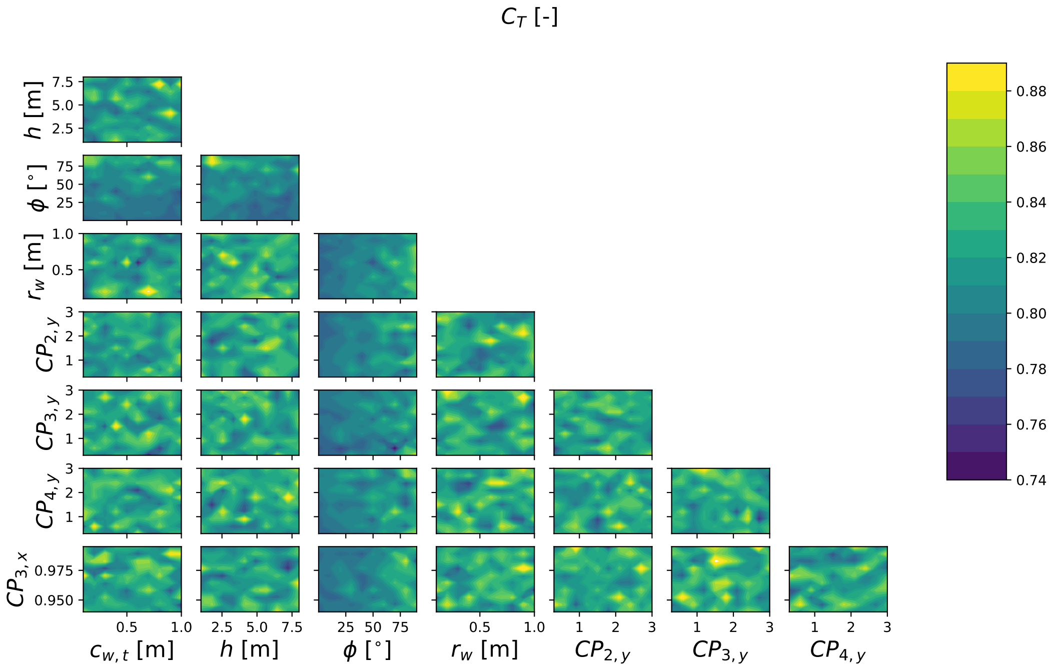

Figure D.10: Landscape plot for C_T of a BNN

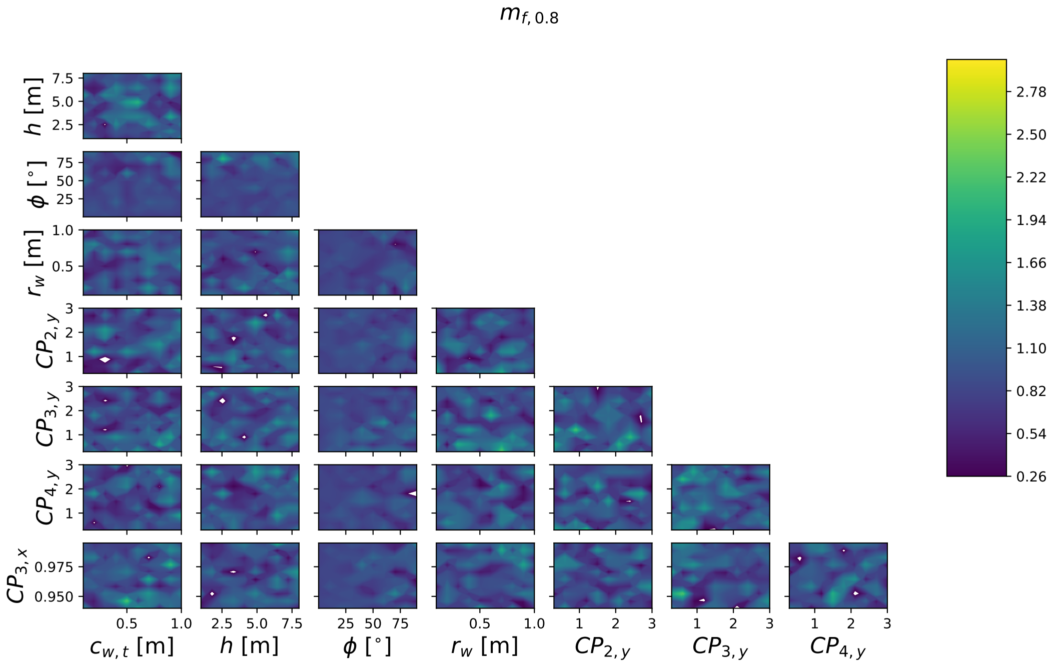

Figure D.11: Landscape plot for $m_{f,0.8}$ of a BNN

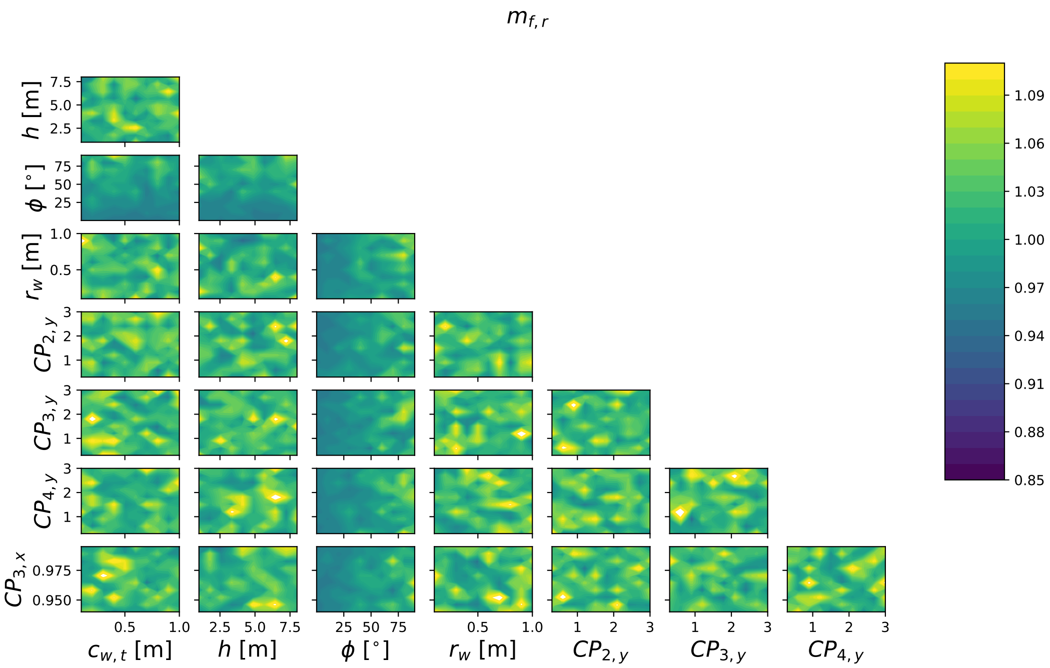

Figure D.12: Landscape plot for $m_{f,r}$ of a BNN